Canadian Boreal Forest Wildfires: An Analysis of CO, HCHO, and NO_2 in Wildfire Smoke

by

Tadhg Hearne

A thesis submitted in conformity with the requirements
for the degree of Doctor of Philosophy

Department of Physics
University of Toronto

Canadian Boreal Forest Wildfires: An Analysis of CO, HCHO, and NO_2 in Wildfire Smoke

Tadhg Hearne
Doctor of Philosophy

Department of Physics
University of Toronto
2026

Abstract

Wildfires in Canada significantly impact atmospheric chemistry and public health. Biomass burning produces carbon monoxide (CO), nitrogen dioxide (NO_2), and formaldehyde (HCHO), and can lead to ozone (O_3) formation. The research in this thesis uses a 1-D advection model and the Gaussian-flux method to calculate enhancement rates of CO, HCHO, and NO_2 for Canadian boreal forest wildfires from the summers of 2023, 2024, and 2025 using satellite data.

Enhancement rates for each species were calculated along the length of the plume using single-overpass TROPOspheric Monitoring Instrument (TROPOMI) measurements and MODerate resolution Imaging Spectroradiometer (MODIS) fire radiative power (FRP). The spatial variation of enhancement rates as a plume aged downwind was analysed and results were compared to data provided for three fires from the summer 2019 Fire Influence on Regional to Global Environments and Air Quality (FIREX-AQ) campaign. Spatial variations confirmed CO emission primarily from the fire centre, with HCHO and NO_2 primarily resulting from secondary formation in the plume.

Enhancement ratios of vertical column density enhancements for 26 boreal wildfire plumes were examined for each species and were within margins of error of previous research using in-situ measurements. Analysis of spatial and temporal variations of HCHO/NO_2 ratios provided insight into potential changes in surface-level ozone formation as the plume aged downwind. These results can help evaluate chemical

transport modelling of species evolution within a wildfire plume using TROPOMI data.

Lastly, the diurnal variation of CO emission rates was studied for 38 fire plumes as they aged. Using plume age to convert emission rates to local emission, TROPOMI data were consistent with similar changes in fire intensity observed in Geostationary Operational Environmental Satellite (GOES) FRP over the diurnal cycle of a fire from smouldering to flaming phases. Temporal changes in emission rates also showed strong correlation with variation in GOES FRP, which could provide a novel way to calculate diurnal changes in emission coefficients with a single TROPOMI overpass.

To 落合留美 *for giving me a reason to finish my PhD and to* 落合泰子 *for supporting me through the roughest parts of the last two years. Also to my best friends O'Renji and Maxwell for always being there when I needed them.*

Acknowledgements

I would first like to recognise my advisor, Kimberly Strong. I was distraught and considering leaving graduate school when I came to your office. You gave me an opportunity to join your group and follow my own project. Reading other theses from recent PhD recipients, I truly have no idea how you manage to do all the things you do, while still staying calm, polite, level-headed, and always willing to make time to speak with your students, follow their progress, mentor them, and provide them with extensive career experience and opportunities (even when it was expensive to do so). You mean so much to your students. Whenever there was a something that needed to be done to help your students, even if it was the last minute and you had a million other things to do, you somehow always did it on time with no lack of effort. You truly are a machine and I hope more people aspire to be like you. (I have no idea how you managed to have the time and patience to reread my papers so many times.) I genuinely would not have finished a PhD if you had not given me an opportunity to join your group years ago.

I want to acknowledge and thank Joseph Hung for not losing patience with me as I stared blankly at 1000s of lines of code and had no idea what I was doing. Without your help troubleshooting the code, I never would have been able to even write one chapter. Thank you also to Debora Griffin for taking the time out of your schedule to help me get the code running and all your endless and valuable help reviewing my research and providing deep insight into the field and how to better communicate my research. The time you dedicated without hesitation essentially made you my second advisor to my PhD. Thank you for all your help and patience with me.

I also want to thank Chelsea E. Stockwell for taking so much time to read and break down the research on my first paper with all the enthusiasm to build it back up. Many people would have just provided their data and moved on, but you took deep interest and care into my paper and provided invaluable knowledge into the field. Your generosity with your time is a real inspiration that I hope I can remember to pay forward to young scientists one day.

I would like to recognise my doctoral committee Professors Dylan Jones and Paul Kushner for giving me a chance to prove I could complete this work. Dylan, I could only hope to one day have your happy demeanour. Whenever I had to speak to you about something, you were always supportive and generous with your time. Paul, we sure knocked that colloquium out of the park during the roughest times of COVID. It was not easy, but we made a good team.

My research would not have been completed without the help of many other

scientists. I want to show my appreciation to my paper co-authors that took the time to read through my very lengthy papers and provide feedback: Debora Griffin, Chelsea E. Stockwell, Joseph Hung, Alan Fried, Jeff Peischl, Ilann Bourgeois, and Sarah Toshiko Moser. Also to the contributors of the FIREX-AQ campaign data: Chelsea E. Stockwell, Alan Fried, Jeff Peischl, Ilann Bourgeois, Petter Weibring, Dirk Richter, James Walega, Thomas Ryerson, Thomas Frost Hanisco, Glenn Diskin and the NASA Langley DACOM group. My research and my experience as a researcher was also financially supported by the Natural Sciences and Engineering Research Council of Canada, the School of Graduate Studies, and the Centre for Global Change Science.

Lastly, to the undergraduate students I have taught along the way, who will absolutely never read this, thank you for putting up with my lectures and mentoring. I had a profound experience teaching and learning from all of you and I greatly appreciate your patience with me and willingness to learn. Being able to teach all of you was one of the most enjoyable parts of my PhD and I learned so much from each of you. May you all live long and prosper as scientists.

Contents

Abstract ii

Acknowledgements v

List of Tables x

List of Figures xi

List of Abbreviations xix

1 Motivation 1

1.1 Canadian Wildfires . . . 1
1.2 Fire Dynamics . . . 6
1.3 Chemistry . . . 8
1.3.1 Carbon Monoxide . . . 8
1.3.2 Nitrogen Dioxide . . . 10
1.3.3 Formaldehyde . . . 12
1.3.4 Formaldehyde-Nitrogen Ratios . . . 13
1.4 Limitations in Wildfire Emissions Analysis . . . 19
1.5 Thesis Overview . . . 21
1.5.1 Scientific Objectives . . . 21
1.5.2 Methods . . . 21
1.5.3 Contributions . . . 22
1.5.4 Thesis Outline . . . 23

2 Datasets and Methods 24

2.1 Datasets . . . 24
2.1.1 TROPOMI . . . 24
2.1.2 FIREX-AQ . . . 31

2.1.3 MODIS . . . 32
2.1.4 GOES . . . 33
2.1.5 ECMWF ERA5 . . . 35
2.1.6 ESA Land Cover Product . . . 35
2.2 Gaussian-Flux Method . . . 37
2.2.1 Flux Method Theory . . . 37
2.2.2 Gaussian Method and Application . . . 41
2.3 Enhancement Rate Calculation and Adjustments . . . 44
2.4 Limitations of the Gaussian-Flux Method . . . 48
2.5 Uncertainties . . . 50
2.6 Important Definitions . . . 51

3 Summer 2023 Canadian Wildfires: CO, HCHO, and NO_2 53
3.1 Datasets and Methods . . . 54
3.2 Enhancement Rates for FIREX-AQ . . . 55
3.3 Western Canadian Wildfires . . . 65
3.3.1 Enhancement Rates . . . 65
3.3.2 Enhancement Ratios . . . 70
3.4 Conclusions . . . 77

4 Canadian Wildfires: Formaldehyde-Nitrogen Ratios 81
4.1 Datasets . . . 82
4.2 Methods . . . 82
4.3 Results and Discussion . . . 85
4.3.1 Enhancement Rates . . . 85
4.3.2 Formaldehyde to Nitrogen Dioxide Ratios . . . 86
4.4 Conclusions . . . 95

5 Diurnal Variability of TROPOMI CO Versus GOES FRP 98
5.1 Datasets . . . 99
5.2 Methods . . . 99
5.2.1 Gaussian-Flux Methodology . . . 99
5.2.2 Method Modifications . . . 104
5.3 Carbon Monoxide in Wildfire Plumes . . . 104
5.3.1 Evolution of Emission Rates . . . 104
5.3.2 Diurnal Variability . . . 106
5.4 Conclusions . . . 117

6 Conclusions and Future Work **121**
6.1 Summary 121
6.2 Future Work 124

Bibliography **127**

List of Tables

2.1 Uncertainties in the enhancement rates derived for each species. All values in each uncertainty type are summed in quadrature for totals, while Total Uncertainty is a quadrature sum of Total Random and Total Systematic. 51

2.2 Relevant terms for calculated and retrieved values analysed in this thesis, their units, relevant equations, and definitions. N/A stands for "not applicable." 52

3.1 Wildfires from NOAA's DC-8 FIREX-AQ summer 2019 campaign flights that are within a few hours of TROPOMI overpass times. For each date, the following information is provided: the FIREX-AQ-designated name and fire code, the initial and final aircraft transect times, the coordinates of the fire centre, the TROPOMI overpass orbit number and time of overpass. All times are in UTC. Greyed out fields indicate no second orbit was observed. The highlighted fires were fires that showed the most distinguished plume and were able to be analysed by this method. *Note: End times that cross midnight are on the next date.* 55

3.2 The naming convention for the Western Canadian fires discussed in this paper, with the province of origin, TROPOMI orbit number and dates (YYYYMMDD) and times of overpass in UTC, the coordinates of the fire centre used, and the ESA CCI Land Product type of each fire. 67

4.1 The 2023 fires used in this study, with the naming convention coordinates, adapted from Table 3.2 of Chapter 3, including the province or territory of origin, TROPOMI orbit number, date of fire (YYYYMMDD), time of overpass in UTC, coordinates of the fire centre, and the CCI Land Product type of each fire. 83

4.2 The 2025 fires used in this study, with naming convention and coordinates in this study in the same format as Table 4.1. 84

4.3 FNRs indicating VOC- or NO_2-sensitive O_3 production from Jin et al. (2020), derived from OMI satellite data and model data. 86

5.1 The naming convention for the summer 2023 fires discussed in this paper, with the province of origin, TROPOMI orbit number and dates (YYYYMMDD) and times of overpass in UTC, the coordinates of the fire centre, and the ESA CCI Land Product type of each fire. 101

5.2 Same as Table 5.1 for the summer 2024 wildfires used in this study. 102

5.3 Same as Table 5.1 for the summer 2025 wildfires used in this study. 103

List of Figures

1.1 Map of the total land cover in Canada burned from 1972 to 2024, with data from NRCan in red and the Canadian National Fire Database (NFDB) in orange (NRCan, 2025a). . . . 2

1.2 The total area burned in Canada from May 1 to September 30 for 2012 to 2025, using aggregated data from NRCan (NRCan, 2025b). Data provided for 2025 go to September 21. . . . 3

1.3 The total area burned, in hectares, in Canada per year, for the whole year, using data from the Canadian Interagency Forest Fire Centre and NRCan (CIFFC, 2025a). Data provided for 2025 go to September 21. . . . 4

1.4 Global map showing: (a) the global annual mean of PM2.5 concentrations for the 2023 Canadian wildfires; (b/c/d) the regional annual mean (weighted by population) of PM2.5 concentrations for Canada, the USA, and Europe, respectively; (e) the global percentage of the annual mean from Canadians wildfires in 2023 to total fire-related PM2.5 concentrations; (f-h) the regional percentage of the annual mean PM2.5 exposure for Canada, the USA, and Europe, respectively. Data retrieved from a combination of chemical transport models, global fire emission inventories, satellite aerosol optical depth, and machine learning. *Image from Zhang, Q. et al. (2025).* . . . 5

1.5 Photos showing (a) the flaming and smouldering of surface fuels where the flaming phase dominates, (b) flaming and smouldering of large fuels such as logs and surrounding grass and foliage where the smouldering phase dominates, and (c) short- and long-term smouldering occurring in the combustion of a large log. *Figure from Liu et al. (2022).* . . . 7

1.6 A visualisation demonstrating the concept of the changes in combustion efficiency over time and total fuel consumed for a large fire with abundant fuel (red dotted line), a small fire with localised temperature inversions and minimal combustion (orange dotted line), and a low-intensity prescribed fire (grey dotted line). As fuel is consumed, combustion efficiency decreases and the fire transitions into the smouldering phase. *Figure from Liu et al. (2022).* . . . 8

1.7 A map adapted from Copernicus Sentinel-5P Mapping Portal showing the average CO total column volume mixing ratio averaged from June 1 to August 31, 2023, with greater concentrations in red, using TROPOMI data (ESA, 2023, 2025). *Note: Image slightly modified from source to increase size of legend.* . . . 9

1.8 Probability of O_3 production exceeding 70 ppbv plotted as a function of OMI HCHO/NO_2 tropospheric column ratios for seven American cities from 1996-2016. The vertical dashed lines indicate the maximum of the fitted curve (first number in legend) for each city, with black representing all selected cities. Vertical shading is the range of the highest 10% of fitted probability curve (in brackets in the legend), and two standard deviations are in parentheses, in the legend, and represented as coloured shading on each curve. *Figure from Jin et al. (2020).* 15

1.9 Relationship between O_3 and CO mixing ratios from the BORTAS-B campaign. The black diamonds represent medium to low aerosol (CH_3CN < 300 pptv), the red diamonds represent high aerosol (CH_3CN > 300 pptv), and the green circles represent Flight B626. (a) O_3 plotted as a function of CO with linear fits for each population of data points. (b) Enhancements of O_3 relative to CO versus photochemical age, which was calculated from the ratio of the ln(C_3H_8/C_2H_6). *Figure from Parrington et al. (2013).* 16

1.10 Scatter plot of the log of the difference between O_3 and CO enhancements as a function of their enhancement ratio for the (a) BORTAS-B and (b) ARCTAS-B campaigns. The data are filtered by photochemical age, determined from ln(C_3H_8/C_2H_6). *Figure from Parrington et al. (2013).* 17

1.11 (a) Scatter plot of ozone production efficiency (ΔOx/ΔNOz) as a function of NOx mixing ratios from the BORTAS-B campaign for the nighttime low and high aerosol (hollow black and red diamonds, respectively), the daytime low and high aerosol (solid black and red diamonds, respectively), and Flight B626 (green circles). (b) Scatter plot of O_3 mixing ratios as a function of ozone production efficiency for the BORTAS-B (black diamonds), ARCTAS-B (red upward triangles), and ABLE 3B (green downward triangles). *Figure from Parrington et al. (2013).* 18

1.12 Figure from Robinson et al. (2021) showing (a) modelled O_3, modelled with the Framework for 0-D Atmospheric Modelling, with volume mixing ratios over all modelled fires averaged by the time of day sampled, (b) modelled normalised (background-subtracted) excess O_3 dilution to CO averaged by time of day sampled (shading represents one standard deviation), (c) ratio of NO_x lost to reaction with HO_x radicals (L_n) to total HO_x loss (Q) which is HO_x self-radical loss (Lr) plus L_n all plotted as function of reaction time for afternoon and evening fires. Panel (c) shows the VOC- and NO_x-sensitive regions as solid and dashed lines, respectively. 19

2.1 A schematic of the TROPOMI swath for the SWIR spectral band (7 km changes to 5.5 km for all other bands after August 6, 2019). Each wavelength observed by TROPOMI is shown linearly with dark-grey squares. In 1 second, a spectrum is measured by a two-dimensional detector. After each second, a new measurement is started in the across-track direction. *Image from Veefkind et al. (2012).* 26

2.2 TROPOMI spectral ranges compared to the OMI, SCIAMACHY, and GOME instruments. *Image from Veefkind et al. (2012).* 27

2.3 Examples of TROPOMI vertical sensitivity for (a) CO and (b) HCHO retrievals. Panel (a) from Veefkind et al. (2012) shows a CO averaging kernel (A_c) divided by geometrical thickness (Δz) of the corresponding model layer as function of altitude for different geometrical cloud fractions (f_c) and for a cloud of optical depth 20 located between 4 and 5 km. Sensitivity below the cloud decreases as cloud fraction increases. Panel (b) from Lambert et al. (2024) plots a typical total column HCHO averaging kernels, AK, for Fourier Transform Infrared (FTIR) spectrometer (blue), Multi Axis Differential Optical Absorption Spectroscopy (MAX-DOAS) retrieval (green), and TROPOMI (red). 28
2.4 Examples of TROPOMI vertical sensitivity for NO_2 retrievals. Douros et al. (2023) show the mean TROPOMI averaging kernel logarithmically for rural France (black squares) and the city of Paris (black diamonds) averaged for the whole month of (a) January and (b) July as it changes with altitude (km), with unity shown as a dashed line. 29
2.5 A diagram demonstrating the S-shaped flight path of the FIREX-AQ DC-8 aircraft as it performed cross-sectional transects along the length of a wildfire plume to measure emissions. *Image from Stockwell et al. (2022).* 31
2.6 A history of the GOES satellite series. From the early GOES-1 launched in 1975 to the current satellites, from GOES-16, launched in 2016 (currently a primary backup), to GOES-19, launched in 2024, to the GeoXO slotted to replace the GOES series in 2032. *Image from NOAA (2025).* 34
2.7 A sample image of the CCI LC product viewer map for Canada's Central and Western provinces. Each colour pixel indicates a different land type, with greens representing different tree covers, yellows and oranges representing shrubbery, herbaceous cover, and grasslands, and blues representing water, to name a few. Needleleaved tree cover are indicated in dark greens. For a complete list of all land types and their colours, see ESA (2017) and ESA (2022). 36
2.8 A rectangular box drawn over OMI tropospheric NO_2 column densities (molec/cm^2) with MODIS fire detections (red plus symbols) and North American Regional Reanalysis wind vectors (black arrows) for a Nevada wildfire observed by Mebust11 on August 25, 2008. *Figure taken from Mebust et al. (2011).* 38
2.9 An annotated photo of the Horsefly Fire on August 6, 2019 demonstrating how the Gaussian-flux method is calculated from the side-view (y,z) direction, where the x-direction is out of the paper. Note: The photo and segments are not to scale. These are approximations for illustrative purposes only. *Original photo by Wyatt (2019).* . 42
2.10 (a)A top-down [(x,y) direction] image of the Horsefly Fire on August 6, 2019 (NASA, 2024a), with annotation demonstrating the Gaussian-flux method calculations, and (b) a heat-map of TROPOMI CO ΔVCD enhancements from the same fire using the Gaussian-flux method. Boxes are to scale in both figures. 43
2.11 Two panels from Griffin24 Figure 1 that show the (b) Gaussian distribution across the ΔVCDs (molec/cm^2) for CO of a 2019 New Mexico fire and (c) the centre of the Gaussian plume for each 4-km segment (blue dot) with three standard deviations (blue line) from each fit. 43

2.12 A flowchart summarising the step-by-step process for calculating enhancement rates, using the Gaussian-flux method, for the FIREX-AQ summer 2019 and Western Canada summer 2023 fires. 46

3.1 Spatial distribution heatmaps of the satellite-derived CO, HCHO, and NO_2 ΔVCDs, for the FIREX-AQ fires Shady (row a), Horsefly (row b), and Williams Flats (row c). ΔVCDs are in units of molec/cm^2. 57

3.2 Satellite-derived enhancement rates for (a,b) CO, (c,d) HCHO, and (e,f) NO_2 for the FIREX-AQ Shady (a,c,e) and Horsefly (b,d,f) fires versus estimated plume age and downwind direction, dy, for assumed lifetimes, τ. TROPOMI overpasses were at 20:37 and 20:13 UTC for each fire, respectively, with aircraft sampling occurring between 22:25-3:50 UTC and 22:26-0:53 UTC, respectively. The average aircraft-derived rates are also shaded as a red, dashed line with $\pm$ 1 standard deviation shown in red and the full range shaded in blue. Aircraft rates are only shown when the emission time was expected to be within two hours of a TROPOMI overpass. For CO only (a,b), satellite-derived rates from Griffin24 for these two fires are indicated by dashed blue lines, with a total uncertainty of 57% (not shown). Error bars represent reported uncertainty for each species in Table 2.1. 58

3.3 Satellite-derived enhancement rates for (a) CO, (b) HCHO, and (c,d) NO_2 for the FIREX-AQ William Flats fire versus estimated plume age and downwind direction, dy, for assumed lifetimes, τ, similar to Figure 3.2. Overpass was at 19:55 UTC with aircraft sampling occurring between 23:03-3:00 UTC. Plot (d) is zoomed in so that the details of the NO_2 enhancement rates can be seen clearly. Same shading and error bar conventions as Figure 3.2 *Note: The FIREX-AQ (represented as FireX) average and Griffin24 CO values nearly overlap in Panel (a) making it difficult to distinguish them.* 59

3.4 Calculated enhancement rates versus emission time (in UTC) for (a) CO, (c) HCHO, and (e) NO_2, for the FIREX-AQ Shady fire and (b) CO, (d) HCHO, and (f) NO_2 for the Horsefly fire. TROPOMI enhancement rates from the Gaussian-flux method are in blue, with FIREX-AQ enhancement rates provided in orange. τ is the lifetime used for calculations of each species. FRP from GOES 16 (GEOS East) and 17 (GOES West) are shown as purple and green triangles, respectively. The grey dashed line shows the start of the next day. Error bars represent the uncertainty of each species as reported in Table 2.1. 61

3.5 Calculated enhancement rates versus emission time (in UTC), same as Figure 3.4, for the FIREX-AQ William Flats fire. Error bars represent the uncertainty of each species as reported in Table 2.1. 62

3.6 Heatmap of the satellite-derived TROPOMI CO, HCHO, and NO_2 ΔVCDs, for the 2019 New Mexico fire used in Figure 1 of Griffin24 (see Table 3.2). ΔVCDs are in units of molec/cm^2. 63

3.7 Calculated enhancement rates versus downwind direction and plume age for the 2019 New Mexico fire found in Figure 1 of Griffin24 for the species (a) CO, (b) HCHO, and (c) NO_2, with uncertainties from Table 2.1 indicated by the error bars. Different lifetimes, τ, are shown for calculated enhancement rates. 64

3.8 A figure demonstrating the method for CO emissions of the 2019 NewMexico fire taken from Griffin24. Panel (a) shows longitude-latitude unmodified TROPOMI VCDs, (b) shows a Gaussian fit in the crosswind direction for each 4 km box for 40 km downwind, (c) is the peak x_0 with three standard deviations shown as blue dots and bars, respectively, (d) provides Gaussian-corrected VCDs for each 4 km box with three standard deviations, (e) is the enhancement rate as a function of distance downwind (*Correction: figure says downwind direction is x, but it should be y*), and (f) is the enhancement rates from (e) but projected as time since emission. 65

3.9 Enhancement rates of CO (yellow), HCHO (red), and NO_2 (blue) versus downwind direction and plume age for the first eight of sixteen total plumes from fires in Western Canadian boreal forests during summer 2023. For each plume, the enhancement rates have been normalised by the maximum enhancement rate for each species. The maximum enhancement rate used for normalisation is provided in the legend, as well as the averaged FRP for the fire within a few hours of overpass time. The naming convention for the fires can be found in Table 3.2. 68

3.10 Same as Figure 3.9 for the remaining eight of sixteen plumes from fires in Western Canadian boreal forests summer 2023. *Note: EntiakoParkBC fires had no FRP data for the day of the fire so FRP averages are taken from FRP data within a few hours of the TROPOMI overpass on the following day. FoxMountainNWT_o29714 and _o29715 did not have FRP values within three hours of overpass time (19:31 and 21:10 UTC, respectively). For these fires, FRP average was taken from the next closest MODIS overpass with FRP data (05:53 and 07:31 UTC, same day in UTC).* 69

3.11 Enhancement ratios of TROPOMI HCHO and CO ΔVCDs downwind of fifteen plumes (with MaxhamishLake11_o29332 omitted as it does not have HCHO data) of nine boreal forest wildfires in Western Canada during summer 2023. The "Avg Ratio" in the legend is the average EnhR for each fire. Correlations are plotted without systematic bias being added or removed for each species (Section 2.5 Table 2.1), however, the average slope, which is the average of the slopes from all fires, is provided with bias adjustment as "Bias-Adjusted Avg," in the figure. The uncertainties reported for the Avg Slope, Bias-Adjusted Avg, and Avg Ratio are the SEM. 72

3.12 Enhancement ratios of TROPOMI NO_2 and CO ΔVCDs (background-subtracted enhancements) downwind of sixteen plumes from nine boreal forest wildfires in Western Canada during summer 2023 plotted the same way as Figure 3.11. The y-axis has been limited to 0.006 to allow all slopes to be visually distinguishable. The uncertainties reported for the Avg Slope, Bias-Adjusted Avg, and Avg Ratio are the SEM. 73

3.13 Figure taken from Anderson et al. (2023) showing their results for analysing the diurnal change of a series of fires in California, Oregon, and Washington. Their panels show: (a) $\Delta NO_2/\Delta CO$ over time, (b) the average FRP versus days from start, (c) $\Delta NO_2/\Delta CO$ as a function of average FRP, and (d) $\Delta HCHO/\Delta CO$ as a function of time. 74

3.14 Enhancement ratios of TROPOMI HCHO and NO_2 ΔVCDs, plotted the same way as Figure 3.11 for fourteen plumes (with with MaxhamishLake11_o29332 not containing HCHO data and EntiakoParkBC_o29757 having no HCHO/NO_2 overlap). The y-axis has been limited to 500 to make slopes to be visually distinguishable. The uncertainties reported for the Avg Slope, Bias-Adjusted Avg, and Avg Ratio are the SEM. 75

3.15 Maximum enhancement rates, for fires analysed in Figures 3.9, and 3.10, as a function of MODIS daily-averaged fire radiative power (FRP) for (a) CO, (b) HCHO, and (c) NO_2. Maximum enhancement rates show a positive linear relationship with FRP for all three species, with CO showing the strongest statistical correlation of R^2. The error bars indicate the enhancement rate uncertainties for each species reported in Table 2.1. 77

4.1 Normalised enhancement rates of CO (orange diamonds), NO_2 (blue triangles), and HCHO (red squares) (rearranged to match Figures 3.9 and 3.10) for twelve plumes from the 2025 wildfires as a function of downwind direction and plume age. Enhancement rates of each fire have been normalised to the maximum rate of each species, which are shown in the legend along with the average FRP. FRP is averaged from MODIS FRP within three hours of each TROPOMI overpass. Naming convention in Table 4.2. 87

4.2 Calculated ΔVCD FNRs versus plume age, with downwind direction on the top x-axis, for the fourteen plumes from the 2023 Canadian wildfires. The VOC-sensitive regime (FNR below 3.2) appear as a blue box, while the NO_2-sensitive regime (FNR above 4.1) is a green box. Grey dashed lines separate the upper and lower numerical regions of the VOC- and NO_2-sensitive regimes, called the transition region. Average FRP is provided for FRP occurring within a three hours of each TROPOMI overpass. Errors are the uncertainties detailed in Table 2.1 summed in quadrature for HCHO and NO_2. For the naming convention, see Table 4.1 89

4.3 Calculated ΔVCD FNRs versus plume age and downwind direction from the twelve plumes for the 2025 Canadian wildfires, plotted the same way as Figure 4.2. For the naming convention, see Table 4.2. Error bars defined the same as Figure 4.2. 90

4.4 (a) A 3D histogram heatmap of TROPOMI ΔVCD FNR values for the 2023 and 2025 wildfires as a function of downwind direction and plume age. Bins in the horizontal axis are linearly binned, while the vertical axis uses logarithmic spacing for binning. Both x- and y-axis are presented on a linear scale for easy reading. Dashed lines have been added to demonstrate the VOC-sensitive (orange line and below) and NO_2-sensitive (white line and above) regimes. (b) A 2D histogram of FNR with plume age binned into one-hour blocks, each with a different colour, as seen in the legend. The legend shows how many counts of each plume age block exist in region with FNR $\leq$ 3.2 (visualised as an orange dashed line) and $\geq$ 4.1 (visualised as a blue dashed line). The legends for the dashed lines also show the total counts that meet the qualifications they represent. SouthAtikakiParkMB was omitted from these results. *Note: There are no similarities or correlations in binning methods between (a) and (b).* 92

4.5 $HCHO/NO_2$ ratios as a function of plume age for the fourteen plumes from nine Canadian boreal wildfires in summer 2023. The upper panel has a linear x-axis, while the lower panel shows the x-axis on a logarithmic scale. The centre legend has each fire colour coordinated with the linear slope, R^2, and average FNR (Avg FNR) for each linear fit. Both the upper and lower panels use the same colour and naming scheme (see Table 4.1 for the naming convention). Correlations are plotted without systematic bias being added or removed for each species (Section 2.5, Table 2.1), however, the average slope, which is the average of the slopes from all fires, is provided with bias adjustment as "Bias-Adjusted Avg," in the top panel. The uncertainties reported for the Avg Linear Slope and Bias-Adjusted Avg Linear Slope are the SEM. 93
4.6 $HCHO/NO_2$ ratios as a function of plume age for the twelve plumes from seven Canadian boreal wildfires in summer 2025 plotted the same way as Figure 4.5. See Table 4.2 for the naming convention. SouthAtikakiParkMB was omitted from these results. The uncertainties reported for the Avg Linear Slope and Bias-Adjusted Avg Linear Slope are the SEM. 94

5.1 Normalised TROPOMI emission rate versus plume age plotted in (a) linear plume age and (b) logarithmic plume age for 38 wildfire plumes from 27 boreal forest wildfires during the 2023 to 2025 summers in Central and Western Canada. The ER for each fire is normalised by the maximum ER observed for the same fire. The relative point density is provided, with total number of points plotted per year. 105
5.2 Calculated TROPOMI CO emission rates (black) and GOES-16 (green triangle) and GOES-18 (purple triangle) FRP as a function of local time (in 2400 hour clock format) for the 15 plumes from summer 2023 wildfires. Titles provide the fire name, date, and TROPOMI orbit number for each plume. 108
5.3 Calculated TROPOMI CO emission rates (black) and GOES-16 (green triangle) and GOES-18 (purple triangle) FRP as a function of local time (in 2400 clock format) for the five wildfires observed in summer 2024. Titles provide the fire name, date, and TROPOMI orbit number for each plume. 110
5.4 Calculated TROPOMI CO emission rates (black) and GOES-18 (purple triangle) and GOES-19 (orange square) FRP as a function of local time (in 2400 clock format) for the 14 plumes from summer 2025 wildfires. Titles provide the fire name, date, and TROPOMI orbit number for each plume. 111
5.5 CO emission rates from aircraft measurements, using an NRCan aircraft (red triangle), TROPOMI (black triangle), and CFFEPS (orange dots) are compared with GOES-R FRP (grey dots) as a function of local time for a boreal forest wildfire on the border of Alberta and Saskatchewan over a 24-hour period, on June 24th 2018. *Figure from Hayden et al. (2022).* 113
5.6 Single emission rates taken at 20 km downwind for 842 wildfires under the *broadleaved evergreen* land type from GLC2000 plotted as a function of MODIS FRP. Figure from Griffin24. 114

5.7 (a) TROPOMI CO ER versus GOES FRP for all TROPOMI ERs that are within ±10 minutes of a GOES FRP measurement along the plume of each of the 38 wildfire plumes from 2023 to 2025. The grey points represent data from plumes ChaseParkBC_o29331 and ChaseParkBC_o29332 that were omitted from the fit. The red dashed line represents an OLS regression and the blue dashed line represents a York regression, both forced through the origin. Both fits show the 95% confidence interval with shading. Panel (b) shows a zoomed-in view of the inner region of the majority of data points. 115
5.8 Summary of GOES VZA for each plume observed in this study for GOES-E and GOES-W. Red is above the 80° threshold for detection, orange is above the ideal region of > 65°, and green is in the ideal region of below 65°. 117
5.9 A linear-logarithmic plot of TROPOMI CO ER versus GOES FRP similar to Figure 5.7, but with a colour map of plume age. Plume age was set from 0 to 5 hours and any ERs that fell outside this threshold were coloured grey. The red dashed line represents the OLS regression fit forced through the origin. Plumes ChaseParkBC_o29331 and ChaseParkBC_o29332 are included in OLS fit. 118

List of Abbreviations

ABI ..... Advanced Baseline Imager

ABLE 3B .... Atmospheric Boundary Layer Experiment summer 1990 campaign

Adams19 ..... Adams et al. (2019)

AER_LH .... TROPOMI Aerosol Layer Height

AML ..... Aerodyne Mobile Laboratory

AOT ..... Aerosol Optical Thickness

AQS ..... US Air Quality System

ARCTAS .... Arctic Research of the Composition of the Troposphere from Aircraft and Satellites

ASAR ..... Advanced Synthetic Aperture Radar

AVHRR ..... Advanced Very High Resolution Radiometer

BIRA-IASB . Royal Belgian Institute for Space Aeronomy

BIRD ..... Bi-spectral Infrared Detection satellite

BORTAS ..... BOReal forest fires on Tropospheric oxidants over the Atlantic using Aircraft and Satellites

C3S ..... Copernicus Climate Change System

CAAQS ..... Canadian Ambient Air Quality Standards

CALIOP ..... Cloud-Aerosol Lidar with Orthogonal Polarization instrument

CALIPSO .... Cloud-Aerosol Lidar and Infrared Pathfinder Satellite Observation

CAMS ..... Copernicus Atmosphere Monitoring Service

CARB ..... California Air Resources Board

CCI ..... Climate Change Initiative

CDS ..... Copernicus Climate Data Store

CFFEPS ..... Canadian Forest Fire Emissions Prediction System

CIFFC ..... Canadian Inter-agency Forest Fire Centre

CMME ..... Canadian Council of Ministers of the Environment

CONUS ..... Continental United States

CrIS ..... Cross-track Infrared Sounder

DACOM ..... Differential Absorption Carbon Monoxide Measurement instrument

DOAS ..... Differential Optical Absorption Spectroscopy retrieval

DOMINO .... Dutch Ozone Monitoring Instrument Nitrogen Oxide algorithm

DRAGON ... Distributed Regional Aerosol Gridded Observation Network

dwd ..... Gaussian Distribution downwind correction

ECCC ..... Environment and Climate Change Canada

ECMWF ..... European Centre for Medium-Range Weather Forecasts

EF ..... Emission Factor

EnhR ..... Enhancement Ratio

EOSDIS ..... NASA's Earth Observing System Data and Information System

ERA5 ..... European Centre for Medium-Range Weather Forecasts Reanalysis 5

ERS-2 ..... Second European Remote Sensing Satellite

ESA ..... European Space Agency

FDC ..... GOES Fire Detection and Characterisation product

FIREX-AQ .. Fire Influence on Regional to Global Environments and Air Quality

FNR ..... Formaldehyde-Nitrogen Ratio

FRP ..... Fire Radiative Power

FTIR ..... Fourier Transform Infrared spectrometer

GeoXO ..... Geostationary Extended Observer

GEM-MACH Global Environmental Multiscale-Modelling Air-quality and Chemistry

GEMS ..... Geostationary Environment Monitoring Spectrometer

GES DISC ... NASA's Goddard Earth Sciences Data Information Services Center

GFAS ..... Global Fire Assimilation System

GHG ..... Greenhouse Gas

GLC2000 .... Global Land Cover 2000

GOES ..... Geostationary Operational Environmental Satellite

GOME ..... Global Ozone Monitoring Experiment

Griffin21 ..... Griffin et al. (2021)

Griffin24 ..... Griffin et al. (2024)

HiR.2 ..... High Resolution version 2

HSRL ..... NASA Langley airborne High Spectral Resolution Lidar

ISAF ..... In Situ Airborne Formaldehyde instrument

IASI ..... Infrared Atmospheric Sounding Interferometer

KDE ..... Kernel Density Estimation

KNMI ..... Royal Netherlands Meteorological Institute

LC ..... Land Cover

LCCS ..... Land Cover Classification System

M3 ..... NRCan Fire Monitoring, Mapping, and Modelling data set

MACH-2 ..... NASA's Mobile Aerosol Characterisation Laboratory 2

MAX-DOAS . Multi Axis Differential Optical Absorption Spectroscopy

MCD12C1 ... C005 Global 500 m Land Cover Type product

Mebust11 .... Mebust et al. (2011)

MER ..... Mass Enhancement Rate

MERIS ..... Medium Resolution Imaging Spectrometer

MetOp ..... Meteorological Operational satellite

MISR ..... Multi-angle Imaging SpectroRadiometer instrument

MODIS ..... Moderate Resolution Imaging Spectroradiometer

MODTRAN5 Atmospheric band model radiative transfer software

NASA ..... National Aeronautics and Space Administration

NARR ..... North American Regional Reanalysis

NDACC ..... Network for the Detection of Atmospheric Composition Change

NFDB ..... Canadian National Fire Database

NIR ..... Near Infrared spectral range

NOAA ..... National Oceanic and Atmospheric Administration

NRCan ..... Natural Resources Canada

NRTI ..... TROPOMI Near Real Time product version

NSO ..... Netherlands Space Office

OFFL ..... TROPOMI Offline product version

OLS ..... Ordinary Least Squared regression

OMI ..... Ozone Monitoring Instrument

PAN ..... Peroxyacetyl nitrate

ppbv ..... parts per billion by volume

pptv ..... parts per trillion by volume

PROBA-V ... PROject for On-Board Autonomy - Vegetation

RPRO ..... TROPOMI Reprocessed product version

S-5P Sentinel-5P

S-NPP ..... Suomi National Polar-orbiting Partnership satellite

SCIAMACHY SCanning Imaging Absorption spectroMeter for Atmospheric CHartographY

SEM ..... Standard Error of the Mean

SPOT-VGT .. Satellite Pour l'Observation de la Terre –Vegetation

SRON ..... Netherlands Institute for Space Research

SWIR ..... Short-wave Infrared spectral range

TCCON ..... Total Carbon Column Observing Network

TEMPO ..... Tropospheric Emissions: Monitoring of Pollution

TROPOMI .. TROPOspheric Monitoring Instrument

UV-VIS ..... Ultraviolet-Visible spectral range

VCD ..... Vertical Column Density

VIIRS ..... Visible Infrared Imaging Radiometer Suite

VOC ..... Volatile Organic Compound

VZA ..... View Zenith Angle

xdir ..... Gaussian distribution horizontal position correction

Chapter 1

Motivation

1.1 Canadian Wildfires

Wildfires are an increasing topic of concern. As anthropogenic-induced climate change continues to increase surface temperatures (e.g., Chen and Dong, 2019; Michail et al., 2019; IPCC, 2023), Canada is experiencing increased severe weather, including both droughts (Kirchmeier-Young et al., 2019) and climate-change-induced extreme weather resulting in increased lightning risk (Veraverbeke et al., 2017). These increasingly fire-prone landscapes increase the likelihood of wildfires in the future (Bowman et al., 2017), with fires in Canada setting several records in the last few years, such as the British Columbia fires of 2017 that burned 1,216,100 hectares (ha) (12,161 square kilometres) of land (Province of British Columbia, 2023). Figure 1.1 from Natural Resources Canada (NRCan, 2025a) shows the total amount of Canadian land cover burnt by wildfires from 1972 to 2024. In the summer of 2023, record-breaking wildfires burned in Quebec, Alberta, and British Columbia, having a significant impact on the atmosphere of the Northern Hemisphere (Zhang, S. et al., 2024; Flood et al., 2025b; Zhang, Q. et al., 2025). The 2023 wildfire season had 834 large fires exceeding 200 ha, which is 2.5 times the 1986 to 2022 average, and had 60 fires exceeding 50,000 ha. These 60 large fires, up from seven in the same period in the previous year, were responsible for 73% of the total area burned in 2023 (Jain et al., 2024). According to CAMS (2023), 2023 produced the largest annual emissions of carbon in

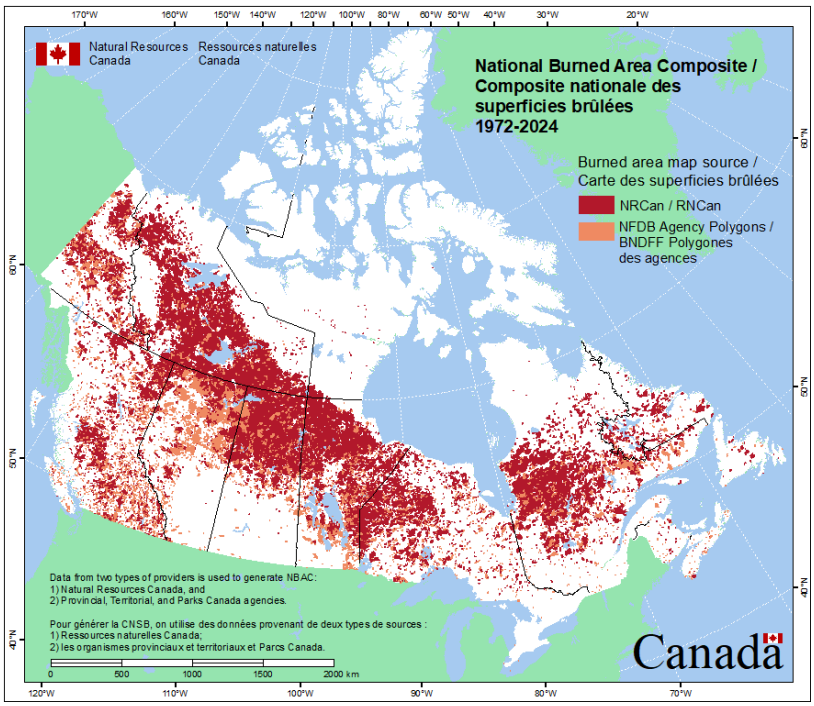

Figure 1.1: Map of the total land cover in Canada burned from 1972 to 2024, with data from NRCan in red and the Canadian National Fire Database (NFDB) in orange (NRCan, 2025a).

the 21 years of data from the Copernicus Atmosphere Monitoring Service (CAMS) Global Fire Assimilation System (GFAS) with 160 megatonnes of carbon emissions, by the end of June 2023. The Intergovernmental Panel on Climate Change (IPCC), to lower the warming caused by carbon dioxide (CO_2), recommends caps, or upper limits, to the cumulative CO_2 emissions from anthropogenic sources, often called the carbon budget (Rogelj et al., 2016). From May to September 2023, the total carbon emissions from Canadian wildfires was comparable to anthropogenic emissions from most large nations, at 647 Tg of carbon emitted (Byrne et al., 2024).

Wildfires have increased in intensity in Canada in recent years. Figure 1.2, using data from NRCan Fire Monitoring, Mapping, and Modelling (M3) data set (NRCan, 2025b), shows the total area burned for each year from May to September for 2012 to 2025. The September totals from 2023 to 2025 each exceeded those of the previous ten years and, in the case of 2023 and 2025, the total area was larger than the totals of the previous years within the first two months. Looking at total area burned by year since 1983 (Figure 1.3), 2023 and 2025 both exceeded the totals for all prior

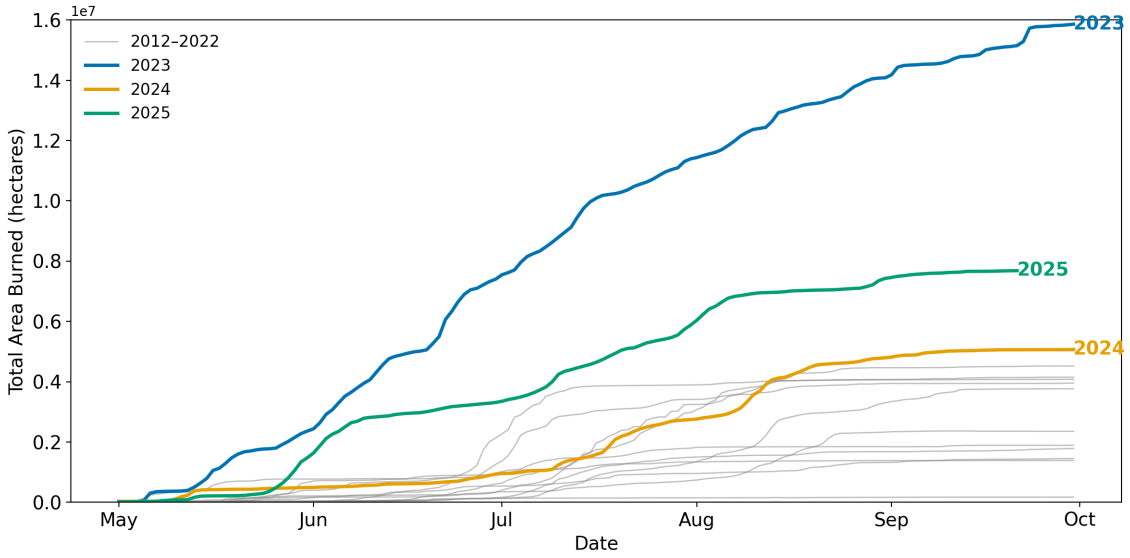

Figure 1.2: The total area burned in Canada from May 1 to September 30 for 2012 to 2025, using aggregated data from NRCan (NRCan, 2025b). Data provided for 2025 go to September 21.

seasons, with the total area burned by the 2023 wildfires at 17.3 million ha, which is 42% of the total area burned in Canada over the 10 years prior. That season had fires 3.8 and 2.4 times larger (in total area) than the two largest fire seasons in the prior two decades, with 2014 and 1995 having 4.608 and 7.106 million ha total area burned, respectively (CIFFC, 2025b). The 2025 wildfire season continued this pattern, becoming the second-worse wildfire season on record. Fires burned across the country and were particularly massive in Manitoba and Saskatchewan, resulting in a total of 8.8 million ha burned across Canada, as of September 12, which is larger than the province of New Brunswick (CIFFC, 2025a). Models predict that annual area burned will increase, especially in Western Canada (Boulanger et al., 2014), so developing methods to quantify the wildfire emissions in plumes using remote sensing is important for understanding the environmental impact of wildfire seasons and their contribution to the carbon budget and air pollution.

Wildfires result in substantial biomass burning that produces many by-products, such as particulate matter of diameter < 2.5 µm (PM2.5), nitrogen monoxide (NO), nitrogen dioxide (NO_2), carbon monoxide (CO), and volatile organic compounds (VOCs), such as formaldehyde (HCHO), depending on the burning phase of the fire

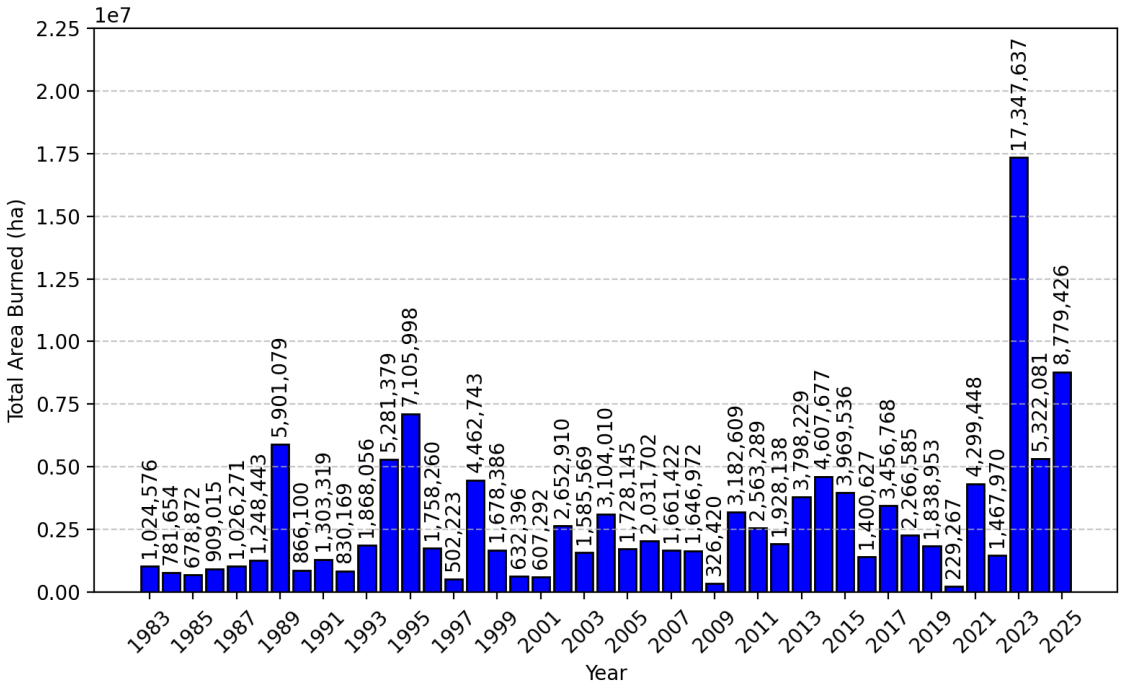

Figure 1.3: The total area burned, in hectares, in Canada per year, for the whole year, using data from the Canadian Interagency Forest Fire Centre and NRCan (CIFFC, 2025a). Data provided for 2025 go to September 21.

(e.g., smouldering or flaming) (Andreae and Merlet, 2001; Andreae, 2019). These compounds can have significant impacts on public health, with PM2.5, CO, and NO_2 leading to cardiovascular and respiratory disease, and HCHO being a known carcinogen (Raub, 1999; Chen et al., 2007; Zhu et al., 2017; Matz et al., 2020; Xue et al., 2023; Flood et al., 2025a; Zhang, Q. et al., 2025). Figure 1.4 from Zhang, Q. et al. (2025) shows the global impact of increased PM2.5 concentrations from the 2023 Canadian wildfires, derived from a combination of a chemical transport model, MODIS aerosol optical depth, global emission fire inventories, and machine learning. The Canadian Council of Ministers of the Environment's (CMME) Canadian Ambient Air Quality Standards (CAAQS) handbook sets the maximum PM2.5 concentrations to an annual average of 8.8 µg/m^3 (CMME, 2025). Figure 1.4(a/b) shows annual concentrations exceeding those values for the majority of Canada in 2023, with some regions exceeding the 24-hour-averaged limit set by the CMME CAAQS of 27 µg/m^3. New methods for analysing wildfire emissions using satellite data are needed for better

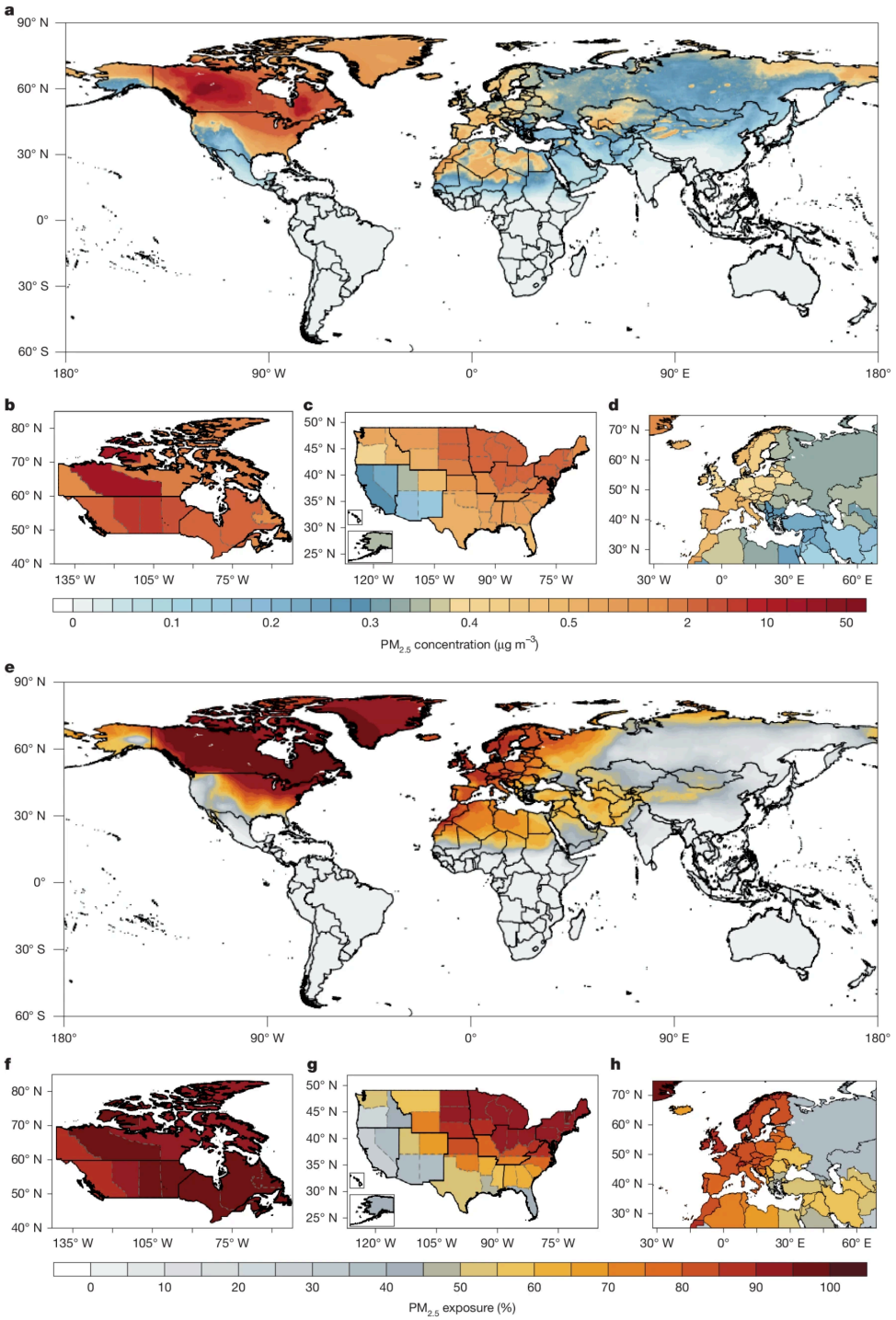

Figure 1.4: Global map showing: (a) the global annual mean of PM2.5 concentrations for the 2023 Canadian wildfires; (b/c/d) the regional annual mean (weighted by population) of PM2.5 concentrations for Canada, the USA, and Europe, respectively; (e) the global percentage of the annual mean from Canadians wildfires in 2023 to total fire-related PM2.5 concentrations; (f-h) the regional percentage of the annual mean PM2.5 exposure for Canada, the USA, and Europe, respectively. Data retrieved from a combination of chemical transport models, global fire emission inventories, satellite aerosol optical depth, and machine learning. *Image from Zhang, Q. et al. (2025).*

understanding of how the emitted species evolve in wildfire plumes to determine the global impacts of biomass burning (Griffin et al., 2024). While the majority of adverse health impacts are within the first few kilometres of the fire core where aerosols and buoyant lift dominate (Akagi et al., 2011; Paugam et al., 2016), long-range transport of plumes is also associated with adverse health impacts (e.g., Matz et al., 2020; Magzamen et al., 2021; Hahn et al., 2021; Mahsin et al., 2022; Gao et al., 2023; Flood et al., 2025a; Zhang, Q. et al., 2025).

1.2 Fire Dynamics

Combustion occurs when available fuel chemically ignites and consists of two primary phases: smouldering and flaming (Akagi et al., 2011; Andreae, 2019; Liu et al., 2022). Loosely packed or sparse fuels such as shrubs in shrublands, tree canopies in forests, or surface-level smaller combustibles like grass, leaves, or small twigs, are primarily consumed during the flaming phase due to an abundance of oxygen necessary to support flaming (Liu et al., 2022). Smouldering is common in more densely packed fuels such as organic soils and decaying logs (Liu et al., 2022). During any sufficiently large fire, both the smouldering and flaming phases can occur at the same time (Andreae, 2019). Figure 1.5 shows photos that demonstrate (a) a fire with both phases where flaming dominates, (b) a fire with both phases where smouldering dominates, and (c) a fire where only smouldering occurs. In boreal forests, 90% of emissions come from the burning of deep-ground fuels such as peatland soils (van der Werf et al., 2010; Thompson and Waddington, 2014). The efficiency of fuel combustion varies based on multiple factors such as the time of day, total fuel availability, and type of fuel. Combustion efficiency is at its highest during initial ignition, resulting in the flaming phase dominating. As fuel is consumed, the efficiency decreases and the fire transitions into smouldering, as seen in Figure 1.6.

Diurnal variability also exists in the transitions between flaming and smouldering. During the night, the smouldering phase dominates. This is due to local temperature inversions at night causing air flow to be more stagnant, reducing the supply of oxy-

Figure 1.5: Photos showing (a) the flaming and smouldering of surface fuels where the flaming phase dominates, (b) flaming and smouldering of large fuels such as logs and surrounding grass and foliage where the smouldering phase dominates, and (c) short- and long-term smouldering occurring in the combustion of a large log. *Figure from Liu et al. (2022).*

gen to the fuel and limiting combustion propagation (Wallace and Hobbs, 2006). The smouldering phase has lower combustion efficiency, which results in higher PM2.5 emission compared to the flaming phase (Andreae, 2019). The temperature inversion at night also prevents heat and smoke from fires rising as high as they do during the day. The increased particulate matter and smoke trapped due to inversions and stagnant air creates nucleation points for moisture to collect and can generate a super-saturated air mass called a superfog (Achtemeier, 2006; Engelhart et al., 2012). This warm, smoky, moist air further prevents flaming from occurring. During the day, as the sun heats the surface, smoke can rise higher in the atmosphere as the temperature inversion rises, surface moisture decreases, and wind flow increases, giving more oxy-gen for combustion. This leads to an increase in flaming and fire activity, typically in

the afternoon (Wallace and Hobbs, 2006; Andreae, 2019; Liu et al., 2022). Whether a fire is in the flaming or smouldering phase affects which species are emitted from biomass burning.

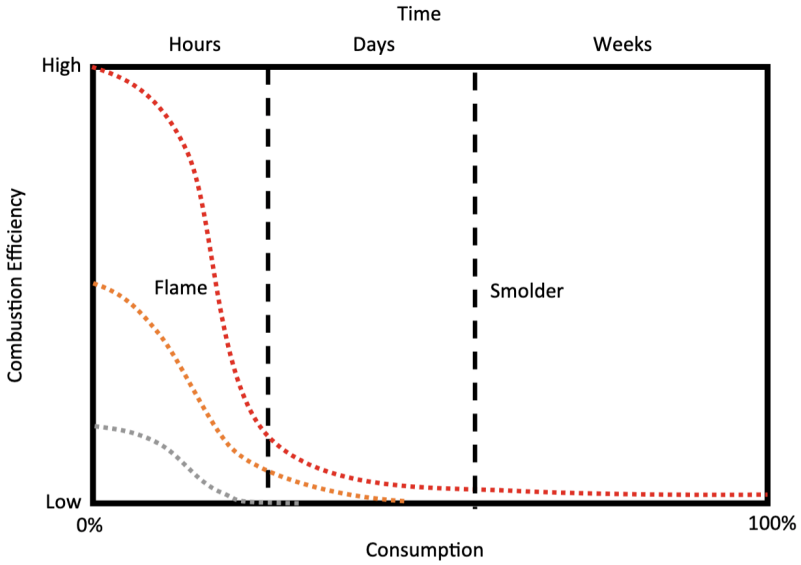

Figure 1.6: A visualisation demonstrating the concept of the changes in combustion efficiency over time and total fuel consumed for a large fire with abundant fuel (red dotted line), a small fire with localised temperature inversions and minimal combustion (orange dotted line), and a low-intensity prescribed fire (grey dotted line). As fuel is consumed, combustion efficiency decreases and the fire transitions into the smouldering phase. *Figure from Liu et al. (2022).*

1.3 Chemistry

1.3.1 Carbon Monoxide

One of the by-products of biomass burning, CO, plays an active role in tropospheric ozone (O_3) and CO_2 production. CO is mostly produced in the smouldering phase of biomass burning (Andreae and Merlet, 2001; Andreae, 2019). The long average lifetime of wildfire CO, typically two weeks (Yurganov et al., 2011; R'Honi et al., 2013; Whitburn et al., 2015), with some research showing lifetimes of one to two months (e.g., Yurganov and Rakitin, 2022), means it is capable of long-distance travel, allowing it to have an impact on public health on locations far beyond the source of the fire. Its long lifetime also makes it a good indicator of both the source of the fire and the trajectory of wildfire smoke (e.g., Viatte et al., 2013; Lutsch et al., 2016;

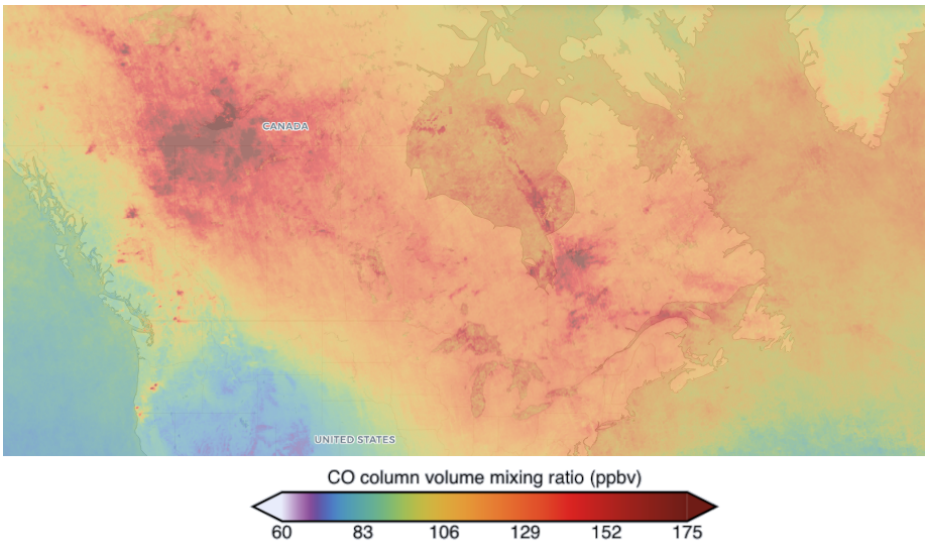

Figure 1.7: A map adapted from Copernicus Sentinel-5P Mapping Portal showing the average CO total column volume mixing ratio averaged from June 1 to August 31, 2023, with greater concentrations in red, using TROPOMI data (ESA, 2023, 2025). *Note: Image slightly modified from source to increase size of legend.*

Yamanouchi et al., 2020; Magaritz-Ronen and Raveh-Rubin, 2021; Schneider et al., 2021; Wizenberg et al., 2023) and comparing other species against CO allows for a better understanding of co-emission and dilution in the plume (e.g., Goode et al., 2000; Simpson et al., 2011). Figure 1.7, which shows the CO column volume mixing ratio from June 1 to August 31, 2023, demonstrates how this species produced in fires in Western Canada can be transported and impact much of North America.

CO can react with naturally-occurring and biomass-produced atmospheric hydroxyl radicals (OH) (Equation 1.1a) to produce CO_2. This reaction creates free hydrogen (H) that reacts with oxygen (O_2) (Equation 1.1b), through a tertiary reactant (M), to produce a peroxyl radical (HO_2), which then reacts with NO to produce NO_2 (Equation 1.1c). NO_2 is capable of photodissociating into NO and a highly-reactive oxygen atom ($O(^1D)$) (Equation 1.1d). This oxygen atom, through a tertiary reaction, combines with O_2 to produce O_3. The net reaction consumes two O_2 to produce CO_2 and O_3 (Equation 1.1e), in the presence of nitrogen oxides ($NO_x = NO_2 + NO$) in the atmosphere, increasing the atmospheric and health impacts due to wildfire smoke (Fowler et al., 2008; Wan et al., 2023). Since CO is produced primarily in the smouldering phase and is the leading sink for tropospheric OH (Fowler et al., 2008),

emission ratios of species versus CO are an effective proxy for observing combustion efficiency to distinguish smouldering and flaming combustion (Andreae and Merlet, 2001; Akagi et al., 2011; Andreae, 2019) and serve as a way of understanding wildfire impacts on atmospheric chemistry. There are a number of studies on tropospheric CO using ground and satellite-based measurements to observe the impacts of CO on public health (e.g., Flood et al., 2025a,b) and the environment (e.g., Warner et al., 2010; Zhao et al., 2011; Konovalov et al., 2016; Lutsch et al., 2016; Adams et al., 2019; Lama et al., 2020; Wizenberg et al., 2021; Rowe et al., 2022; Wan et al., 2023; Griffin et al., 2024).

$$\mathrm{CO} + \mathrm{OH} \longrightarrow \mathrm{H} + \mathrm{CO_2} \tag{1.1a}$$

$$\mathrm{H} + \mathrm{O_2} + \mathrm{M} \longrightarrow \mathrm{HO_2} + \mathrm{M} \tag{1.1b}$$

$$\mathrm{HO_2} + \mathrm{NO} \longrightarrow \mathrm{NO_2} + \mathrm{OH} \tag{1.1c}$$

$$\mathrm{NO_2} + h\nu \longrightarrow \mathrm{NO} + \mathrm{O} \tag{1.1d}$$

$$\mathrm{O} + \mathrm{O_2} + \mathrm{M} \longrightarrow \mathrm{O_3} + \mathrm{M} \tag{1.1e}$$

$$\text{NET}: \mathrm{CO} + 2\,\mathrm{O_2} \longrightarrow \mathrm{CO_2} + \mathrm{O_3} \tag{1.1f}$$

1.3.2 Nitrogen Dioxide

Nitrogen dioxide, which has been shown to be a photodissociative (Uselman and Lee, 1976; Schinke et al., 2008) secondary by-product of nitrogen monoxide (NO) emission in the flaming phase of a fire (Akagi et al., 2011; Andreae, 2019), has also been shown to be an important indicator of nitrous acid (HONO) production in wildfires. After direct emission from combustion sources, HONO is capable of reversibly transitioning between NO_x species (NO_2 + NO), in the presence of light (Vasudev, 1990) and a tertiary molecule (Equations 1.2a and 1.2b) (Roberts et al., 2020; Fredrickson et al., 2023). HONO can be produced by reactions involving NO_x and atmospheric water (Equations 1.2c and 1.2d). A sequence of three reactions results in a net reaction between HONO and HO_2 that creates two tropospheric OH radicals (Equation

1.3d) that greatly affect near-field atmospheric chemistry (Fredrickson et al., 2023), including O_3 production.

Termination of the cycle for the production of O_3 involves the loss of NO_2 through reactions with OH radicals to produce nitric acid (HNO_3) (Jacob, 1999; Lin and Cheng, 2007). During the night, however, OH abundance is diminished due to no sunlight for photodissociative reactions. At night, NO_2 is oxidised by surface-level O_3 to produce dinitrogen pentoxide (N_2O_5). Both HNO_3 and N_2O_5 are stable molecules with lifetimes of weeks and days, respectively, and serve as reservoirs for NO_x (Jacob, 1999). These two by-products, however, quickly photodissociate back into NO_2 during the day (Lin and Cheng, 2007).

Reactions for reversible transition between HONO and NO_x:

$$\mathrm{HONO} + h\nu \longrightarrow \mathrm{OH} + \mathrm{NO} \tag{1.2a}$$

$$\mathrm{NO} + \mathrm{OH} + \mathrm{M} \longrightarrow \mathrm{HONO} + \mathrm{M} \tag{1.2b}$$

$$\mathrm{NO} + \mathrm{NO_2} + \mathrm{H_2O} \longrightarrow 2\,\mathrm{HONO} \tag{1.2c}$$

$$2\,\mathrm{NO_2} + \mathrm{H_2O} \longrightarrow \mathrm{HONO} + \mathrm{HNO_3} \tag{1.2d}$$

Net formation of OH from HONO:

$$\mathrm{HO_2} + \mathrm{NO} \longrightarrow \mathrm{NO_2} + \mathrm{OH} \tag{1.3a}$$

$$\mathrm{NO_2} + h\nu \longrightarrow \mathrm{NO} + \mathrm{O} \tag{1.3b}$$

$$\mathrm{HONO} + \mathrm{O} \longrightarrow \mathrm{NO_2} + \mathrm{OH} \tag{1.3c}$$

$$\text{NET: } \mathrm{HONO} + \mathrm{HO_2} \longrightarrow \mathrm{NO_2} + 2\,\mathrm{OH} \tag{1.3d}$$

Although NO_2 is primarily emitted by anthropogenic sources, biomass burning contributes an average of 15% of the annual NO_2 budget (Denman et al., 2007) and there is rapid interconversion between NO and NO_2 (Roberts et al., 2020). Despite NO_2 being a short-lived species, with an average lifetime of just two hours (Mebust et al., 2011; Griffin et al., 2021), NO_x has a number of reservoirs, including HONO

and organic nitrates like peroxynitrates ($ROONO_2$) and alkyl nitrates ($RONO_2$), with longer lifetimes that can lead to long-range transport (Mebust et al., 2011; Fischer et al., 2014; Zhang, J. et al., 2020; Jin et al., 2021; Fredrickson et al., 2023). It also reacts with peroxyacetyl radicals ($CH_3C(O)O_2$) that are produced through the oxidation of VOCs with OH, to create a compound that is meta-stable with NO_2 called peroxyacetyl nitrate (PAN) (Zhang, J. et al., 2020; Jin et al., 2021; Fredrickson et al., 2023). PAN can photodissociate and release NO_2. PAN has an average lifetime of one month, but that lifetime doubles for every 4 K temperature decrease, meaning the higher in the troposphere it is formed, the longer the lifetime (Fischer et al., 2014). These reservoirs can transport NO_2 long distances into cities much further away from the wildfire, further increasing local NO_2 levels, with possible public health impacts (Alvarado et al., 2010). There are numerous examples of satellite and ground-based measurements expanding our understanding of tropospheric NO_x and its growing impact on the environment (e.g., Adams et al., 2019; Jin et al., 2021; Griffin et al., 2021; Acdan et al., 2023; Wan et al., 2023).

1.3.3 Formaldehyde

Formaldehyde can be a primary emission product of biomass burning and is also a secondary product of VOC oxidation chains (Equations 1.4a - 1.4d, with VOC represented as RH and bolding highlighting dependencies on compounds discussed in the research in this thesis). Hydrogen species ($HO_x = OH + HO_2 + RO_2$), where RO_2 are peroxyl radicals such as CH_3O_2 [a by-product of methane (CH_4) and OH radicals], are also capable of producing O_3 through reactions of VOCs with OH (Equation 1.4k) (Uselman and Lee, 1976; Vasudev, 1990; Finlayson-Pitts and Pitts Jr, 1993; Martin et al., 2001; Pope et al., 2005; Schinke et al., 2008; Roberts et al., 2020). The net reaction production of this chain has a single VOC consume eight O_2 to produce CO, four OH radicals, and four O_3. HCHO has been used as a proxy for OH abundance and reactivity and for VOCs, which are abundant in boreal forest soil and plants (Mäki et al., 2019; Isidorov et al., 2022). HCHO is one of only a few VOCs capable of being observed from satellites and HCHO columns have been used to investigate

other VOC emissions, such as isoprene (Fu et al., 2007; Millet et al., 2008; Stavrakou et al., 2009; Marais et al., 2014; Kaiser et al., 2018). HCHO can also be an indicator of OH as OH shows similar variability, increasing linearly as HCHO concentrations increase (Valin et al., 2016; Wolfe et al., 2019).

$$\mathbf{RH} + \mathrm{OH} \longrightarrow \mathrm{R} + \mathrm{H_2O} \tag{1.4a}$$

$$\mathrm{R} + \mathrm{O_2} + \mathrm{M} \longrightarrow \mathrm{RO_2} + \mathrm{M} \tag{1.4b}$$

$$\mathrm{RO_2} + \mathrm{NO} \longrightarrow \mathrm{RO} + \mathbf{NO_2} \tag{1.4c}$$

$$\mathrm{RO} + \mathrm{O_2} \longrightarrow \mathbf{HCHO} + \mathrm{HO_2} \tag{1.4d}$$

$$\mathbf{HCHO} + h\nu \longrightarrow \mathrm{HCO} + \mathrm{H} \tag{1.4e}$$

$$\mathrm{H} + \mathrm{O_2} + \mathrm{M} \longrightarrow \mathrm{HO_2} + \mathrm{M} \tag{1.4f}$$

$$\mathrm{HCO} + \mathrm{O_2} \longrightarrow \mathrm{HO_2} + \mathrm{CO} \tag{1.4g}$$

$$3\times: \ \mathrm{HO_2} + \mathrm{NO} \longrightarrow \mathbf{NO_2} + \mathrm{OH} \tag{1.4h}$$

$$4\times: \ \mathbf{NO_2} + h\nu \longrightarrow \mathrm{NO} + \mathrm{O} \tag{1.4i}$$

$$4\times: \ \mathrm{O} + \mathrm{O_2} + \mathrm{M} \longrightarrow \mathrm{O_3} + \mathrm{M} \tag{1.4j}$$

$$\text{NET}: \ \mathrm{RH} + 8\,\mathrm{O_2} \longrightarrow \mathrm{CO} + 2\,\mathrm{OH} + 4\,\mathrm{O_3} + \mathrm{H_2O} \tag{1.4k}$$

1.3.4 Formaldehyde-Nitrogen Ratios

Satellites are limited in their ability to observe surface-level O_3 fluctuations due to the greater abundance of stratospheric O_3. Studies have shown that $HCHO/NO_2$ tropospheric column ratios (formaldehyde-nitrogen ratios or FNRs) are a good indicator of surface-level O_3 production in the lower atmosphere, with measurements of this ratio indicating VOC- or NO_2-concentration dependence (Sillman, 1995; Jin et al., 2020; Acdan et al., 2023). Figure 1.8, taken from Jin et al. (2020), shows the probability of O_3 levels exceeding 70 parts per billion by volume (ppbv) as a function of FNR. Jin et al. (2020) compared the in-situ measurements of O_3 by the US Air Quality System (AQS) from 1996 to 2016 to $HCHO/NO_2$ tropospheric columns from the three satel-

lite instruments, the Global Ozone Monitoring Experiment (GOME), the SCanning Imaging Absorption spectroMeter for Atmospheric CHartographY (SCIAMACHY) and the Ozone Monitoring Instrument (OMI), for seven metropolitan areas, for the same period. From Figure 1.8, in the NO_2-sensitive regime (FNR $>$ 4.1), where NO_x concentrations are low and HO_x concentrations are high, the probability of O_3 production increases linearly with NO_x, while high-HO_x suppresses O_3 production through HO_x + HO_x reactions. In the VOC-sensitive regime (FNR $<$ 3.2), where NO_x is abundant and HO_x is scarce, O_3 production increases linearly with increasing VOC concentrations, with high-NO_x suppressing O_3 through NO_x + HO_x reactions (Sillman, 1999; Millet et al., 2008). The regime between 3.2 and 4.1 is referred to as the "Transition Zone" (the brown-green shading in Figure 1.8) and is where O_3 probability scales linearly with both NO_x and VOC tropospheric columns. It can be seen from the figure that the transition zone showed changing dependency on both NO_2 and HCHO column increases as the dependency transitioned between NO_2 and HCHO. There are few studies looking at wildfire FNRs from satellite data, but aircraft campaign measurements have examined the evolution of O_3, NO_2, and VOCs in wildfires.

ARCTAS and BORTAS

The NASA Arctic Research of the Composition of the Troposphere from Aircraft and Satellites (ARCTAS) campaign in 2008 made measurements of biomass burning plumes in central Canada, with the spring and summer campaigns being referred to as ARCTAS-A and B, respectively (Alvarado et al., 2010; Singh et al., 2010). Meanwhile the BOReal forest fires on Tropospheric oxidants over the Atlantic using Aircraft and Satellites (BORTAS) campaign, conducted in two phases, measured emissions from boreal forest wildfires in eastern Canada in summer 2010 (phase A) and summer 2011 (phase B) (Parrington et al., 2012; Palmer et al., 2013). Parrington et al. (2013) analysed aircraft measurements of CO, NO_2, and O_3 from ARCTAS-B, BORTAS-B, and a NASA aircraft campaign in summer 1990 over northern and western Alaska called the Atmospheric Boundary Layer Experiment (ABLE 3B) (Harriss et al., 1994). They

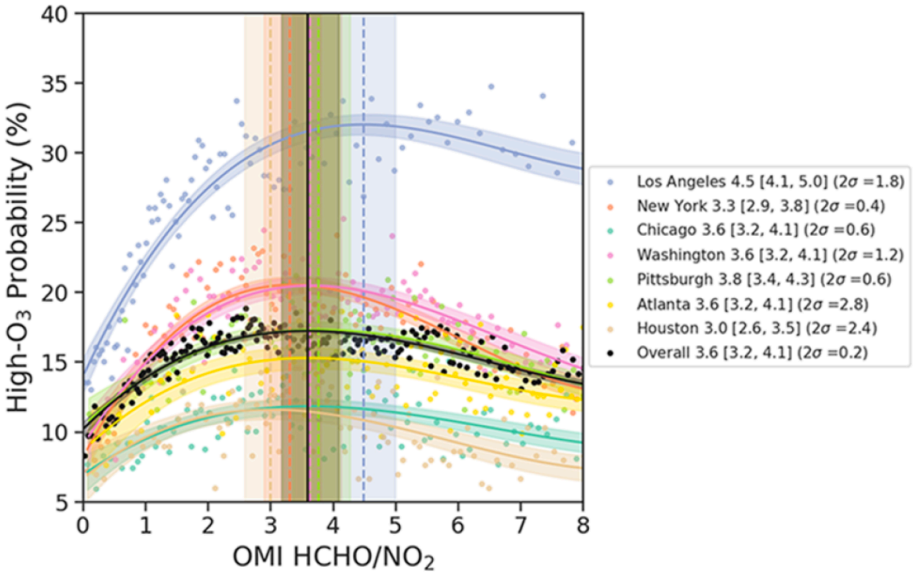

Figure 1.8: Probability of O_3 production exceeding 70 ppbv plotted as a function of OMI $HCHO/NO_2$ tropospheric column ratios for seven American cities from 1996-2016. The vertical dashed lines indicate the maximum of the fitted curve (first number in legend) for each city, with black representing all selected cities. Vertical shading is the range of the highest 10% of fitted probability curve (in brackets in the legend), and two standard deviations are in parentheses, in the legend, and represented as coloured shading on each curve. *Figure from Jin et al. (2020).*

used acetonitrile (CH_3CN) volume mixing ratio threshold of 150 parts per trillion by volume (pptv) as a metric of biomass burning following Palmer et al. (2013) who determined that CH_3CN is predominantly emitted from biomass burning and is primarily removed from the atmosphere through reaction with OH and through uptake by oceans, with a lifetime of about 25 days (Bange and Williams, 2000; Parrington et al., 2013; Palmer et al., 2013). Parrington et al. (2013) established a threshold of 150 to 300 pptv of CH_3CN as an indicator of moderate to low aerosol emissions from wildfires and $>$ 300 pptv as high aerosol emissions.

Parrington et al. (2013) also examined the formation of O_3 by comparing it to CO mixing ratios in ppbv from the BORTAS-B measurements (Figure 1.9). The photochemical age was calculated by taking the natural log of the ratio of propane (C_3H_8) to ethane (C_2H_6), assuming a constant average OH concentration of 2 x 10^6 molec/cm^3, as C_3H_8 reacts with OH to produce a less reactive C_2H_6. The details of how the photochemical age was determined are found in Parrington et al. (2013). Figure 1.9(a) shows that measurements with the highest CH_3CN mixing ratios (typ-

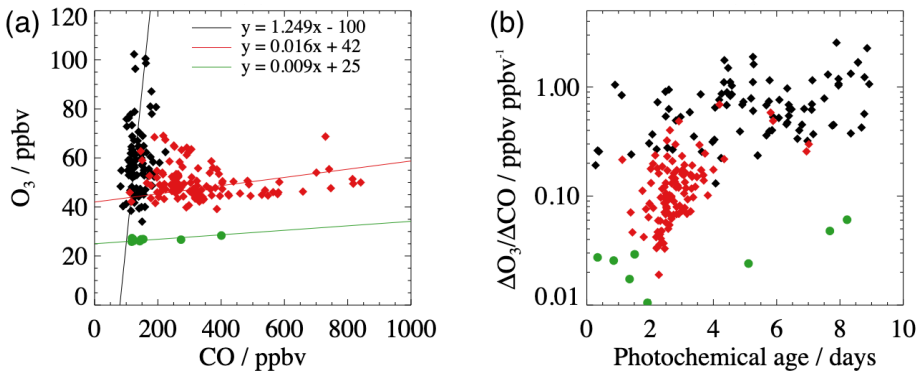

Figure 1.9: Relationship between O_3 and CO mixing ratios from the BORTAS-B campaign. The black diamonds represent medium to low aerosol (CH_3CN < 300 pptv), the red diamonds represent high aerosol (CH_3CN > 300 pptv), and the green circles represent Flight B626. (a) O_3 plotted as a function of CO with linear fits for each population of data points. (b) Enhancements of O_3 relative to CO versus photochemical age, which was calculated from the ratio of the $\ln(C_3H_8/C_2H_6)$. *Figure from Parrington et al. (2013).*

ically younger air masses with photochemical ages of 2 to 4 days) suggest a slight increase in O_3 production compared to measurements with moderate CH_3CN (typically a photochemical age of > 4 days), while moderate CH_3CN had an increased O_3 production compared to the higher aerosol and Flight B626. It is worth noting that Flight B626 was separated from the rest of the results as measurements were made at a lower altitude than the other flights (less than 1.5 km). The observed differences between these measurements suggests an an increase in O_3 production as the plume ages. This is observed in Figure 1.9(b) which shows an increase in the enhancement (background subtracted, given the background of clean air mixing ratios) ratios of O_3 to CO as a function of photochemical age, in days. This relationship is further examined by looking at the enhancement difference between O_3 and CO as a function of their enhancement ratios, with respect to photochemical age for both BORTAS-B [Figure 1.10(a)] and ARCTAS-B [Figure 1.10(b)]. For photochemical ages less than 4 days, O_3 enhancements are typically smaller than CO enhancements ($\log_{10}(\Delta O_3 - \Delta CO) < 0$ and $\Delta O_3/\Delta CO$ <1), while air masses with photochemical ages greater than 4 days show O_3 enhancements becoming greater than the CO enhancements.

Examining the dependence of O_3 formation on NO_x concentrations, Parrington et al. (2013) first defined NO_y as the surrogate species for all reactive and oxidised nitrogen species in an air mass, including NO_x, and then defined NO_z as the photo-

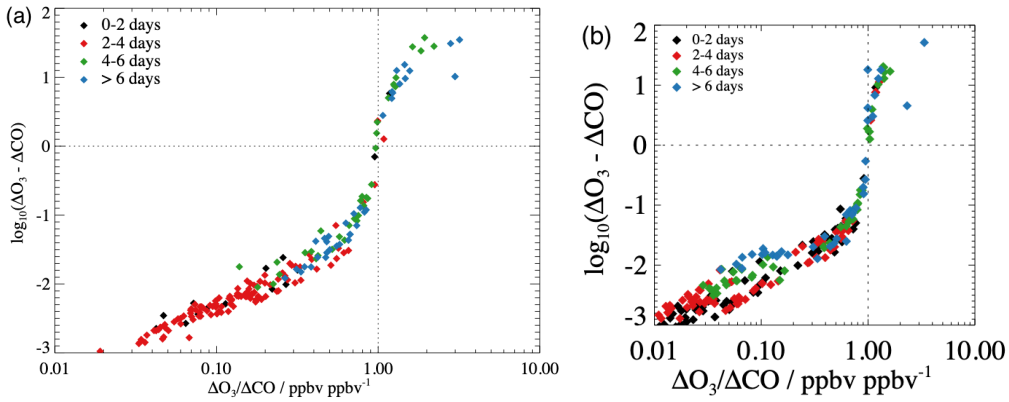

Figure 1.10: Scatter plot of the log of the difference between O_3 and CO enhancements as a function of their enhancement ratio for the (a) BORTAS-B and (b) ARCTAS-B campaigns. The data are filtered by photochemical age, determined from $\ln(C_3H_8/C_2H_6)$. *Figure from Parrington et al. (2013).*

oxidation products of reactive nitrogen species (=NO_y – NO_x). The enhancement ratios of O_x to NO_z (the ozone production efficiency) were compared to NO_x mixing ratios for daytime and nighttime high and low aerosol measurements, with B626 included separately, in Figure 1.11(a). There is a clear difference between nighttime and daytime measurements, with nighttime showing higher mixing ratios for both high and low aerosol conditions. The large range of NO_x, but relatively little change in the enhancement ratios for high aerosol conditions (showing a lack of NO_x conversion to O_3) suggests that high aerosol conditions (younger plumes closer to the source) are in the VOC-sensitive region, while low aerosol conditions show the reciprocal trend, suggesting older plumes further from the source are in the NO_x-sensitive regime. Figure 1.11(b) compares O_3 mixing ratios as a function of the ozone production efficiency for the BORTAS-B, ARCTAS-B, and ABLE 3B campaigns. Parrington et al. (2013) conclude that there is a distinct difference between these relationships for each campaign. However, all three demonstrate a similar trend in the increase of O_3 production with production efficiency, which is dependent on NO_x and suggests a correlation of O_3 production with NO_x.

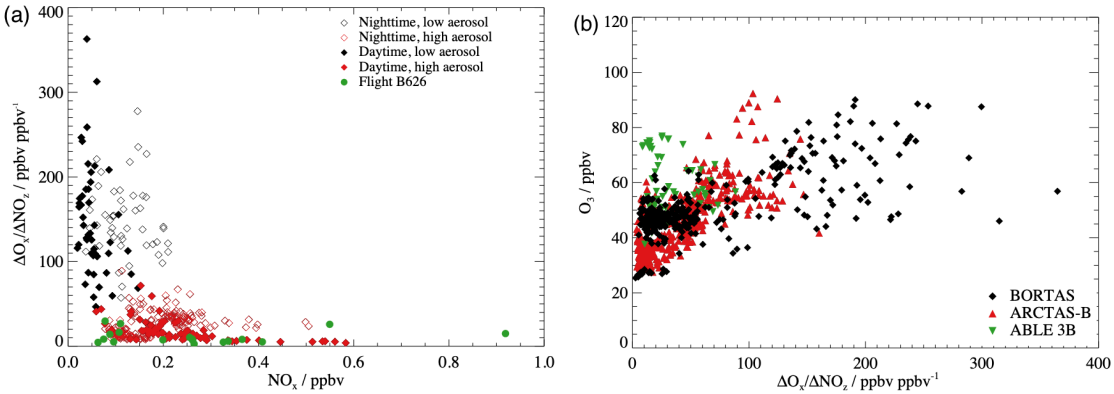

Figure 1.11: (a) Scatter plot of ozone production efficiency (ΔOx/ΔNOz) as a function of NOx mixing ratios from the BORTAS-B campaign for the nighttime low and high aerosol (hollow black and red diamonds, respectively), the daytime low and high aerosol (solid black and red diamonds, respectively), and Flight B626 (green circles). (b) Scatter plot of O_3 mixing ratios as a function of ozone production efficiency for the BORTAS-B (black diamonds), ARCTAS-B (red upward triangles), and ABLE 3B (green downward triangles). *Figure from Parrington et al. (2013).*

FIREX-AQ and Model Data

The NASA and National Oceanic and Atmospheric Administration (NOAA) FIREX-AQ was a campaign in summer 2019 that provided in-situ measurements of trace gas and aerosols from wildfires and prescribed burns in the western United States (Warneke et al., 2023). Robinson et al. (2021) combined model O_3 data with in-situ FIREX-AQ measurements of NO_2 and HCHO. In Figure 1.12(a/b), taken from their paper, O_3 concentrations and O_3 dilution to CO were plotted as a function of reaction time for fires observed in the evening and afternoon. Robinson et al. (2021) showed that O_3 production from biomass burning is five times higher than non-fire production in urban areas (not shown in the figure) and that afternoon fires produce twice as much O_3 in half the time as evening fires. Figure 1.12(c) presents the ratio of the rate of removal of NO_x by reaction with HO_x (L_n) to total loss (Q), which is loss due to L_n and HO_x self-removal (HO_x reactions with other HO_x species, such as in Equations 1.4a to 1.4j) (L_r), with $Q = L_n + L_r$ as a function of reaction time. This shows that afternoon fires rapidly transitioned from the VOC-sensitive to the NO_x-sensitive regime, downwind, within an average of 26 minutes, whereas evening plumes transitioned into the NO_x-sensitive regime more slowly than afternoon fires, taking twice the time as afternoon fires.

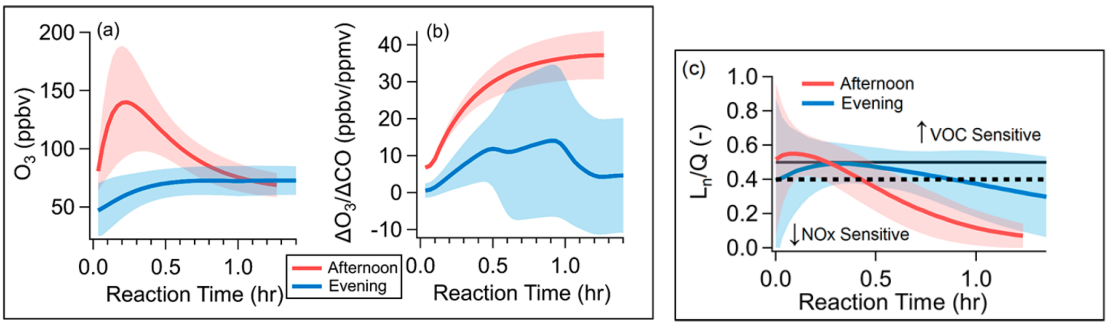

Figure 1.12: Figure from Robinson et al. (2021) showing (a) modelled O_3, modelled with the Framework for 0-D Atmospheric Modelling, with volume mixing ratios over all modelled fires averaged by the time of day sampled, (b) modelled normalised (background-subtracted) excess O_3 dilution to CO averaged by time of day sampled (shading represents one standard deviation), (c) ratio of NO_x lost to reaction with HO_x radicals (L_n) to total HO_x loss (Q) which is HO_x self-radical loss (Lr) plus L_n all plotted as function of reaction time for afternoon and evening fires. Panel (c) shows the VOC- and NO_x-sensitive regions as solid and dashed lines, respectively.

These results suggest that using satellite data with overpasses in the afternoon, such as the TROPOspheric Monitoring Instrument (TROPOMI) on the European Space Agency (ESA) Sentinel-5P satellite (Veefkind et al., 2012; NASA, 2024b), with local overpass time of 13:30, could be used to predict O_3 formation probability from FNRs. Ozone concentrations have been linked to severe health issues like respiratory failure, heart disease, and increased mortality (Hu and Yang, 2024; Hua et al., 2025), asthma in children (Koumpagioti et al., 2025), and causes damage to crops and plant life (Zhang, G. et al., 2024; Nowroz et al., 2024). Understanding how surface-level O_3 evolves from wildfires is important for public health.

1.4 Limitations in Wildfire Emissions Analysis

CO, HCHO, and NO_2 emissions from wildfires can be measured during field campaigns (e.g., Yokelson et al., 2007; Alvarado et al., 2010; Lindaas et al., 2021; Stockwell et al., 2022) and controlled laboratory experiments (e.g., McMeeking et al., 2009; Roberts et al., 2020). Laboratory fires cannot, however, accurately recreate variables such as size, flaming and smouldering fractions, fuel moisture, and structural and meteorological characteristics that are typical of large-scale wildfires (Mebust et al., 2011). Ground-based and aircraft measurement campaigns are limited in their ability

to get emissions estimates close to the source, due to Temporary Flight Restriction zones, are often limited to select locations at specific times of the year, and may provide limited spatial coverage (Griffin et al., 2021). Satellite measurements can close the data gap for fires that are unreachable or unmeasured by campaigns or unreproducible in a laboratory control burn.

Modelling of surface-level O_3 with transport models tends to overestimate O_3 abundance, with models struggling to accurately simulate downwind plume ageing and the effects on O_3 formation (e.g., Singh et al., 2012; Fiore et al., 2014; Zhang et al., 2014; Baker et al., 2016, 2018; Zhang et al., 2020; Bourgeois et al., 2021; Tang et al., 2022; Lin et al., 2024). There are large uncertainties in partitioning reactive nitrogen, with PAN and organic nitrates in smoke typically underestimated in chemical models, both of which are necessary for modelling NO_x sources and sinks (Arnold et al., 2015; Cai et al., 2016). When examining O_3 production dependence on NO_x and VOCs, models can underestimate VOCs due to plume dilution, which emphasises a need for better VOC emission inventories or that there is missing secondary production in the model (Lin et al., 2024). Analysing HCHO, NO_2, and FNRs using satellite measurements could provide better emission estimates on the rates of change of these species as a plume ages downwind, information that can be used to evaluate model simulations.

1.5 Thesis Overview

1.5.1 Scientific Objectives

The primary objectives of the research in this thesis are as follows:

1. To determine the temporal and spatial variations of CO, HCHO, and NO_2 in the downwind direction of wildfire plumes and examine how they evolve as the plume ages for 2019 FIREX-AQ fires and the 2023 Canadian boreal forest wildfires.

2. To calculate downwind formaldehyde-nitrogen ratios for Canadian boreal forest wildfires from the summers of 2023 and 2025 and examine the downwind transitions from a NO_x-sensitive to a VOC-sensitive regime of surface O_3 formation probability.

3. To evaluate the diurnal variability of single-overpass TROPOMI CO emission rates and compare them to fire radiative power derived from satellite observations.

1.5.2 Methods

Research in this thesis uses data from TROPOMI on the Sentinel-5P (S-5P) satellite (Veefkind et al., 2012; NASA, 2024b) for trace gas columns, and the Moderate Resolution Imaging Spectroradiometer (MODIS) (Kaufman et al., 1998; Giglio et al., 2021) on NASA's Terra and Aqua satellites and Geostationary Operational Environmental Satellites (GOES) (Menzel and Purdom, 1994) for fire radiative power (FRP). The Gaussian-flux method developed by Mebust et al. (2011), Adams et al. (2019), Griffin et al. (2021), and Griffin et al. (2024) is used to calculate enhancement rates in metric tonnes per hour (t/h) and background-subtracted tropospheric vertical column densities (molec/cm^2) from TROPOMI CO, HCHO, and NO_2 data. The European Centre for Medium-Range Weather Forecasts (ECMWF) ERA5 reanalysis is used to get wind speed and direction, and the TROPOMI aerosol layer height data product

is used to determine the plume height. Using these methods, this research focuses on understanding the evolution of CO, HCHO, and NO_2 within wildfire plumes. Satellite observations of these species can provide broader spatial coverage compared to targeted aircraft campaigns. Satellite instruments in sun-synchronous orbits, such as TROPOMI and MODIS, and geostationary orbits, such as GOES, can provide daily global coverage of wildfires. Developing new ways to evaluate how trace gases evolve in the downwind smoke plume using satellite data is important for understanding the atmospheric chemistry occurring within the smoke and filling the gap in ground-based and in-situ observations.

1.5.3 Contributions

This work in this thesis is novel research led by Tadhg Hearne, but utilises a method developed by Mebust et al. (2011), Adams et al. (2019), Griffin et al. (2021), and Griffin et al. (2024). Additional contributions are described below.

The research in Chapter 3 was done by Tadhg Hearne with code provided by Debora Griffin of Environment and Climate Change Canada (ECCC). The project was developed by Tadhg Hearne with input from Debora Griffin, Chelsea E. Stockwell of the NOAA, and Kimberly Strong. Data from the FIREX-AQ campaign, provided by Chelsea E. Stockwell, was generated by Alan Fried, Jeff Peischl, Ilann Bourgeoi, and Chelsea E. Stockwell. GOES FRP was provided by Debora Griffin using code developed by Sarah Toshiko Moser. Help with getting the code running on the servers was provided by Joseph Hung.

The research in Chapter 4 was done by Tadhg Hearne with input provided by Debora Griffin and Kimberly Strong.

The research in Chapter 5 was done by Tadhg Hearne and was based on future-work suggestions in Griffin et al. (2024). Input on analysis was provided by Kimberly Strong and Debora Griffin. GOES and MODIS FRP was provided by Debora Griffin. GOES FRP was collected using code developed by Sarah Toshiko Moser.

1.5.4 Thesis Outline

The structure of this thesis is as follows:

Chapter 1 describes the motivation for this thesis, including the necessary background into the atmospheric chemistry analysed in this work, a brief overview of the work, and the scientific objectives.

Chapter 2 details the satellite and other datasets used in this work, as well as the theory behind the Gaussian-flux method and the adjustments made to extend the method to HCHO, beyond its application to NO_2 and CO in previous research. The uncertainties and limitations of the Gaussian-flux method can also be found in this chapter.

Chapter 3 presents research comparing the Gaussian-flux method enhancement rates using TROPOMI data to data from the summer 2019 FIREX-AQ in-situ campaign for CO, HCHO, and NO_2. The research then analyses the evolution of CO, HCHO, and NO_2 TROPOMI-derived enhancement rates downwind as a function of distance and plume age for seventeen wildfire plumes in Canada's boreal forests from summer 2023.

Chapter 4 presents a research study into the NO_x- and VOC-sensitive regimes for O_3 production in the downwind direction and as a function of plume age for 26 wildfire plumes from Canada's boreal forests in the summers of 2023 and 2025, applying the Gaussian-flux method to TROPOMI measurements.

Chapter 5 details research into the diurnal variability of CO using data from single TROPOMI overpasses and comparing observed emission rates to GOES FRP for 38 wildfire plumes fro the 2023 and 2025 Canadian wildfires.

Chapter 6 provides the conclusions and summary of the results presented in this thesis and suggestions for future work.

Chapter 2

Datasets and Methods

This chapter introduces the datasets used in the research discussed in Chapters 3 through 5. The details of each dataset are followed by the consolidation of the theory behind, and a detailed explanation of, the Gaussian-flux method used in the studies within the aforementioned chapters including: modifications to the method from previous literature and the limitations of the method for analysing CO, HCHO, and NO_2. Finally this chapter breaks down the uncertainties that exist with the method, including random and systematic uncertainty associated with the TROPOMI CO, HCHO, and NO_2 data products.

2.1 Datasets

2.1.1 TROPOMI

The research in this thesis utilises TROPOMI CO total column, HCHO tropospheric vertical column, NO_2 tropospheric column, and aerosol layer height (AER_LH) data products. TROPOMI is a nadir-viewing instrument on the ESA S-5P sun-synchronous satellite that has four spectrometers in the ultraviolet (UV), visible (VIS), near infrared (NIR), and short-wave infrared (SWIR) (Veefkind et al., 2012). TROPOMI is the latest iteration of a series of spectrometers from GOME launched 1995 onboard ESA's second European Remote Sensing Satellite (ERS-2) (Eisinger and Burrows,

1998; Koelemeijer et al., 2003) to SCIAMACHY launched in 2002 onboard ESA's Envisat, to GOME-2 launched in 2006 onboard the ESA Meteorological Operational satellite-A (MetOp-A) (Callies et al., 2000), and finally OMI launched in 2004 on the NASA Aura satellite (Levelt et al., 2006), which until TROPOMI provided the best horizontal resolution among other instruments of its class (Fioletov et al., 2013). TROPOMI has better spatial-temporal coverage and higher spatial resolution compared to its predecessors, making it possible to distinguish single plumes with a pixel resolution of 7 x 7 km^2, which was later increased in resolution to 7 x 5.5 km^2 for SWIR and 5.5 x 3.5 km^2 for all remaining spectral bands after August 6, 2019 (ESA, 2024f; NASA, 2024b). The S-5P satellite overpasses around 1:30 p.m. local time, and with TROPOMI having a swath of 7 x 2600 km^2 (for SWIR, and 5.5 x 2600 km^2 for other spectral bands after August 2019) per 1 second of flight, it provides near-daily global coverage (Veefkind et al., 2012). As the satellite moves, the instrument measures each wavelength on a two-dimensional detector for ground pixels extending 7 km (for SWIR). After 1 second, a new measurement is started (Figure 2.1). Due to the size of the swath, high-latitude regions, like Canada, may have more than one orbital overpass a day.

The four spectrometers on TROPOMI provide a wider spectral range than previously available from its predecessor, OMI. The UV and visible spectral bands cover 270 to 500 nm, with the NIR and SWIR bands covering 675 to 775 nm and 2305 to 2385 nm, respectively. Spectral resolution varies from 1 nm for UV to 0.25 nm for SWIR, with the resolution of the remaining bands at 0.5 nm. TROPOMI also has extended the wavelength range of the NIR and SWIR bands compared to OMI. The NIR covers the oxygen A-band (758 to 770 nm) providing more information on cloud pressure and cloud fraction, while the SWIR band includes 2.3 µm, allowing for the observation of CO and CH_4 (Veefkind et al., 2012). Figure 2.2 shows how the spectral ranges of TROPOMI compare to the OMI, SCIAMACHY, and GOME instruments. TROPOMI has also been shown to have an improved signal-to-noise ratio compared to OMI and SCIAMACHY by as much as a factor of 2 to 5 (Veefkind et al., 2012). For the summer 2019 fires examined in Chapter 3, the Level 2 (L2) reprocessed (RPRO)

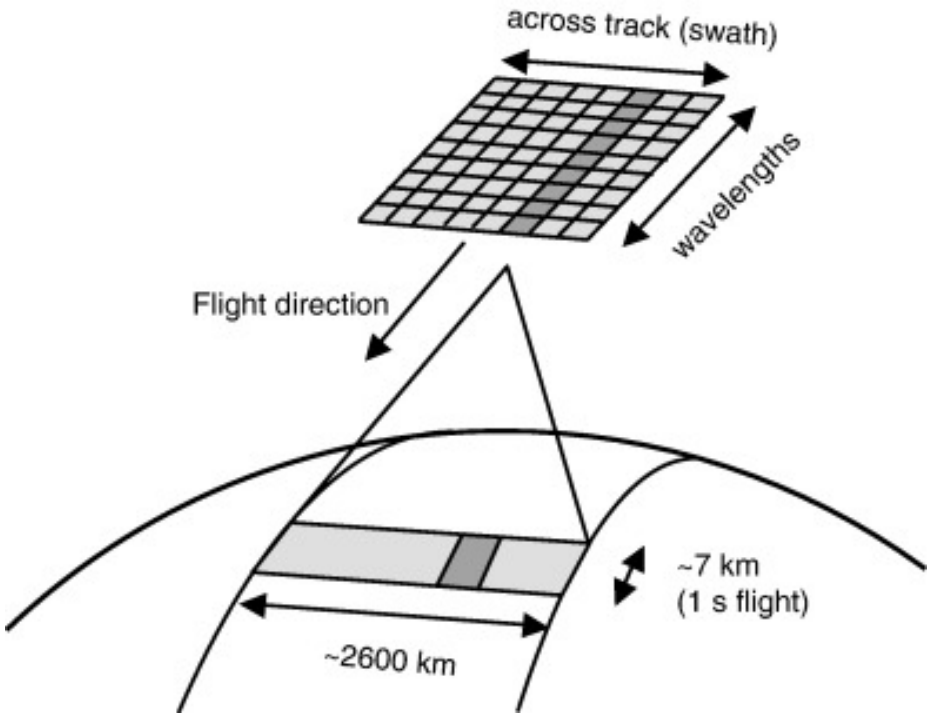

Figure 2.1: A schematic of the TROPOMI swath for the SWIR spectral band (7 km changes to 5.5 km for all other bands after August 6, 2019). Each wavelength observed by TROPOMI is shown linearly with dark-grey squares. In 1 second, a spectrum is measured by a two-dimensional detector. After each second, a new measurement is started in the across-track direction. *Image from Veefkind et al. (2012).*

high-resolution version 2.4 data product was used. For fires in the 2023 to 2025 fire seasons examined in Chapters 3, 4, and 5, the L2 offline (OFFL) version 2.5 data product was used for all species and AER_LH, as RPRO data was not available at the time of the research conducted in this thesis.

Total column CO is retrieved from the SWIR spectra, at 2.3 µm, using the Shortwave Infrared CO retrieval algorithm, by the Netherlands Institute for Space Research (SRON) (Borsdorff et al., 2018, 2019). These retrievals have been validated with ground-based (Borsdorff et al., 2019) and satellite-based observations (Martínez-Alonso et al., 2020), both demonstrating precision error below 10%. Validation against Total Carbon Column Observing Network (TCCON) and Network for the Detection of Atmospheric Composition Change (NDACC) measurements showed TROPOMI CO total columns had a high bias of about 10% (Sha et al., 2021; Griffin et al., 2024; ESA, 2024b). The vertical sensitivity of TROPOMI to the CO profile, quantified by

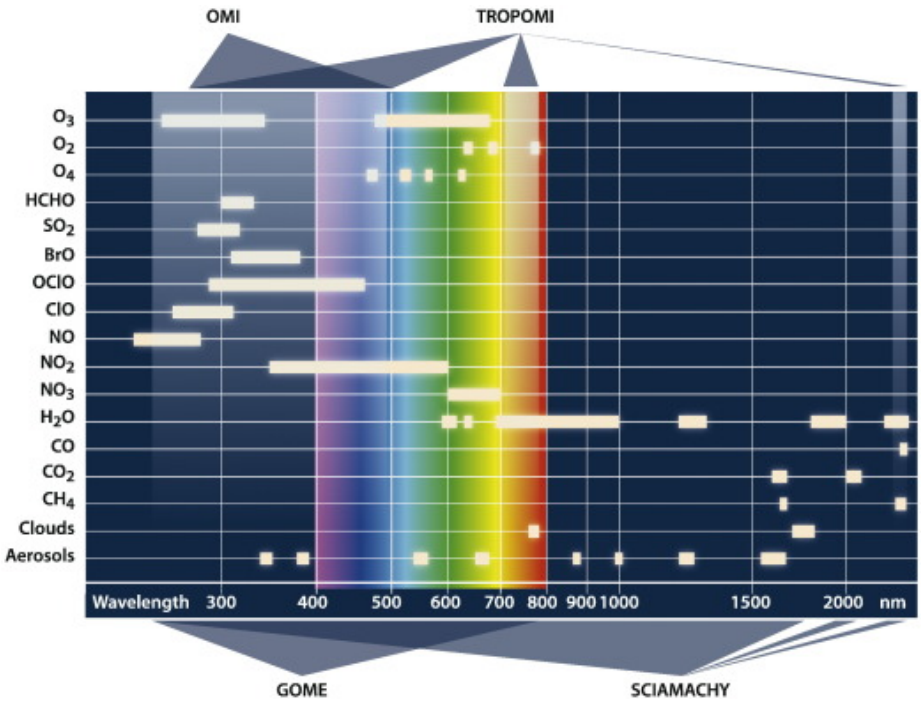

Figure 2.2: TROPOMI spectral ranges compared to the OMI, SCIAMACHY, and GOME instruments. *Image from Veefkind et al. (2012).*

the averaging kernel (with 0 being poor sensitivity and 1 being ideal sensitivity), is close to 1 within the boundary layer for cloud-free conditions (Schneising et al., 2020; Griffin et al., 2024). This sensitivity decreases with increasing cloud fraction due to the wavelength of CO retrieval. This can be seen in Figure 2.3(a) from Veefkind et al. (2012) where they plot a typical CO averaging kernel by altitude divided by geometrical thickness, as a function of increasing cloud fractions for a cloud at altitude of 4-5 km with an optical thickness of 20. This limitation prevents retrieval of CO enhancements from fires during cloudy days or in areas having considerable upwind smoke.

Formaldehyde tropospheric vertical columns are retrieved from UV-VIS spectra (325-360 nm) using differential optical absorption spectroscopy (DOAS) by the Royal Belgian Institute for Space Aeronomy (BIRA-IASB) (De Smedt et al., 2018). The HCHO data product shows a overall agreement, within defined mission parameters, with ground-based NDACC and OMI satellite data, with a positive bias of +32% and low uncertainty due to random errors over clean areas ($<2.5\text{x}10^{15}$ molec/cm^2),

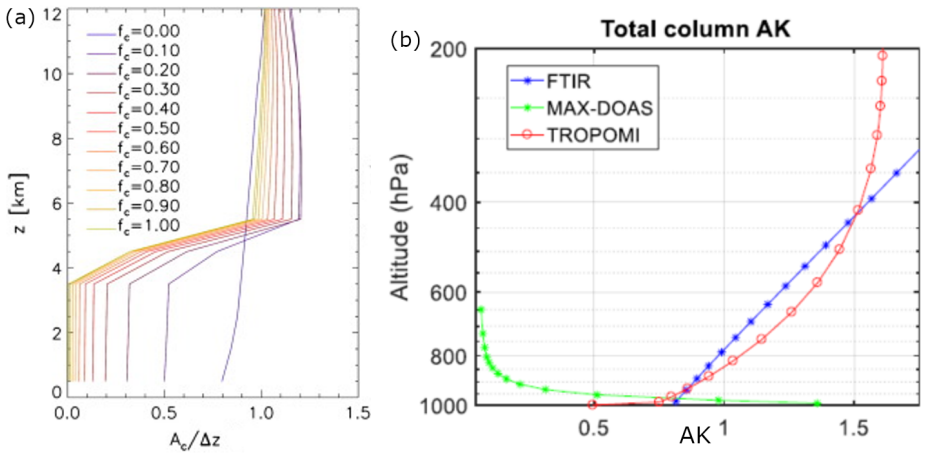

Figure 2.3: Examples of TROPOMI vertical sensitivity for (a) CO and (b) HCHO retrievals. Panel (a) from Veefkind et al. (2012) shows a CO averaging kernel (A_c) divided by geometrical thickness (Δz) of the corresponding model layer as function of altitude for different geometrical cloud fractions (f_c) and for a cloud of optical depth 20 located between 4 and 5 km. Sensitivity below the cloud decreases as cloud fraction increases. Panel (b) from Lambert et al. (2024) plots a typical total column HCHO averaging kernels, AK, for Fourier Transform Infrared (FTIR) spectrometer (blue), Multi Axis Differential Optical Absorption Spectroscopy (MAX-DOAS) retrieval (green), and TROPOMI (red).

and a negative bias of -30% over polluted areas (>8x10^{15} molec/cm^2) (ESA, 2024d; De Smedt et al., 2018). A typical averaging kernel of HCHO from Lambert et al. (2024) (Figure 2.3(b)) shows the TROPOMI averaging kernel as a function of altitude, in red. TROPOMI shows high sensitivity to HCHO at the typical plume height of a wildfire plume of 800 hPa (roughly 2 km) (Griffin et al., 2020), with values greater than 1.

Due to the combined effect of Rayleigh and Mie scattering, satellite retrieval sensitivity to HCHO in the boundary layer is limited. Compared to other UV-VIS absorbers, such as NO_2, absorption signatures of HCHO are weaker, causing the satellite retrievals to be sensitive to noise and prone to error. As such, negative total columns are often observed in the TROPOMI HCHO data product. In boreal forests, which often have large background HCHO concentrations due to an abundance of VOCs, calculated enhancement rates can have a slight negative bias due to the subtraction of high background HCHO concentrations. While negative total columns were filtered from analysis, background HCHO values and noise along the length of plumes could cause overestimation of emissions. Due to background subtraction, these

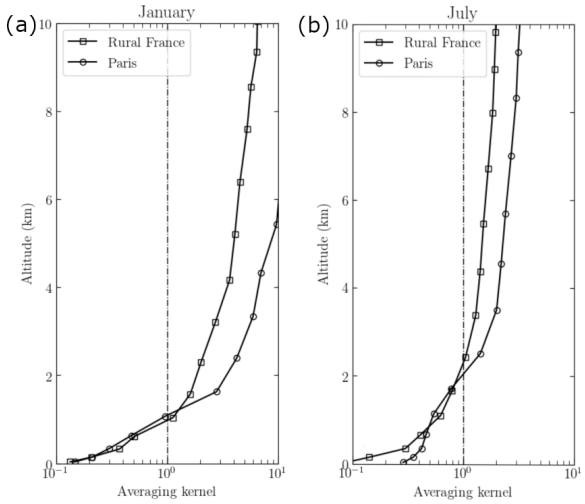

Figure 2.4: Examples of TROPOMI vertical sensitivity for NO_2 retrievals. Douros et al. (2023) show the mean TROPOMI averaging kernel logarithmically for rural France (black squares) and the city of Paris (black diamonds) averaged for the whole month of (a) January and (b) July as it changes with altitude (km), with unity shown as a dashed line.

contributions to the results in this thesis are negligible compared to enhancements, but a slight overestimation is possible.

NO_2 tropospheric columns are retrieved from the UV-NIR spectra (405-465 nm) by the Royal Netherlands Meteorological Institute (KNMI) using the DOMINO algorithm also used for the OMI (van Geffen et al., 2019; Van Geffen et al., 2020). NO_2 tropospheric columns agree within mission-defined parameters with ground-based data and OMI NO_2 data, with OFFL and RPRO both showing biases of -29%, which is better than the mission requirement of $< 50\%$ bias, for the tropospheric product (Van Geffen et al., 2020; ESA, 2024e; Lambert et al., 2024). TROPOMI vertical sensitivity to NO_2 can be seen in the mean averaging kernels from Douros et al. (2023) as a function of altitude (km) for rural France and the city of Paris in the months of January (Figure 2.4(a)) and July (Figure 2.4(b)). TROPOMI NO_2 sensitivity is at unity near 2 km in the summer time, when wildfire activity is greatest, and sensitivity increases below 2 km during the winter.

Lastly, the TROPOMI AER_LH data product was used in the research in this thesis to determine the average plume height for the enhancement rate calculations. The AER_LH algorithm was developed by KNMI for estimating plume heights by taking advantage of absorption by the O_2 A-band. The O_2 A-band has a very distinct

spectral absorption band at 760 to 761 nm. Aerosol layers in the atmosphere reduce backscattered solar radiation, due to the scattering of the aerosol layer, leading to a reduction in the absorption. Aerosol layer mid-height is then estimated by comparing measurements to a simplified, single-aerosol layer model simulation of the O_2 A-band reflectance on optimal, cloud-free conditions. The final height reported is the difference between the top and bottom pressure of the uniform scattering layer with constant thickness of 50 hPa. AER_LH is more robust over dark surfaces like sea and oceans (Nanda et al., 2019; Griffin et al., 2020; de Graaf et al., 2022).

The AER_LH data product uses a different method for retrieval than other instruments capable of observing the altitude of smoke plumes, such as the Multi-angle Imaging SpectroRadiometer (MISR) and the Cloud-Aerosol Lidar with Orthogonal Polarisation (CALIOP). AER_LH is systematically lower compared to MISR aerosol plume height by about 600 m, caused mostly by the difference in algorithms and sensitivity of the instruments. When compared against CALIOP, TROPOMI bias depends on plume thickness. TROPOMI plume height is biased lower by 2.1 km for thin smoke (<1.5 km), while the mean bias for thick plumes (>1.5 km) is lower by 0.68 km. This difference decreases to only 50 m for the layer height of very thick plumes (>3 km) (Griffin et al., 2020). Both are within the 100 hPa mission requirement for uncertainty due to systematic effects (ESA, 2024a; de Graaf et al., 2022). Wildfires from forests, such as those analysed in this thesis, often have very thick plumes compared to fires from other sources such as agriculture or grassland (Griffin et al., 2020), resulting in low overall uncertainty in plume height estimation. AER_LH variability is large due to cloud contamination and surface effects. To adjust for this, extensive cloud screens allowed for 50% of pixels to be within 1 km of CALIOP's weighted extension height. Accounting for the expected bias, this is within the required 50 hPa uncertainty due to random effects (Griffin et al., 2020; de Graaf et al., 2022; ESA, 2024a).

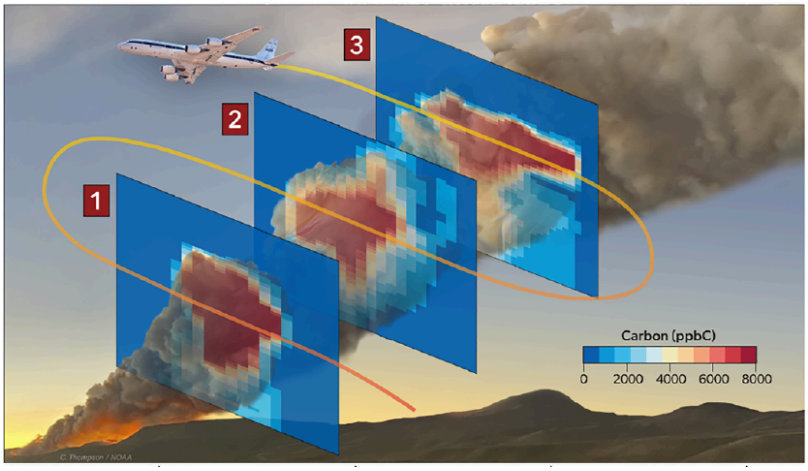

Figure 2.5: A diagram demonstrating the S-shaped flight path of the FIREX-AQ DC-8 aircraft as it performed cross-sectional transects along the length of a wildfire plume to measure emissions. *Image from Stockwell et al. (2022).*

2.1.2 FIREX-AQ

In Chapter 3, the method used in this thesis is evaluated by comparing to enhancement rates derived from FIREX-AQ CO, HCHO, and NO_2. FIREX-AQ was a campaign led by NOAA and NASA in the summer of 2019 that utilised ground-, aircraft-, and satellite-based instruments to observe trace gas and aerosols from wildfires and prescribed burns (Warneke et al., 2023). The research in Chapter 3 utilises measurements made aboard the DC-8 aircraft, where the typical sampling approach consisted of cross-sectional transects of the fire plume initiated near the fire centre and continuing downwind, similar to the diagram shown in Figure 2.5 from Stockwell et al. (2022).

HCHO was measured by both the In Situ Airborne Formaldehyde (ISAF) instrument and the Compact Atmospheric Multispecies Spectrometer, as detailed in Gkatzelis et al. (2024). NO_2 was measured by the NOAA Chemiluminescence instrument (Bourgeois et al., 2022) and CO with a Differential Absorption Carbon Monoxide Measurement (DACOM) instrument (Sachse et al., 1987; Warner et al., 2010).

Total carbon enhancement rates were estimated for each aircraft plume transect using methods outlined in Stockwell et al. (2022). Briefly, vertical profiles of aerosol

extinction measured by NASA's Airborne High Spectral Resolution Lidar (Hair et al., 2008) were scaled to estimate a spatial distribution of total carbon from the ratio of all in-situ carbon measurements to in-situ aerosol extinction. A total carbon flux was estimated through each lidar pixel area by applying horizontal wind speeds and then integrating through the height and width of each plume transect (aircraft entry to exit). The mass enhancement rate of CO, HCHO, and NO_2 was determined as the product of the total carbon enhancement rate (g/s), the in-situ enhancement ratio relative to total carbon, and the molar mass to carbon atomic mass ratio. These calculations follow equations outlined in Stockwell et al. (2022). The derived rates ideally represent emissions at the fire source, where the time of emission was calculated from wind speed and sampling distance downwind. Uncertainties varied by fire from ∼20% to 60%, but are likely higher for more reactive species including HCHO and NO_2, which can be rapidly produced or lost during transport and prior to aircraft sampling. Data from FIREX-AQ are publicly available (https://csl.noaa.gov/projects/firex-aq/data.html).

2.1.3 MODIS

For the method used in this thesis, wildfire locations are found using MODIS FRP, which is the rate of biomass combustion (in MW). MODIS instruments are on board NASA's Terra and Aqua satellites, which each have two overpass times of 10:30 a.m./p.m. and 1:30 a.m./p.m. local time, respectively, providing thermal anomaly Level 2 hotspot detection products MOD14 for Terra and MYD14 for Aqua. Due to the diurnal variability of wildfires, at the time of a 1:30 p.m. TROPOMI overpass, fire activity is typically increasing, so FRP values from Aqua that are closer to the TROPOMI overpass time are used for determining fire centres. MODIS provides near real-time detection of hotspots by detecting fires using an algorithm that employs infrared spectral channels at 4 and 11 µm with 1-km spatial resolution. These thermal anomalies are clustered together within a minimum summed FRP of 1 GW, within a 5-km radius. FRP for each fire pixel is provided via an empirical relationship with brightness temperatures of the 4-µm band (Kaufman et al., 1998; Griffin et al., 2024).

MODIS is limited in its ability to detect fire hotspots during cloud cover and for

small fires (under 1000 m^2). Sensitivity studies giving theoretical average standard error associated with the relationship between the brightness temperatures of the 4-µm band report ±16%, which is greater for smaller fires and reduced for energetic fires (Kaufman et al., 1998). Validation of FRP using the Bi-spectral InfraRed Detection (BIRD) satellite found that the two instruments agree on FRP values within 15% but MODIS underestimates less intense radiating fire pixels, which are not detected by the algorithm, by 46% (Wooster et al., 2003; Mebust et al., 2011).

To reduce the uncertainty of detection and false alarms, the MODIS L2 product provides a detection confidence value as a percentage to help distinguish between a low-, nominal-, and high-confidence fire detection (Giglio et al., 2021). To reduce uncertainty due to cloud cover or false alarms, FRP values that had a detection confidence of greater than 85% were used in this work to determine fire centres, which would classify as a fire mask pixel class of *high confidence fire, land or water*. FRP values whose coordinates are closest to the NASA's Earth Observing System Data and Information System's (EOSDIS) Worldview-observed fire centres were selected for this research, in the case of fire plumes with many hotspot detections in a cluster. FRP averages, however, were calculated by averaging MODIS FRP from Terra and Aqua with overpasses within a few hours of the TROPOMI overpass.

2.1.4 GOES

NOAA's GOES satellite series are geostationary weather satellites with coverage over the United States and Canada. The GOES-R series consist of four satellites, GOES-R, -S, -T, and -U, called GOES-16, -17, -18, and -19, in orbit. GOES-16, launched in 2016, was positioned at 137°W and GOES-17, launched in 2018, was positioned at 75°W (referred to as GOES West and East, respectively), replacing GOES-14 and GOES-15. GOES-16 and -17 were later replaced by GOES-18 and GOES-19 in 2022 and 2024, respectively, with GOES-16 being kept as a primary back up for GOES-East and -West (NOAA, 2023). Figure 2.6 shows the history of the GOES series, including the satellite poised to replace GOES once the current R-series reach the end of their operational lifetime, the Geostationary Extended Observer (GeoXO) set

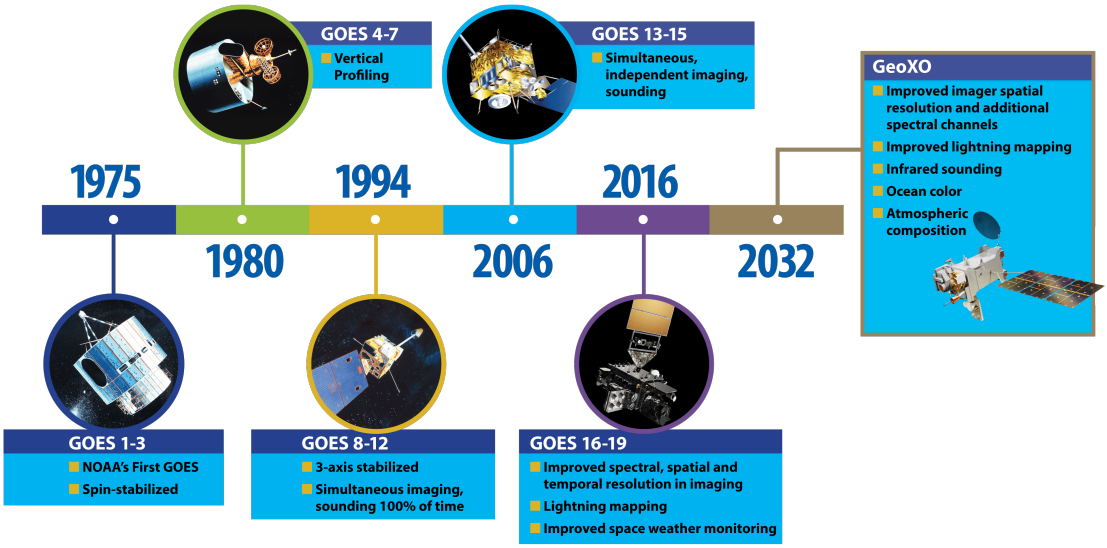

Figure 2.6: A history of the GOES satellite series. From the early GOES-1 launched in 1975 to the current satellites, from GOES-16, launched in 2016 (currently a primary backup), to GOES-19, launched in 2024, to the GeoXO slotted to replace the GOES series in 2032. *Image from NOAA (2025).*

to launch in 2032 (NOAA, 2025). The GOES-R series satellites have multiple instruments, but this research focuses primarily on the Advanced Baseline Imager (ABI) by Harris Corporation and the FRP/hot spot Fire Detection and Characterisation (FDC) product (Schmidt et al., 2013; Sullivan, 2020). The FDC, prior to 2019, provided FRP every 15 minutes with a resolution of 3 km. After 2019, the FDC provided FRP every 10 minutes with a resolution of 2 km for the full-disk scan sector of the satellite (NOAA, 2023; Hall et al., 2023).

GOES FRP is used in the research in Chapters 3 and 5. In Chapter 3, FRP from GOES-16 was used to compare the method's satellite-derived enhancement values against FIREX-AQ enhancements, while GOES-18 was used for the 2023 fires (GOES-17 data was only available for the 2019 NewMexico fire). In Chapter 5, FRP from GOES-16 and GOES-18 are used for fires in 2023, with no GOES-17 data, and GOES-18 and GOES-19 are used for fires beyond 2024. FRP from GOES is limited in its ability to observe small, cool fires, with FRP values less than 50 MW (Roberts and Wooster, 2008), largely due to the coarser spatial resolution than other instruments

like MODIS, and in its ability to detect fire hotspots during cloud cover. Due to these limitations, the FDC product may not contain FRP values for all times. Additionally, as the GOES series are geostationary satellites, FRP retrievals lose accuracy at large viewing zenith angles (VZA) (Li et al., 2019). Due to this, both GOES West and East satellite data are used, if available, for each fire for increased accuracy of comparison to enhancement values.

2.1.5 ECMWF ERA5

For wind speed and direction at the TROPOMI aerosol layer height, ECMWF ERA5 wind data were utilised. The ERA5 reanalysis dataset, which provides an hourly output with a resolution of 0.25° x 0.25°, was used for u- and v-wind components at 1000 to 300 hPa in 50-hPa steps (Hersbach et al., 2020). Wind speed and direction were extracted for the altitude of the plume determined by the AER_LH product for a specific fire location, which has been found to be a good proxy for the average height of a fire plume (Griffin et al., 2019). If no good quality AER_LH was available for a fire, a default of 2 km (800 hPa) was used for the height (Griffin et al., 2020). This method for finding the appropriate wind field altitudes has been used in satellite-derived NO_x and CO emissions from biomass burning to successfully improve accuracy (Griffin et al., 2021, 2024). The uncertainty of ERA5 wind speed data is approximately 0.5 m s^{-1} for 95% confidence interval (Gualtieri, 2022). The average wind speed obtained across all three species and all observed fires was 8.8 m s^{-1}, with 0.5 m s^{-1} uncertainty; for this reason a 6% wind speed uncertainty is assumed.

2.1.6 ESA Land Cover Product

The Global Monitoring of Essential Climate Variables project, known as the ESA Climate Change Initiative (CCI), provides land cover state and seasonality data (Plummer et al., 2017). It is based on the delivery of climate variables from various collection, calibration, and validation methods (ESA, 2024c).

The CCI Land Cover (LC) product is broken up into categories: LC state and

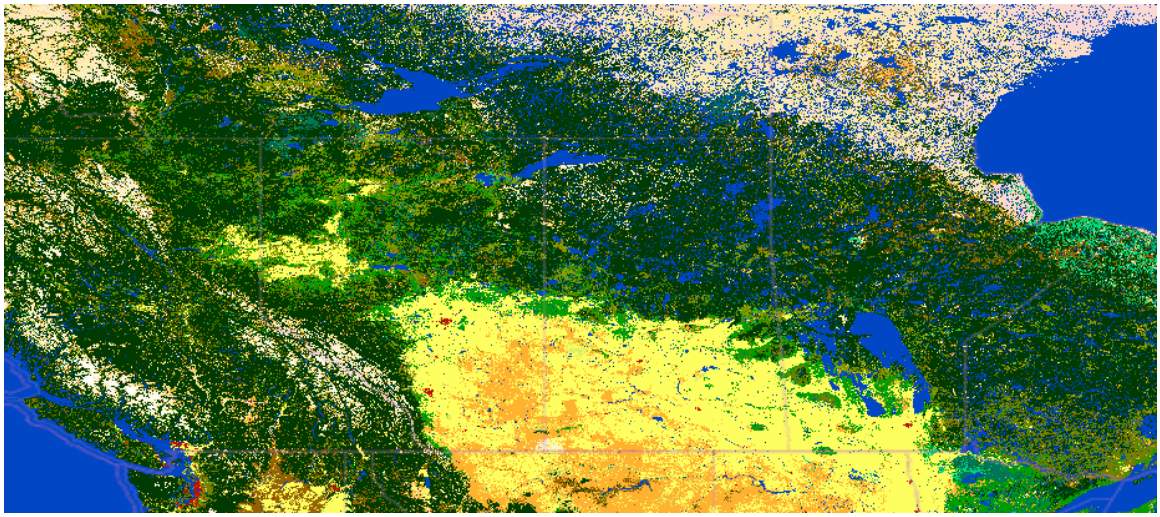

Figure 2.7: A sample image of the CCI LC product viewer map for Canada's Central and Western provinces. Each colour pixel indicates a different land type, with greens representing different tree covers, yellows and oranges representing shrubbery, herbaceous cover, and grasslands, and blues representing water, to name a few. Needleleaved tree cover are indicated in dark greens. For a complete list of all land types and their colours, see ESA (2017) and ESA (2022).

LC seasonality (Bontemps et al., 2012; ESA, 2024c). LC state comprises land-cover features that are stable and do not change over time and are independent of any sources of temporary or natural variability, while LC seasonality encompasses observable variables such as open water presence, burned area occurrence, snow coverage, and green vegetation phenology that relate directly to temporal or natural variability. Annual LC maps are available that provide a 300-m spatial and 1-year temporal resolution using data from the Medium Resolution Imaging Spectrometer (MERIS) full resolution/reduced resolution, Satellite Pour l'Observation de la Terre - Vegetation (SPOT-VGT), Advanced Very High Resolution Radiometer (AVHRR), and Project for On-Board Autonomy - Vegetation (PROBA-V), with the water body product being derived from the Envisat Advanced Synthetic Aperture Radar (ASAR) archives. These maps use the United Nations Food and Agriculture Organisation Land Cover Classification System (LCCS) (Di Gregorio, 2005), which is compatible with other land cover products such as the Global Land Cover 2000 (GLC2000) (Bartholome and Belward, 2005; European Commission, 2025) product and GlobCover 2005/2009 (Arino et al., 2007; Team et al., 2011). Global LC maps are currently available from 1992 to 2022 (ESA, 2017). Figure 2.7 shows a sample image from the CCI LC map

2022 for Central and Western provinces of Canada. Since the research in this thesis focuses on fires in the boreal forests of Western Canada, the ESA CCI LC land types that fall into the LCCS category of "*tree cover, needleleaved, evergreen*" with either the condition of *closed* (>40%) or *closed to open* (>15%) was used when selecting fires to calculate enhancement rates.

2.2 Gaussian-Flux Method

2.2.1 Flux Method Theory

The following is a theoretical derivation for equation used to calculate emission rates and enhancement rates in this thesis, described by Griffin et al. (2024) (Griffin24), which is adapted from methods developed by Mebust et al. (2011) (Mebust11), Adams et al. (2019) (Adams19), and Griffin et al. (2021) (Griffin21), and is henceforth referred to as the Gaussian-flux method. Mebust11 utilises OMI NO_2 vertical column density (VCD) to calculate the total mass emitted by each fire by converting aerosol optical thickness (AOT) to NO_2 column mass density (Ichoku and Kaufman, 2005). To select a fire, Mebust11 draws a rectangular box around a cluster of MODIS FRP hotspots (Figure 2.8) and makes the box large enough to encompass the plume in order to account for dispersion. (Note: for the derivations below, some variables and coordinates have been changed from the original source methods, for consistency. See the original publications for their derivations.)

The total NO_2 mass emitted (in kg), given a downwind direction of y, is calculated as

$$M_{NO_2} = (Y_{NO_{2,f}} - Y_{NO_{2,b}}) \cdot A_R \tag{2.1}$$

where $Y_{NO_{2,f}}$ is the NO_2 column obtained from averaging all OMI columns within rectangular area A_R, $Y_{NO_{2,b}}$ is the background NO_2 column for 60 days before and after the fire averaged within A_R, with MODIS FRP pixels removed, and A_R is the regional area of the box. The standard deviation on M_{NO_2} is

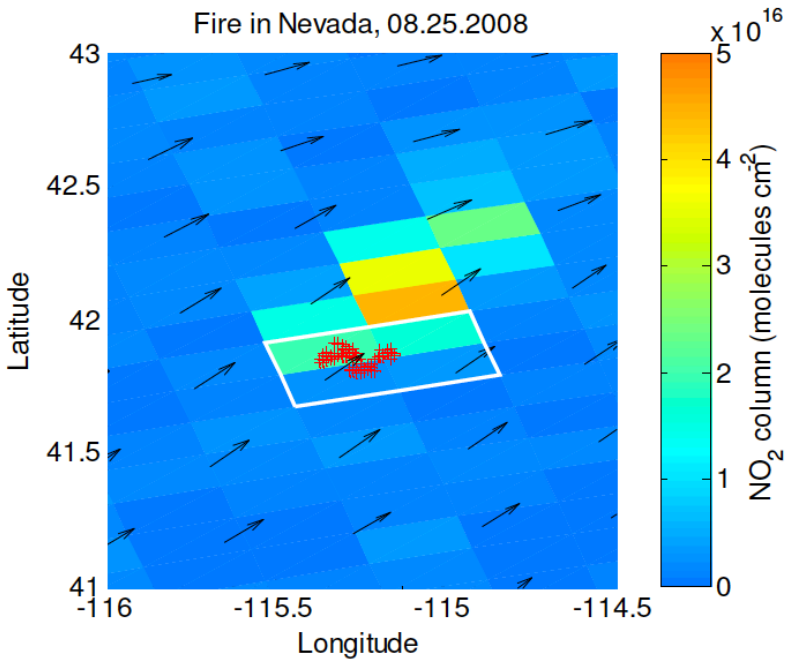

Figure 2.8: A rectangular box drawn over OMI tropospheric NO_2 column densities (molec/cm^2) with MODIS fire detections (red plus symbols) and North American Regional Reanalysis wind vectors (black arrows) for a Nevada wildfire observed by Mebust11 on August 25, 2008. *Figure taken from Mebust et al. (2011).*

$$\sigma_{M_{NO_2}} = (\sigma_{NO_{2,f}} - \sigma_{NO_{2,b}}) \cdot A_R \tag{2.2}$$

where $\sigma_{NO_{2,f}}$ and $\sigma_{NO_{2,b}}$ are the standard deviations of the column and background, respectively.

The time it takes for the species to clear the box, the clear time, is $t_c = \frac{d_c}{\omega_y}$ (seconds), where d_c is the distance from the centre of the rectangle (defined at the average position of all fire pixels within the fire) to the end of the box in the wind direction, and ω_y is the wind speed downwind, taken from the North American Regional Reanalysis (NARR). The standard error of d_c is 2 km (twice the resolution of MODIS), for small fires, and is the standard error associated with measuring the fire's centre, for larger fires. The percent standard error of t_c is defined as the percent standard error of d_c. The mass enhancement rate (MER) is then $MER = M_{NO_2}/t_c$, with a standard error of 30%, between 15% and 46% as reported in Wooster et al. (2003).

Mebust11 then develops a 1-D advection model that assumes: ω_y is constant over the dependent axis, horizontal diffusion and vertical diffusion can be neglected, and first-order kinetics, with rate constant k (s^{-1}) and lifetime $\tau = 1/k$. The concentration as a function of distance follows a 1-D, point source, diffusion model,

$$C(y) = C_0 \exp\left(-\frac{t}{\tau}\right) = C_0 \exp\left(-\frac{k}{\omega_y} y\right) \tag{2.3}$$

where C_0 is the concentration (kg/km in the 1-D model) immediately over the source and the age of the smoke is $t = \frac{y}{\omega_y}$ (in s). To get the total mass emitted (in kg), Equation 2.3 is integrated from the centre to the edge of the box, y_0, along the wind direction,

$$\begin{aligned} M_{NO_2} &= \int_0^{y_0} C(y)dy = C_0 \int_0^{y_0} \exp\left(-\frac{k}{\omega_y} y\right) dy \\ &= C_0 \frac{\omega_y}{k} \left[1 - \exp\left(-\frac{k}{\omega_y} y_0\right)\right]. \end{aligned} \tag{2.4}$$

Taking the clear time to be $t_c = \frac{y_0}{\omega_y}$ (where $d_c = y_0$) and considering that $C_0 y_0$ is the total mass (in kg) without decay, then the initial MER is $MER_{init} = C_0 \frac{y_0}{t_c}$. With the definition of the rate constant in terms of lifetime, the total mass can be defined from Equation 2.4 as

$$M_{NO_2} = MER_{init} \tau \left[1 - \exp\left(-k t_c\right)\right] \tag{2.5}$$

$$MER_{meas} = MER_{init} \frac{\tau}{t_c} \left[1 - \exp\left(-\frac{t_c}{\tau}\right)\right] \tag{2.6}$$

where Equation 2.6, the measured MER, is obtained by dividing both sides of Equation 2.5 by the clear time, t_c.

Adams19 expanded on this method by considering a 3-D Gaussian model where horizontal diffusion and vertical diffusion cannot be neglected. It is worth noting that Adams19 derives this method using molecules as the unit and later converts to mass. The following derivation uses that approach to maintain the same units as Adams19, and then converts molecules to mass at the end. A Gaussian model for a plume travelling downwind, in direction y, has a molecular concentration (molec/cm^3) given by

$$C(x,y,z) = \frac{E}{2\pi u \epsilon_x \epsilon_z} \cdot \exp\left[-\left(\frac{x}{\sqrt{2}\epsilon_x}\right)^2\right] \cdot \exp\left[-\left(\frac{z}{\sqrt{2}\epsilon_z}\right)^2\right] \cdot e^{-y/\tau u}, \tag{2.7}$$

where τ is lifetime (s), u is wind speed (m/s), E is the rate of molecular emission (molec/s) and ϵ_x and ϵ_z are constants of diffusion (m^2/s) in the crosswind (x) and vertical (z) directions (Stockie, 2011). This equation represents the steady-state advection-diffusion equation, with no deposition, constant wind, and constant diffusion coefficients, assuming diffusion is neglected downwind.

To convert this into a VCD (molec/cm^2), Equation 2.7 is integrated over z from the surface to the top of the troposphere to get:

$$V(x,y) = \frac{E}{\sqrt{2\pi} u \epsilon_x(y)} \cdot \exp\left[-\left(\frac{x}{\sqrt{2}\epsilon_x(y)}\right)^2\right] \cdot e^{-y/\tau u}. \tag{2.8}$$

Integrating across the crosswind direction, x, gives a 1-D molecular line density (molec/cm) as

$$L(y) = \frac{E}{u} \cdot e^{-y/\tau u}. \tag{2.9}$$

Total mass m (kg), which is obtained by converting molecules to kg using molecular mass $n = M_m/N_A$, the ratio of the molar mass of the species M_m (kg/mole) to Avogadro's number N_A (molec/mole), can be attained by integrating Equation 2.9 from the source to the edge of the box, y_c, in the downwind direction

$$\begin{aligned} m &= n\int L(y)dy = n\frac{E}{u}\int_0^{y_c} e^{-y/\tau u}dy \\ &= n\frac{E}{u}\tau u(1-e^{-y_c/\tau u}) = nE\tau(1-e^{-t_c/\tau}), \end{aligned} \tag{2.10}$$

which can be rearranged as

$$E = \frac{um}{n\int_0^{y_c} e^{-y/\tau u}dy} = \frac{m}{n\tau\left(1-e^{-t_c/\tau}\right)}, \tag{2.11}$$

where t_c is the clear time, defined similarly to Mebust11 as $t_c = y_c/u$ and E is in units of kg/s (as metric tonnes per hour, t/h). Equation 2.11 is the fundamental equation

used for the calculation of emission rates, in this research. Equation 2.11 was used to calculate emission rates or enhancement rates depending on the species being observed. Which term is used to describe Equation 2.11 and why will be discussed in the relevant chapters. Emission rates and enhancement rates also need to account for background, which is discussed in the following section.

2.2.2 Gaussian Method and Application

The Gaussian-flux method uses Equation 2.11 as the fundamental equation to calculate enhancement and emission rates. Griffin21 and Griffin24 expanded on the methods of Mebust11 and Adams19, discussed in Section 2.2.1, by replacing one rectangular area by a series of boxes of 4-km length from the fire centre to 150 km downwind. The width of the box, in the crosswind direction, is set to encompass the plume and the widths chosen will be discussed in the Section 2.3. Figures 2.9 and 2.10(a) are visual demonstrations of how enhancement rates are calculated using a modified photo, for instructional purposes, taken of the FIREX-AQ Horsefly Fire on August 6, 2019 (Wyatt, 2019) in a side-view and a top-down view taken from EOSDIS Worldview, respectively. The following steps explain how fire plume enhancement rates are calculated using the flux method developed by Griffin21.

- A cluster of MODIS FRP hotspots is found for the target fire, and the fire centre (transparent red line in Figure 2.9) is determined (see Section 2.3).
- TROPOMI AER_LH is used to determine the average aerosol height for the plume. If aerosol data are not available for the plume, the plume height defaults to 2 km (800 hPa), the average height of a plume (as detailed in Section 2.1.1, Griffin21, and Griffin24). This is demonstrated in Figure 2.9 as the blue box, where the upper and lower bounds of the aerosol height data are indicated and the blue dashed line represents the average aerosol height.
- ERA5 data are then used to determine the wind direction and speed (indicated by the solid, unidirectional white arrow on Figures 2.9 and 2.10(a)) for that height.

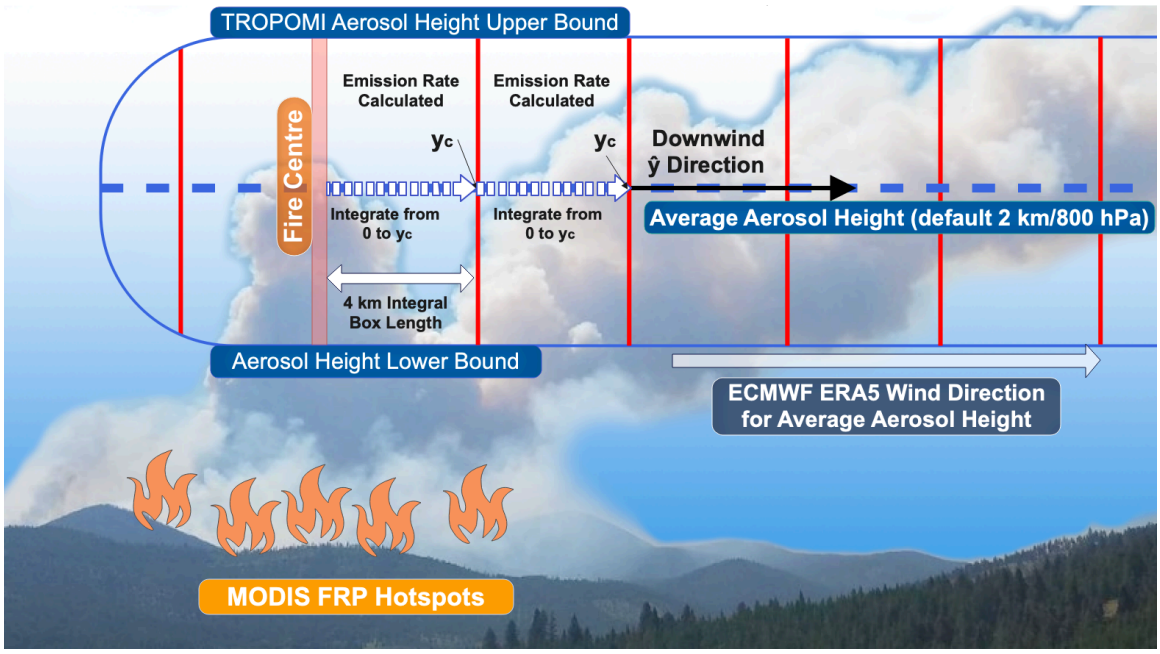

Figure 2.9: An annotated photo of the Horsefly Fire on August 6, 2019 demonstrating how the Gaussian-flux method is calculated from the side-view (y,z) direction, where the x-direction is out of the paper. Note: The photo and segments are not to scale. These are approximations for illustrative purposes only. *Original photo by Wyatt (2019).*

- The plume is then rotated around the fire centre until the majority of the plume faces the downwind, y, direction (black arrows on Figures 2.9 and 2.10(a)).

- In Mebust11, the background was calculated as the average of all tropospheric VCDs over the study area within the (x,y) box for 60 days before and after the first observation of the hotspot, with MODIS FRP pixels removed. Griffin21 analysed different backgrounds for this method and found that taking the background between 20 and 50 km upwind provided the best results (see limitations in Section 2.4 for HCHO limitations for this method). ΔVCDs were created by subtracting this background from VCDs calculated using Equation 2.8.

- The plume is not always pointing in the ERA5-determined wind direction due to errors and lack of precision in ERA5 data. To ensure that the plume is correctly rotated towards the downwind direction, a Gaussian distribution is added over the ΔVCDs (Griffin24), which determines the centre of the plume and corrects the initial ERA5 rotation to ensure the plume is downwind. Figure

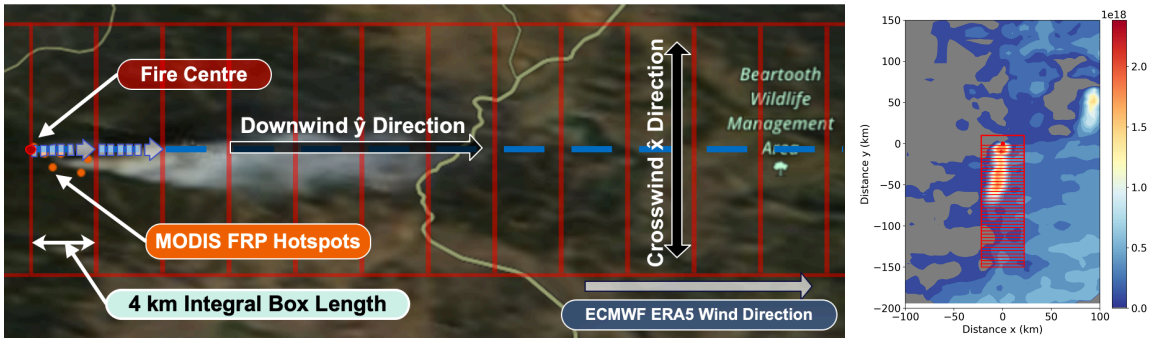

Figure 2.10: (a)A top-down [(x,y) direction] image of the Horsefly Fire on August 6, 2019 (NASA, 2024a), with annotation demonstrating the Gaussian-flux method calculations, and (b) a heat-map of TROPOMI CO ΔVCD enhancements from the same fire using the Gaussian-flux method. Boxes are to scale in both figures.

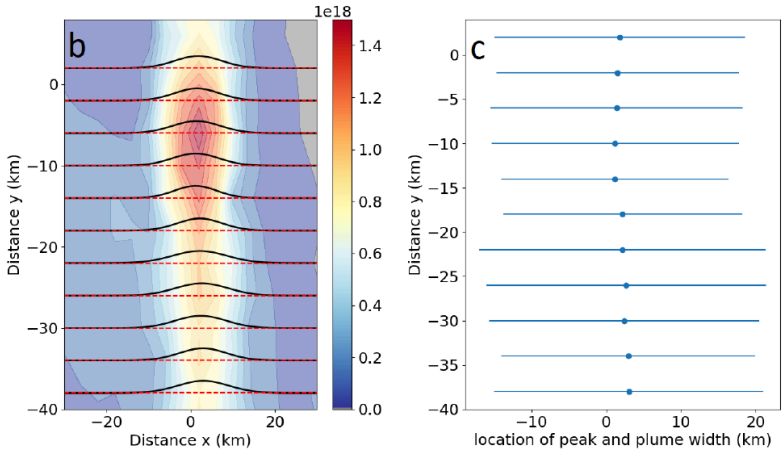

Figure 2.11: Two panels from Griffin24 Figure 1 that show the (b) Gaussian distribution across the ΔVCDs (molec/cm^2) for CO of a 2019 New Mexico fire and (c) the centre of the Gaussian plume for each 4-km segment (blue dot) with three standard deviations (blue line) from each fit.

2.11(b) shows a Gaussian distributed across the ΔVCDs of TROPOMI CO for a 2019 New Mexico fire from Griffin24. The centre of each Gaussian distribution in the 4-km integration segments is shown in Figure 2.11(c) as blue dots, with the blue lines representing three standard deviation. This is used to determine the true centre of the plume for the correction of the ERA5 rotation. This three-sigma correction is also capable of translating the fire centre in the horizontal (x) direction to ensure the majority of plume is in the centre of the boxes. The downwind direction, after correction, is seen in Figure 2.10(a) as the dashed blue line.

- Adams19 used an exponential curve fit plotted against the line density as a function of the downwind direction, Equation 2.9, to determine the trace gas lifetime. Griffin21 found that the best lifetime for NO_2 was 2 h. The TROPOMI overpass occurring at 1:30 p.m. local time, when fire activity is typically increasing, will impact any attempt to estimate the lifetime of short-lived species like NO_2 and HCHO with the method used in Adams19. Lifetimes, as a result, were set to the typical values for each species: 2 h for NO_2 (Mebust11, Griffin21), 6 h for HCHO, and 336 h (2 weeks) for CO (Yurganov et al., 2011; R'Honi et al., 2013; Whitburn et al., 2015).
  - The lifetimes of NO_2 and CO were determined to be the best for the method, from the the listed references, and fall within accepted lifetime ranges. HCHO has a typical photochemical lifetime of 4 to 5 hours (De Smedt et al., 2015; Stavrakou et al., 2015) with analysis in-situ measurements showing photolysis lifetimes of over 8 hours (Liao et al., 2021). For this reason a lifetime between these observations, of 6 hours, was selected.
- Equation 2.11 is then applied for each 4-km long box, where 0 is the start of the box on the up-wind side, and it is integrated to the end of the box, 4 km downwind, y_c, demonstrated as a series of white dashed arrows in Figures 2.9 and 2.10(a) for each box downwind up to 150 km. This provides the enhancement or emission rates, depending on the species analysed, for each 4-km segment along the plume, allowing us to observe the change of enhancements downwind.

2.3 Enhancement Rate Calculation and Adjustments

The method above was used to determine: (1) the CO, HCHO, and NO_2 enhancement rates of the Shady, Horsefly, and Williams Flats fires during FIREX-AQ (three plumes) and nine Western Canada fires in the summer of 2023 (sixteen plumes) in Chapter 3; (2) the HCHO, NO_2, and CO enhancement rates and FNRs for nine wildfires (fourteen plumes) in Western Canada in 2023 and seven wildfires (twelve plumes)

in 2025 from Central and Western Canada in Chapter 4; and (3) the CO emission rates of 27 wildfires from 38 plumes between 2023 to 2025 during Central and Western Canada's summer wildfire season in Chapter 5. Some fires have multiple TROPOMI overpasses due to the high latitude of some fire locations.

HCHO concentrations are usually not as concentrated in the centre of the plume as the other two species and so it can be difficult to fit a Gaussian distribution across the plume. Therefore, the Gaussian distribution downwind correction for HCHO (dwd) and the horizontal adjustment to the fire centre (xdir) were often incorrect. The method used in this thesis corrects for these issues and, therefore, differs slightly from how the method was used by Griffin21 and Griffin24 (Section 2.2.2). The exact method for determining fire locations and the selection of downwind directions and widths also differ from their method. A description of how data were collected for the fires studied is given below and is summarised in the flowchart in Figure 2.12.

1. Using NASA Worldview maps NASA (2024a) and MODIS FRP data, fires are located for FIREX-AQ and the western provinces of Canada.

    - To avoid contamination from other plumes of upwind fires, fires are only selected if they are upwind of other fires.
    - To ensure fires are selected from boreal forests, only fires in land types *Tree cover, needleleaved, evergreen*, taken from ESA CCI LC Product, with canopy at either *closed* (>40%) or *closed to open* (>15%) are selected.

2. Once a fire is located, the coordinates for MODIS FRP hotspots, with detection confidence ≥85%, near the most upwind portion of the plume are selected as the fire centre.

3. Enhancement rates are calculated using the Gaussian-flux method described in Sections 2.2.1 and 2.2.2, applying Equation 2.11 for CO, HCHO, and NO_2.

4. Not all plumes have well-formed Gaussian distributions of ΔVCDs and so the Gaussian will not fit properly. This causes the subsequent downwind correction, dwd, and x-position offset correction, xdir, to be incorrect for some species of

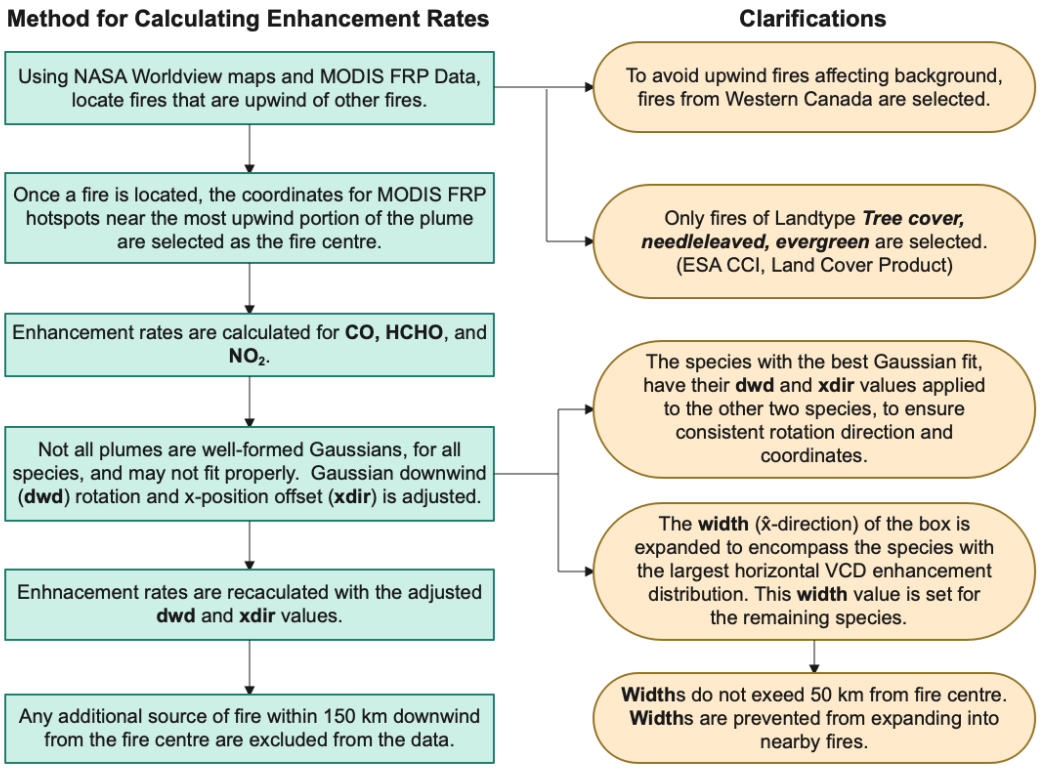

Figure 2.12: A flowchart summarising the step-by-step process for calculating enhancement rates, using the Gaussian-flux method, for the FIREX-AQ summer 2019 and Western Canada summer 2023 fires.

the same fire, most often HCHO. To correct for this, the following actions are taken:

- The species that has the best Gaussian distribution fit provides a more accurate dwd correction and xdir adjustment. The original rotation of the best-fit species is added to the dwd to get a total rotation in degrees. The dwd adjustment for the other two species is manually set so that the total rotation is the same for all three species.
  - Due to CO emissions being more prominent in the hottest part of the fire (highest FRP), the CO ΔVCDs are located and the fire centre coordinates are occasionally manually adjusted to within the upwind portion of the plume with the highest CO values, similar to Figure 2.10(b), deviating a bit from the exact fire centre coordinate locations

of Step 2.

- The width of the box is expanded manually to encompass all three species contained in the plume, deviating from the 3σ determination of width in Griffin24. As NO_2 and CO enhancements are usually more centralised in the plume, with higher concentrations toward the centre of the plume downwind, the boxes are typically expanded to a width that includes HCHO ΔVCDs. This width is then standardised for the remaining species. The width can also be adjusted to contain asymmetric plumes that are not perfectly straight due to crosswinds. This also ensures that horizontal dispersion is equally accounted for, for all three species.
  - Widths do not exceed $\pm$50 km from the fire centre.
  - Widths are prevented from being expanded into nearby fire sources. Some horizontal dispersion is lost in these cases, but fires with additional fires sources too near by are filtered, as will be discussed in the next section.
- Enhancement rates are then calculated again, with the new, adjusted dwd and xdir parameters for all three species.
- Any fires that have additional fire sources within 150 km directly downwind from fire centre have the data from the secondary source excluded from any data being used for plotting and analysis. This causes some of the plume data in the results section to not extend the full length of 150 km.

The calculated TROPOMI enhancement and emission rates are compared to the downwind direction, plume age, and emission time for each plume. An approximated plume age is calculated at the location of each enhancement rate by dividing the location of the enhancement rate (in km) by the wind speed (in km/h) averaged from the fire centre to 150 km downwind of the plume. The plume age is used to back-calculate emission times by subtracting plume age (in hours) from TROPOMI overpass time (in UTC).

2.4 Limitations of the Gaussian-Flux Method

The Gaussian-flux method has a number of limitations. It does not work for fires that fall into any of the following categories and so such fire plumes were filtered from the results: fires with large background columns; areas with large amounts of ambient HCHO; plumes that exceed 150 km in length or 50 km in width; fires that have nearby fire sources in the crosswind direction; fires with secondary downwind sources; initial wind corrections significantly >15°; and fires with plumes shorter than 10 km downwind.

Fires with large background VCDs, such as those that have fire sources within 20 to 50 km upwind, increase the background concentrations and make discerning the plume difficult or cause ΔVCDs and enhancement rates to be underestimated. Generally, if fires have background VCDs greater than 0.5 x 10^{19}, 0.6 x 10^{16}, and 0.6 x 10^{16} molec/cm^2 for CO, HCHO, and NO_2, respectively, this is an indicator that a large fire source is further upwind. This is a bigger issue for longer-lived species like CO. Fires burning in Quebec in summer 2023, for example, may have greater CO due to fires burning in Alberta. These chosen numbers are not hard limits and fires can be assessed case by case. Fires were selected with backgrounds that allowed for observation of a distinct plume profile.

Some land types, such as boreal forests, have a lot of naturally occurring HCHO due to reactions of VOCs. This ambient HCHO affects measurements due to the sensitivity of concentrations near the boundary layer from dispersion (Section 2.1.1). Absorption signals are weaker for HCHO and so concentrations may be negatively biased. Plume areas with large concentrations of surrounding background HCHO should be filtered if background concentrations are a significant component of HCHO measurements. Failure to do so may underestimate HCHO enhancements. Additionally, plumes that exceed 150 km in length stretch the capabilities of this method. Analysis of plumes longer than 150 km is possible, but crosswind dispersion often affects these plumes the further downwind they are observed, especially for species that exist throughout the width of the plume, such as HCHO. These would cause the

width to be extended, but widths that are larger than 50 km from the source break the assumption of a point source for the 1-D advection model in the Gaussian-flux method.

Longer plumes and wider plumes also increase the chances of encountering a secondary source. Fires that have nearby fire sources in the crosswind or downwind direction can lead to enhancement rates being overestimated, down-plume, as enhancement rates will include the contributions from the other fire. Secondary fire sources that are closer than 50 km in the crosswind direction (width) can be avoided by adjusting the width to remove the secondary source, as long as the plume from the second source is distinguishable enough to remove completely. Fires that have secondary sources and are >50 km downwind can be removed from data analysis, unless they are contained within the plume of the fire being investigated. In this case, the source fire cannot be analysed with this method as this violates the assumption of a point source.

As the Gaussian-flux method uses a Gaussian distribution to provide additional downwind rotation correction, too large of a rotation can affect the results. Initial wind corrections much greater than 15° can cause convergence issues and can violate the requirement of steady-state flow. Initial Gaussian correction refers to the downwind correction of the species that has the best Gaussian fit. Fires were selected to reduce this dwd rotation correction to the plume's direction for the best-fit species to as close to <15° as possible. Those species for which a Gaussian distribution could not be fitted (see Section 2.3) had their initial rotations corrected to match the best-fit species and this number did, on occasion, exceed 15°. The overall initial Gaussian correction of the plume, however, did not exceed an additional 10°.

Lastly, fires with a plume shorter than 10 km downwind push the limit of the ability to observe down-plume fluctuations in enhancement rates. Using the Gaussian-flux method to analyse enhancement rate changes in the plume to assess chemical formation or decay of different species will not provide quality data for fires this small. The flux method used to calculate total emissions, such as in Griffin24 and Griffin21, are not affected by this limitation.

There were a number of fires, due to the latitude of the fire, that had more than one TROPOMI overpass (usually two, but occasionally three). The additional overpasses did not always produce good quality data. Sometimes cloud cover or thick aerosol affected data results, especially for HCHO, which already has a low absorption signal and so is most susceptible to dispersion and scattering. For this reason, some overpasses showed good data for two species but not the third. The good data for the two species of the same orbit were kept and the third species was filtered out. Additionally, some orbits did not provide good data for any species or only one and so were filtered while the other orbit is kept. Orbit numbers are included in plotted data, for reference.

2.5 Uncertainties

The Gaussian-flux method uncertainty was calculated as 34% for CO by Griffin24 and 28% for NO_2 emission estimates by Griffin21. For consistency with for all species, including HCHO, the larger of the two is assumed for this study: 34%. This method uncertainty is assumed to ensure no underestimation of errors. The wind speed random error was calculated in Section 2.1.5 as 6% from Gualtieri (2022), with Griffin24 reporting a 20% wind altitude uncertainty.

For TROPOMI CO total columns, Sha et al. (2021) report a high bias of +10% and Rowe et al. (2022) report an averaging kernel correction of +6%. Taking the random uncertainty (34% for the method, 6% for wind speed, and 20% for wind altitude) summed in quadrature gives a total random uncertainty of 40%. Summing that in quadrature with the averaging kernel correction and satellite VCD bias, gives a total uncertainty of 42% for CO.

For NO_2 and HCHO, the method random error is also taken as 40%, as calculated above. With NO_2 having a -29% tropospheric bias (Van Geffen et al., 2020; ESA, 2024e; Lambert et al., 2024) for tropospheric columns, the systematic error summed in quadrature with the random error of 40% gives a total uncertainty of 49% for NO_2. HCHO has a negative bias over polluted areas, such as the boreal forests observed in

Table 2.1: Uncertainties in the enhancement rates derived for each species. All values in each uncertainty type are summed in quadrature for totals, while Total Uncertainty is a quadrature sum of Total Random and Total Systematic.

CO Total Column		HCHO Tropospheric Vertical Column		NO_2 Tropospheric Column	
Type	Uncertainty	Type	Uncertainty	Type	Uncertainty
Method	34%[1]	Method	34%[1]	Method	34%[1]
Wind Speed	6%[2]	Wind Speed	6%[2]	Wind Speed	6%[2]
Wind Altitude	20%[1]	Wind Altitude	20%[1]	Wind Altitude	20%[1]
Total Random	**40%**	**Total Random**	**40%**	**Total Random**	**40%**
Averaging Kernel	+6%[3]	Systematic Bias	-30%[5,6]	Systematic Bias	-29%[7,8,9]
Satellite VCD	+10%[4]				
Total Systematic	**12%**	**Total Systematic**	**-30%**	**Total Systematic**	**-29%**
Total Uncertainty	**42%**	**Total Uncertainty**	**50%**	**Total Uncertainty**	**49%**

[1]Griffin et al. (2024).
[2]Gualtieri et al. (2022).
[3]Rowe et al. (2022).
[4]Sha et al. (2021).
[5]ESA, (2024c).
[6]De Smedt et al. (2018).
[7]Van Geffen et al. (2020).
[8]ESA, (2024d).
[9]Lambert et al. (2024).

this study, of -30% (De Smedt et al., 2018; ESA, 2024d). Summing this systematic bias with the random error gives a total uncertainty of 50% for HCHO. More details about the uncertainties and systematic biases are in Section 2.1.1. These results are summarised in Table 2.1.

2.6 Important Definitions

Table 2.2 provides the terms for all important values calculated and analysed in Chapters 3, 4, and 5. The units, relevant equation for calculating it (if applicable), and a brief definition are provided for each term.

Table 2.2: Relevant terms for calculated and retrieved values analysed in this thesis, their units, relevant equations, and definitions. N/A stands for "not applicable."

Term	Units	Relevant Equation	Definition
VCD	molec/cm^2	Equation 2.8	Vertical Column Density
ΔVCD	molec/cm^2	Equation 2.8	Background-subtracted (BS) Vertical Column Density
Enhancement Rate	t/h	Equation 2.11	BS Enhancement per unit Time for CO, NO_2, and HCHO in Chapters 3 and 4
FRP	MW	N/A	Fire Radiative Power
EnhR	unitless	EnhR = $\Delta VCD_x/\Delta VCD_y$	Enhancment Ratio, ratio of ΔVCD of species x to ΔVCD of species y
FNR	unitless	FNR = $HCHO/NO_2$	Formaldehyde-Nitrogen Ratios, ratio of HCHO ΔVCD to NO_2 ΔVCD
ER	t/h	Equation 2.11	BS Emission Rate (Emission per unit Time) for CO in Chapter 5
EC	g/MJ	EC = ER/FRP	Emission Coefficient, ratio of Emission Rate to Fire Radiative Power

Chapter 3

Summer 2023 Canadian Boreal Forest Wildfires: An Analysis of CO, HCHO, and NO_2 Downwind Enhancement Rates

This chapter looks at the downwind enhancement rates of CO, HCHO, and NO_2 in wildfire plumes. The first goal was to validate the Gaussian-flux method enhancement rates against three wildfires studied during the summer 2019 FIREX-AQ in-situ campaign, using enhancement rate data provided by Chelsea E. Stockwell of the NOAA, with a method detailed in Stockwell et al. (2022), and total CO emissions data provided by Debora Griffin, using the method detailed in Griffin24, for the FIREX-AQ wildfires Shady, Horsefly, and Williams Flats. The enhancement rates for CO, HCHO, and NO_2 were then calculated for sixteen plumes from nine wildfires in Western Canadian boreal forests during the summer of 2023. The evolution of these enhancements in the downwind direction and as the plumes aged were examined to observe chemical production and evolution in the plume and any dependencies of maximum enhancement rates on FRP. ΔVCD enhancement ratios were also examined against plume age for HCHO/CO, NO_2/CO, and HCHO/NO_2 to further evaluate chemical dilution

and production of these species. This work has been reviewed by all co-authors and has been submitted for review to the *Journal of Geophysical Research: Atmospheres* (Hearne et al., 2025b), and the corresponding data have been published in Hearne et al. (2025a), at https://doi.org/10.5683/SP3/2RRB4Q.

3.1 Datasets and Methods

This work uses the TROPOMI CO total column, HCHO tropospheric vertical column, and NO_2 tropospheric column data products to calculate enhancement rates, with the AER_LH data product being used to determine plume height. The MODIS MOD14 and MYD14 FRP data products from Terra and Aqua, respectively, were used to determine fire centre for fires and to determine average FRP for each fire. The ECMWF ERA5 wind data product was used to get wind speed and direction at the AER_LH determined plume height or at 2 km (800 hPa) if plume height was unavailable. The GOES FDC FRP product, from GOES-16 and GOES-17, was used when observing diurnal effects of the FIREX-AQ summer 2019 fires. The CCI LC product was used to ensure wildfire fuel was coming from boreal forest land types. For more information on these datasets and their uses, see Chapter 2.

Lastly, this research uses the FIREX-AQ dataset discussed in Section 2.1.2. Of the fires sampled by the DC-8 (a full list can be found in Warneke et al. (2023)), the flights in Table 3.1 are for fires that are within a few hours of one TROPOMI overpass. Shady (RF07), Horsefly (RF12), and Williams Flats (RF13) wildfires were selected for their distinct, downwind plume shapes.

Table 3.1: Wildfires from NOAA's DC-8 FIREX-AQ summer 2019 campaign flights that are within a few hours of TROPOMI overpass times. For each date, the following information is provided: the FIREX-AQ-designated name and fire code, the initial and final aircraft transect times, the coordinates of the fire centre, the TROPOMI overpass orbit number and time of overpass. All times are in UTC. Greyed out fields indicate no second orbit was observed. The highlighted fires were fires that showed the most distinguished plume and were able to be analysed by this method. *Note: End times that cross midnight are on the next date.*

	FIREX-AQ						TROPOMI			
Date	Code	Name	Start Time	End Time	Latitude	Longtitude	Orbit 1 Number	Overpass 1 Time	Orbit 2 Number	Overpass 2 Time
20190725	RF07	Shady	22:25	3:50	44.53	-115.05	9228	20:37		
20190729	RF08	North Hills	22:42	1:15	46.75	-111.96	9284	19:23	9285	21:04
20190729	RF08	Tucker	22:42	1:15	41.73	-121.24	9284	19:23	9285	21:04
20190802	RF10	Ridge Top	22:13	23:48	47.48	-108.23	9341	19:48		
20190802	RF10	Lick Creek	0:23	2:29	47.16	-115.91	9341	19:48	9342	21:29
20190803	RF11	Williams Flats	22:28	1:22	47.97	-118.62	9355	19:31	9356	21:10
20190806	RF12	Horsefly	22:36	0:53	46.96	-112.44	9398	20:13		
20190806	RF12	Williams Flats	18:51	22:03	48.00	-118.55	9398	20:13	9399	21:55
20190807	RF13	Williams Flats	23:03	3:00	47.98	-118.62	9412	19:55	9413	21:36
20190808	RF14	Williams Flats	0:48	2:27	47.99	-118.50	9426	19:37	9427	21:16
20190812	RF15	Castle	23:17	3:49	36.48	-112.27	9483	19:58	9484	21:38
20190813	RF16	Castle	22:33	3:28	36.51	-112.29	9497	19:39	9498	21:20

This research follows the methods described in Sections 2.2 and 2.3, with details on the limitations and uncertainties found in Sections 2.4 and 2.5, respectively. Griffin24 used the Gaussian-flux method to calculate emission rates for CO, which is a stable species emitted directly from fires, with limited secondary production as is expected for HCHO and NO_2. Since rates in this chapter are estimated for species that can be both directly emitted and secondarily formed, these estimates are referred to as enhancement rates for all species, but they could also be referred to as net formation rates.

3.2 Enhancement Rates for FIREX-AQ

To assess the Gaussian-flux method for deriving enhancement rates, calculated enhancement rates were compared with estimates for fires from the NOAA FIREX-AQ summer 2019 campaign. The method requires a reasonably distinct, downwind plume that can be contained in a Gaussian fit. For this reason, the fires Shady (RF07),

Horsefly (RF12), and William Flats (RF13), orbit 9412, from Table 3.1 were selected. These fires worked best for this method and also demonstrate the application of the method to fires of different shapes and sizes. Figure 3.1 shows the output of the satellite-derived ΔVCDs plotted along the downwind y-direction for Shady (row a), Horsefly (row b), and Williams Flats (row c) fires for CO, HCHO, and NO_2, as outlined in Section 2.3. Each fire demonstrates the variability of the wildfire plumes shapes and sizes as well as variability of background levels, especially in regards to HCHO. The abundance of background HCHO in boreal forests can be seen in the retrievals. The widths of the boxes were defined to encompass the plumes, while reducing background HCHO. Other secondary fire sources of HCHO can be seen in Williams Flats (Figure 3.1 row c). This has been accounted for in the data through reduction of box length.

Enhancement rates were calculated for these three fires along the length of the plumes, downwind, limiting secondary fire emission sources, as shown in Figure 3.2(a,c,e), Figure 3.2(b,d,f), and Figure 3.3 for the Shady, Horsefly, and Williams Flats fires, respectively. Emission estimates for CO for all three fires were provided by Griffin24 (blue-dashed lined) and CO, HCHO, and NO_2 enhancement rates were provided by Stockwell et al. (2022). Rates were calculated with different lifetimes, τ, for HCHO and NO_2 to analyse the impact of lifetime on enhancement rates. The lifetimes used for each species were 336 hours, for CO, 1.5, 3.0, and 6.0 hours for HCHO, and 1.0, 2.0, 4.0, and 6.0 hours for NO_2. Each figure caption provides the time of the TROPOMI overpass on that day as well as the FIREX-AQ measurement start time (the time of the first plume transect sampling by the aircraft) and end time (the final plume transect) in UTC. End times that are past midnight 00:00 UTC are on the following day. Note that the times of the TROPOMI and in-situ measurements differ by two or three hours.

Diurnal variability of a fire could impact emissions over several hours as the TROPOMI overpass at 1:30 p.m. local time is typically when fire intensity is increasing. Aircraft enhancement rates were estimated as the integrated vertical distribution from in-situ plume transects, which differs from the satellite-method integrating hor-

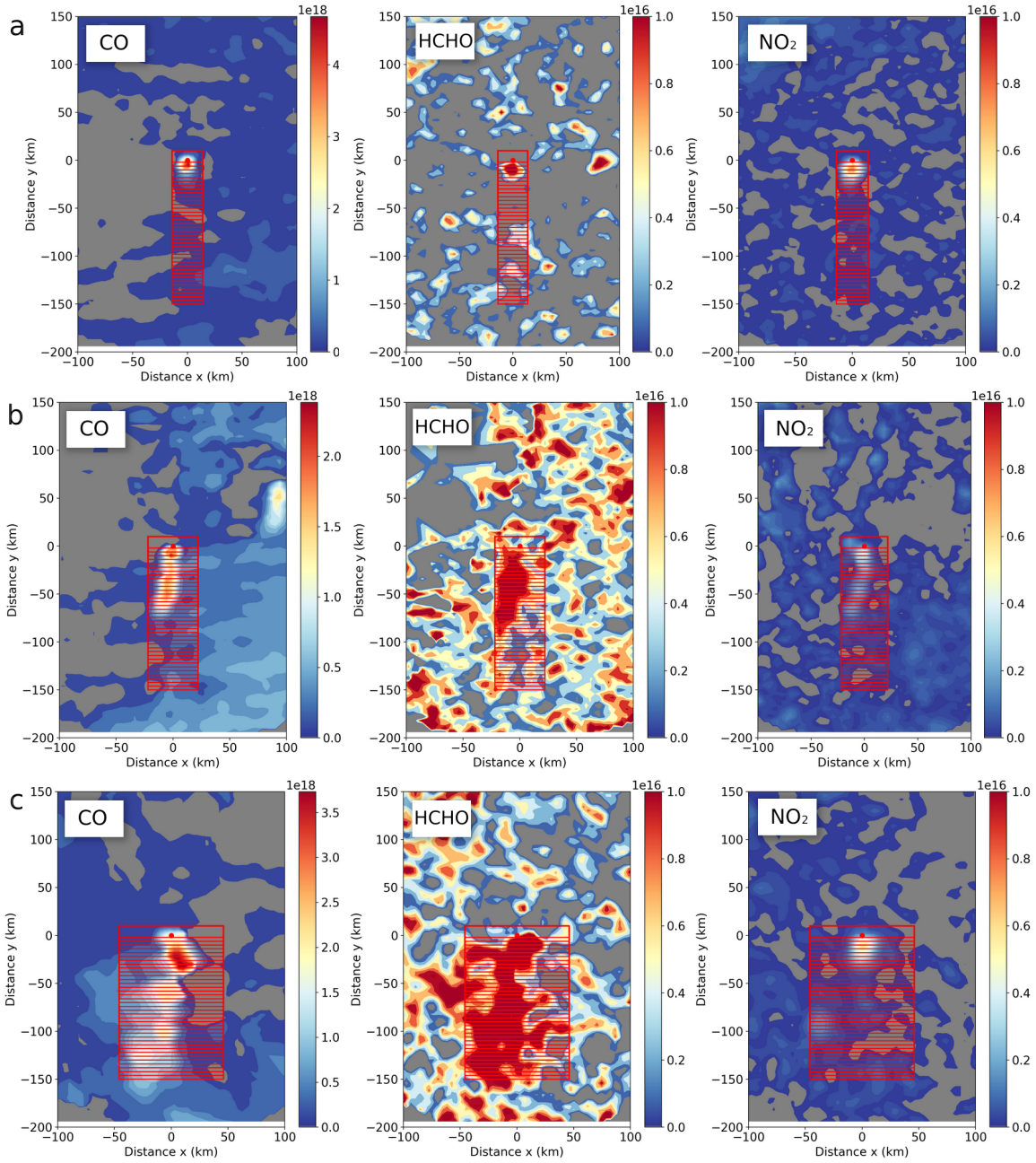

Figure 3.1: Spatial distribution heatmaps of the satellite-derived CO, HCHO, and NO_2 ΔVCDs, for the FIREX-AQ fires Shady (row a), Horsefly (row b), and Williams Flats (row c). ΔVCDs are in units of molec/cm^2.

izontally in 4-km increments. Therefore, the enhancement rate average (red-dashed line), one standard deviation (red-shaded area), and the upper and lower enhancements observed (blue-shaded area) for calculated emission times (not transect times), which were calculated by subtracting the plume age from the transect time, two hours

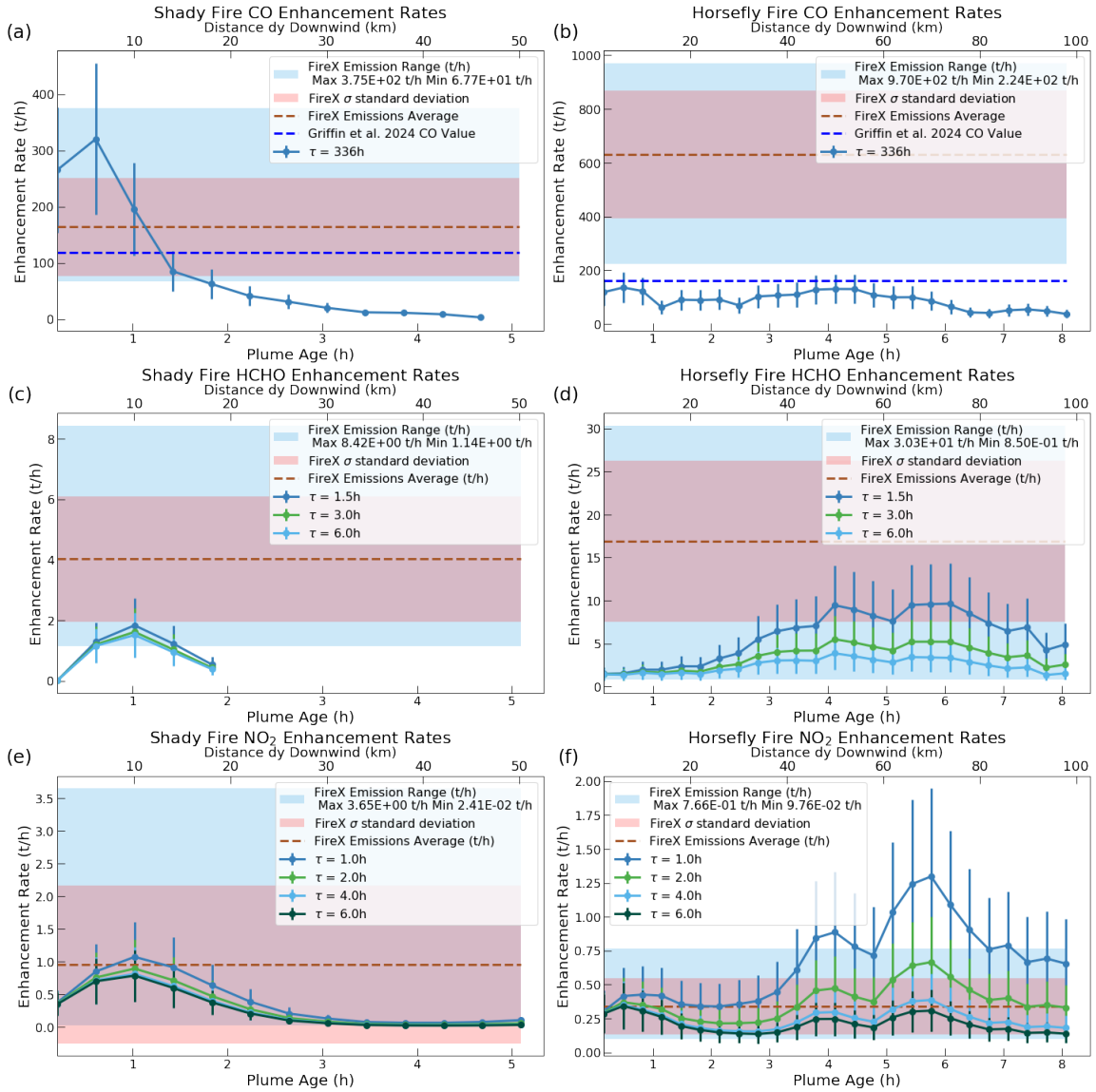

Figure 3.2: Satellite-derived enhancement rates for (a,b) CO, (c,d) HCHO, and (e,f) NO_2 for the FIREX-AQ Shady (a,c,e) and Horsefly (b,d,f) fires versus estimated plume age and downwind direction, dy, for assumed lifetimes, τ. TROPOMI overpasses were at 20:37 and 20:13 UTC for each fire, respectively, with aircraft sampling occurring between 22:25-3:50 UTC and 22:26-0:53 UTC, respectively. The average aircraft-derived rates are also shaded as a red, dashed line with $\pm$ 1 standard deviation shown in red and the full range shaded in blue. Aircraft rates are only shown when the emission time was expected to be within two hours of a TROPOMI overpass. For CO only (a,b), satellite-derived rates from Griffin24 for these two fires are indicated by dashed blue lines, with a total uncertainty of 57% (not shown). Error bars represent reported uncertainty for each species in Table 2.1.

before and after TROPOMI overpass time are compared, in the downwind direction, to the results as a function of distance and plume age. Two hours was selected as the threshold for calculated emission times to ensure comparison of FIREX-AQ rates

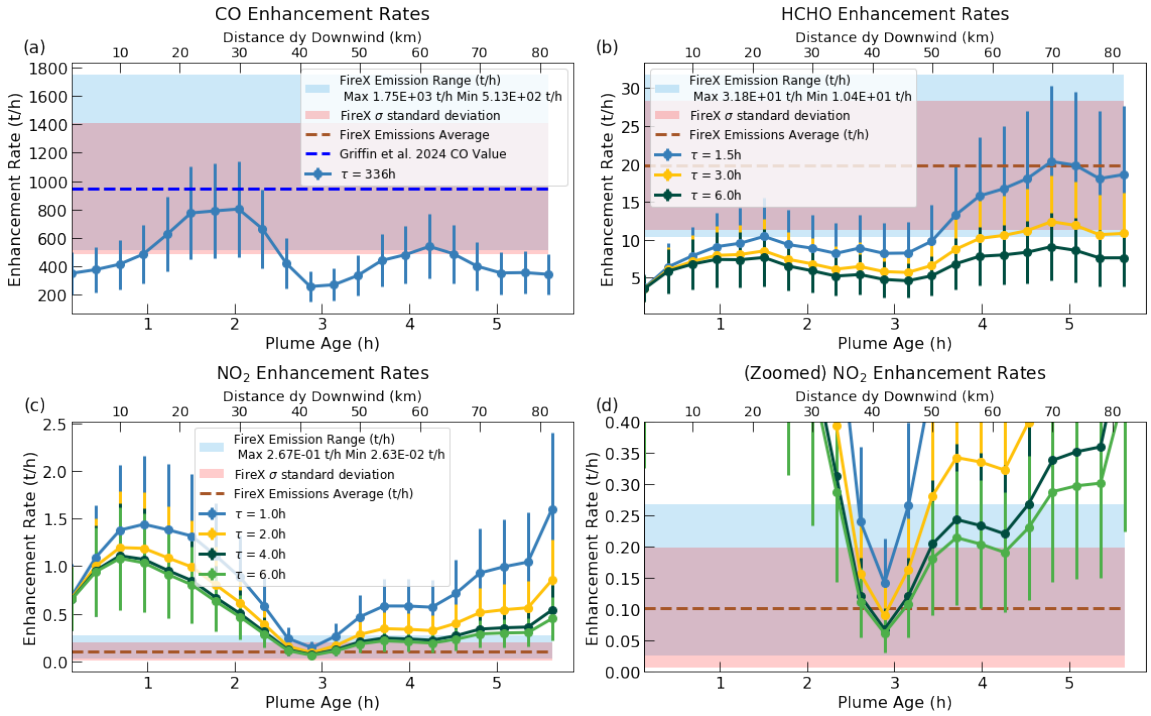

Figure 3.3: Satellite-derived enhancement rates for (a) CO, (b) HCHO, and (c,d) NO_2 for the FIREX-AQ William Flats fire versus estimated plume age and downwind direction, dy, for assumed lifetimes, τ, similar to Figure 3.2. Overpass was at 19:55 UTC with aircraft sampling occurring between 23:03-3:00 UTC. Plot (d) is zoomed in so that the details of the NO_2 enhancement rates can be seen clearly. Same shading and error bar conventions as Figure 3.2 *Note: The FIREX-AQ (represented as FireX) average and Griffin24 CO values nearly overlap in Panel (a) making it difficult to distinguish them.*

closer to TROPOMI overpass times to limit diurnal variable effects.

The average enhancement rates of the FIREX-AQ data being generally larger than the calculated values in this research is largely due to FIREX-AQ sampling occurring a few hours later than TROPOMI. When looking at the wide range of the enhancement rates, it is possible to further observe the diurnal differences between FIREX-AQ transect and TROPOMI overpass times by plotting the enhancement rate versus emission time, seen in Figures 3.4 and 3.5, for the Shady/Horsefly and Williams Flats fires, respectively. Emission times, like those for FIREX-AQ, were calculated by using the plume age in hours, taking the TROPOMI overpass time, and subtracting the plume age from the overpass. This effectively flips enhancement rates Figures 3.2 and 3.3 on the x-axis as enhancement rates go backward in time. To observe the diurnal nature and its affect on emissions, all available GOES-16 and

GOES-17 FRP data are plotted for the time window of both observation methods. While HCHO and NO_2 can be secondarily formed in a fire, their respective estimated enhancement rates generally increase with fire intensity since they are also directly emitted compounds. It can be seen from Figures 3.4 and 3.5 that from the time of TROPOMI overpass (the furthest right blue data point) is when FRP is starting to increase, leading to larger FIREX-AQ enhancement estimates.

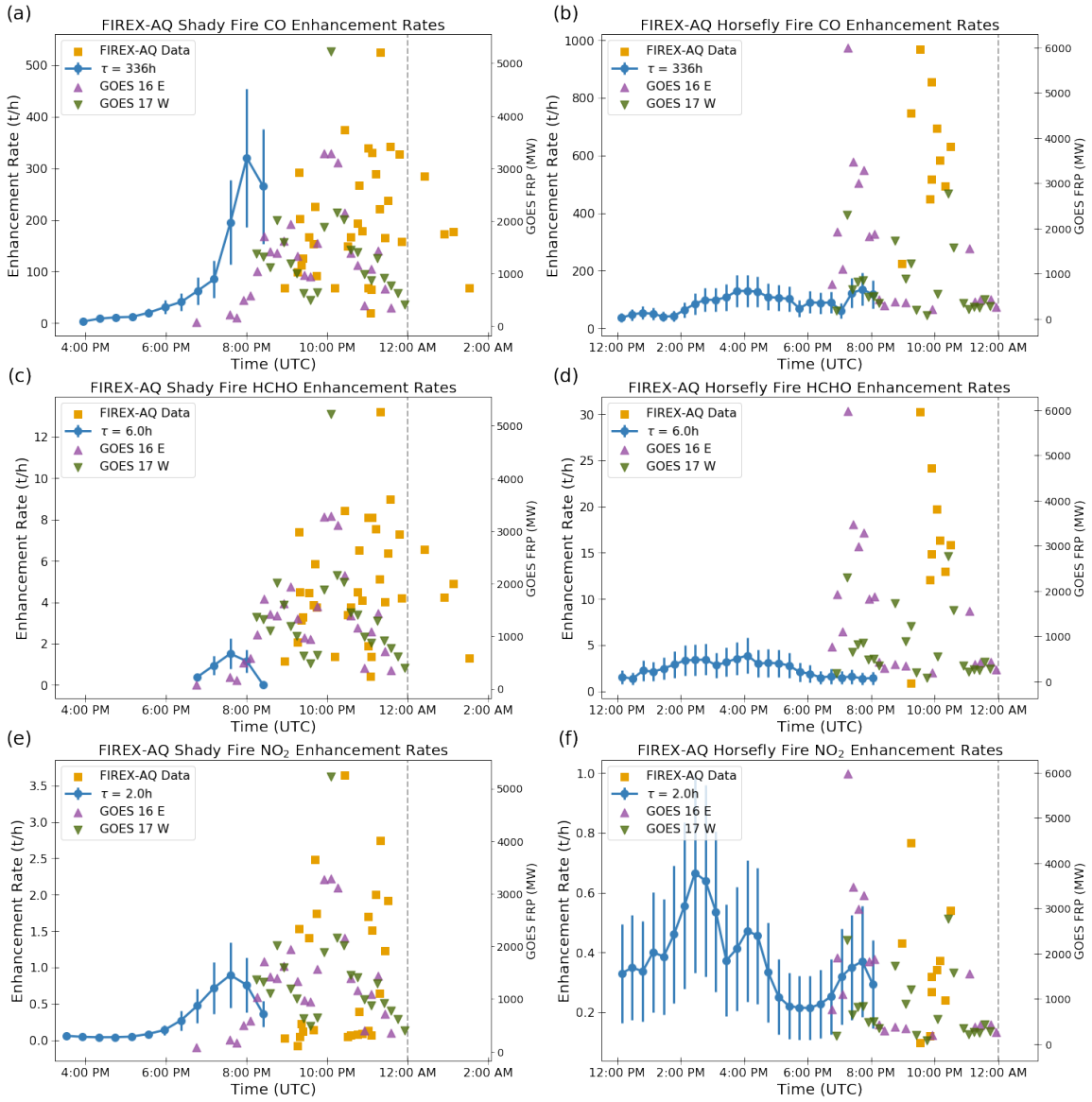

Figure 3.4: Calculated enhancement rates versus emission time (in UTC) for (a) CO, (c) HCHO, and (e) NO_2, for the FIREX-AQ Shady fire and (b) CO, (d) HCHO, and (f) NO_2 for the Horsefly fire. TROPOMI enhancement rates from the Gaussian-flux method are in blue, with FIREX-AQ enhancement rates provided in orange. τ is the lifetime used for calculations of each species. FRP from GOES 16 (GEOS East) and 17 (GOES West) are shown as purple and green triangles, respectively. The grey dashed line shows the start of the next day. Error bars represent the uncertainty of each species as reported in Table 2.1.

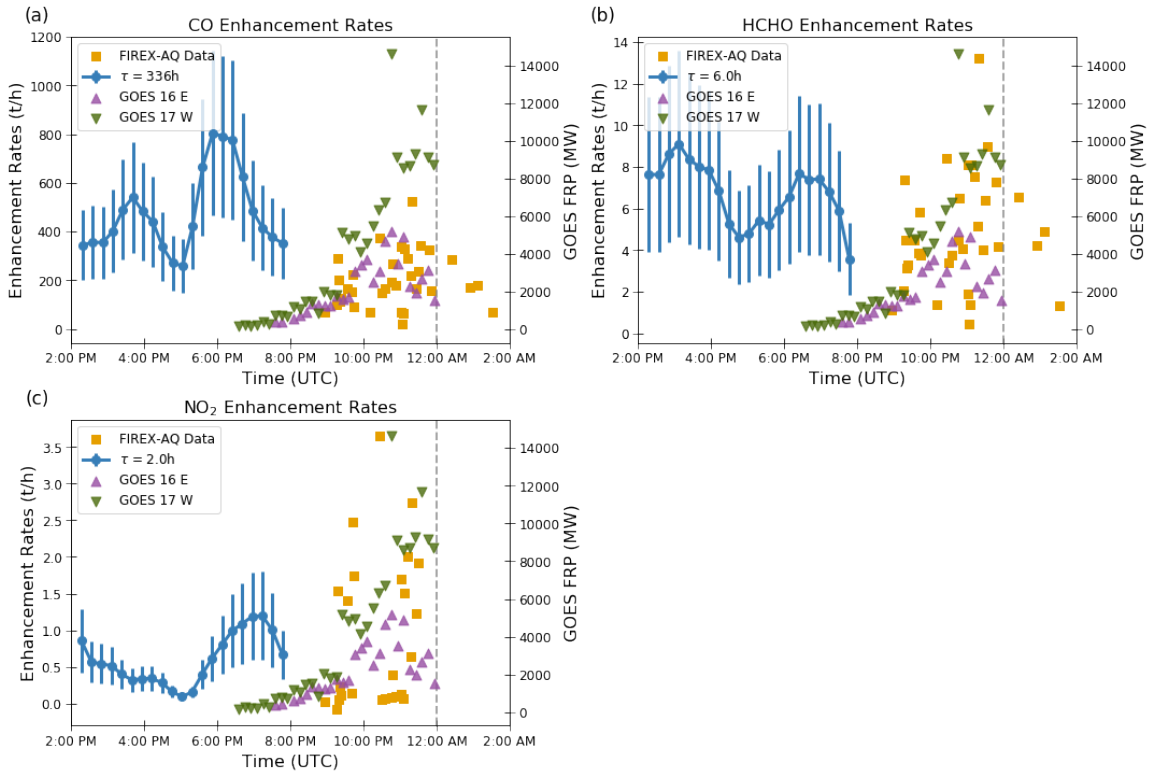

Figure 3.5: Calculated enhancement rates versus emission time (in UTC), same as Figure 3.4, for the FIREX-AQ William Flats fire. Error bars represent the uncertainty of each species as reported in Table 2.1.

Figures 3.2 and 3.3, along with Figures 3.4 and 3.5, generally demonstrate consistency with FIREX-AQ calculated enhancement rates. All three fires are, within 30 km downwind and allowing for uncertainty, comparable with the single-emission estimates for CO provided by Griffin24. Calculated enhancement rates are also accordant with FIREX-AQ ranges and within one standard deviation of the average at various points downwind, within uncertainty, for all three fires except for Horsefly's CO. NO_2 enhancement rates for Williams Flats are greater near TROPOMI overpass time, but Figure 3.5 shows that these rates are aligned with in-situ measurements across all measurements. These results demonstrate consistency with FIREX-AQ in situ enhancement rates and Griffin24 CO single-emission-rate estimates. The variable lifetimes used for enhancement rates of HCHO and NO_2 did not have a significant impact on how well the results correlated with FIREX-AQ and Griffin24. Therefore, the lifetimes for HCHO and NO_2 were chosen as 6.0 h and 2.0 h, respectively, to

align with lifetimes used by Adams19, for HCHO, and the best lifetime determined by Griffin21, for NO_2.

Griffin24, while demonstrating the Gaussian-flux method, used a 2019 fire in New Mexico that fit the Gaussian profile very well as an example of an ideal plume that fits a Gaussian functions without significant background concentrations. For further validation of calculated results, the enhancement rates for this fire (details of the fire can be found in Table 3.2) were examined for each species in Figures 3.6 and 3.7. Figure 3.8(e), taken from Griffin24, shows a similar CO profile to Figure 3.7(a) downwind, for the New Mexico fire, with enhancement rates near 500 t/h near the source of the fire and rates near 150 t/h at 100 km matching the calculated results of this study, within uncertainty.

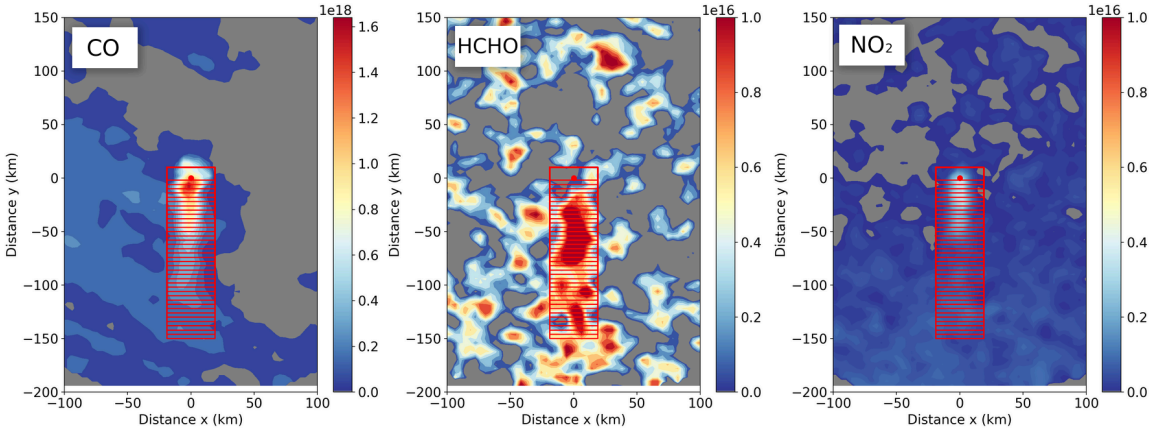

Figure 3.6: Heatmap of the satellite-derived TROPOMI CO, HCHO, and NO_2 ΔVCDs, for the 2019 New Mexico fire used in Figure 1 of Griffin24 (see Table 3.2). ΔVCDs are in units of molec/cm^2.

These four fires (Figures 3.2, 3.3, and 3.7) demonstrate the versatility of the method for determining the down-plume enhancement from fires with plumes having various spatial distributions. The biggest issue with the HCHO analysis, which can be seen in the satellite heatmaps (Figures 3.1 and 3.6), is that HCHO can be found throughout the plume and typically does not match a Gaussian profile. CO and NO_2, unlike HCHO, are found primarily in the centre of the plume in a distribution sometimes similar to Gaussian. There are some benefits to this, however. Because HCHO appears throughout the plume, this allows for an observable means to determine the shape of the plume itself, with some uncertainty due to noise, helping reduce the

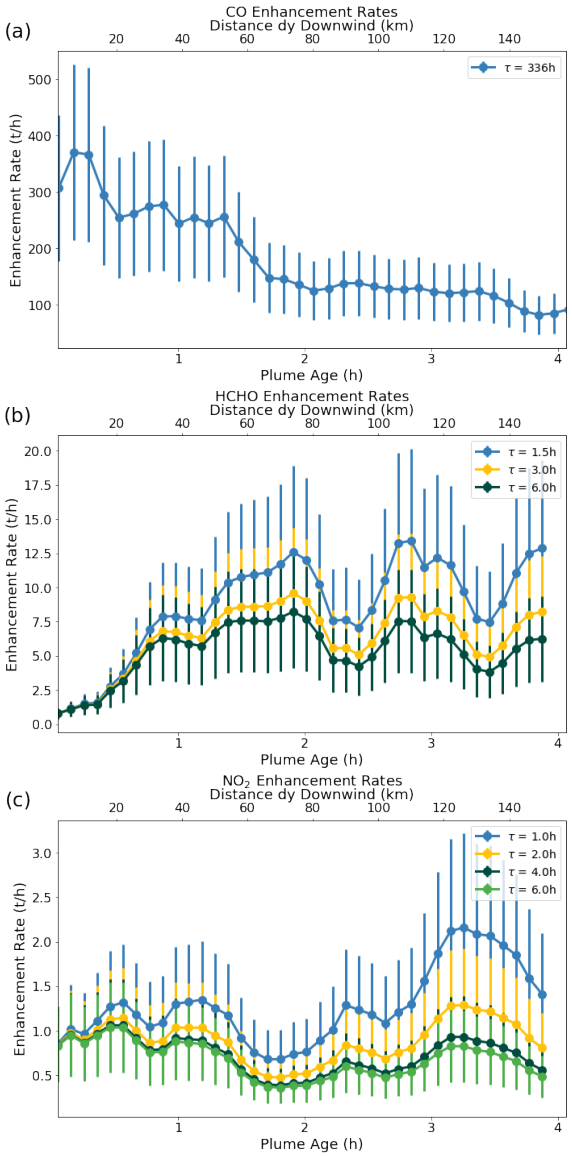

Figure 3.7: Calculated enhancement rates versus downwind direction and plume age for the 2019 New Mexico fire found in Figure 1 of Griffin24 for the species (a) CO, (b) HCHO, and (c) NO_2, with uncertainties from Table 2.1 indicated by the error bars. Different lifetimes, τ, are shown for calculated enhancement rates.

ambiguity of crosswind diffusion when defining the plume width. A pattern of where the enhancement rates occur in the plume, for each species, will be explored in greater detail in the following section.

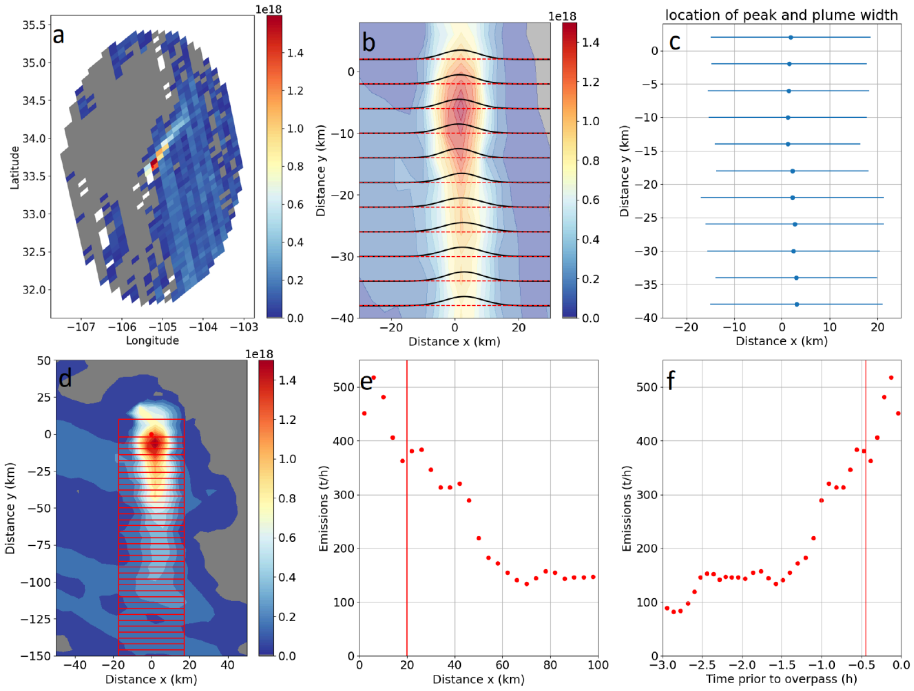

Figure 3.8: A figure demonstrating the method for CO emissions of the 2019 NewMexico fire taken from Griffin24. Panel (a) shows longitude-latitude unmodified TROPOMI VCDs, (b) shows a Gaussian fit in the crosswind direction for each 4 km box for 40 km downwind, (c) is the peak x_0 with three standard deviations shown as blue dots and bars, respectively, (d) provides Gaussian-corrected VCDs for each 4 km box with three standard deviations, (e) is the enhancement rate as a function of distance downwind (*Correction: figure says downwind direction is x, but it should be y*), and (f) is the enhancement rates from (e) but projected as time since emission.

3.3 Western Canadian Wildfires

3.3.1 Enhancement Rates

This study of the 2023 Canadian wildfires focuses on the western provinces of Canada where there was no significant wildfire source upwind. All fires were selected based on the CCI Land Product classification of needleleaved evergreen during the 2023 summer fire season: nine fires were selected, with sixteen plumes being analysed by this method. The fires are named by their approximate location near geographic landmarks and their corresponding TROPOMI overpass orbit numbers, if applicable for multiple overpasses. The naming convention for these fires and the details of the dates and fire centre locations can be found in Table 3.2. The ΔVCDs and

enhancement rates for each plume were calculated for CO, HCHO, and NO_2. Some fire plumes do not extend the full 150 km, to remove either background interference or secondary sources. Additionally, not all orbits, despite multiple orbits being sometimes available, provided usable data as some plumes were indiscernible or obscured due to limitations in the method that are discussed in Section 2.4.

The downwind enhancement rates for each plume for each species were plotted and normalised by their respective maximum values in Figures 3.9 and 3.10 as a function of downwind direction and plume age. Rates were normalised to allow for visual comparison of each species as they evolve in the plume because rates often differed by orders of magnitude from each other. The maximum enhancement rates used for normalisation of each species are given in the legend. Average FRP was calculated from MODIS, which has overpass times of 10:30 a.m./p.m. and 1:30 a.m./p.m. local time on Terra and Aqua, respectively. As the TROPOMI overpass is near 1:30 p.m. local time, these FRPs are usually from Aqua, however, due to the high latitude of some of the fires, there are occasionally additional overpasses from Terra within a few hours of Aqua. To account for all the FRP data available, FRP was averaged from values obtained within three hours of a TROPOMI overpass to limit diurnal affects on FRP. The exceptions to this were the EntiakoParkBC and FoxMountainNWT as there were no MODIS FRP values for the days of the TROPOMI overpass, which were July 11, 2023 and July 8, 2023, respectively. The FRP for the EntiakoParkBC fires is averaged from all FRP near the TROPOMI overpass on the following day (July 12, 2023). Meanwhile, the FRP for the FoxMountainNWT fires is averaged from the next closest MODIS overpass, which was 10:30 p.m. local time on the previous day (July 7, 2023) by Terra, as there are no Terra or Aqua FRP available on the day of TROPOMI overpass or the following day. EntiakoParkBC and FoxMountainNWT FRPs are therefore only estimations of fire intensity and are subject to diurnal effects. The FRPs for these two fires are only provided to help gauge the intensity of the fire and are not included in analysis of FRP data.

Looking at each panel in Figures 3.9 and 3.10, a noticeable pattern can be observed regarding the CO, HCHO, and NO_2 enhancement rates. CO is directly emitted by the

Table 3.2: The naming convention for the Western Canadian fires discussed in this paper, with the province of origin, TROPOMI orbit number and dates (YYYYMMDD) and times of overpass in UTC, the coordinates of the fire centre used, and the ESA CCI Land Product type of each fire.

Name Code	Province	Orbit Number	Date	Overpass Start UTC	Overpass End UTC	Latitude	Longitude	ESA CCI Land Cover Product Type
NewMexico	New Mexico, USA	8645	20190621	7:31:45 PM	7:32:45 PM	33.60	-105.24	Tree cover, needleleaved, evergreen, closed to open (>15%)
NormanWellsNWT	Northwest Territories	29658	20230704	8:46:17 PM	8:47:16 PM	65.50	-126.75	Tree cover, needleleaved, evergreen, closed (>40%)
MaxhamishLake	British Columbia	29318	20230610	9:35:36 PM	9:36:31 PM	59.83	-123.58	Tree cover, needleleaved, evergreen, closed to open (>15%)
MaxhamishLake11_o29331	British Columbia	29331	20230611	7:36:33 PM	7:37:32 PM	59.83	-123.58	Tree cover, needleleaved, evergreen, closed to open (>15%)
MaxhamishLake11_o29332	British Columbia	29332	20230611	9:16:31 PM	9:17:30 PM	59.83	-123.58	Tree cover, needleleaved, evergreen, closed to open (>15%)
MaxhamishLake13	British Columbia	29360	20230613	8:38:48 PM	8:39:47 PM	59.83	-123.58	Tree cover, needleleaved, evergreen, closed to open (>15%)
TweedsmuirBC_o30225	British Columbia	30225	20230813	7:52:35 PM	7:53:32 PM	53.04	-125.98	Tree cover, needleleaved, evergreen, closed (>40%)
TweedsmuirBC_o30226	British Columbia	30226	20230813	9:32:11 PM	9:33:11 PM	53.04	-125.98	Tree cover, needleleaved, evergreen, closed (>40%)
ChaseParkBC_o29331	British Columbia	29331	20230611	7:36:10 PM	7:37:10 PM	57.10	-124.80	Tree cover, needleleaved, evergreen, closed (>40%)
ChaseParkBC_o29332	British Columbia	29332	20230611	9:15:50 PM	9:16:49 PM	57.30	-124.40	Tree cover, needleleaved, evergreen, closed (>40%)
TumblerRidgeBC	British Columbia	29275	20230607	8:11:53 PM	8:12:53 PM	52.93	-125.67	Tree cover, needleleaved, evergreen, closed (>40%)
EntiakoParkBC_o29757	British Columbia	29757	20230711	8:50:04 PM	8:51:03 PM	55.21	-120.53	Tree cover, needleleaved, evergreen, closed (>40%)
EntiakoParkBC_o29758	British Columbia	29758	20230711	9:52:01 PM	9:53:02 PM	52.98	-125.42	Tree cover, needleleaved, evergreen, closed (>40%)
DeaseLakeBC	British Columbia	29701	20230707	9:28:47 PM	9:29:46 PM	59.62	-129.58	Tree cover, needleleaved, evergreen, closed (>40%)
DenetiahParkBC	British Columbia	29701	20230707	9:28:36 PM	9:29:36 PM	59.11	-127.56	Tree cover, needleleaved, evergreen, closed to open (>15%)
FoxMountainNWT_o29714	Northwest Territories	29714	20230708	7:31:21 PM	7:32:22 PM	61.75	-134.70	Tree cover, needleleaved, evergreen, closed (>40%)
FoxMountainNWT_o29715	Northwest Territories	29715	20230708	9:10:44 PM	9:11:43 PM	61.96	-134.52	Tree cover, needleleaved, evergreen, closed (>40%)

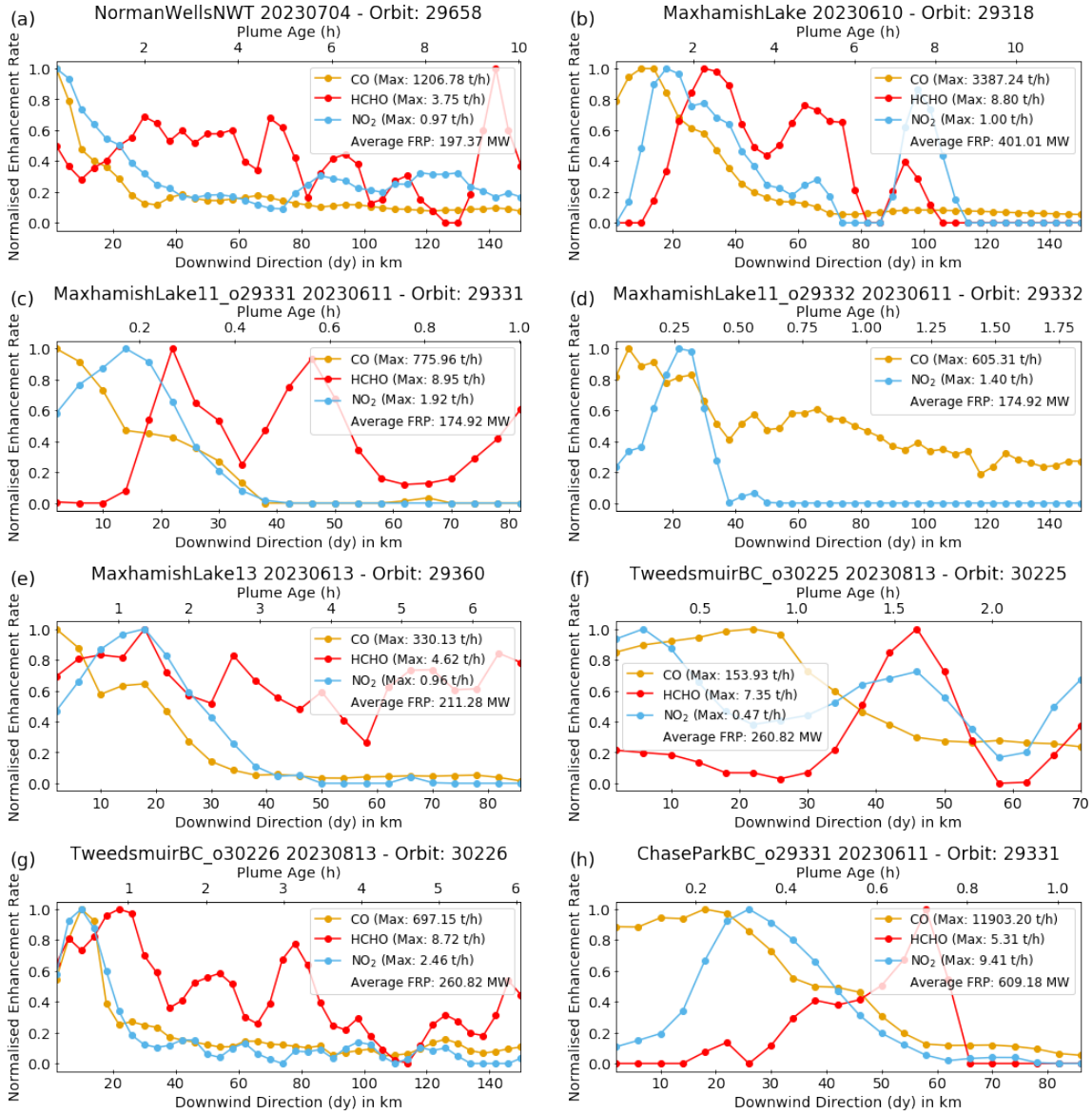

Figure 3.9: Enhancement rates of CO (yellow), HCHO (red), and NO_2 (blue) versus downwind direction and plume age for the first eight of sixteen total plumes from fires in Western Canadian boreal forests during summer 2023. For each plume, the enhancement rates have been normalised by the maximum enhancement rate for each species. The maximum enhancement rate used for normalisation is provided in the legend, as well as the averaged FRP for the fire within a few hours of overpass time. The naming convention for the fires can be found in Table 3.2.

fires and rates show dependence on FRP, with dilution occurring further downwind. NO_2, however, shows enhancements starting further down the plume than the fire centre. This suggests NO_2 is rapidly formed in the plume. NO_2 is a secondary by-product of NO, which are produced in the flaming and smouldering phase, respectively (Roberts et al., 2020), before being converted to other nitrogen products downwind.

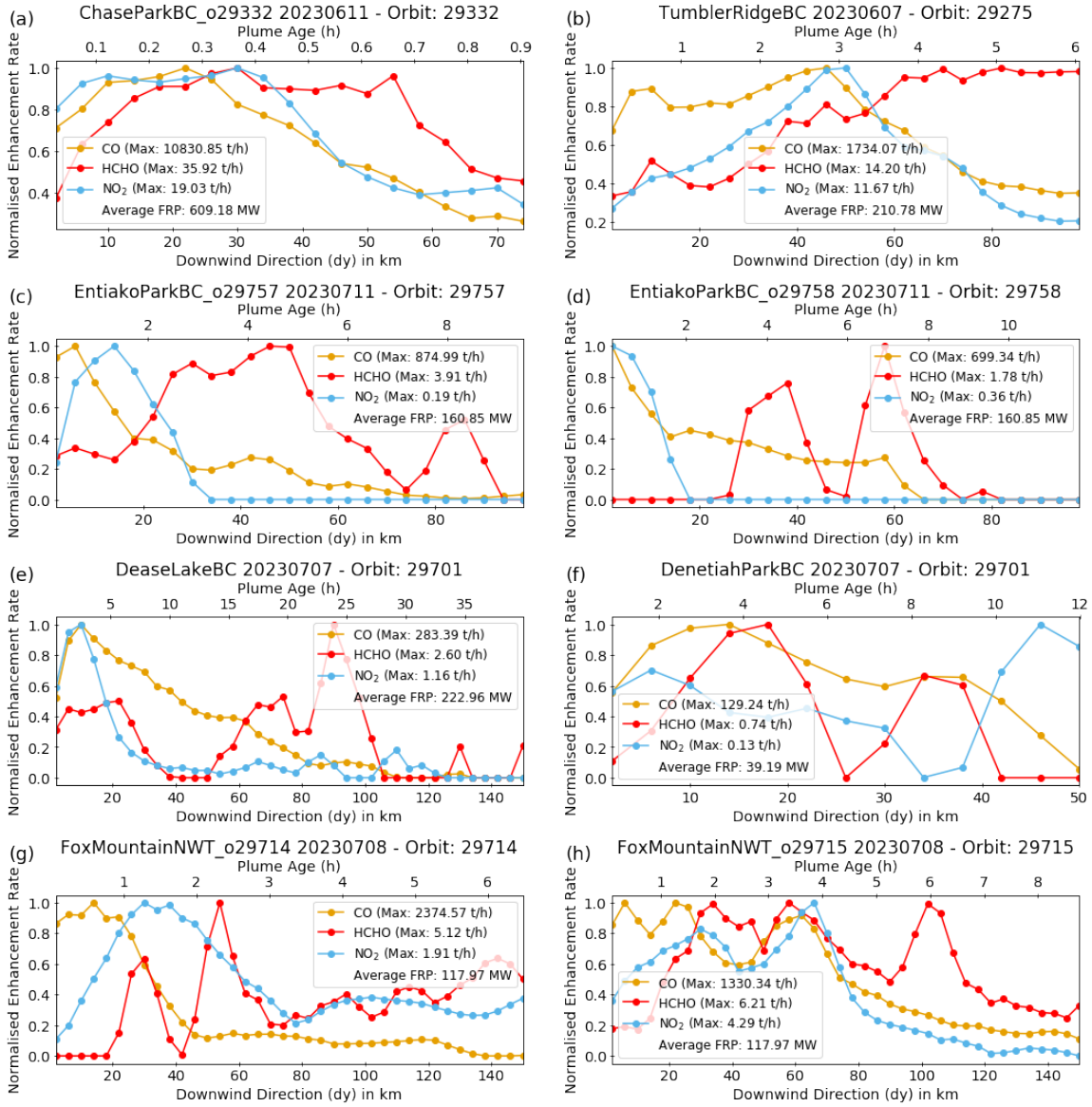

Figure 3.10: Same as Figure 3.9 for the remaining eight of sixteen plumes from fires in Western Canadian boreal forests summer 2023. *Note: EntiakoParkBC fires had no FRP data for the day of the fire so FRP averages are taken from FRP data within a few hours of the TROPOMI overpass on the following day. FoxMountainNWT_o29714 and _o29715 did not have FRP values within three hours of overpass time (19:31 and 21:10 UTC, respectively). For these fires, FRP average was taken from the next closest MODIS overpass with FRP data (05:53 and 07:31 UTC, same day in UTC).*

HCHO also appears as a secondary emission in the plume, but this generally takes place after rates of NO_2 begin to decline. The HCHO enhancement rates vary and even increase at times along the plume even with the continued decrease of NO_2, suggesting that a secondary source of HCHO exists in the plume, which can be formed from VOC oxidation. It is clear from these plots that HCHO is more

prominent further down the plume, while ΔVCDs (Figure 3.1) suggest that it also expands in the cross-wind direction, downwind. This suggests that concerns regarding atmospheric and health impacts of downwind HCHO should be focused on the plume further from the source.

These downwind changes in NO_2 and HCHO can also be examined with respect to the age of the plume, calculated by using the location from the fire centre and the average wind speed. The age of the plume, added to Figures 3.9 and 3.10, provides insight into the evolution of species within a plume, using TROPOMI. Given the plume age, it is clear that species with shorter lifetimes, such as NO_2 and HCHO, should decrease as the plume ages, downwind, if there were no secondary formation. NO_2 emission rates increasing as the plume ages away from the fire centre shows NO_2 as a secondary by-product, with rates seemingly decreasing within a few hours. HCHO enhancements fluctuating, as the plume ages, indicates a secondary source in the plume, from VOC oxidation chains, with minimal contribution due to background HCHO. The downwind relationships between species observed in the Canadian wildfires are also observable in the non-normalised enhancement rate plots of the Griffin24 New Mexico and FIREX-AQ fires (Figures 3.2, 3.3, and 3.7).

3.3.2 Enhancement Ratios

These enhancement rates along the length of the plume indicate the change in concentration as the plume ages. The rates, however, are insufficient, on their own, to confirm secondary production in the plume. Rates show concentration differences in each segment, but these differences might reflect changes in emissions, fire intensity, or dilution. Secondary formation in the plume is better observed through species enhancement ratios (EnhR) NO_2/CO, HCHO/CO, and HCHO/NO_2 of downplume ΔVCDs, using the Gaussian-flux method. The downwind enhancement ratios (ΔVCD/ΔVCD) for each plume can be plotted for each of the EnhRs mentioned as a function of plume age as seen in Figures 3.11, 3.12, and 3.14. Not all plumes had overlapping enhancements for the species being observed; these plumes were excluded from EnhR plots.

Figure 3.11 demonstrates the evolution of HCHO ΔVCD in the plume by ratioing it against a stable species like CO to account for physical dilution as the plume is transported. Two fires had CO ΔVCDs at very nearly background levels, causing very large ratios (DeaseLakeBC and FoxMountainNWT_o29714) that were filtered out. The average slope of the all slopes calculated for each fire shown in Figure 3.11 was $1.25\text{x}10^{-2}$ ($\pm$ $5.77\text{x}10^{-3}$) per hour (h^{-1}) with the same average of all slopes adjusted for bias of $7.79\text{x}10^{-3}$ ($\pm$ $3.61\text{x}10^{-3}$) h^{-1} with the term in the brackets being the standard error of the mean (SEM; note that all $\pm$ terms on the average slopes below also refer to the standard error on the mean). The bias-adjusted average slope was calculated by adding or subtracting the bias for each species ΔVCD (Section 2.5) prior to calculating the slope for each fire. All fires show a positive slope as the plume ages, indicating that HCHO is formed from processes within the plume, after accounting for dilution. These HCHO/CO EnhRs showed moderate correlations, with five fires having $R^2 > 0.50$ and an average R^2 of 0.40 for all fires. A number of studies have investigated the composition of wildfire plumes in boreal forests. Goode et al. (2000) and Simpson et al. (2011) estimate EnhRs for various species measured via aircraft for boreal forest fires in Alaska and Canada, respectively. Goode et al. (2000) and Simpson et al. (2011) determined an average HCHO/CO EnhR of $2.14\text{x}10^{-2}$ and $1.75(\pm 0.3)\text{x}10^{-2}$, respectively. The results from this study show an average EnhR of $1.58\text{x}10^{-2}$ ($\pm$ $4.77\text{x}10^{-3}$), which is within uncertainty of Simpson et al. (2011). Several HCHO/CO EnhRs for each fire plume are also within the same range of Goode et al. (2000) and Simpson et al. (2011), with ratios increasing as the plume ages.

Down-plume concentration relationships of NO_2 versus CO are examined in Figure 3.12. NO_2 also had three fires (MaxhamishLake11_o29331, MaxhamishLake13, and EntiakoParkBC_o29757) with single, near-background data points causing extremely large EnhRs that were filtered out. The majority of plumes show a negative slope as the plume ages, with an overall average slope across all plumes of $-2.13\text{x}10^{-4}$ ($\pm$ $1.35\text{x}10^{-4}$) h^{-1} with an average adjusted to account for bias (Section 2.5) of $-1.35\text{x}10^{-4}$ ($\pm$ $8.53\text{x}10^{-5}$) h^{-1}. This EnhR showed an average of $1.22\text{x}10^{-3}$ ($\pm$ $1.98\text{x}10^{-4}$) and a weaker correlation with plume age compared to HCHO/CO with average R^2 of 0.23.

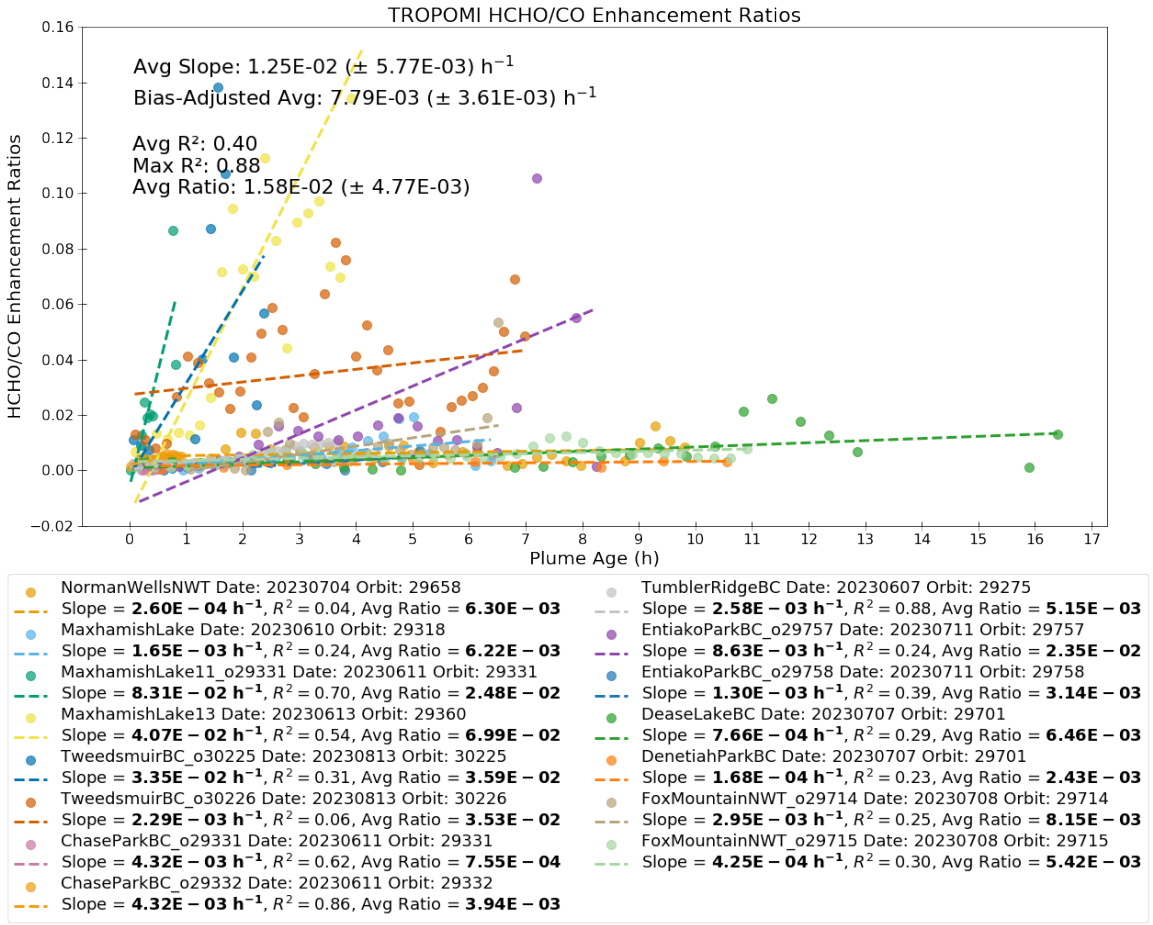

Figure 3.11: Enhancement ratios of TROPOMI HCHO and CO ΔVCDs downwind of fifteen plumes (with MaxhamishLake11_o29332 omitted as it does not have HCHO data) of nine boreal forest wildfires in Western Canada during summer 2023. The "Avg Ratio" in the legend is the average EnhR for each fire. Correlations are plotted without systematic bias being added or removed for each species (Section 2.5 Table 2.1), however, the average slope, which is the average of the slopes from all fires, is provided with bias adjustment as "Bias-Adjusted Avg," in the figure. The uncertainties reported for the Avg Slope, Bias-Adjusted Avg, and Avg Ratio are the SEM.

Seven plumes had correlation coefficients higher than average, and one plume showing an R^2 of 0.84 with a negative slope. The normalised maximum enhancement rates (Figures 3.9 and 3.10) show how NO_2 concentrations initially increase further along in the plume than CO, before being consumed. This pattern can also be observed in Figure 3.12, with the average slope being negative, showing NO_2 being higher than CO, before being consumed.

Calculated NO_2/CO EnhRs are comparable to Goode et al. (2000) (1.57×10^{-3} with NO_x in the form of NO) and Simpson et al. (2011) ($5.6(\pm 0.3) \times 10^{-3}$ ppbv/ppbv with NO_x in the form of NO_2) within the same order of magnitude as the average EnhR of

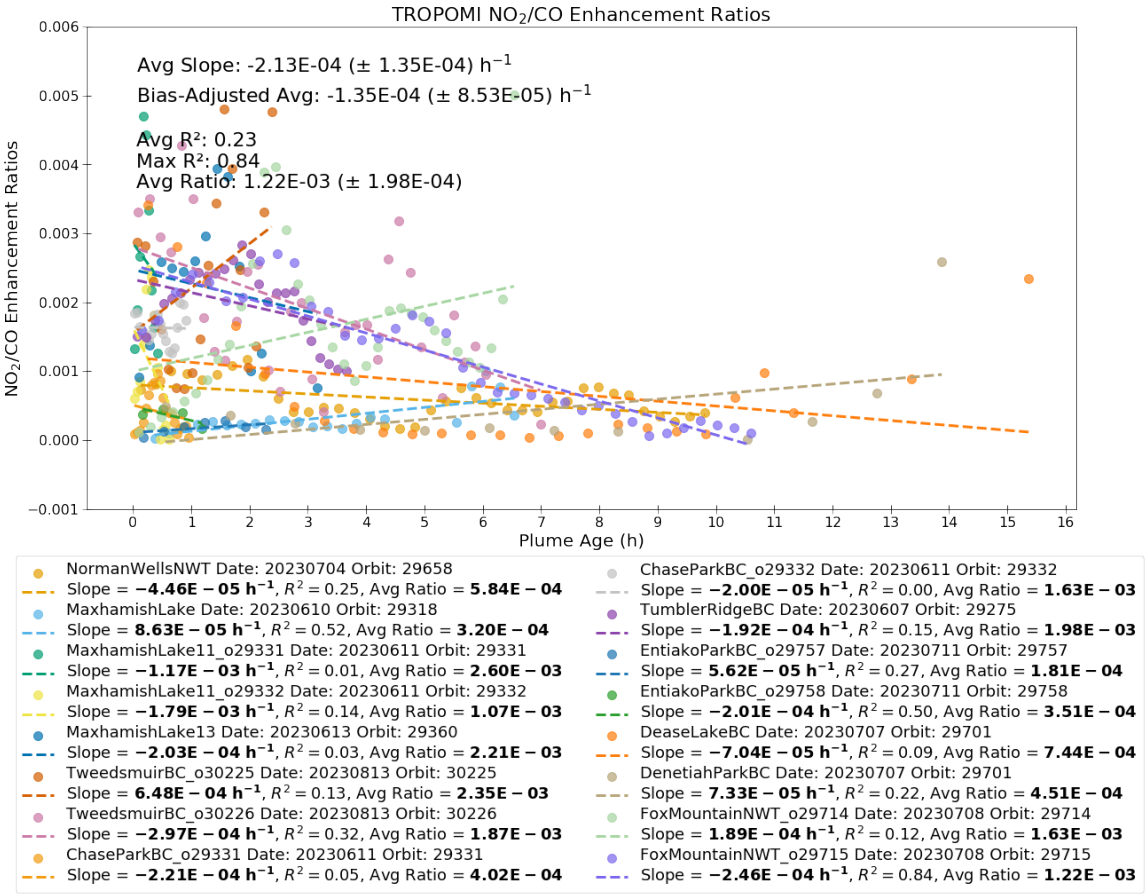

Figure 3.12: Enhancement ratios of TROPOMI NO_2 and CO ΔVCDs (background-subtracted enhancements) downwind of sixteen plumes from nine boreal forest wildfires in Western Canada during summer 2023 plotted the same way as Figure 3.11. The y-axis has been limited to 0.006 to allow all slopes to be visually distinguishable. The uncertainties reported for the Avg Slope, Bias-Adjusted Avg, and Avg Ratio are the SEM.

$1.22\text{x}10^{-3}$ ($\pm$ $1.98\text{x}10^{-4}$) across all fires in this work. Anderson et al. (2023) employed another method using TROPOMI data to analyse the change of total emission ratios of HCHO and NO_2 with CO over the lifetime of a series of fires in California, Oregon, and Washington, showing that EnhRs had larger values at the start of the fire and dropped off exponentially as the fires aged (Figure 3.13(a) taken from Anderson et al. (2023)). The calculated values in this work are consistently within the upper and lower range they observed for NO_2/CO with $1.01\text{x}10^{-3}$ ($\pm$ $1\text{x}10^{-5}$) and $2.34\text{x}10^{-4}$ ($\pm$ $1\text{x}10^{-6}$) for the upper and lower range, respectively, with some of their EnhRs exceeding ours.

The down-plume relationship between HCHO and NO_2, with HCHO increasing while NO_2, decreases can be seen in the EnhR relative to plume age, with all fires

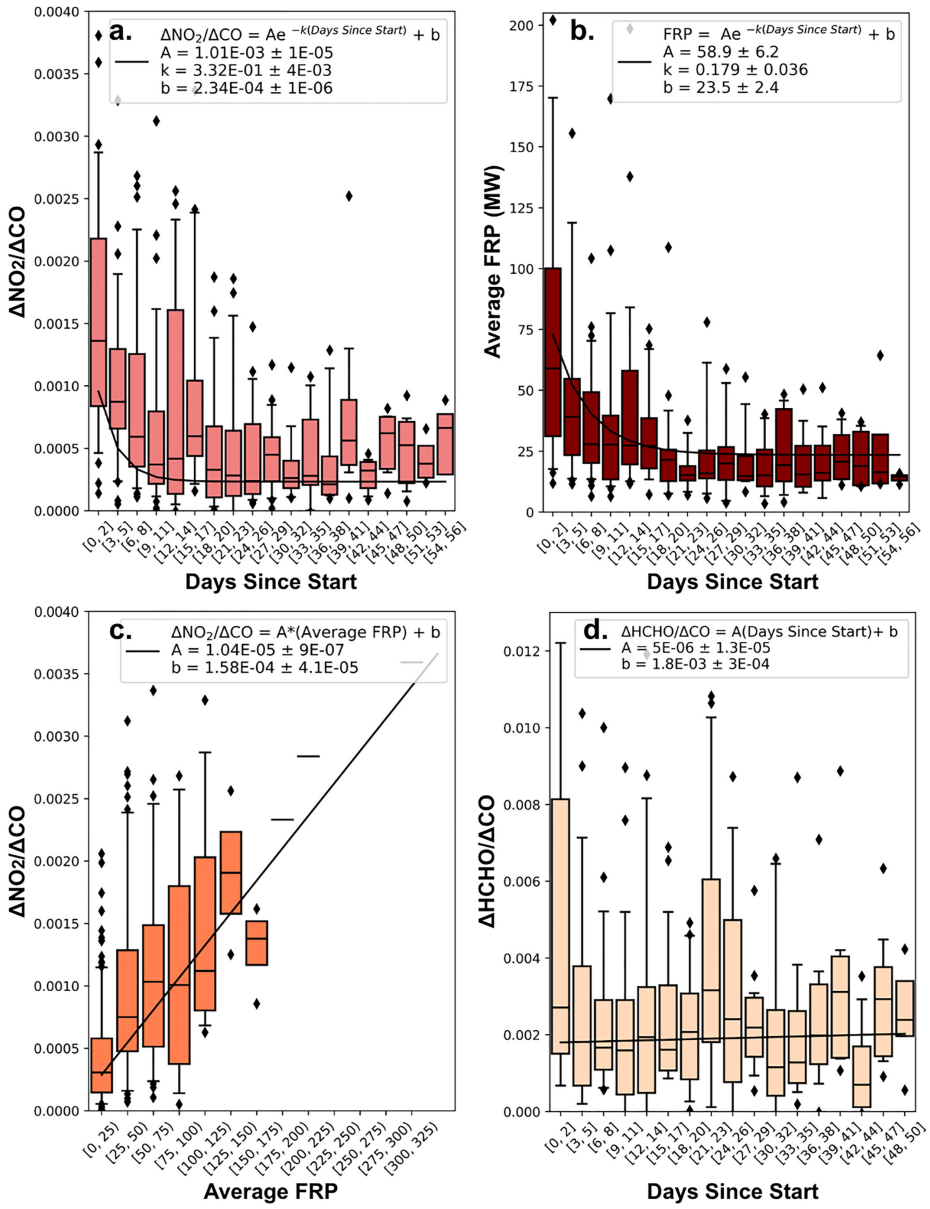

Figure 3.13: Figure taken from Anderson et al. (2023) showing their results for analysing the diurnal change of a series of fires in California, Oregon, and Washington. Their panels show: (a) $\Delta NO_2/\Delta CO$ over time, (b) the average FRP versus days from start, (c) $\Delta NO_2/\Delta CO$ as a function of average FRP, and (d) $\Delta HCHO/\Delta CO$ as a function of time.

showing a positive slope as a plume ages. Figure 3.14 shows that HCHO increases along the length of the plume, relative to NO_2. An average slope of 12.1 ($\pm$ 3.45) h^{-1} with a bias-adjusted average of 12.0 ($\pm$ 3.40) h^{-1} was observed. These EnhRs show strong correlations, with nine fires having $R^2 > 0.50$. The average EnhR is 15.4 ($\pm$ 2.80), with an average R^2 of 0.49. Figures 3.11, 3.12, and 3.14 demonstrate how

the Gaussian-flux method, applied to TROPOMI (or satellite) data, can be used to provide insight into the chemical evolution of various species along the length of the plume as the plume ages.

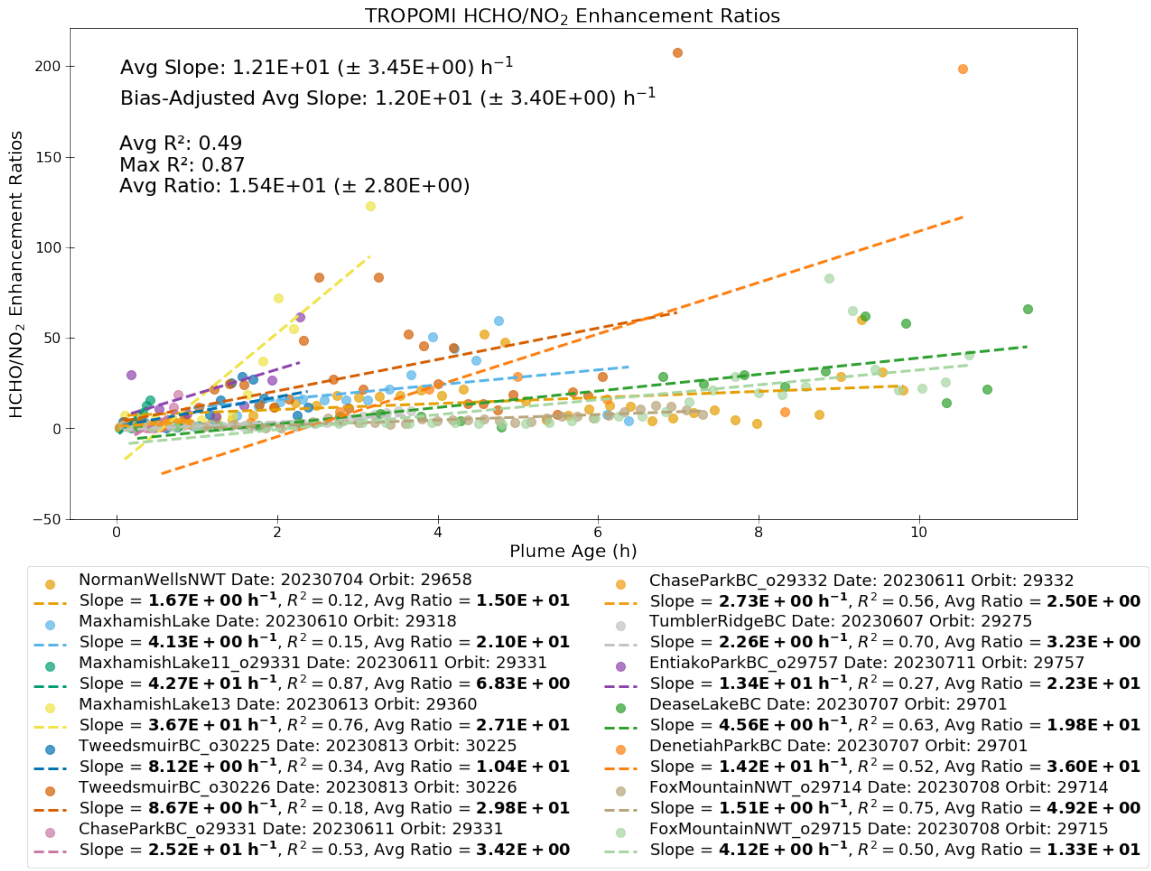

Figure 3.14: Enhancement ratios of TROPOMI HCHO and NO_2 ΔVCDs, plotted the same way as Figure 3.11 for fourteen plumes (with with MaxhamishLake11_o29332 not containing HCHO data and EntiakoParkBC_o29757 having no HCHO/NO_2 overlap). The y-axis has been limited to 500 to make slopes to be visually distinguishable. The uncertainties reported for the Avg Slope, Bias-Adjusted Avg, and Avg Ratio are the SEM.

The maximum enhancement rates of CO, HCHO, and NO_2 for the fires shown in Figures 3.9, and 3.10 are plotted as a function of the averaged FRP in Figure 3.15, for each species. Maximum enhancement rates were examined for any correlation between calculated enhancement rates and observed FRP averages. Higher fire activity (higher FRP) should show increased maximum enhancement rate for all species as high fire activity leads to increased flaming and smouldering (Section 1.2). Maximum enhancement rates, instead of averages, were selected since CO and NO_2

show strong peaks near the fire centre but rates rapidly decrease to near background levels, affecting averages. Maximum enhancement rates better demonstrate CO and NO_2 dependencies. The fire plumes for EntiakoParkBC and FoxMountainNWT were removed from this analysis as there were no MODIS FRP values for the day of the overpass. CO shows a strong correlation with a positive slope of 22.33 t/h·MW, and R^2 of 0.87. HCHO and NO_2 also have positive linear correlations, but with lower R^2 of 0.36 and 0.49, respectively. The larger correlation for CO demonstrates that CO is a better proxy for FRP than secondarily formed species like NO_2 and HCHO. It can be seen from all three plots that larger maximum enhancement rates require greater FRP, but large FRP does not always equate to larger maximum enhancement rates. While larger FRP results in more biomass being burned, allowing for more species production, and boreal forests have an abundance of carbon and VOCs stored in the soil and fallen brush (Akagi et al., 2011; Simpson et al., 2011; Mäki et al., 2019; Isidorov et al., 2022), the age of the fire can also affect the amount and type of biomass available. A larger sample of fires would provide more information about correlations between CO, HCHO, and NO_2 enhancement rates and FRP.

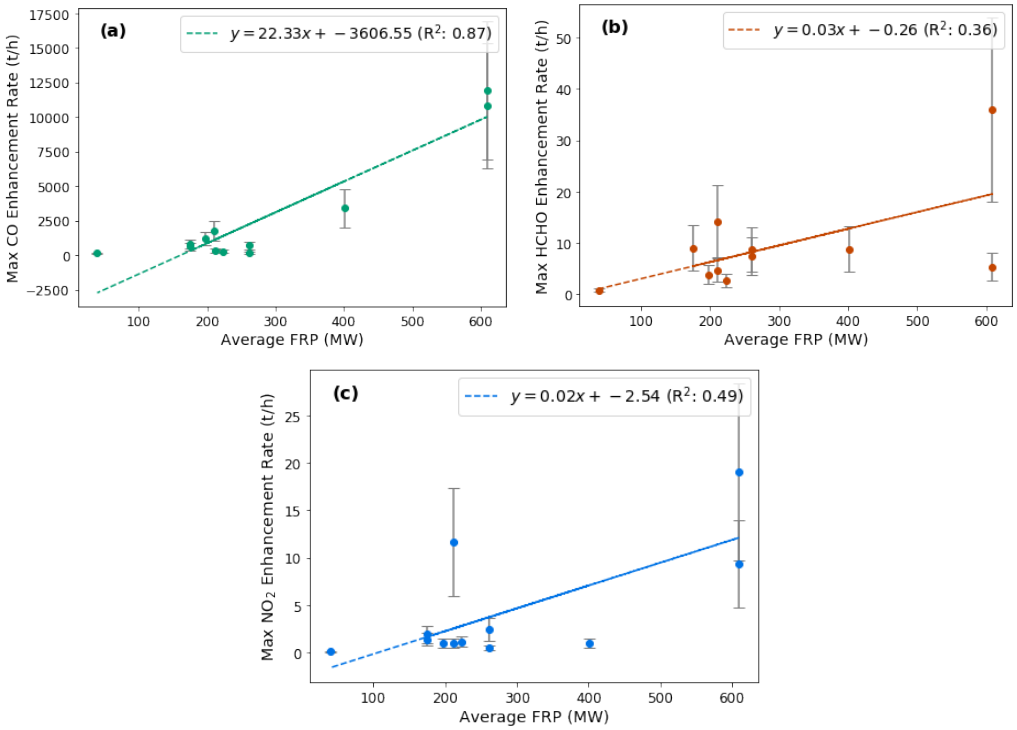

Figure 3.15: Maximum enhancement rates, for fires analysed in Figures 3.9, and 3.10, as a function of MODIS daily-averaged fire radiative power (FRP) for (a) CO, (b) HCHO, and (c) NO_2. Maximum enhancement rates show a positive linear relationship with FRP for all three species, with CO showing the strongest statistical correlation of R^2. The error bars indicate the enhancement rate uncertainties for each species reported in Table 2.1.

3.4 Conclusions

This study analysed down-plume enhancements of CO, HCHO, and NO_2 by applying the Gaussian-flux method to fires from the 2019 FIREX-AQ in-situ campaign and to wildfires in Western Canada during summer 2023. The Gaussian-flux method enhancement rates for three FIREX-AQ wildfires, Shady, Williams Flats, and Horsefly fell within the calculated enhancement rate ranges provided by Stockwell et al. (2022), at various points in the downwind direction, for all three species, except Horsefly CO. The method also provided CO enhancement rates that matched CO single-emission estimates from Griffin24 within the first 30 km, accounting for uncertainty. The calculated results of this study were generally smaller than the FIREX-AQ in-situ results, largely due to increasing fire activity as the in-situ data were collected a few hours after the TROPOMI overpass. This assumption was verified with GOES FRP.

Analysis of different lifetimes for enhancement rate calculations for HCHO and NO_2 showed that maintaining typical lifetimes of six hours and two hours for HCHO and NO_2, respectively, did not significantly alter the calculated enhancement rates compared to FIREX-AQ. Enhancement rates were also determined for a 2019 New Mexico fire studied by Griffin24. The enhancement rates calculated in this study showed a similar downwind profile, matching those observed in Griffin24, within uncertainty. The Gaussian-flux method demonstrated effectiveness in determining downwind enhancement rates, for distinguishable plumes, so long as a Gaussian distribution can be fit for at least one species.

Downwind enhancement rates were calculated for nine fires in Western Canada during summer 2023, totalling sixteen plumes due to multiple TROPOMI orbits for the same fire, with HCHO being observed this way for the first time. Normalising the enhancement rates downwind to the maximum enhancement rate of each species showed that CO is produced primarily at the source of the fire, while NO_2 is formed further down in the plume, as a secondary by-product of photochemical reactions in the plume. HCHO was observed to start forming further down the plume than both CO and NO_2 and after NO_2 enhancement rates started decreasing. This suggests HCHO is being produced as a secondary by-product of VOC oxidation chains, with possible enhancement by the abundance of VOCs present in boreal forests. Enhancement rates for HCHO varied, and even increased, after enhancement rates for NO_2 tended to zero. These chemical changes were also observed when considering the age of the plume for each fire observed in this study. As the plumes aged, NO_2 enhancements increased for older plumes but typically decayed within a few hours, while HCHO formed later in the plume than NO_2.

To demonstrate the evolution of HCHO and NO_2 in the plume, these species were plotted as EnhRs against the more stable CO and then against each other as a function of the age of the plume. HCHO/CO showed a moderate correlation, with positive slopes on all plumes as they aged, further suggesting HCHO increasing in abundance as CO dilutes. The average HCHO/CO EnhR across all plumes was $1.58\text{x}10^{-2}$ ($\pm$ $4.77\text{x}10^{-3}$) (with all reported $\pm$ uncertainty being SEM), which was consistent with

two in-situ studies of boreal wildfires in Alaska (Goode et al., 2000) and Canada (Simpson et al., 2011) of 2.14×10^{-2} and 1.75×10^{-2}, respectively, for these EnhRs. The high standard deviation of EnhR average from this method is due to no consistent pattern of HCHO formation observed in wildfire plumes, compared to CO and NO_2.

EnhRs of NO_2/CO versus plume age showed negative slopes for the majority of fires. NO_2/CO EnhRs showed weaker correlation, with a lower average R^2 than HCHO/CO. The negative slopes are largely due to large EnhRs within one to three hours of plume age when CO enhancements started to decline and NO_2 enhancements were increasing until NO_2 was converted into other nitrogen products downwind. The average NO_2/CO EnhR was 1.22×10^{-3} ($\pm$ 1.98×10^{-4}), which is comparable to boreal in-situ ratios from Goode et al. (2000) (1.57×10^{-3}) and Simpson et al. (2011) [$5.6(\pm 0.3) \times 10^{-3}$]. EnhRs all had positives slopes and $R^2 > 0.50$ for nine fires. The positive slopes of HCHO compared to both shorter lifetime species like NO_2 and a longer lifetime species CO, indicates the continued formation and general increase in abundance, relative to NO_2 and CO, of HCHO in these plumes.

Maximum enhancement rates for each fire compared to the average MODIS FRP, from within a few hours of TROPOMI overpasses, showed a positive, linear trend for all three species. CO showed the strongest correlation, with a positive slope of 22.33 t/h·MW and an R^2 of 0.87. While HCHO and NO_2 have positive correlations with FRP, both have lower R^2 of 0.36 and 0.49, respectively. A larger sample size would be needed to more accurately analyse down-plume enhancement rates as a function of daily averaged FRP, but these results suggest that larger the FRP, the greater the concentration of each species within a plume.

There are a number of limitations for the Gaussian-flux method, such as the possibility of upwind emissions affecting results, the inability to fit some plumes with a Gaussian distribution, the inability to extend plume observations beyond 150 km downwind due to widening plumes, and cross contamination with other source or beyond 50 km in the crosswind direction as it violates the assumption of a point source. Another limitation is that HCHO enhancements are not as distinguishable in plumes due to its weaker absorption signals and sensitivity to Rayleigh and Mie

scattering.

The Gaussian-flux method has proven to be effective at calculating enhancement rates and EnhR changes along the length of a plume, as well as chemical evolution of species within a plume as it ages, an analysis that is normally done with ground and in-situ campaigns. It is also effective at providing EnhRs for wildfires to examine how these species evolve downwind — a method typically limited to the same campaigns. How these species evolve and are transported over long distances in the plume may provide information relevant to understanding the public health implications in cities that are in the path of these plumes. Future work could expand on these findings by applying the Gaussian-flux method to fire seasons in different parts of the globe and to explore how other TROPOMI species, such as HONO and methane, evolve in fire plumes to help better characterise the internal chemistry of wildfire smoke.

Chapter 4

Downwind Formaldehyde to Nitrogen Dioxide Ratios and Implications for Surface Ozone Production

This chapter analyses TROPOMI HCHO, NO_2, and CO VCD enhancements and enhancement rates calculated with the Gaussian-flux method, for fourteen plumes from nine fires in the summer of 2023 and twelve plumes from seven fires in the summer of 2025 from boreal forests in Central and Western Canada. Unlike previous chapters, this chapter will refer to the species in the order of HCHO, NO_2, and CO as this is in the order of importance to the research being conducted. The first objective of the research in this chapter was to observe the evolution of HCHO, NO_2, and CO emission rates downwind and compare them to the fires in Chapter 3. Then HCHO and NO_2 VCD enhancements were used to observe variations in the FNRs along the length of the plume and as the plume ages downwind. This work has been reviewed by coauthors and will shortly be submitted for publication, and the corresponding data have been published in Hearne et al. (2026), at https://doi.org/10.5683/SP3/CJLVQ6.

4.1 Datasets

Research in this chapter uses the TROPOMI HCHO tropospheric vertical column, NO_2 tropospheric column, and CO total column data products to calculate enhancement rates and VCD enhancements, with the AER_LH data product being used to provide plume height. The MODIS MYD14 FRP data product from Aqua is used to determine the fire centre of the fires analysed in this chapter. Plume height was used with ECMWF ERA5 reanalysis wind data to find the wind speed and direction at the correct altitude of the plume. If a plume height could not be found with AER_LH, the altitude was set to the default. To ensure boreal forest wildfires were selected, only fires with the land types *Tree cover, needleleaved, evergreen, closed (>15%)* and *Tree cover, needleleaved, evergreen, closed to open (<15%)* from the CCI LC product were used.

4.2 Methods

This research focuses on 2023 and 2025 Canadian wildfires located in the boreal forests of Central and Western Canada. Data were obtained for fourteen plumes from nine wildfires in the Northwest Territories and British Columbia from the summer 2023 wildfires. Twelve additional plumes from seven wildfires in Saskatchewan, Manitoba, and Alberta during the start of the 2025 wildfire season were also analysed. Fires were given names based on their approximate geographic location and orbit, if multiple orbits exist for the same fire. The names and coordinates for each fire can be found in Tables 4.1 and 4.2 for the 2023 and 2025 wildfires, respectively.

The research in this chapter uses the Gaussian-flux method detailed in Chapter 2 to calculate enhancement rates and VCD enhancements for each plume. VCD enhancements (ΔVCD), or column enhancements, are background-corrected columns, at the determined aerosol layer height, from the TROPOMI HCHO tropospheric vertical, NO_2 tropospheric, and CO total column data product. The naming convention of calling the rates in this study enhancement rates follows Chapter 3. Since HCHO and

Table 4.1: The 2023 fires used in this study, with the naming convention coordinates, adapted from Table 3.2 of Chapter 3, including the province or territory of origin, TROPOMI orbit number, date of fire (YYYYMMDD), time of overpass in UTC, coordinates of the fire centre, and the CCI Land Product type of each fire.

Name Code	Province	Orbit Number	Date	Overpass Start UTC	Overpass End UTC	Latitude	Longitude	ESA CCI Land Cover Product Type
NormanWellsNWT	Northwest Territories	29658	20230704	8:46:17 PM	8:47:16 PM	65.50	-126.75	Tree cover, needleleaved, evergreen, closed (>40%)
MaxhamishLake	British Columbia	29318	20230610	9:35:36 PM	9:36:31 PM	59.83	-123.58	Tree cover, needleleaved, evergreen, closed to open (>15%)
MaxhamishLake11_o29331	British Columbia	29331	20230611	7:36:33 PM	7:37:32 PM	59.83	-123.58	Tree cover, needleleaved, evergreen, closed to open (>15%)
MaxhamishLake13	British Columbia	29360	20230613	8:38:48 PM	8:39:47 PM	59.83	-123.58	Tree cover, needleleaved, evergreen, closed to open (>15%)
TweedsmuirBC_o30225	British Columbia	30225	20230813	7:52:35 PM	7:53:32 PM	53.04	-125.98	Tree cover, needleleaved, evergreen, closed (>40%)
TweedsmuirBC_o30226	British Columbia	30226	20230813	9:32:11 PM	9:33:11 PM	53.04	-125.98	Tree cover, needleleaved, evergreen, closed (>40%)
ChaseParkBC_o29331	British Columbia	29331	20230611	7:36:10 PM	7:37:10 PM	57.10	-124.80	Tree cover, needleleaved, evergreen, closed (>40%)
ChaseParkBC_o29332	British Columbia	29332	20230611	9:15:50 PM	9:16:49 PM	57.30	-124.40	Tree cover, needleleaved, evergreen, closed (>40%)
TumblerRidgeBC	British Columbia	29275	20230607	8:11:53 PM	8:12:53 PM	52.93	-125.67	Tree cover, needleleaved, evergreen, closed (>40%)
EntiakoParkBC_o29757	British Columbia	29757	20230711	8:50:04 PM	8:51:03 PM	55.21	-120.53	Tree cover, needleleaved, evergreen, closed (>40%)
DeaseLakeBC	British Columbia	29701	20230707	9:28:47 PM	9:29:46 PM	59.62	-129.58	Tree cover, needleleaved, evergreen, closed (>40%)
DenetiahParkBC	British Columbia	29701	20230707	9:28:36 PM	9:29:36 PM	59.11	-127.56	Tree cover, needleleaved, evergreen, closed to open (>15%)
FoxMountainNWT_o29714	Northwest Territories	29714	20230708	7:31:21 PM	7:32:22 PM	61.75	-134.70	Tree cover, needleleaved, evergreen, closed (>40%)
FoxMountainNWT_o29715	Northwest Territories	29715	20230708	9:10:44 PM	9:11:43 PM	61.96	-134.52	Tree cover, needleleaved, evergreen, closed (>40%)

Table 4.2: The 2025 fires used in this study, with naming convention and coordinates in this study in the same format as Table 4.1.

Name Code	Province	Orbit Number	Date	Overpass Start UTC	Overpass End UTC	Latitude	Longitude	ESA CCI Land Cover Product Type
FysonLakeSK_o39290	Saskatchewan	39290	20250513	6:30:24 PM	6:31:24 PM	53.68	-104.67	Tree cover, needleleaved, evergreen, closed (>40%)
FysonLakeSK_o39291	Saskatchewan	39291	20250513	8:10:09 PM	8:11:10 PM	53.68	-104.67	Tree cover, needleleaved, evergreen, closed (>40%)
SuggiLakeSK22	Saskatchewan	39418	20250522	7:01:37 PM	7:02:37 PM	54.65	-102.61	Tree cover, needleleaved, evergreen, closed (>40%)
SeversonLakeSK	Saskatchewan	39418	20250522	7:02:04 PM	7:03:03 PM	56.01	-104.04	Tree cover, needleleaved, evergreen, closed to open (>15%)
KississingLakeMB_o39446	Manitoba	39446	20250524	6:24:27 PM	6:25:24 PM	55.04	-101.31	Tree cover, needleleaved, evergreen, closed (>40%)
KississingLakeMB_o39447	Manitoba	39447	20250524	8:04:28 PM	8:05:29 PM	55.04	-101.31	Tree cover, needleleaved, evergreen, closed (>40%)
SuggiLakeSK25_o39446	Saskatchewan	39446	20250524	6:24:31 PM	6:25:30 PM	54.65	-102.60	Tree cover, needleleaved, evergreen, closed (>40%)
SuggiLakeSK25_o39447	Saskatchewan	39447	20250524	8:04:23 PM	8:05:23 PM	54.65	-102.60	Tree cover, needleleaved, evergreen, closed (>40%)
BesnardLakeSK25	Saskatchewan	39461	20250525	7:45:46 PM	7:46:45 PM	55.21	-105.95	Tree cover, needleleaved, evergreen, closed (>40%)
SouthAtikakiParkMB	Manitoba	39460	20250525	6:04:26 PM	6:05:24 PM	50.91	-95.48	Tree cover, needleleaved, evergreen, closed (>40%)
BesnardLakeSK26	Saskatchewan	39475	20250526	7:27:00 PM	7:27:59 PM	55.21	-105.95	Tree cover, needleleaved, evergreen, closed (>40%)
ChipewyanLakeAB	Alberta	39503	20250528	6:50:57 PM	6:51:55 PM	56.80	-113.81	Tree cover, needleleaved, evergreen, closed (>40%)

NO_2 can be emitted from the fire but also secondarily formed in the plume, they are more accurately enhancement rates than emission rates, enhanced after background correction.

Lifetimes used in this study were 6 hours, 2 hours, and 2 weeks for HCHO, NO_2, and CO, respectively. Enhancement rates and ΔVCDs were calculated by subtracting background concentrations from 20 to 50 km upwind. NO_2 data values that were close to background, resulting in unusually high FNRs, were filtered out. CO was used, when available, to determine the fire source location, as CO is found in larger concentrations near the source (Griffin24, Chapter 3), but were not used in FNR calculations. FRP averages were determined using all available MODIS FRP values that were within a few hours of TROPOMI overpass.

4.3 Results and Discussion

4.3.1 Enhancement Rates

Enhancement rates for the 2023 and 2025 fires were calculated for HCHO, NO_2, and CO as a function of downwind distance and plume age. Plume age was determined using the location of each calculated enhancement rate, downwind, divided by the average wind speed downwind. Enhancement rates for the 2023 wildfires used in this chapter are available in Figures 3.9 and 3.10 and those for the 2025 wildfires can be found in Figure 4.1. Compared to the enhancement rates from the 2023 fires shown in Chapter 3, the 2025 fires in Figure 4.1 show similar characteristics in the downwind direction and with plume age. CO enhancements are typically larger nearer to the centre of the plume, while NO_2 enhancements begin to appear further down the plume as the plume ages before dropping off rapidly. HCHO enhancements typically begin to increase as the plume ages and continue to remain high even after CO and NO_2 rates decline. For more detailed explanation and analysis of these trends, see Chapter 3. SouthAtikakiParkMB had very stagnant air at the determined plume height [plume altitude of 2004 m with an average of 0.61 m/s (2.18 km/h)], which

provided unrealistic plume ages. The fire was kept for the analysis in Figure 4.1, as it maintains a characteristic downwind (in km) plume shape, but was removed from any future analysis related to plume age.

4.3.2 Formaldehyde to Nitrogen Dioxide Ratios

FNRs have been shown to be a good indicator for the dependence of surface O_3 formation in the atmosphere on VOC or NO_2 concentrations (Section 1.3.4). Jin et al. (2020) found that VOC-sensitive formation of surface O_3, where concentrations of O_3 increase linearly with increasing concentrations of VOCs, occurs at FNR values of 3.2 and below, while NO_2-sensitive formation occurs at FNR of 4.1 and above, with FNR between 3.2 and 4.1 being a transition zone where O_3 production can be reduced by decreasing either NO_2 or VOC emissions. A summary of this can be found in Table 4.3.

Table 4.3: FNRs indicating VOC- or NO_2-sensitive O_3 production from Jin et al. (2020), derived from OMI satellite data and model data.

Source	VOC-Sensitive	Transition Zone	NO_x-Sensitive
Jin et al. (2020)	FNR < 3.2	3.2 < FNR < 4.1	FNR > 4.1

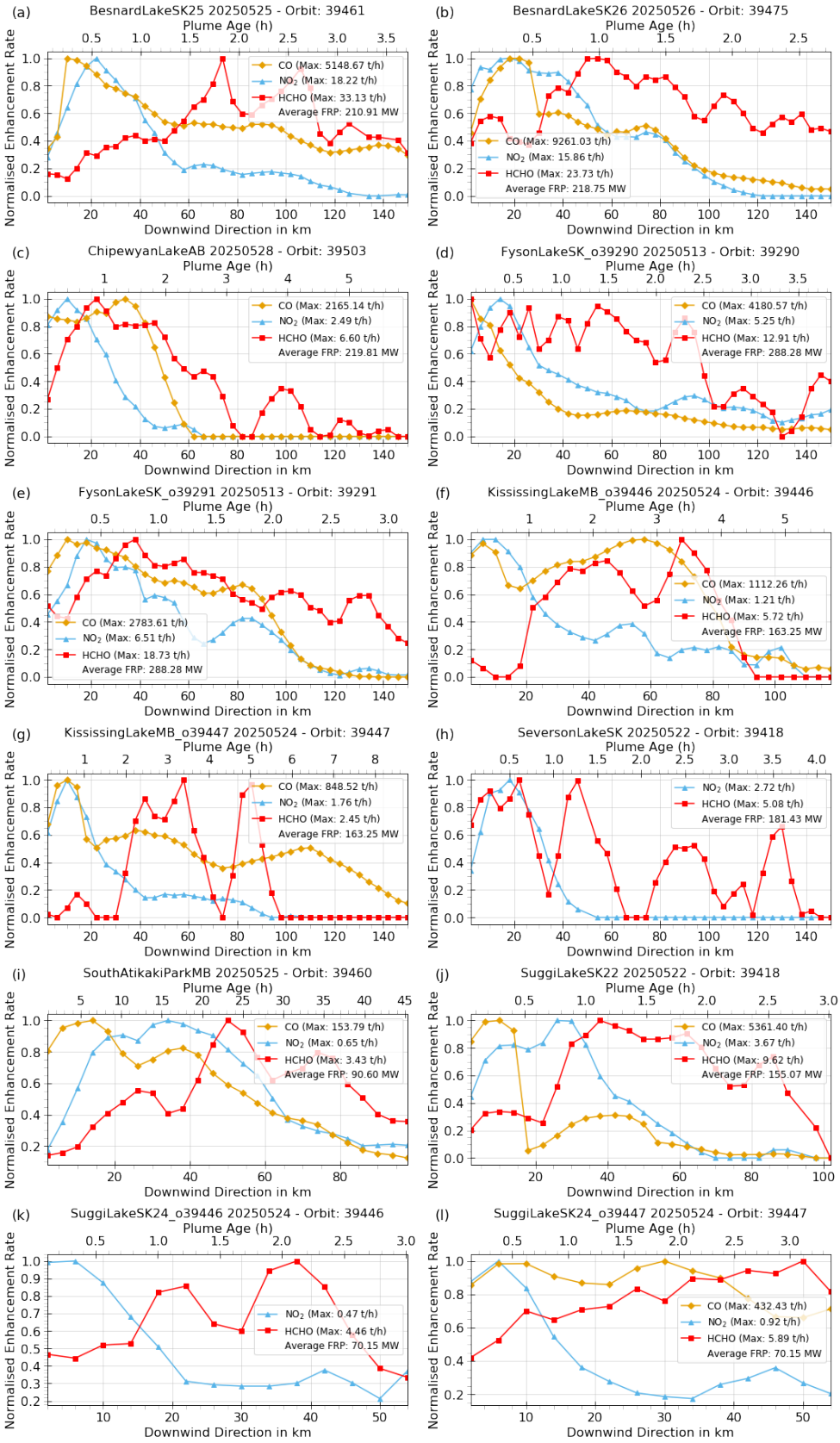

Figure 4.1: Normalised enhancement rates of CO (orange diamonds), NO_2 (blue triangles), and HCHO (red squares) (rearranged to match Figures 3.9 and 3.10) for twelve plumes from the 2025 wildfires as a function of downwind direction and plume age. Enhancement rates of each fire have been normalised to the maximum rate of each species, which are shown in the legend along with the average FRP. FRP is averaged from MODIS FRP within three hours of each TROPOMI overpass. Naming convention in Table 4.2.

Jin et al. (2020) primarily focused on urban environments, as did several other FNR studies (e.g., Jin et al., 2021; Acdan et al., 2023). However, Parrington et al. (2013) and Robinson et al. (2021) found similar correlations of surface-level O_3 formation with NO_x and VOCs, using in situ measurements from boreal forest campaigns during wildfires. Robinson et al. (2021) also found that wildfires produce five times more O_3 than urban environments. One issue for boreal forests is that they often have measurable background HCHO concentrations due to oxidation cycles of natural occurring VOCs in soil (Mäki et al., 2019; Isidorov et al., 2022). These background concentrations, however, are usually small enough compared to wildfire HCHO formation concentrations to not have a significant impact on results, but could occasionally cause enhancement rates and HCHO ΔVCDs to be underestimated due to background subtractions.

ΔVCD FNRs were calculated using the Gaussian-flux method for the 2023 and 2025 wildfires and plotted as a function of downwind direction in Figure 4.2 for 2023 and Figure 4.3 for 2025. These figures show that the fires from both years start off with a high NO_2 and low HCHO environment (small FNR), increasing the probability of O_3 formation varying linearly with VOC concentrations. This VOC-sensitive regime could increase O_3 production due to the abundance of VOCs in boreal forests. However, further downwind, the majority of plumes rapidly transition to a NO_2-sensitive regime (larger FNR) and remain so for the remainder of the downwind direction. If these plumes were transported over a NO_2-rich environment, such as a city in the day time, O_3 concentrations could increase in the downwind plume. Cities can often be in the path of wildfire smoke and these patterns may continue in the plume beyond the distances observed in this study.

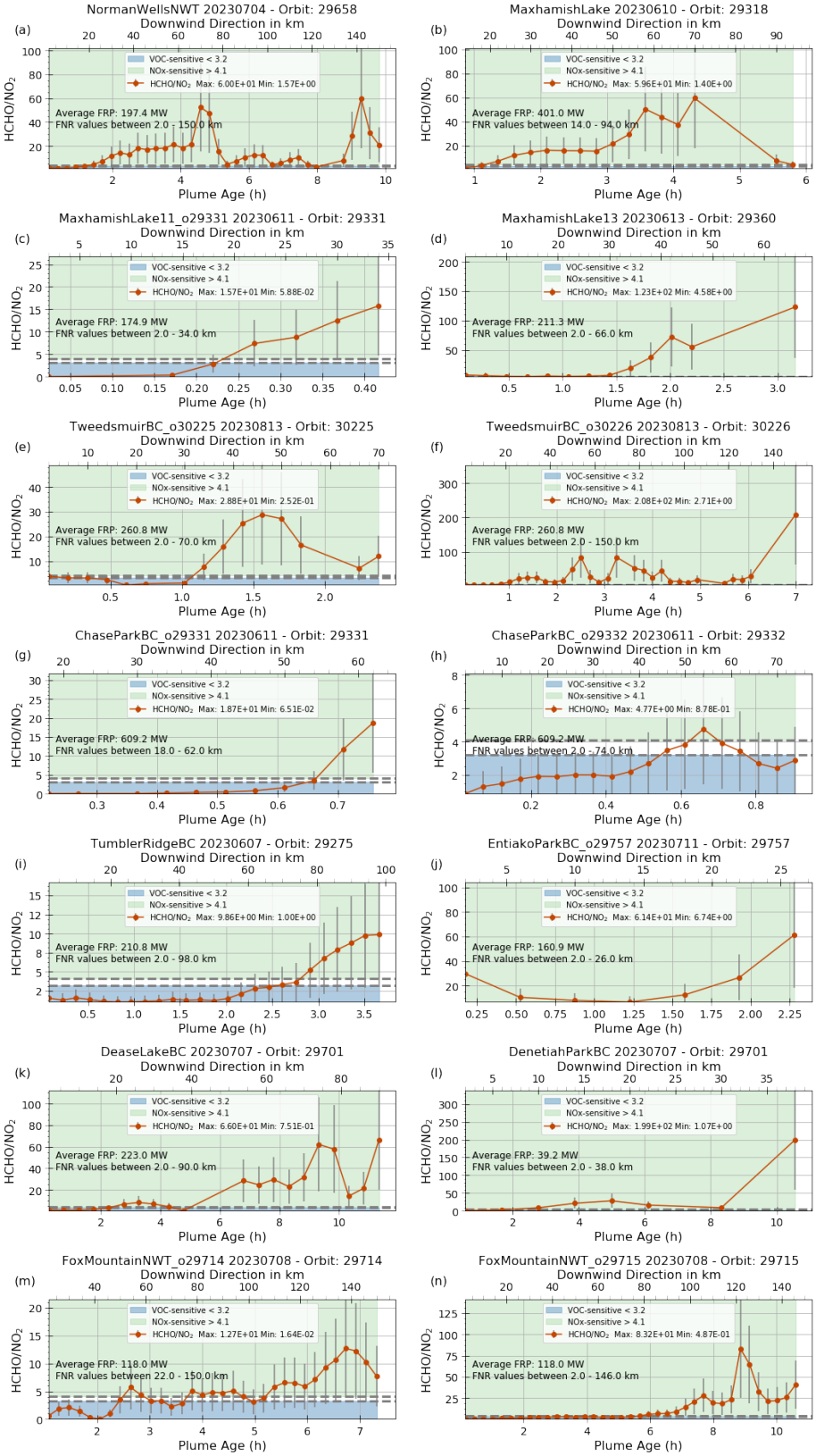

Figure 4.2: Calculated ΔVCD FNRs versus plume age, with downwind direction on the top x-axis, for the fourteen plumes from the 2023 Canadian wildfires. The VOC-sensitive regime (FNR below 3.2) appear as a blue box, while the NO_2-sensitive regime (FNR above 4.1) is a green box. Grey dashed lines separate the upper and lower numerical regions of the VOC- and NO_2-sensitive regimes, called the transition region. Average FRP is provided for FRP occurring within a three hours of each TROPOMI overpass. Errors are the uncertainties detailed in Table 2.1 summed in quadrature for HCHO and NO_2. For the naming convention, see Table 4.1

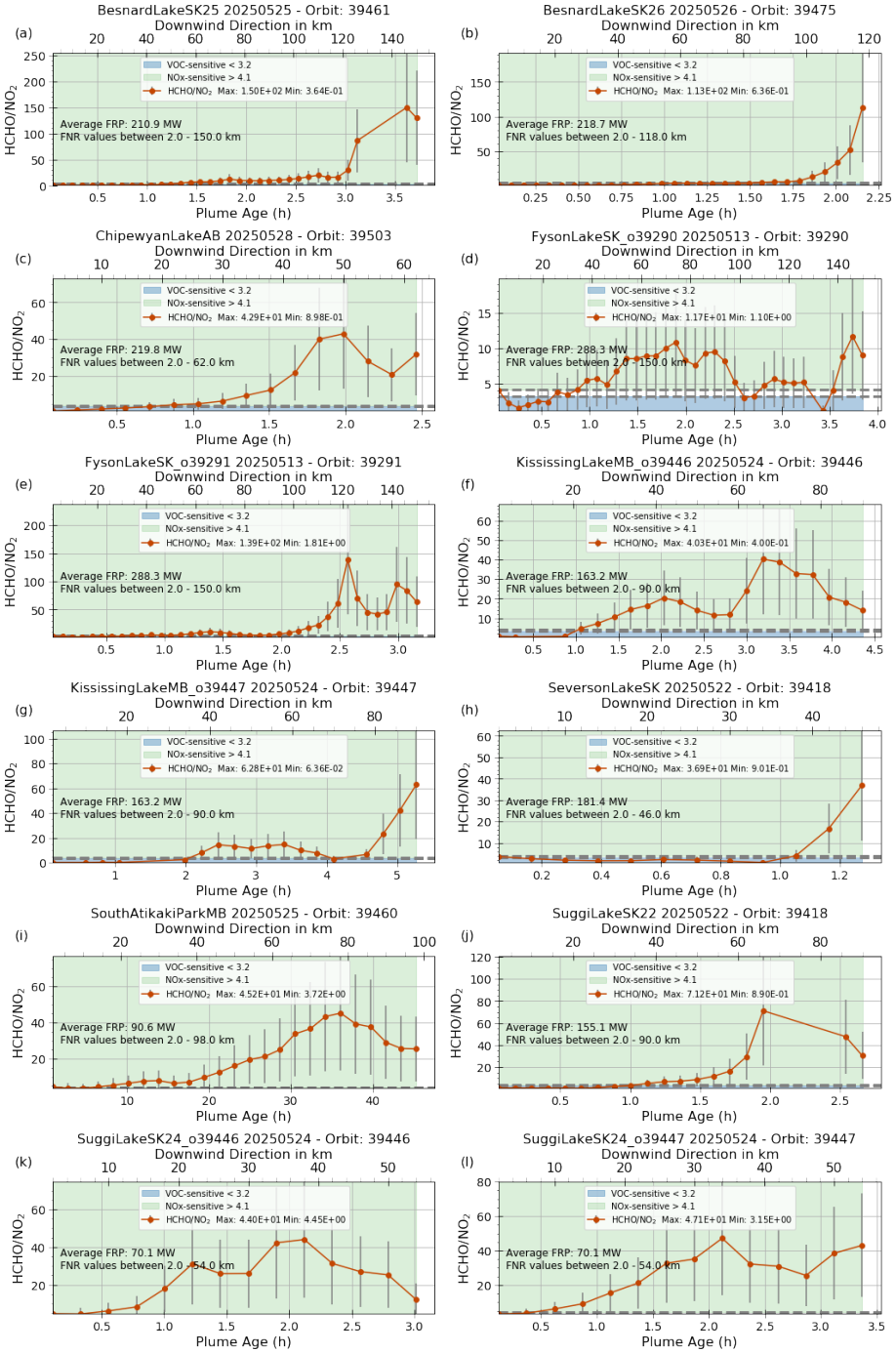

Figure 4.3: Calculated ΔVCD FNRs versus plume age and downwind direction from the twelve plumes for the 2025 Canadian wildfires, plotted the same way as Figure 4.2. For the naming convention, see Table 4.2. Error bars defined the same as Figure 4.2.

To better visualise consistency of VOC- to NO_x-sensitive regime transitions, a three-dimensional heatmap of all the plumes from both years can be seen in Figure 4.4(a). FNRs are plotted as a function of plume age in the lower x-axis and distance

downwind in the top x-axis. The horizontal axis is divided into equally spaced distance bins, while the vertical axis uses logarithmically spaced bins between 0.1 and 100 (with additional bins centred at 3.2 and 4.1 added). This binning scheme provides higher resolution for low-ratio values—where most of the ratio values cluster—while still covering the full dynamic range of the ratios. Each cell is coloured according to the number of samples that fall within the corresponding bin, with warmer colours indicating higher counts. Dashed lines (white and orange) mark the bins that contain the reference ratios FNR = 3.2 and FNR = 4.1. The y-axis is presented on a linear scale for ease of reading, even though the underlying bin edges are logarithmic, allowing for directly observing the absolute ratios associated with each colour band. The heatmap shows that close to the fire source, the majority of fires are in the VOC-sensitive regime (below the orange line) but rapidly transition into the NO_2-sensitive regime. The majority of plumes have transitioned into NO_2 sensitive regime 50-80 km downwind, depending on the plume. Some plumes did not extend the full length of 150 km, but all plumes except one (ChaseParkBC_o29332) transitioned into NO_2 sensitive regime before the end of the plume.

The age of the plume indicates that across all fires, the transition starts after the first hour and fully transitions into the NO_2-sensitive regime within 2 to 3 hours of the plume formation. This is better visualised in Figure 4.4(b), which shows a two-dimensional histogram with FNR values binned by plume age in one-hour blocks represented by different colours. Dashed orange and blue lines represent the boundaries of the VOC and NO_2 regimes. (Note: binning for Figure 4.4(a) and (b) are not related or correlated.) The majority of counts in the VOC region (FNR < 3.2) come from plumes with an age of 0 to 3 hours. This can be seen in the legend. Counts for 0-1 h are the highest in the ≤ 3.2 bins, with the number of counts in that region decreasing quickly for each additional hour. The majority of counts in the FNR $\geq$ 4.1 region are for plumes aged 3 hours and longer.

HCHO/NO_2 ΔVCDs ratios were plotted against plume age in Figures 4.5 and 4.6 to examine how FNR evolves in an ageing plume, with the upper panel of Figure 4.5 being a replication of Figure 3.14. The effectiveness of this method was demonstrated

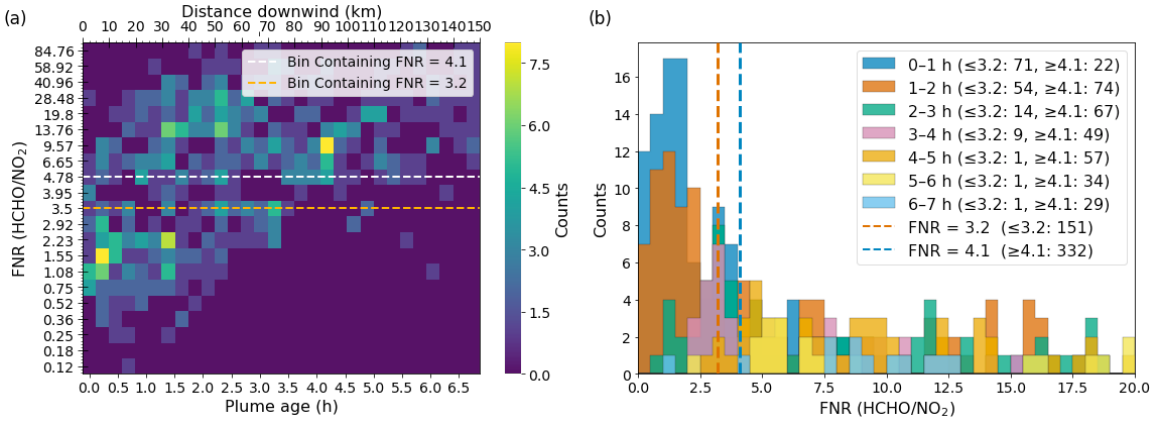

Figure 4.4: (a) A 3D histogram heatmap of TROPOMI ΔVCD FNR values for the 2023 and 2025 wildfires as a function of downwind direction and plume age. Bins in the horizontal axis are linearly binned, while the vertical axis uses logarithmic spacing for binning. Both x- and y-axis are presented on a linear scale for easy reading. Dashed lines have been added to demonstrate the VOC-sensitive (orange line and below) and NO_2-sensitive (white line and above) regimes. (b) A 2D histogram of FNR with plume age binned into one-hour blocks, each with a different colour, as seen in the legend. The legend shows how many counts of each plume age block exist in region with FNR $\leq$ 3.2 (visualised as an orange dashed line) and $\geq$ 4.1 (visualised as a blue dashed line). The legends for the dashed lines also show the total counts that meet the qualifications they represent. SouthAtikakiParkMB was omitted from these results. *Note: There are no similarities or correlations in binning methods between (a) and (b).*

in Chapter 3 by comparing to in-situ observations. FNRs versus plume age for the 2025 wildfires in Figure 4.6 have a similar average slope of 14.00 ($\pm$ 2.18) h^{-1}, as the 2023 wildfires with 12.14 ($\pm$ 3.45) h^{-1}, seen in Figure 4.5 and Figure 4.6, with both uncertainties being the SEM (note, all $\pm$ uncertainties reported in this study are the SEM). For both the 2023 and 2025 wildfires, the FNR increases as the plume ages. The 2025 results show strong correlation, with five plumes having $R^2 > 0.50$ and all but one having $R^2 > 0.30$, while the 2023 fires showed eight plumes with $R^2 > 0.50$. Taking the logarithm of the plume age for both years, as in the lower panels of Figures 4.5 and 4.6, shows how quickly FNRs increase after 1 hour of ageing, with plumes then tending toward the NO_2-sensitive regime. Robinson et al. (2021), using a combination of models and in-situ data, showed that daytime fires transitioned into sensitivity to NO_2 within 30 minutes of plume ageing, twice as fast as night fires, but both transitioned within an hour, similar to the results seen here.

Combining the measurements of three aircraft campaigns looking at boreal forest fires over central and eastern Canada and northern and western Alaska in the

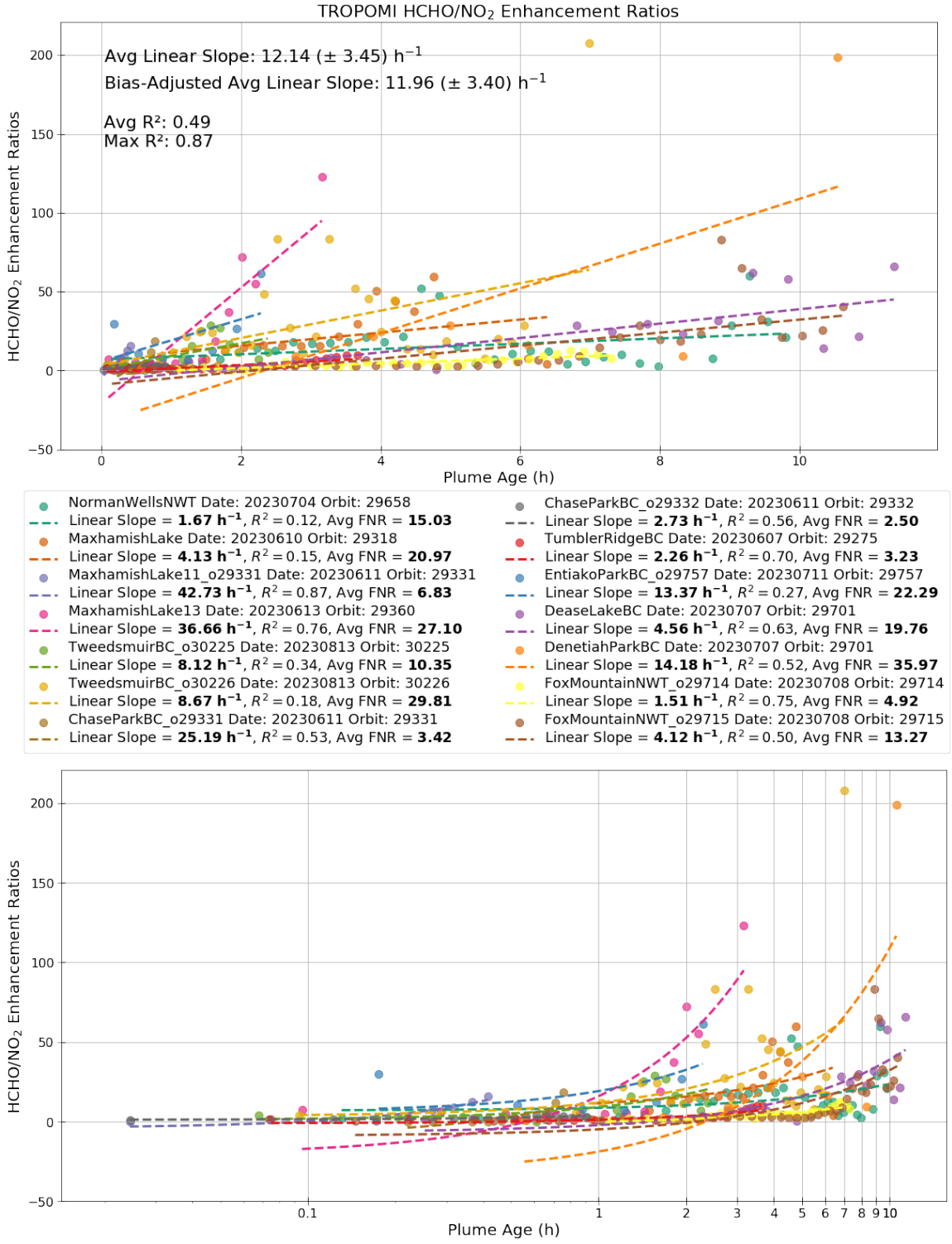

Figure 4.5: $HCHO/NO_2$ ratios as a function of plume age for the fourteen plumes from nine Canadian boreal wildfires in summer 2023. The upper panel has a linear x-axis, while the lower panel shows the x-axis on a logarithmic scale. The centre legend has each fire colour coordinated with the linear slope, R^2, and average FNR (Avg FNR) for each linear fit. Both the upper and lower panels use the same colour and naming scheme (see Table 4.1 for the naming convention). Correlations are plotted without systematic bias being added or removed for each species (Section 2.5, Table 2.1), however, the average slope, which is the average of the slopes from all fires, is provided with bias adjustment as "Bias-Adjusted Avg," in the top panel. The uncertainties reported for the Avg Linear Slope and Bias-Adjusted Avg Linear Slope are the SEM.

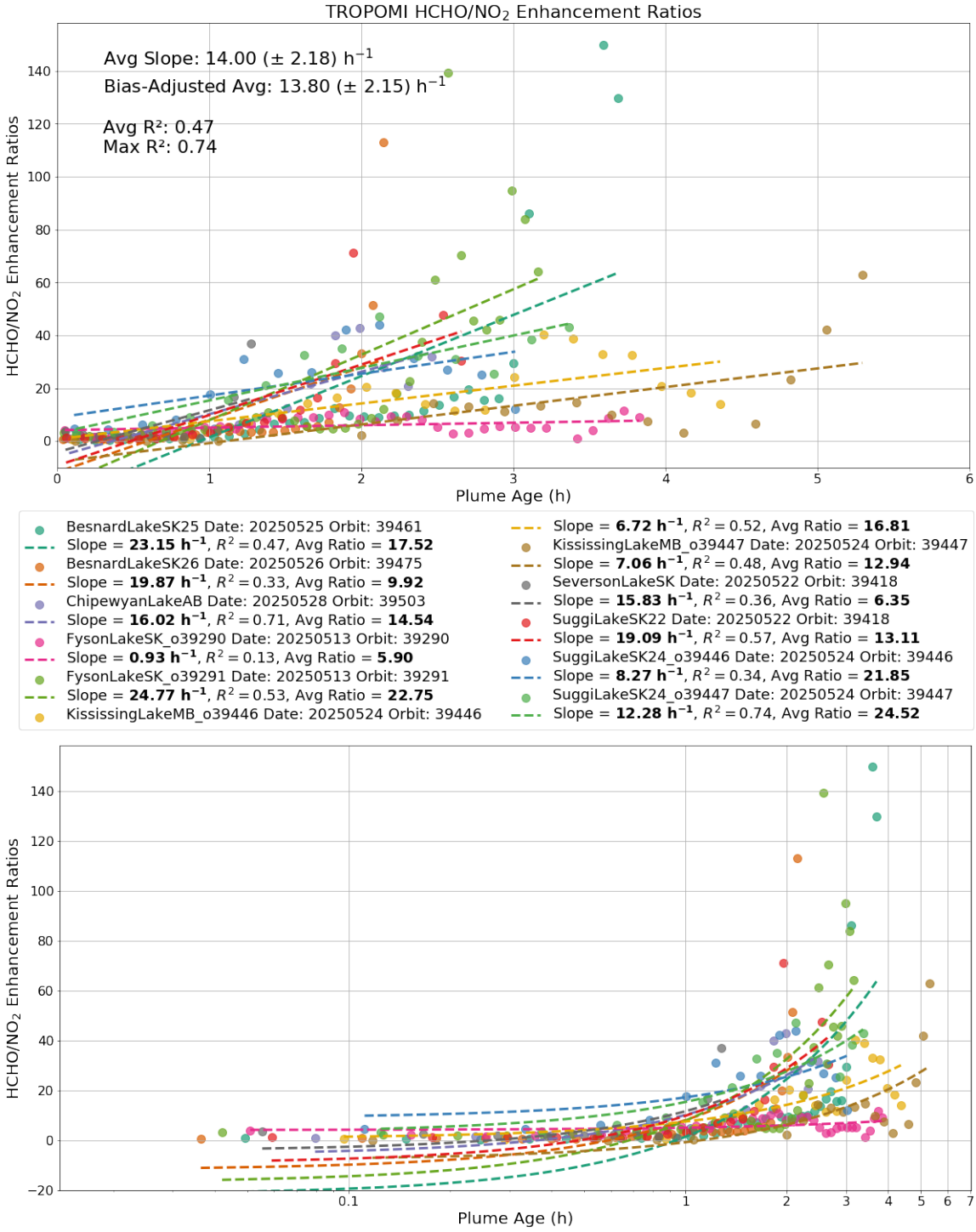

Figure 4.6: $HCHO/NO_2$ ratios as a function of plume age for the twelve plumes from seven Canadian boreal wildfires in summer 2025 plotted the same way as Figure 4.5. See Table 4.2 for the naming convention. SouthAtikakiParkMB was omitted from these results. The uncertainties reported for the Avg Linear Slope and Bias-Adjusted Avg Linear Slope are the SEM.

summers of 1990, 2008, and 2010, Parrington et al. (2013) analysed the relationship of O_3 formation with CO and NO_2. They found that O_3 formation was greater in older plumes with longer photochemical ages and lower aerosol concentrations than in younger plumes with shorter photochemical ages and higher aerosol concentrations, which are typically closer to the fire centre. Similar to the results in Figures 4.2, 4.3, and 4.4, Parrington et al. (2013) also found that plumes with high aerosol had low dependence of O_3 formation on NO_x concentrations, suggesting plumes closer to the fire source are in the VOC-sensitive regime, while older plumes with lower aerosol concentrations showed stronger dependence on NO_x, suggesting downwind NO_x-sensitive regime.

4.4 Conclusions

Using TROPOMI satellite observations, the Gaussian-flux method was applied to fourteen wildfire plumes from 2023 and twelve wildfire plumes from 2025 in Central and Western Canadian boreal forests to calculate downwind enhancement rates and ΔVCD FNRs. The majority of the 26 plumes across both years were found to initially be in the VOC-sensitive regime of O_3 production but rapidly transitioned into the NO_2-sensitive regime downwind. This was further observed by plotting HCHO/NO_2 as a function of plume age. As the plumes aged, FNRs increased, creating a more NO_2-sensitive environment as NO_2 ΔVCDs decreased and HCHO ΔVCDs continued to increase in the plume. This pattern was also observed by Parrington et al. (2013) who found, from combined measurements of three boreal forest aircraft campaigns, that O_3 formation is greater in older plumes downwind with increased O_3 sensitivity to NO_2 as the plume aged.

FNR as a function of plume age for the 2025 wildfires demonstrated an increase as the plume aged downwind, similar to the 2023 wildfires analysed in Chapter 3. These ratios for 2025 also showed a good correlation with increasing plume age, with six plumes having $R^2 > 0.50$ and all but one plume having $R^2 > 0.30$. HCHO/NO_2 from the 2023 fires also showed good correlation versus plume age, with eight plumes

having $R^2 > 0.50$. Both the 2023 and 2025 wildfires had similar averages of all linear slopes and average ratio across all fires with 12.14 ($\pm$ 3.45) h^{-1} and 14.00 ($\pm$ 2.18) h^{-1}, respectively. A logarithmic plot of the FNRs with plume age from both years showed that FNR increases rapidly after only 1 hour. A 3D histogram of FNR versus plume age and a 2D histogram of FNR counts in one-hour bins both showed transitions to the NO_2-sensitive regime rapidly occurring with the first hour, with nearly all fires transitioning to this regime within 3 hours. This pattern was also observed by Robinson et al. (2021) who found, with combined modelling and in-situ measurements, that daytime fires rapidly transition from VOC- to NO_2-sensitive O_3 production within 30 minutes, half as long as for nighttime fires.

As the VOC-sensitive regime is primarily near the fire centre, the O_3 production probability could increase linearly in the forest itself as boreal forests are abundant in VOCs. As a plume ages, however, the smoke rapidly transitions to NO_2-sensitive O_3 production. This could pose a health risk to the general public if boreal forest wildfire smoke were transported over a NO_2-rich environment like a city because O_3 levels could increase. Research suggests biomass-burning-induced O_3 production can be up to five times higher than urban production (Robinson et al., 2021).

While previous studies of FNRs have primarily focused on urban environments, this is the first time TROPOMI has been used to look at wildfire emissions and how variations in downwind FNRs could give insight into possible O_3 production. Unlike previous research using in-situ data and models to analyse the transitions between these two regimes of O_3 formation in wildfires, TROPOMI data can be used to observe the immediate impact of specific fire plumes and give a more real-time (daily) analysis solely through satellite observations, using the Gaussian-flux method.

In this study, analysis of O_3 formation using the Gaussian-flux method with TROPOMI O_3 total columns was attempted. However, tropospheric O_3 enhancements were not discernable in the currently available O_3 data products. The Gaussian-flux method, however, could be used for determining FNRs and their transitions between NO_x- and VOC-sensitive regime by combining atmospheric chemical transport models to provide insight into how these FNRs could affect air quality further

downwind and how continued ageing of the plume and dispersion might affect HCHO concentrations and O_3 production. This method is also not limited to boreal forests. Any sufficiently large and well-defined fire plume could be analysed using TROPOMI data. Considering the coverage of TROPOMI, the method allows for global observation of changes in FNRs for various biomass fuel types and fire locations where species evolution and atmospheric conditions may differ from those found in the boreal forests of Canada.

Chapter 5

A Diurnal Variability Study of TROPOMI-derived CO Emission Rates Using GOES Fire Radiative Power

This chapter examines the variability of TROPOMI-derived CO emission rate (ER), calculated with the Gaussian-flux method, as the plume ages downwind for 38 wildfire plumes from 27 boreal forest fires in Central and Western Canada during the summers of 2023 to 2025. The first goal of this study was to analyse the evolution of CO ERs downwind of the fire centre to observe any patterns across all fire plumes using plume age. Taking advantage of CO having an atmospheric lifetime from two weeks to two months, plume age was used to calculate emission time of each ER by calculating backward from the TROPOMI overpass time. The second goal was to analyse the diurnal variability of CO within a plume as it ages by comparing these ERs to GOES FRP at the same time, for all plumes for which FRP data were available. The relationship between CO ERs and FRP as a function of emission time was analysed to validate the viability of using TROPOMI to observe diurnal changes in CO emissions using single-pass satellite data. This work is being prepared for publication.

5.1 Datasets

Emission rates for CO were calculated using the TROPOMI CO total column product, with the AER_LH data product providing plume height. The plume height was used to determine the altitude for wind speed and direction data from the ECMWF ERA5 wind data product. If plume height could not be determined, the altitude used for wind speed data was set at 2 km (800 hPa). The MODIS MYD14 FRP data product was used from Aqua to determine the location and fire centre of wildfires. To ensure the fires studied were in boreal forests, the CCI LC product was consulted to ensure all fires had either *Tree cover, needleleaved, evergreen, closed (>40%)* or *Tree cover, needleleaved, evergreen, closed to open (>15%)* land types. Lastly, GOES FDC FRP was used to determine the diurnal changes in FRP. FRP was taken from GOES-18, with GOES-16 providing back-up data, for fires in 2023, while FRP from GOES-18 and GOES-19 was used for fires after 2024. No GOES-17 data were available. For more information on these datasets and their use, see Chapter 2.

5.2 Methods

5.2.1 Gaussian-Flux Methodology

The research in this chapter uses the Gaussian-flux method (described in Section 2.2) to calculate the majority of ERs for CO, with the limitations and uncertainties of the method found in Sections 2.4 and 2.5, respectively. Additional limitations for this work will be discussed further in this section. Twenty-seven wildfires were selected from Central and Western Canada during the summers of 2023, 2024, and 2025 providing 38 wildfire plumes, with several fires in the same location on different days counted as the same fire. The names, coordinates, and details for which plumes were studied in this work can be found in Tables 5.1, 5.2, and 5.3 for 2023, 2024, and 2025, respectively. Fires were selected for their distinct plume shape, downwind. As the 2024 fire season was smaller in comparison to the other two years, fewer fires were selected in this year compared to 2023 and 2025, due to limitations discussed

in Section 2.4. Unlike NO_2 and HCHO, which in previous chapters had derived rates referred to as enhancement rates due to having atmospheric lifetimes of a few hours and can be both emitted directly and secondarily formed, CO has a long lifetime and is primarily emitted directly by the fire. While HCHO, produced by biomass burning and VOC oxidation cycles (Section 1.3.3) is capable of secondarily forming CO, concentrations of HCHO are significantly smaller than those of CO, so the contribution from HCHO to overall CO emission rates is assumed to be negligible. For this reason, rates calculated for these wildfire plumes are referred to as emission rates.

Background-subtracted emission rates were calculated for each wildfire plume along with plume age (Equation 2.11 in Section 2.2.1). Plume age was calculated by taking the location of each ER and dividing it by the average wind speed along the length of the plume. Local times were calculated by first taking the plume age (in hours) and subtracting it from the TROPOMI overpass start time (in 2400 hours) to get emission time in UTC. As CO is formed primarily in the fire itself, overpass times were set to the location with the highest concentration of CO in the plume and the emission times were calculated from that location. Then, the coordinates of the fire centre were used to find the time zone in which the fire was located and emission times were adjusted from UTC to the local time for that location. Due to the high latitude of some fires, there were occasionally additional overpasses by TROPOMI and some measurements for a fire were obtained before or after the typical 1:30 p.m. local time overpass (Section 2.1.1).

Emission rates of CO as a function of local time were also compared with GOES FRP to analyse the diurnal variability of CO emissions based on changes in FRP throughout the day. GOES FRP data were not always available throughout the day, due to limitations discussed in Section 2.1.4. Four of the wildfire plumes observed (EntiakoParkBC_o29757, EntiakoParkBC_o29758, SikanniOldGrowthParkBC, and ManigotaganLakeMB) did not have any FRP data and were removed from any analysis involving FRP, but were kept for emissions and plume age analysis.

Table 5.1: The naming convention for the summer 2023 fires discussed in this paper, with the province of origin, TROPOMI orbit number and dates (YYYYMMDD) and times of overpass in UTC, the coordinates of the fire centre, and the ESA CCI Land Product type of each fire.

Name Code	Province	Orbit Number	Date	Overpass Start UTC	Overpass End UTC	Latitude	Longitude	ESA CCI Land Cover Product Type
BrazeauReservoirAB	Alberta	28807	20230505	9:08:40 PM	9:09:40 PM	57.30	-124.40	Tree cover, needleleaved, evergreen, closed (>40%)
TumblerRidgeBC	British Columbia	29275	20230607	8:11:53 PM	8:12:53 PM	52.93	-125.67	Tree cover, needleleaved, evergreen, closed (>40%)
MaxhamishLake	British Columbia	29318	20230610	9:35:36 PM	9:36:31 PM	59.83	-123.58	Tree cover, needleleaved, evergreen, closed to open (>15%)
ChaseParkBC_o29331	British Columbia	29331	20230611	7:36:10 PM	7:37:10 PM	57.10	-124.80	Tree cover, needleleaved, evergreen, closed (>40%)
ChaseParkBC_o29332	British Columbia	29332	20230611	9:15:50 PM	9:16:49 PM	57.30	-124.40	Tree cover, needleleaved, evergreen, closed (>40%)
MaxhamishLake11_o29331	British Columbia	29331	20230611	7:36:33 PM	7:37:32 PM	59.83	-123.58	Tree cover, needleleaved, evergreen, closed to open (>15%)
MaxhamishLake11_o29332	British Columbia	29332	20230611	9:16:31 PM	9:17:30 PM	59.83	-123.58	Tree cover, needleleaved, evergreen, closed to open (>15%)
MaxhamishLake13	British Columbia	29360	20230613	8:38:48 PM	8:39:47 PM	59.83	-123.58	Tree cover, needleleaved, evergreen, closed to open (>15%)
NormanWellsNWT	Northwest Territories	29658	20230704	8:46:17 PM	8:47:16 PM	65.50	-126.75	Tree cover, needleleaved, evergreen, closed (>40%)
DeaseLakeBC	British Columbia	29701	20230707	9:28:47 PM	9:29:46 PM	59.62	-129.58	Tree cover, needleleaved, evergreen, closed (>40%)
DenetiahParkBC	British Columbia	29701	20230707	9:28:36 PM	9:29:36 PM	59.11	-127.56	Tree cover, needleleaved, evergreen, closed to open (>15%)
FoxMountainNWT_o29714	Northwest Territories	29714	20230708	7:31:21 PM	7:32:22 PM	61.75	-134.70	Tree cover, needleleaved, evergreen, closed (>40%)
FoxMountainNWT_o29715	Northwest Territories	29715	20230708	9:10:44 PM	9:11:43 PM	61.96	-134.52	Tree cover, needleleaved, evergreen, closed (>40%)
EntiakoParkBC_o29757	British Columbia	29757	20230711	8:50:04 PM	8:51:03 PM	55.21	-120.53	Tree cover, needleleaved, evergreen, closed (>40%)
EntiakoParkBC_o29758	British Columbia	29758	20230711	9:52:01 PM	9:53:02 PM	52.98	-125.42	Tree cover, needleleaved, evergreen, closed (>40%)
TweedsmuirBC_o30225	British Columbia	30225	20230813	7:52:35 PM	7:53:32 PM	53.04	-125.98	Tree cover, needleleaved, evergreen, closed (>40%)
TweedsmuirBC_o30226	British Columbia	30226	20230813	9:32:11 PM	9:33:11 PM	53.04	-125.98	Tree cover, needleleaved, evergreen, closed (>40%)

Table 5.2: Same as Table 5.1 for the summer 2024 wildfires used in this study.

Name Code	Province	Orbit Number	Date	Overpass Start UTC	Overpass End UTC	Latitude	Longitude	ESA CCI Land Cover Product Type
SikanniOldGrowthParkBC	British Columbia	34354	20240530	9:08:40 PM		58.26	-120.85	Tree cover, needleleaved, evergreen, closed (>40%)
BistchoLakeAB	Alberta	34780	20240629	8:11:53 PM		59.89	-118.56	Tree cover, needleleaved, evergreen, closed (>40%)
ThultueLakeAB_o34779	Alberta	34779	20240629	7:36:10 PM		59.36	-113.94	Tree cover, needleleaved, evergreen, closed (>40%)
ThultueLakeAB_o34780	Alberta	34780	20240629	9:15:50 PM		59.36	-113.94	Tree cover, needleleaved, evergreen, closed (>40%)
KotchoLakeBC	British Columbia	34879	20240706	9:35:36 PM		58.50	-120.99	Tree cover, needleleaved, evergreen, closed (>40%)
WolfLakeNWT	Northwest Territories	34908	20240708	7:36:33 PM		60.70	-131.97	Tree cover, needleleaved, evergreen, closed (>40%)

Table 5.3: Same as Table 5.1 for the summer 2025 wildfires used in this study.

Name Code	Province	Orbit Number	Date	Overpass Start UTC	Overpass End UTC	Latitude	Longitude	ESA CCI Land Cover Product Type
FysonLakeSK_o39290	Saskatchewan	39290	20250513	6:30:24 PM	6:31:24 PM	53.68	-104.67	Tree cover, needleleaved, evergreen, closed (>40%)
FysonLakeSK_o39291	Saskatchewan	39291	20250513	8:10:09 PM	8:11:10 PM	53.68	-104.67	Tree cover, needleleaved, evergreen, closed (>40%)
ManigotaganLakeMB	Manitoba	39418	20250522	7:00:08 PM	7:01:06 PM	50.67	-95.47	Tree cover, needleleaved, evergreen, closed to open (>15%)
SuggiLakeSK22	Saskatchewan	39418	20250522	7:01:37 PM	7:02:37 PM	54.65	-102.61	Tree cover, needleleaved, evergreen, closed (>40%)
KississingLakeMB_o39446	Manitoba	39446	20250524	6:24:27 PM	6:25:24 PM	55.04	-101.31	Tree cover, needleleaved, evergreen, closed (>40%)
KississingLakeMB_o39447	Manitoba	39447	20250524	8:04:28 PM	8:05:29 PM	55.04	-101.31	Tree cover, needleleaved, evergreen, closed (>40%)
SuggiLakeSK24	Saskatchewan	39447	20250524	8:04:23 PM	8:05:23 PM	54.65	-102.60	Tree cover, needleleaved, evergreen, closed (>40%)
BesnardLakeSK25	Saskatchewan	39461	20250525	7:45:46 PM	7:46:45 PM	55.21	-105.95	Tree cover, needleleaved, evergreen, closed (>40%)
BesnardLakeSK26	Saskatchewan	39475	20250526	7:27:00 PM	7:27:59 PM	55.21	-105.95	Tree cover, needleleaved, evergreen, closed (>40%)
WinefredLakeMB	Manitoba	39518	20250529	8:11:15 PM	8:12:14 PM	55.43	-110.80	Tree cover, needleleaved, evergreen, closed (>40%)
ThickwoodHillsAB	Alberta	39518	20250529	8:11:41 PM	8:12:39 PM	56.70	-112.90	Tree cover, needleleaved, evergreen, closed to open (>15%)
CelibetaLakeNWT	Northwest Territories	39532	20250530	6:50:57 PM	6:51:55 PM	60.30	-121.66	Tree cover, needleleaved, evergreen, closed (>40%)
BisonLakeAB	Alberta	39532	20250530	7:53:15 PM	7:54:15 PM	57.15	-116.20	Tree cover, needleleaved, evergreen, closed (>40%)
EtshoPlateauBC	British Columbia	39575	20250602	8:38:00 PM	8:39:00 PM	59.50	-121.80	Tree cover, needleleaved, evergreen, closed (>40%)
StoneRangeBC	British Columbia	39575	20250602	8:37:56 PM	8:38:56 PM	58.69	-124.55	Tree cover, needleleaved, evergreen, closed (>40%)

5.2.2 Method Modifications

Additional limitations exist for this study that were not discussed in Chapter 2 as they arise only from this study. The Gaussian fit across the fire plume did not always provide the correct downwind adjustment. To correct for this, in previous work, the NO_2 Gaussian-corrected rotation was used for other species, such as CO. As CO was the only species investigated in this study, wildfires for which the Gaussian-corrected rotation did not rotate the plume accurately had the Gaussian correction turned off (the addition to the method by Griffin24). For these plumes, calculated ERs were based on the flux method used by Mebust11, Adams19, and Griffin21. Eight of the 38 plumes analysed in this study fell into this category: MaxhamishLake, MaxhamishLake13, NormanWellsNWT, DeaseLakeBC, FoxMountainNWT_o29715, EntiakoParkBC_o29757, SikanniOldGrowthParkBC, and BesnardLakeSK26. Any additional fires surveyed for candidacy in this study for which the flux method also did not provide the correct downwind rotation were filtered out and not used (20 additional fires were filtered out of this study due to this condition, leaving 27 remaining).

5.3 Carbon Monoxide in Wildfire Plumes

5.3.1 Evolution of Emission Rates

To analyse the evolution of ERs within a plume as the plume ages downwind, rates were calculated for all 38 plumes and plotted as a function of plume age. As each plume would have different ER values depending on the intensity and life of the fire, the rates were normalised by taking the maximum ER calculated for a plume and setting all rates as a fraction of the maximum ranging from 0 to 1, for each plume studied, as previous research has suggested the highest emissions are near the centre of the fire (Sections 3.3.1 and 4.3.1). In Figure 5.1, all the normalised emissions are plotted for all fires collectively against plume age, with the Figure 5.1(a) in linear space and Figure 5.1(b) having logarithmic plume age. The maximum ER is set to a

plume age of zero and the downwind plume age is plotted along the x-axis for each fire. A relative point density (kernel density estimation or KDE) was mapped on top of the points to demonstrate the density of points at a specific location, where 1.0 is the greatest density.

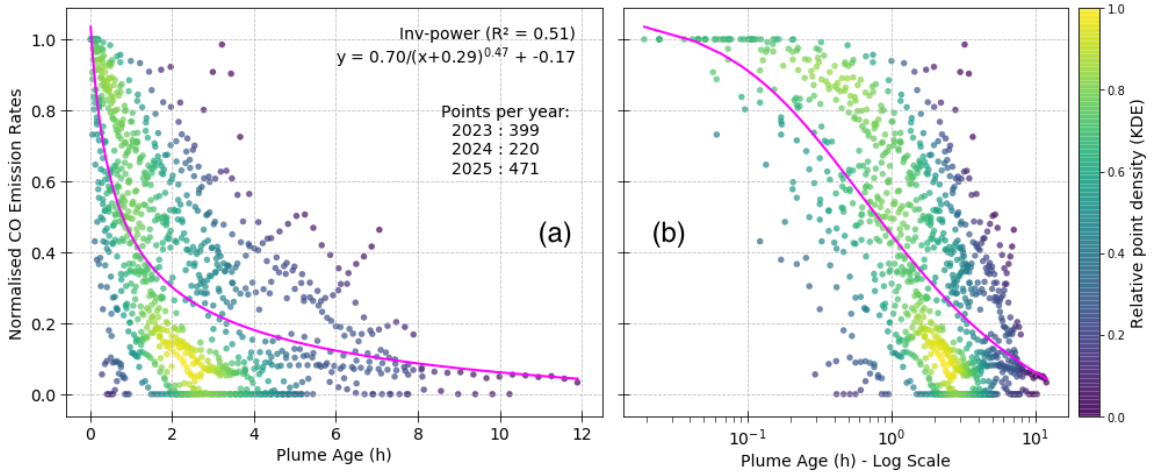

Figure 5.1: Normalised TROPOMI emission rate versus plume age plotted in (a) linear plume age and (b) logarithmic plume age for 38 wildfire plumes from 27 boreal forest wildfires during the 2023 to 2025 summers in Central and Western Canada. The ER for each fire is normalised by the maximum ER observed for the same fire. The relative point density is provided, with total number of points plotted per year.

The collection of ERs as the plumes age downwind are fit with an inverse power fit, which is the best fit for the collective data points of all fires. The more constrained an inverse power decay is, the more of a right angle it becomes. How quickly the fit tends to zero emissions (zero y-axis) demonstrates the change in rate of emissions of CO as the plume ages. By allowing the plume age (x) to vary in the dominator of the equation means there is a gradual decrease in CO emissions with some fires tending toward zero CO emissions slower than other fires. The fit shows a moderate relationship between ER and plume age based on an R^2 of 0.51. This correlation and the more gradual curve is affected by CO ER variation between each plume, with some plumes having slower average wind speeds than others over longer distances, causing longer plume ages.

Figure 5.1(a) demonstrates that the majority of CO ERs tend toward background, low emission values within the first five hours in the plume, with logarithmic scale

of the plume age (Figure 5.1(b)) showing emissions decreasing rapidly after one hour with nearly all plumes reaching near zero emission of CO within the first five to six hours. This provides further evidence that CO emissions are primarily from the source of the fire with minimal formation in the plume, which matches literature regarding the formation of CO from boreal forests (Andreae and Merlet, 2001; Akagi et al., 2011; Andreae, 2019), and is demonstrated across all 27 fires and 38 plumes of different lengths and plume ages. Using the ER as a function of plume age can also provide information about the diurnal changes of CO emissions.

5.3.2 Diurnal Variability

The plume age can be converted into local time by considering the TROPOMI overpass time. As discussed in the previous section, the portion of the plume with the largest CO emission rate is an indication of the fire centre. That location was deemed the centre of the fire and the TROPOMI overpass time for the plume (Tables 5.1, 5.2, and 5.3) was set to that location, following the same method for each plume. As discussed in Section 5.2, the plume age (in hours) for each ER was subtracted from the TROPOMI overpass to get an estimated emission time, UTC. Each emission time was then converted to local time using the coordinates of the fire to determine the local time zone of the fire and adjusting emission times to that time zone (on a 24-hour time scale). These ERs were then plotted as a function of local time with FRP taken from the GOES data available for the date of each plume. Figure 5.2 for 2023, Figure 5.3 for 2024, and Figure 5.4 for 2025, show the TROPOMI ERs as a function of local time along with FRP. FRP was not available at all times throughout the day, but it can be seen from the figures that TROPOMI ERs follow similar patterns to those of FRP. As the TROPOMI overpass time is nominally 1:30 p.m., emissions are typically observed when fire activity is increasing. The rise in emissions linked to heightened fire activity is reflected in the growing TROPOMI ER values, which correspond with the higher FRP measurements.

Emission rates from TROPOMI also follow a similar pattern to those observed by a study on the transition from the smouldering to flaming phase of a Canadian

boreal forest fire. Hayden et al. (2022) flew an NRCan Convair-580 research aircraft through a boreal forest wildfire on the Alberta/Saskatchewan border in June 2018, with 15 instruments on board measuring 193 compounds. They were able to observe diurnal variability in CO, among other species, by combining aircraft measurements of CO with Canadian Forest Fire Emissions Prediction System (CFFEPS) modelled ERs, TROPOMI CO ERs, and GOES FRP (Figure 5.5). The combined method by Hayden et al. (2022) provides insight into how transitioning from the smouldering phase to a period of higher activity (flaming phase) causes a sharp increase in CO emissions. The TROPOMI results from the Gaussian-flux method show a similar pattern over the age of the plume. A limitation to the method used in this work is that a constant wind speed is assumed, however, wind speed and direction may change throughout the day, leading to some dilution of CO in an aged plume. For this reason, the method used in this study provides an approximation of observed ER diurnal variation. Correlations exist, however, between TROPOMI ER and GOES FRP in local time.

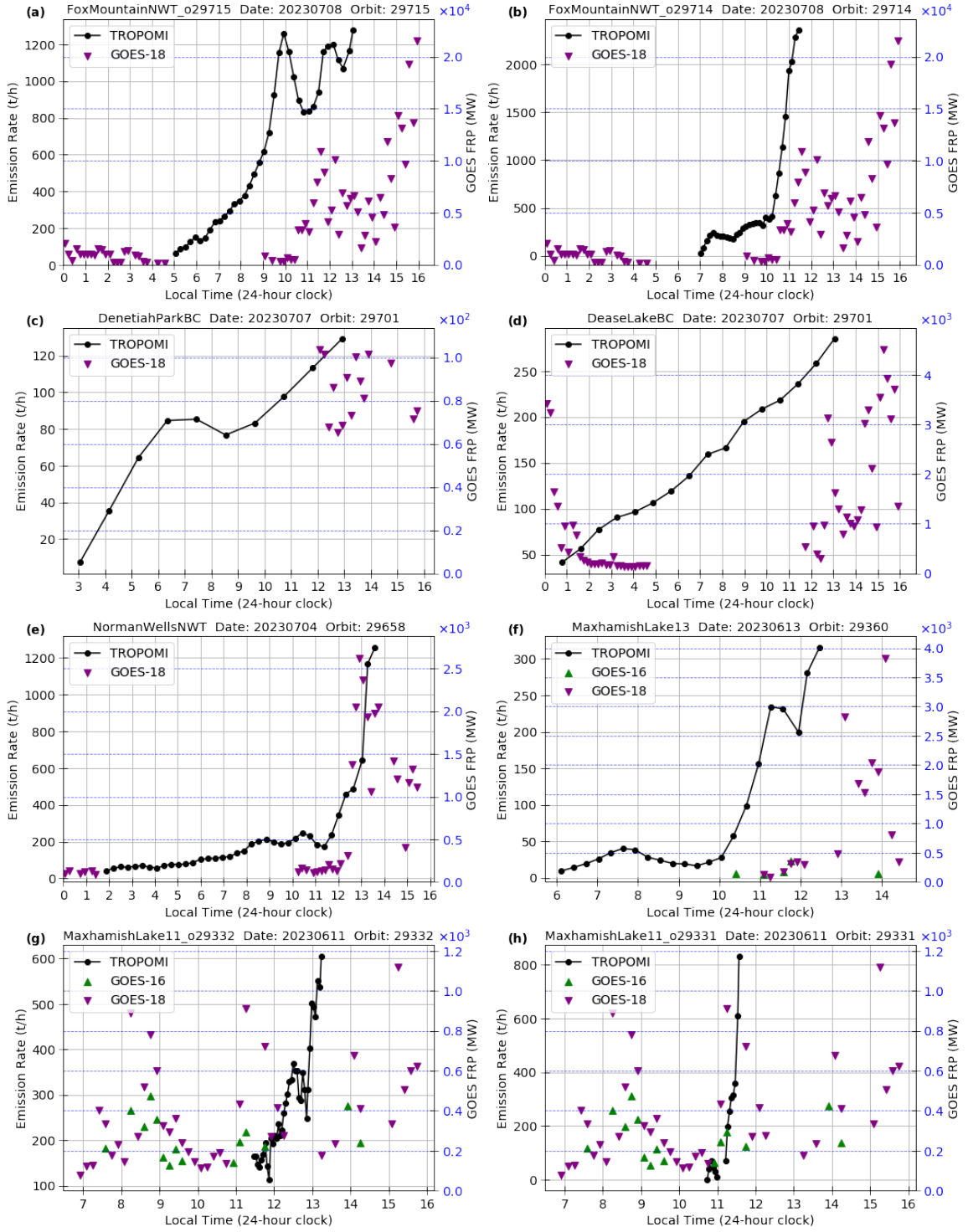

Figure 5.2: Calculated TROPOMI CO emission rates (black) and GOES-16 (green triangle) and GOES-18 (purple triangle) FRP as a function of local time (in 2400 hour clock format) for the 15 plumes from summer 2023 wildfires. Titles provide the fire name, date, and TROPOMI orbit number for each plume.

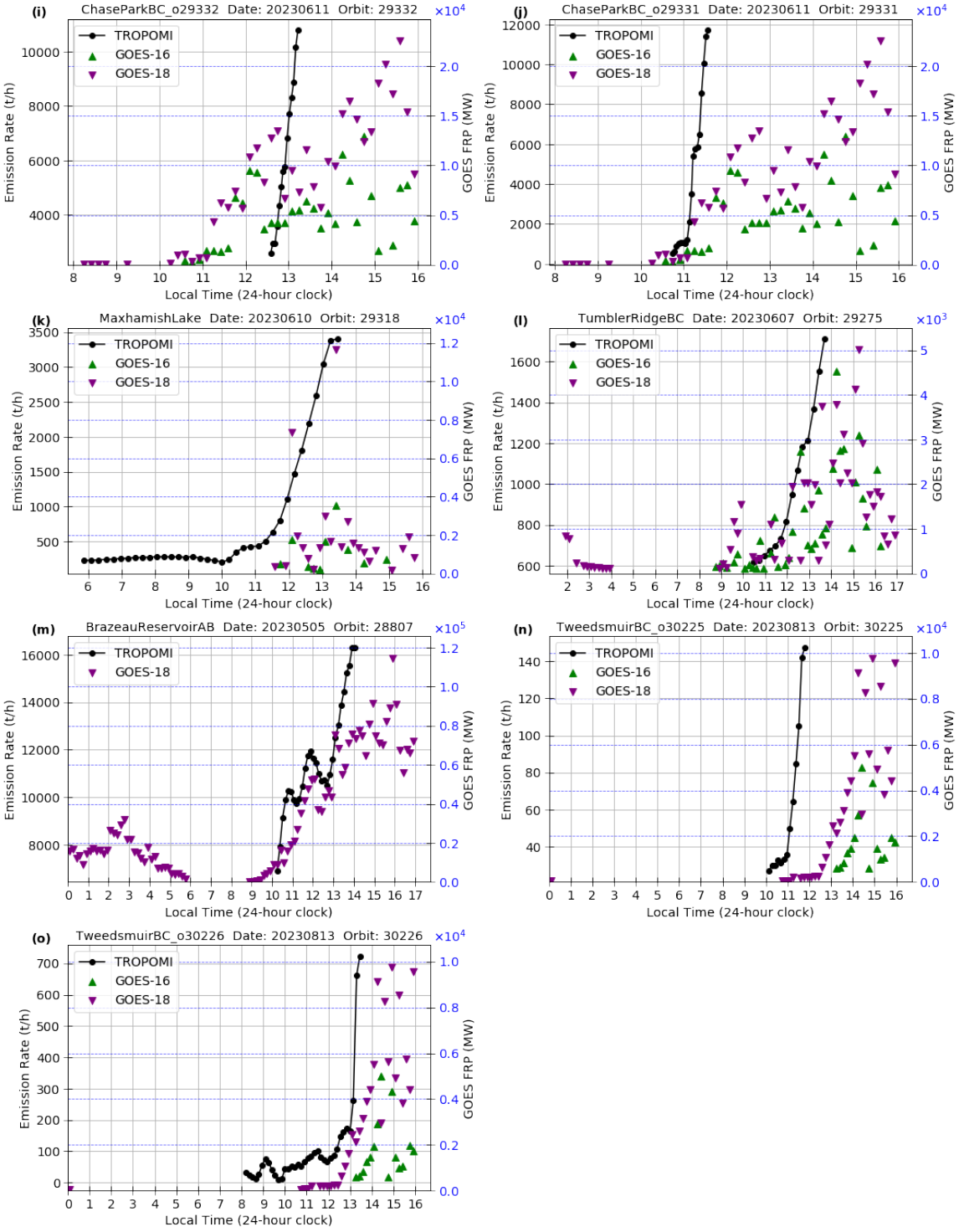

Figure 5.2: (continued)

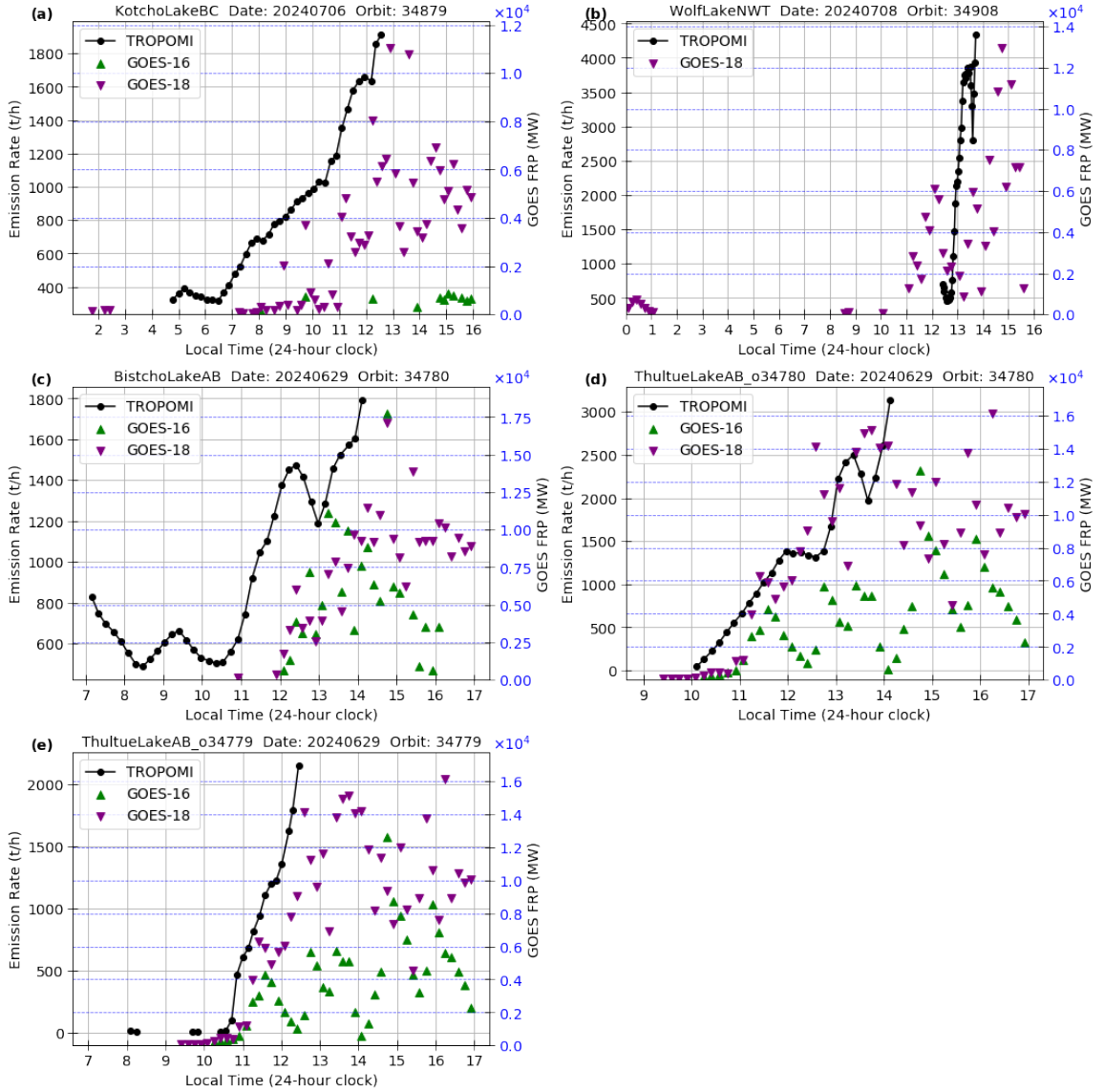

Figure 5.3: Calculated TROPOMI CO emission rates (black) and GOES-16 (green triangle) and GOES-18 (purple triangle) FRP as a function of local time (in 2400 clock format) for the five wildfires observed in summer 2024. Titles provide the fire name, date, and TROPOMI orbit number for each plume.

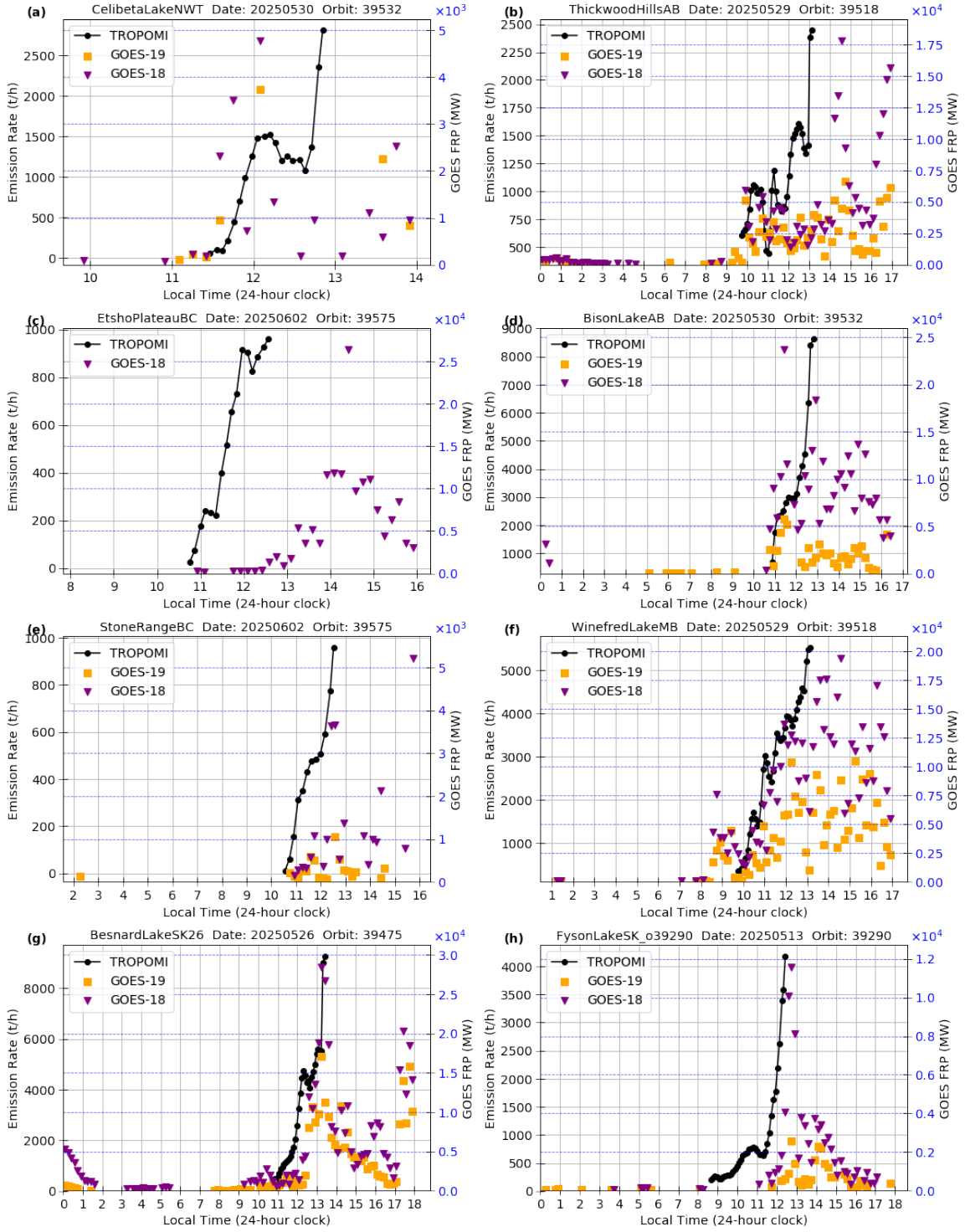

Figure 5.4: Calculated TROPOMI CO emission rates (black) and GOES-18 (purple triangle) and GOES-19 (orange square) FRP as a function of local time (in 2400 clock format) for the 14 plumes from summer 2025 wildfires. Titles provide the fire name, date, and TROPOMI orbit number for each plume.

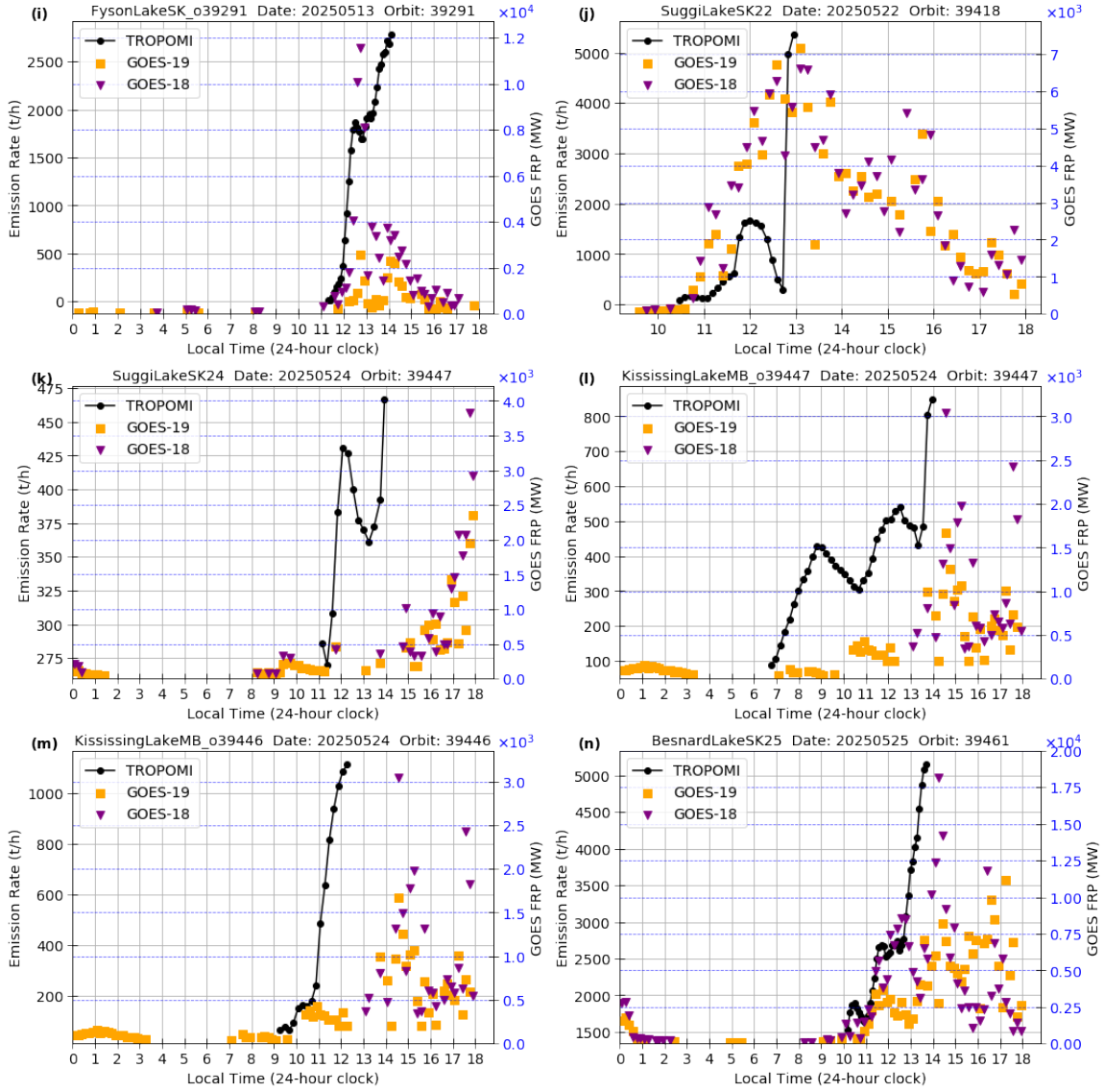

Figure 5.4: (continued)

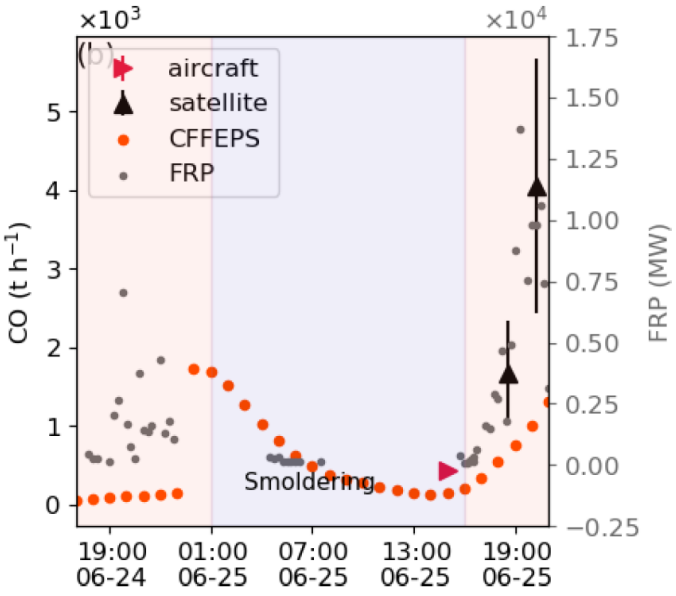

Figure 5.5: CO emission rates from aircraft measurements, using an NRCan aircraft (red triangle), TROPOMI (black triangle), and CFFEPS (orange dots) are compared with GOES-R FRP (grey dots) as a function of local time for a boreal forest wildfire on the border of Alberta and Saskatchewan over a 24-hour period, on June 24th 2018. *Figure from Hayden et al. (2022).*

The correlation between TROPOMI ER and MODIS FRP was observed by Griffin24 by evaluating single ERs 20 km downwind of the fire source for 842 wildfires with the *broadleaved evergreen* land type from GLC2000 (Figure 5.6). They were able to calculate a linear slope of 94.718 g/MJ and a good correlation with an R^2 of 0.70. To expand on their work, the diurnal ERs from the fires in this chapter were compared against GOES FRP. To do this, each GOES FRP available from GOES-W and GOES-E throughout a 24-hour period were used to find a derived TROPOMI ER within ±10 minutes of the FRP and then those two data points were plotted as ER versus FRP. If no TROPOMI ER existed, the FRP was skipped and the next FRP in time followed the same criteria until an ER was located. Using this method ensures every TROPOMI ER that has a FRP value within ±10 minutes is plotted but no ER is counted twice. Both GOES-E and GOES-W were used to ensure all available FRP was compared against TROPOMI ER, without missing any ER if possible. There were no qualifications of whether it was GOES-E or GOES-W being used, only a FRP value was compared against an ER within ±10 minutes. Due to both GOES estimating FRP differently, this could lead to individual calculated emission

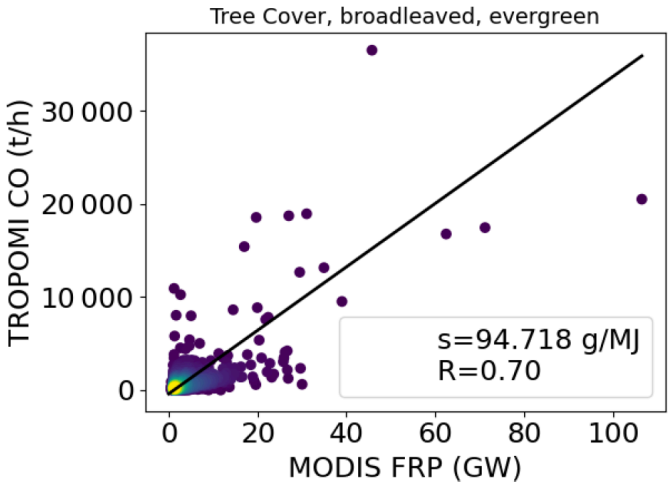

Figure 5.6: Single emission rates taken at 20 km downwind for 842 wildfires under the *broadleaved evergreen* land type from GLC2000 plotted as a function of MODIS FRP. Figure from Griffin24.

coefficients being over- or under-estimated.

Figure 5.7 shows the ER versus FRP from the 2023 to 2025 plumes, with the red line showing an ordinary least square (OLS) regression, which considers errors in y, and the blue line representing a York regression fit, which, unlike OLS, considers errors in both x and y (for more detail see York (1968)). The OLS weights by the uncertainty in calculated ERs but assumes a precise GOES FRP, while the York regression weights by both the 40% random error on ER (Section 2.5) and the standard deviation for the GOES FRP data. The OLS fit has a good correlation with an R^2 of 0.73 and a slope of 73.06 ($\pm$ 0.62) g/MJ, while the York regression also provided a good correlation with R^2 of 0.72 and a slope of 81.26 ($\pm$ 10.79) g/MJ, with both providing the standard error of mean as uncertainty and a 95% confidence interval (shaded area of the same respective colour). Since the York regression considers errors in both x and y, it has a higher uncertainty. Plumes from ChaseParkBC_o29331 and ChaseParkBC_o29332 had unusually low FRP with very high ERs, unlike other plumes. These outliers were removed, which can be seen in grey on Figure 5.7, and omitted from the fits.

The York regression gives more weight to the dense core of points while the OLS regression better fits the larger FRP values. The slope of each fit is the calculated emission coefficient of CO (EC_{CO} in g/MJ). Since Figure 5.6 from Griffin24 shows the EC_{CO} from fires with the classification *broadleaved evergreens*, it is better to

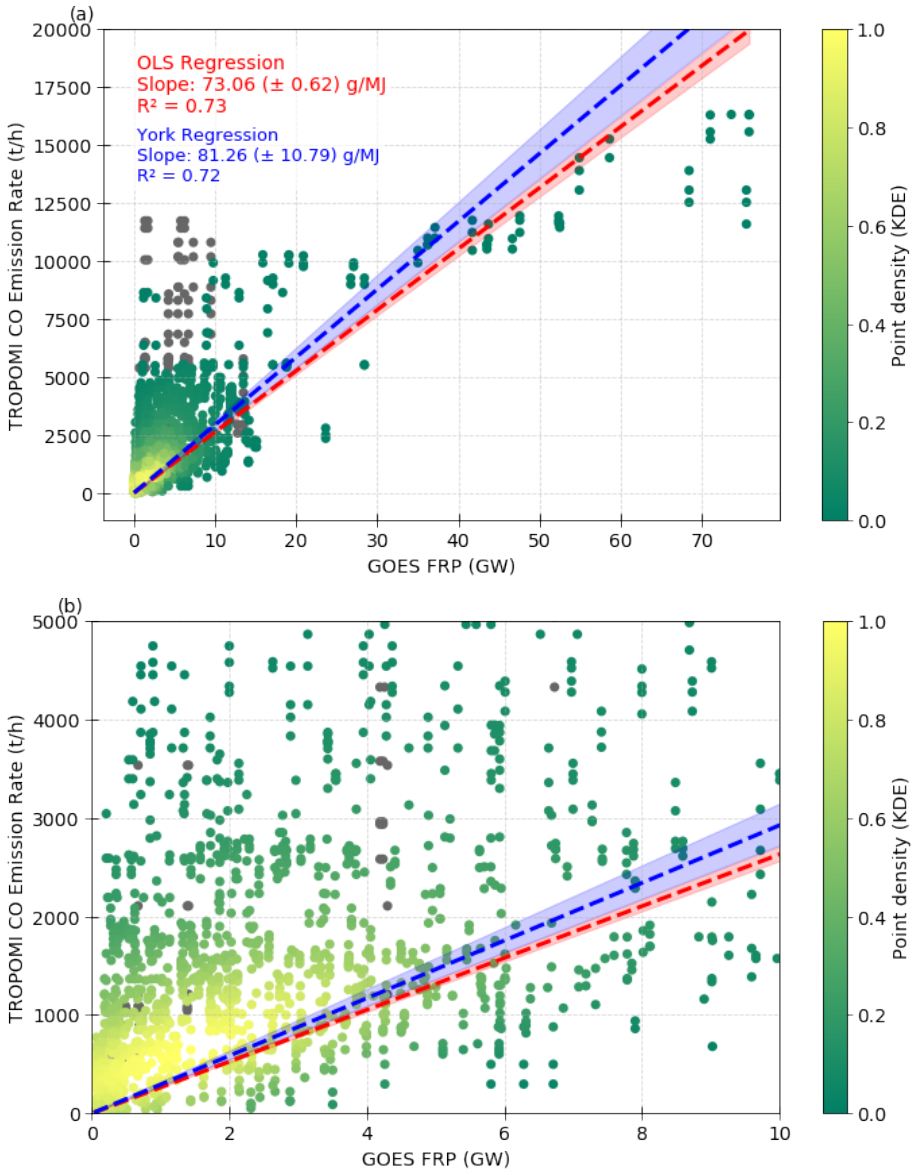

Figure 5.7: (a) TROPOMI CO ER versus GOES FRP for all TROPOMI ERs that are within ±10 minutes of a GOES FRP measurement along the plume of each of the 38 wildfire plumes from 2023 to 2025. The grey points represent data from plumes ChaseParkBC_o29331 and ChaseParkBC_o29332 that were omitted from the fit. The red dashed line represents an OLS regression and the blue dashed line represents a York regression, both forced through the origin. Both fits show the 95% confidence interval with shading. Panel (b) shows a zoomed-in view of the inner region of the majority of data points.

compare to their analysis with the GLC2000 land type *Tree cover, needle-leaved, evergreen* (European Commission, 2023), which is closer to the CCI LC category *Tree cover, needleleaved, evergreen* used in this research. Griffin24 observed an EC_{CO} of 58 ± 2 g/MJ, with an R^2 of 0.53. Of the 15,000 fires they measured 1418 fires

fell into this category. To ensure they were accounting for all fires, they changed the biome classification to the MODIS C005 Global 500 m Land Cover Type product (MCD12C1) classification (NASA, 2025). The biome of *Evergreen needle-leaved forests* was calculated to have an EC_{CO} of 76 ± 4 g/MJ with an R^2 of 0.61 for the 246 of the total fires that now fall into this category. This is much closer to the EC_{CO} from the diurnal ERs calculated in Figure 5.7. While Griffin24 analysed 15,000 fires, swapping between the two classification systems changed which fires fell within each of the above categories, thus changing the number of fires.

The EC_{CO} from the York and OLS regressions are slightly greater than Griffin24 due to a density of large ERs with low FRP, which can be seen in Figure 5.7 (b). This is likely due to the limitations of GOES at high VZA (Section 2.1.4). The theoretical basis document for GOES-R fire/hotspot characterisation (Schmidt et al., 2013) states that GOES data are available up to 80° VZA, with the best results at VZA $< 65°$. Nearly all (37 of 38) plumes exceeded the 65° threshold, with six exceeding the viewing angle of 80° for GOES-E. No FRP was collected from GOES-E for those six fires. GOES-W has 32 out of 38 fires with VZA $> 65°$, but none exceeded 80°, with six $< 65°$ (Figure 5.8). These higher VZAS can cause GOES to underestimate the FRP of some fires (Li et al., 2019). This would shift the data to the left more in Figure 5.7 and cause greater slopes, as can be seen with the York regression that puts more weight on the core density. However, GOES, with FRP data collected every 10 to 15 minutes, provides the best demonstration of diurnal variation compared to other satellites like MODIS and the Visible Infrared Imaging Radiometer Suite (VIIRS), which have only one to two overpasses a day.

The relationship between ER and FRP can be examined further by looking at ER versus the logarithm of GOES FRP. Data in Figure 5.7 were plotted in Figure 5.9, with the FRP on a logarithmic scale and colour mapped with plume age. Because CO ERs in Figure 5.1 show that the majority of fire plumes have normalised CO ERs declining to near zero within the first five hours, the plume age colour map is set between 0 and 5 hours to help better visualise what is occurring in the plume, with data points that fall outside 5 hours coloured grey, but still considered in the fit. The red line represents

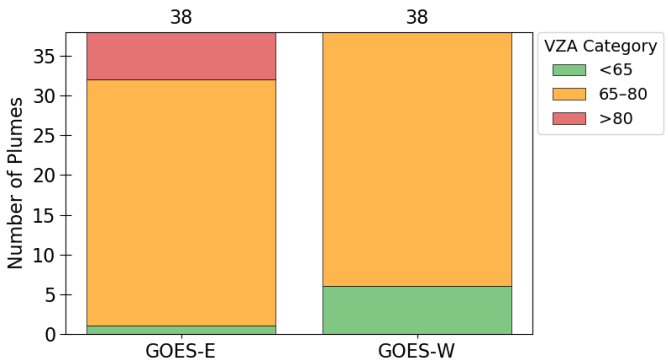

Figure 5.8: Summary of GOES VZA for each plume observed in this study for GOES-E and GOES-W. Red is above the 80° threshold for detection, orange is above the ideal region of $> 65°$, and green is in the ideal region of below 65°.

the OLS regression from Figure 5.7, but with plumes ChaseParkBC_o29331 and ChaseParkBC_o29332 included. There are two distinct regions in the relationship between calculated ER and FRP. As FRP approaches 1 GW, emissions start to trend upward rapidly, and even more beyond ~10 GW, showing an increased correlation of larger ERs on stronger FRP. While CO is primarily produced during the smouldering phase that tends to have lower FRP, in times of high activity both smouldering and flaming can occur. This is why darker colours (younger plumes) tend to be associated with greater FRP, while lighter colours (older plumes) tend toward smaller FRP. As TROPOMI overpasses typically occur when fire activity is increasing (Figure 5.5), which can be seen in Figures 5.2 through 5.4, younger plumes would see greater FRP and CO ER, while older plumes, emitted during the smouldering phase, would have smaller overall FRP and emissions.

5.4 Conclusions

In this work, the evolution of CO within a wildfire plume was analysed with respect to plume age, and CO ER was compared to GOES FRP to observe patterns in diurnal variability. ERs for each fire, derived from TROPOMI measurements and normalised by the maximum emission of each fire, were plotted as a function of plume age, which was calculated using location of the emission and wind speed. CO ER shows rapid

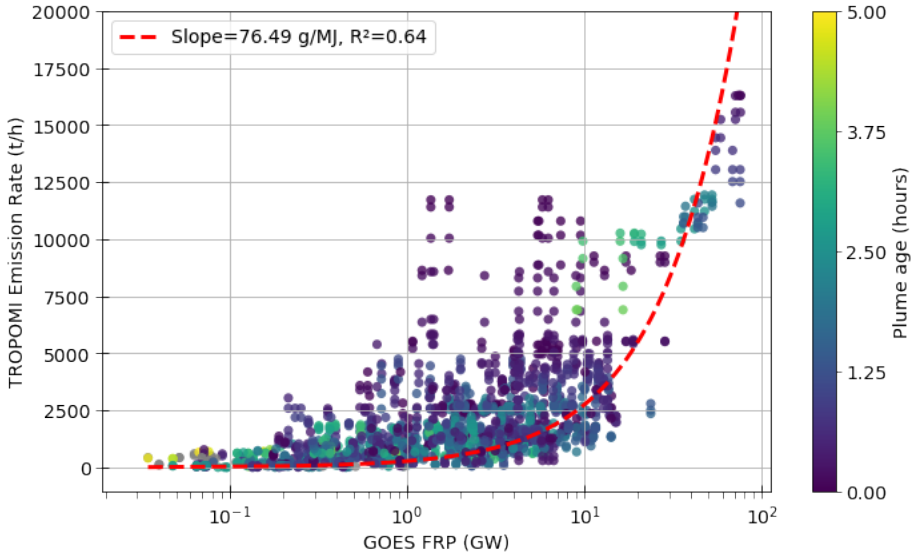

Figure 5.9: A linear-logarithmic plot of TROPOMI CO ER versus GOES FRP similar to Figure 5.7, but with a colour map of plume age. Plume age was set from 0 to 5 hours and any ERs that fell outside this threshold were coloured grey. The red dashed line represents the OLS regression fit forced through the origin. Plumes ChaseParkBC_o29331 and ChaseParkBC_o29332 are included in OLS fit.

decay following an inverse-power-law fit, with the majority of fires showing CO ERs dropping to near background levels within the first five hours after emission. This shows that ERs are stronger near the centre of the fire, following literature observations of CO emissions in fires (Freeborn et al., 2008; Akagi et al., 2011; Andreae, 2019; Li et al., 2020; Hayden et al., 2022). Species with secondary formation in the plume, instead of in the fire itself, would have higher ERs further downwind, as the plume aged. For this reason, species such as NO_2 and HCHO, which demonstrate secondary formation and have relatively short life spans, are not suitable candidates for analysing the diurnal variability of emission. Secondary formation could inflate emission estimates relative to FRP and the short lifetimes (including photochemical sinks such as those of NO_2) could lower emission rates estimates. Diurnal analysis works best with atmospheric species that are primarily formed in the flaming or smouldering phases of the fire and have half-lives that are significantly longer than the typical plume age for a plume of 150 km downwind, which is often below twelve hours.

Using the plume age and TROPOMI overpass times, ERs were plotted as a func-

tion of the local time at the location of the fire, along with GOES FRP. GOES FRP was taken from GOES-16, -18, and -19 depending on the date of the fire and data availability. TROPOMI ERs showed similar trends to FRP, with rates increasing as FRP increases. To examine the dependency of ER on FRP, ER and FRP points were matched with a ±10 min coincidence criterion. OLS and York regression fits were performed on the data, with the York fit showing good correlation with R^2 of 0.72 and a slope of 81.26 (± 10.79) g/MJ, while OLS showed a similar correlation with an R^2 of 0.73 with a slope of 73.06 (± 0.62) g/MJ.

Griffin24 used the Gaussian-flux method to look at single ERs at 20 km downwind, for 15000 fires of different land types. The fires that Griffin24 examined that fell under the GLC2000 land type *Tree cover, needle-leaved, evergreen* had an EC_{CO} of 58 ± 2 g/MJ for 1418 fires, with an R^2 of 0.53. The MODIS classification MCD12C1 for the biome *Evergreen needle-leaved forests* was then used by Griffin24, with 246 fires falling in this classification, to calculate an EC_{CO} of 76 ± 4 g/MJ ($R^2 = 0.61$), which is within a margin of error to the observed EC_{CO} in this paper of 73.06 g/MJ from the OLS fit. Both the York and OLS regression showed a similar order of magnitude for the diurnal ERs calculated in this research, with both being higher than GLC2000 classifications of more fires.

The EC_{CO} calculated in this research may be biased high with a larger slope due to the limitations that exist with the GOES-R series for larger VZAs. The majority of plumes were at coordinates that fell outside the literature suggested threshold of $< 65°$ VZA for the best results, and nearly all fell within the 80° limit of observable data, with the exception of six fires for GOES-E, but no data was provided for those fires from GOES-E. GOES could underestimate FRP for fires that fall outside the 65° threshold, resulting in plumes with large ERs having lower FRP than they should. While this is a limitation with using GOES-R satellites, GOES measures FRP throughout the day shedding light on diurnal fluctuations of FRP compared to other instruments like MODIS or VIIRS, which only provide one or two observations a day.

Lastly, the calculated ERs were compared against a logarithmic GOES FRP with

a colour-mapped plume age. Nearly all plumes had normalised CO ERs decrease to zero within the first five hours, so the colours were mapped from zero to five hours with all plume ages outside five hours coloured grey, but still included in the analysis. The linear OLS was plotted to show this dependence. For FRP greater than 1 GW power, ERs began to increase rapidly, with the majority of the plume ages in this region being within the first few hours of emission. As the 1:30 p.m. TROPOMI overpasses occur when fire activity is increasing, younger plumes would have more CO than plumes with ERs from earlier in the day when fire activity is reduced. While CO emissions are typically largest during the smouldering phase, during times of greater fire activity, both smouldering and flaming phases can occur, causing larger FRP to produce more CO. This can be seen in the data.

TROPOMI has been shown, through this work, to provide a good approximation of diurnal variability of longer-lived species like CO with a single overpass. The main limitation of this method is that the wind speed is averaged over the length of the plume. This assumes a constant wind speed to determine the plume age. Wind, however, may fluctuate throughout the day by changing speed and direction. For this reason, TROPOMI is best at providing an approximation of diurnal variability in CO previously unavailable outside of in-situ and ground-based measurements. Future work could expand on this research by determining the plume age using hourly wind speed data to get a more accurate representation of the age of the plume and comparing these results to prediction models such as CFFEPS to better validate the emissions and help reduce the uncertainties of FRP from the GOES satellites. As TROPOMI provides global coverage, this method could be used to observe diurnal variations in other land types and fires from nearly any region, with expanded analysis using prediction models.

Chapter 6

Conclusions and Future Work

6.1 Summary

Wildfires have proven to be increasingly challenging in the battle against climate change, in recent years. Climate change has increased droughts and lightning-producing storms, causing more wildfires, while biomass burning can emit many atmospheric species that can lead to further climate-change-induced severe weather. This in-turn leads to more wildfires, in a positive feedback. The atmospheric species emitted by biomass burning can also pose a health risk to the public. Developing ways to observe and measure how these species develop in wildfire plumes is important for understanding the impact that wildfires are having on our environment and health. This thesis focused on using TROPOMI measurements to analyse the wildfire by-products CO, HCHO, and NO_2 to investigate their emissions and evolution by addressing three primary objectives:

1. To determine the temporal and spatial variations of CO, HCHO, and NO_2 in the downwind direction of wildfire plumes and examine how they evolve as the plume ages for the 2019 FIREX-AQ fires and the 2023 Canadian boreal forest wildfires.

2. To calculate downwind formaldehyde-nitrogen ratios for Canadian boreal forest wildfires from the summers of 2023 and 2025 and examine the downwind tran-

sitions from a NO_x-sensitive to a VOC-sensitive regime of surface O_3 formation probability.

3. To evaluate the diurnal variability of single-overpass TROPOMI CO emission rates and compare them to fire radiative power derived from satellite observations.

To address the first objective, project 1 (Chapter 3) focused on CO, HCHO, and NO_2 wildfire-plume enhancement rates using TROPOMI measurements. These rates were calculated for three fires observed during the summer 2019 FIREX-AQ campaign and nine wildfires in Western Canada in summer 2023, using the Gaussian-flux method. The Gaussian-flux enhancement rates for the Shady, Williams Flats, and Horsefly FIREX-AQ wildfires fell within the calculated enhancement rates provided by Stockwell et al. (2022), at various points in the downwind direction, for all three species, except Horsefly CO. Enhancement rates were generally smaller than FIREX-AQ results due to the 1:30 p.m. TROPOMI overpasses occurring at a time when wildfire activity is increasing, while in-situ measurements were collected a few hours after TROPOMI overpass, as verified with GOES FRP.

Changes in species concentrations were observed as the wildfire plume aged downwind using a single TROPOMI overpass for each fire, with HCHO being observed with this method for the first time. Enhancement rates show large CO enhancements near the sources of the fires, with NO_2 and HCHO primarily attributed to secondary production, with minor contributions from primary emissions. HCHO enhancement rates increased as NO_2 rates decreased, suggesting some HCHO production due to oxidation cycles of VOCs, which are present in boreal forests. EnhRs were analysed as a function of plume age, showing an overall average positive slope for HCHO/CO and HCHO/NO_2 and a negative slope for NO_2/CO. EnhRs suggest production of HCHO further downwind, as the plume ages, while NO_2 was rapidly produced near the source, but was subsequently destroyed with no clear evidence of formation further downwind. This research showed how the Gaussian-flux method using TROPOMI is comparable to FIREX-AQ results and can be used to analyse CO, HCHO, and NO_2

evolution as a wildfire plume ages downwind.

To address the second objective, project 2 (Chapter 4) used TROPOMI measurements to analyse enhancement rates and VCD enhancement FNRs downwind of fourteen plumes from nine wildfires in 2023 and twelve plumes from seven wildfires in 2025 in Western and Central Canadian boreal forests. Fires from 2023 and 2025 showed similar enhancement rates downwind for CO, HCHO, and NO_2, consistent with results found in Chapter 3. The majority of satellite-derived FNRs showed VOC sensitivity for O_3 production near the source of the smoke and rapidly transitioned to NO_2 sensitivity as the plume aged. This research suggests transition into NO_2-sensitive O_3 formation occurs within an hour of emission, consistent with the in-situ- and model-based study of Robinson et al. (2021). FNR as a function of plume age showed six plumes with R^2 above 0.50 and all but one plume having R^2 above 0.30 for 2025, and eight plumes having R^2 above 0.50 for 2023. This is the first time TROPOMI has been used to observe wildfire down-plume FNRs, demonstrating that this is an effective method for using FNRs to observe NO_2- and VOC-sensitivity of O_3 production.

Finally, the third objective was explored in project 3 (Chapter 5). TROPOMI CO emission rates were calculated for 38 wildfire plumes from boreal forests in Central and Western Canada from 2023 to 2025. CO ERs as a function of plume age showed a rapid decay and followed an inverse-power-law fit, with most plumes showing a decline in ER within the first five hours. ERs were plotted as a function of local time by taking the plume age, converting backward from TROPOMI overpass time, and using the local time of each fire. TROPOMI ERs showed strong agreement with local time GOES FRP, showing increased emissions as FRP increased, demonstrating diurnal dependence captured in TROPOMI down-plume measurements. To verify the dependence on GEOS FRP, ERs were plotted against GOES FRP with an OLS and York regression fit, with the York regression accounting for the 40% random error of the method and the standard deviation of the GOES FRP. The York regression gave an R^2 of 0.72 showing a good correlation, with a slope of 81.26 ($\pm$ 10.79) g/MJ; while the OLS regression also gave a good correlation with an R^2 of 0.73 and a slope of

73.06 (± 0.62) g/MJ.

The OLS was closest to the results of TROPOMI CO versus MODIS FRP from Griffin24 for the 246 fires that fell within the MODIS MCD12C1 classification of *Evergreen needle-leaved forests* (EC_{CO} of 76 ± 4 g/MJ). However, both the York and OLS regressions EC_{CO} were higher than the 1418 fires that fell within the GLC2000 land type classification *Tree cover, needle-leaved, evergreen* (EC_{CO} of 58 ± 2 g/MJ). The EC_{CO} of both fits may have a high bias due to the large viewing zenith angle of the majority of high-latitude fires in Canada being primarily greater than the 65° suggested for the best results from GOES FRP, resulting in higher ERs having lower than FRP than they should. Examining ER against FRP showed that for FRP > 1 GW, ERs increased rapidly with FRP, with larger ERs showing greater dependence on larger FRP within the first few hours of being emitted. This suggests that younger plumes, which are closer to a TROPOMI overpass when fire activity is increasing, have larger CO ERs. During a period of high activity in a fire, both the flaming and smouldering phase can occur at the same time, increasing CO emission, which is primarily produced in the smouldering phase. This study showed that TROPOMI measurements can be used to examine the diurnal variability of CO emissions from wildfire plumes.

6.2 Future Work

One option for future work that builds on all three projects would be to adapt the Gaussian-flux method to work with the higher resolution Tropospheric Emissions: Monitoring of Pollution (TEMPO) spectrometer, which is in geostationary orbit above North America, and compare emission rates calculated from TEMPO vertical column data products to TROPOMI emission rates. TROPOMI is also capable of measuring other species such as methane (CH_4) which is also capable of driving surface O_3 formation. While TROPOMI also measures O_3, it is limited in the ability separate tropospheric O_3 from stratospheric (Mettig et al., 2021). Early research on O_3 retrieval methods with the Geostationary Environment Monitoring Spectrometer

(GEMS), which is similar to TEMPO and Sentinel-4, has preliminarily been able to obtain tropospheric O_3 retrievals (Bak et al., 2025). Expanding the Gaussian-flux method to potential TEMPO, GEMS, and Sentinel-4 tropospheric O_3 columns could enable comparison of FNRs to surface-level O_3 emission rate variations.

Modelling of wildfire O_3 emissions using transport models with resolutions of 4 to 200 km has proven difficult and typically overestimates O_3 production, with many models struggling to observe plume age affects on O_3 production. The method for analysing FNRs could be expanded to evaluate chemical transport models and provide greater insight into the evolution of species within plumes as they age downwind.

Other than O_3, there are additional species of interest in wildfire chemistry that could be analysed with this method. Adapting the method to work with the Infrared Atmospheric Sounding Interferometers (IASI-A and IASI-B) on board the MetOp satellites (Clerbaux et al., 2009) along with the Cross-track Infrared Sounder (CrIS) aboard the Suomi National Polar-orbiting Partnership (S-NPP) satellite (Shephard and Cady-Pereira, 2015) could allow for the analysis of ammonia (NH_3), which is an important precursor to NO and subsequently NO_2 formation in wildfires (Roberts et al., 2020). The method for calculating emission rates could also be expanded to look at NO_x sinks within a wildfire plume to better understand the life cycle of NO_x species within the plume by looking at HONO with IASI (Dufour et al., 2022; Franco et al., 2024) and TROPOMI (Fredrickson et al., 2023; Theys et al., 2025) and PAN with IASI (Franco et al., 2018) and CrIS (Juncosa Calahorrano et al., 2021; Payne et al., 2022; Shogrin et al., 2023). Examining these sinks of NO_x could provide information about the impact of NO_2 on O_3 formation further from wildfires due to long-range transport (Zhai et al., 2024). This method would have to be adapted to account for IASI and CrIS having a lower spatial resolution than TROPOMI.

All three studies performed in this thesis could be expanded to examine different land types. This thesis focused mostly on Canadian boreal forests, particularly the record 2023 and 2025 wildfire seasons, but this method is not limited to fires in forests. It can be used to analyse various fires around the world, based on different land types. Observing the evolution of species within the plumes from different fuel

sources—such as grassland, broadleaved deciduous trees, eucalyptus trees, shrubland, etc.—could provide a more robust understanding of how emission rates of different species evolve downwind. The CCI LC product is capable of differentiating fuel types based on geographic location of fires and allows for the expansion of understanding on the impacts of smoke from various sources and different regions of the world from the recent 2025 Korean and Japanese wildfires to agriculture fires in India and central Africa.

Lastly, the diurnal variability study would greatly benefit from being compared to model outputs such as from CFFEPS, which can provide diurnal changes in emissions for fires being observed. TROPOMI measurements could be used as a tool for measuring diurnal changes in stable species with long lifetimes, such as CO, and to validate model emission outputs. Satellite measurement of diurnal changes in emissions are possible with geostationary satellites, but they are limited in the area they observe. Being able to examine diurnal variations in emission rates solely with TROPOMI and other sun-synchronous satellites, can provide a global coverage for analysing diurnal changes in emissions that are typically limited to laboratory measurements or intense aircraft and ground campaigns.

Bibliography

Acdan, J.J.M., Pierce, R.B., Dickens, A.F., Adelman, Z., Nergui, T., 2023. Examining TROPOMI formaldehyde to nitrogen dioxide ratios in the Lake Michigan region: implications for ozone exceedances. Atmospheric Chemistry and Physics 23, 7867–7885.

Achtemeier, G.L., 2006. Measurements of moisture in smoldering smoke and implications for fog. International Journal of Wildland Fire 15, 517–525.

Adams, C., McLinden, C.A., Shephard, M.W., Dickson, N., Dammers, E., Chen, J., Makar, P., Cady-Pereira, K.E., Tam, N., Kharol, S.K., Lamsal, L.N., Krotkov, N.A., 2019. Satellite-derived emissions of carbon monoxide, ammonia, and nitrogen dioxide from the 2016 Horse River wildfire in the Fort McMurray area. Atmospheric Chemistry and Physics 19, 2577–2599.

Akagi, S., Yokelson, R.J., Wiedinmyer, C., Alvarado, M., Reid, J., Karl, T., Crounse, J., Wennberg, P., 2011. Emission factors for open and domestic biomass burning for use in atmospheric models. Atmospheric Chemistry and Physics 11, 4039–4072.

Alvarado, M.J., Logan, J.A., Mao, J., Apel, E., Riemer, D., Blake, D., Cohen, R.C., Min, K.E., Perring, A.E., Browne, E.C., Wooldridge, P.J., Diskin, G.S., Sachse, G.W., Fuelberg, H., Sessions, W.R., Harrigan, D.L., Huey, G., Liao, J., Case-Hanks, A., Jimenez, J.L., Cubison, M.J., Vay, S.A., Weinheimer, A.J., Knapp, D.J., Montzka, D.D., Flocke, F.M., Pollack, I.B., Wennberg, P.O., Kurten, A., Crounse, J., Clair, J.M.S., Wisthaler, A., Mikoviny, T., Yantosca, R.M., Carouge, C.C., Le Sager, P., 2010. Nitrogen oxides and PAN in plumes from boreal fires

during ARCTAS-B and their impact on ozone: an integrated analysis of aircraft and satellite observations. Atmospheric Chemistry and Physics 10, 9739–9760.

Alvarado, M.J., Logan, J.A., Mao, J., Apel, E., Riemer, D., Blake, D., Cohen, R.C., Min, K.E., Perring, A.E., Browne, E.C., Wooldridge, P.J., Diskin, G.S., Sachse, G.W., Fuelberg, H., Sessions, W.R., Harrigan, D.L., Huey, G., Liao, J., Case-Hanks, A., Jimenez, J.L., Cubison, M.J., Vay, S.A., Weinheimer, A.J., Knapp, D.J., Montzka, D.D., Flocke, F.M., Pollack, I.B., Wennberg, P.O., Kurten, A., Crounse, J., Clair, J.M.S., Wisthaler, A., Mikoviny, T., Yantosca, R.M., Carouge, C.C., Le Sager, P., 2010. Nitrogen oxides and PAN in plumes from boreal fires during ARCTAS-B and their impact on ozone: an integrated analysis of aircraft and satellite observations. Atmospheric Chemistry and Physics 10, 9739–9760.

Anderson, L.D., Dix, B., Schnell, J., Yokelson, R., Veefkind, J.P., Ahmadov, R., de Gouw, J., 2023. Analyzing the impact of evolving combustion conditions on the composition of wildfire emissions using satellite data. Geophysical Research Letters 50, e2023GL105811.

Andreae, M.O., 2019. Emission of trace gases and aerosols from biomass burning–an updated assessment. Atmospheric Chemistry and Physics 19, 8523–8546.

Andreae, M.O., Merlet, P., 2001. Emission of trace gases and aerosols from biomass burning. Global Biogeochemical Cycles 15, 955–966.

Arino, O., Gross, D., Ranera, F., Leroy, M., Bicheron, P., Brockman, C., Defourny, P., Vancutsem, C., Achard, F., Durieux, L., Bourg, L., Latham, J., Di Gregorio, A., Witt, R., Herold, M., Sambale, J., Plummer, S., Weber, J.L., 2007. GlobCover: ESA service for global land cover from MERIS, in: 2007 IEEE International Geoscience and Remote Sensing Symposium, IEEE. pp. 2412–2415.

Arnold, S.R., Emmons, L.K., Monks, S.A., Law, K.S., Ridley, D.A., Turquety, S., Tilmes, S., Thomas, J.L., Bouarar, I., Flemming, J., Huijnen, V., Mao, J., Duncan, B.N., Steenrod, S., Yoshida, Y., Langner, J., Long, Y., 2015. Biomass burning

influence on high-latitude tropospheric ozone and reactive nitrogen in summer 2008: a multi-model analysis based on POLMIP simulations. Atmospheric Chemistry and Physics 15, 6047–6068.

Bak, J., Keppens, A., Choi, D., Hong, S., Kim, J.H., Kim, C.H., Lee, H.J., Jeon, W., Kim, J., Koo, J.H., Kim, J., Beak, K., Yang, K., Liu, X., Abad, G.G., Heue, K.P., Lambert, J.C., Jung, Y., Hong, H., Lee, W.J., 2025. GEMS ozone profile retrieval: impact and validation of version 3.0 improvements. EGUSphere [preprint] 2025, 1–29.

Baker, K., Woody, M., Tonnesen, G., Hutzell, W., Pye, H., Beaver, M., Pouliot, G., Pierce, T., 2016. Contribution of regional-scale fire events to ozone and PM2.5 air quality estimated by photochemical modeling approaches. Atmospheric Environment 140, 539–554.

Baker, K., Woody, M., Valin, L., Szykman, J., Yates, E., Iraci, L., Choi, H., Soja, A., Koplitz, S., Zhou, L., Campuzano-Jost, P., Jimenez, J.L., Hair, J., 2018. Photochemical model evaluation of 2013 California wild fire air quality impacts using surface, aircraft, and satellite data. Science of the Total Environment 637–638, 1137–1149.

Bange, H., Williams, J., 2000. New Directions: Acetonitrile in atmospheric and biogeochemical cycles. Atmospheric Environment 34, 4959–4960.

Bartholome, E., Belward, A.S., 2005. GLC2000: a new approach to global land cover mapping from Earth observation data. International Journal of Remote Sensing 26, 1959–1977.

Bontemps, S., Defourny, P., Brockmann, C., Herold, M., Kalogirou, V., Arino, O., 2012. New global land cover mapping exercise in the framework of the ESA Climate Change Initiative, in: 2012 IEEE International Geoscience and Remote Sensing Symposium, IEEE. pp. 44–47.

Borsdorff, T., Aan de Brugh, J., Hu, H., Aben, I., Hasekamp, O., Landgraf, J., 2018. Measuring carbon monoxide with TROPOMI: First results and a comparison with ECMWF-IFS analysis data. Geophysical Research Letters 45(6), 2826–2832.

Borsdorff, T., aan de Brugh, J., Schneider, A., Lorente, A., Birk, M., Wagner, G., Kivi, R., Hase, F., Feist, D.G., Sussmann, R., Rettinger, M., Wunch, D., Warneke, T., Landgraf, J., 2019. Improving the TROPOMI CO data product: update of the spectroscopic database and destriping of single orbits. Atmospheric Measurement Techniques 12, 5443–5455.

Boulanger, Y., Gauthier, S., Burton, P.J., 2014. A refinement of models projecting future Canadian fire regimes using homogeneous fire regime zones. Canadian Journal of Forest Research 44, 365–376.

Bourgeois, I., Peischl, J., Neuman, J.A., Brown, S.S., Allen, H.M., Campuzano-Jost, P., Coggon, M.M., DiGangi, J.P., Diskin, G.S., Gilman, J.B., Gkatzelis, G.I., Guo, H., Halliday, H.A., Hanisco, T.F., Holmes, C.D., Huey, L.G., Jimenez, J.L., Lamplugh, A.D., Lee, Y.R., Lindaas, J., Moore, R.H., Nault, B.A., Nowak, J.B., Pagonis, D., Rickly, P.S., Robinson, M.A., Rollins, A.W., Selimovic, V., St. Clair, J.M., Tanner, D., Vasquez, K.T., Veres, P.R., Warneke, C., Wennberg, P.O., Washenfelder, R.A., Wiggins, E.B., Womack, C.C., Xu, L., Zarzana, K.J., Ryerson, T.B., 2022. Comparison of airborne measurements of NO, NO_2, HONO, NO_y, and CO during FIREX-AQ. Atmospheric Measurement Techniques 15, 4901–4930.

Bourgeois, I., Peischl, J., Neuman, J.A., Brown, S.S., Thompson, C.R., Aikin, K.C., Allen, H.M., Angot, H., Apel, E.C., Baublitz, C.B., Brewer, J.F., Campuzano-Jost, P., Commane, R., Crounse, J.D., Daube, B.C., DiGangi, J.P., Diskin, G.S., Emmons, L.K., Fiore, A.M., Gkatzelis, G.I., Hills, A., Hornbrook, R.S., Huey, L.G., Jimenez, J.L., Kim, M., Lacey, F., McKain, K., Murray, L.T., Nault, B.A., Parrish, D.D., Ray, E., Sweeney, C., Tanner, D., Wofsy, S.C., Ryerson, T.B., 2021. Large contribution of biomass burning emissions to ozone throughout the global remote troposphere. Proceedings of the National Academy of Sciences 118(52), e2109628.

Bowman, D.M., Williamson, G.J., Abatzoglou, J.T., Kolden, C.A., Cochrane, M.A., Smith, A.M., 2017. Human exposure and sensitivity to globally extreme wildfire events. Nature Ecology and Evolution 1, 0058.

Byrne, B., Liu, J., Bowman, K.W., Pascolini-Campbell, M., Chatterjee, A., Pandey, S., Miyazaki, K., van der Werf, G.R., Wunch, D., Wennberg, P.O., Roehl, C.M., Sinha, S., 2024. Carbon emissions from the 2023 Canadian wildfires. Nature 633, 835–839.

Cai, C., Kulkarni, S., Zhao, Z., Kaduwela, A.P., Avise, J.C., DaMassa, J.A., Singh, H.B., Weinheimer, A.J., Cohen, R.C., Diskin, G.S., Wennberg, P., Dibb, J.E., Huey, G., Wisthaler, A., Jimenez, J.L., Cubison, M.J., 2016. Simulating reactive nitrogen, carbon monoxide, and ozone in California during ARCTAS-CARB 2008 with high wildfire activity. Atmospheric Environment 128, 28–44.

Callies, J., Corpaccioli, E., Eisinger, M., Hahne, A., Lefebvre, A., 2000. GOME-2-Metop's second-generation sensor for operational ozone monitoring. ESA Bulletin 102, 28–36.

CAMS, 2023. Copernicus Atmosphere Monitoring Service. Copernicus: Emissions from Canadian wildfires the highest on record - smoke plume reaches Europe. https://atmosphere.copernicus.eu/copernicus-emissions-canadian-wildfires-highest-record-smoke-plume-reaches-europe. Last Accessed: 7 July 2023.

Chen, T.M., Kuschner, W.G., Gokhale, J., Shofer, S., 2007. Outdoor air pollution: nitrogen dioxide, sulfur dioxide, and carbon monoxide health effects. The American Journal of the Medical Sciences 333(4), 249–256.

Chen, W., Dong, B., 2019. Anthropogenic impacts on recent decadal change in temperature extremes over China: relative roles of greenhouse gases and anthropogenic aerosols. Climate Dynamics 52(5-6), 3643–3660.

CIFFC, 2025a. Canadian Interagency Forest Fire Centre Inc.. National Fire Situation Report For: August 13, 2025. https://ciffc.net/situation/2025-09-16. Last Accessed: 21 September 2025.

CIFFC, 2025b. Canadian Interagency Forest Fire Centre Inc.. Wildfire Graphs. https://ciffc.net/statistics. Last Accessed: 21 September 2025.

Clerbaux, C., Boynard, A., Clarisse, L., George, M., Hadji-Lazaro, J., Herbin, H., Hurtmans, D., Pommier, M., Razavi, A., Turquety, S., Wespes, C., Coheur, P.F., 2009. Monitoring of atmospheric composition using the thermal infrared IASI/MetOp sounder. Atmospheric Chemistry and Physics 9, 6041–6054.

CMME, 2025. Canadian Council of Ministers of the Environment. Canadian Ambient Air Quality Standards Handbook. Canadian Council of Ministers of the Environment. PN 1645.

De Smedt, I., Stavrakou, T., Hendrick, F., Danckaert, T., Vlemmix, T., Pinardi, G., Theys, N., Lerot, C., Gielen, C., Vigouroux, C., Hermans, C., Fayt, C., Veefkind, P., Müller, J.F., Van Roozendael, M., 2015. Diurnal, seasonal and long-term variations of global formaldehyde columns inferred from combined OMI and GOME-2 observations. Atmospheric Chemistry and Physics 15(21), 12519–12545.

De Smedt, I., Theys, N., Yu, H., Danckaert, T., Lerot, C., Compernolle, S., Van Roozendael, M., Richter, A., Hilboll, A., Peters, E., Pedergnana, M., Loyola, D., Beirle, S., Wagner, T., Eskes, H., van Geffen, J., Boersma, K.F., Veefkind, P., 2018. Algorithm theoretical baseline for formaldehyde retrievals from S5P TROPOMI and from the QA4ECV project. Atmospheric Measurement Techniques 11(4), 2395–2426.

Denman, K.L., Brasseur, G., Chidthaisong, A., Ciais, P., Cox, P.M.M., Dickinson, R.E.E., Hauglustaine, D., Heinze, C., Holland, E., Jacob, D., Lohmann, U., Ramachandran, S., Leite da Silva Dias, P., Wofsy, S.C.C., Zhang, X., Arora, V., Baker, D., Bonan, G., Bousquet, P., Canadell, J., Christian, J., Clark, D.A., Dameris, M.,

Dentener, F., Easterling, D., Eyring, V., Feichter, J., Friedlingstein, P., Fung, I., Fuzzi, S., Gong, S., Gruber, N., Guenther, A., Gurney, K., Henderson-Sellers, A., House, J., Jones, A., Jones, C., Kärcher, B., Kawamiya, M., Lassey, K., Le Quéré, C., Leck, C., Lee-Taylor, J., Malhi, Y., Masarie, K., Mcfiggans, G., Menon, S., Miller, J.B., Peylin, P., Pitman, A., Quaas, J., Raupach, M., Rayner, P., Rehder, G., Riebesell, U., Rödenbeck, C., Rotstayn, L., Roulet, N., Sabine, C., Schultz, M.G., Schulz, M., Schwartz, S.E., Steffen, W., Stevenson, D., Tian, Y., Trenberth, K.E., Van Noije, T., Wild, O., Zhang, T., Zhou, L., 2007. Couplings between changes in the climate system and biogeochemistry. Technical Report. Lawrence Berkeley National Lab (LBNL), Berkeley, CA (United States).

Di Gregorio, A., 2005. Land cover classification system: classification concepts and user manual: LCCS. volume 3. UN Food and Agriculture Organisation.

Douros, J., Eskes, H., van Geffen, J., Boersma, K.F., Compernolle, S., Pinardi, G., Blechschmidt, A.M., Peuch, V.H., Colette, A., Veefkind, P., 2023. Comparing Sentinel-5P TROPOMI NO_2 column observations with the CAMS regional air quality ensemble. Geoscientific Model Development 16, 509–534.

Dufour, G., Eremenko, M., Siour, G., Sellitto, P., Cuesta, J., Perrin, A., Beekmann, M., 2022. 24 h Evolution of an Exceptional HONO Plume Emitted by the Record-Breaking 2019/2020 Australian Wildfire Tracked from Space. Atmosphere 13, 1485.

Eisinger, M., Burrows, J.P., 1998. Tropospheric sulfur dioxide observed by the ERS-2 GOME instrument. Geophysical Research Letters 25, 4177–4180.

Engelhart, G.J., Hennigan, C.J., Miracolo, M.A., Robinson, A.L., Pandis, S.N., 2012. Cloud condensation nuclei activity of fresh primary and aged biomass burning aerosol. Atmospheric Chemistry and Physics 12, 7285–7293.

ESA, 2017. European Space Agency. Land Cover CCI Product User Guide Version 2. http://maps.elie.ucl.ac.be/CCI/viewer/download/ESACCI-LC-Ph2-PUGv2_2.0.pdf. Last Accessed: 24 November 2024.

ESA, 2022. European Space Agency. ESA/CCI Viewer. https://maps.elie.ucl.ac.be/CCI/viewer/index.php. Last Accessed: 24 November 2024.

ESA, 2023. European Space Agency. S5P Mission Performance Centre Carbon Monoxide Readme. https://sentinels.copernicus.eu/documents/247904/3541451/Sentinel-5P-Carbon-Monoxide-Level-2-Product-Readme-File. Last Accessed: 28 September 2025.

ESA, 2024a. European Space Agency. Aerosol Layer Height Validation Summary. https://mpc-vdaf.tropomi.eu/index.php/aerosols?start=2. Last Accessed: 24 November 2024.

ESA, 2024b. European Space Agency. Carbon Monoxide Validation Summary. https://mpc-vdaf.tropomi.eu/index.php/carbon-monoxide. Last Accessed: 24 November 2024.

ESA, 2024c. European Space Agency. ESA Climate Change Initiative Land Cover. https://maps.elie.ucl.ac.be/CCI/viewer/index.php. Last Accessed: 1 November 2024.

ESA, 2024d. European Space Agency. Formaldehyde Validation Summary. https://mpc-vdaf.tropomi.eu/index.php/formaldehyde. Last Accessed: 24 November 2024.

ESA, 2024e. European Space Agency. Nitrogen Dioxide Validation Summary. https://mpc-vdaf.tropomi.eu/index.php/nitrogen-dioxide. Last Accessed: 24 November 2024.

ESA, 2024f. European Space Agency. S5P Mission. https://sentiwiki.copernicus.eu/web/s5p-mission. Last Accessed: 24 November 2024.

ESA, 2025. European Space Agency. Copernicus Sentinel-5P Mapping Portal. https://maps.s5p-pal.com/co/season/. Last Accessed: 21 September 2025.

European Commission, 2023. Global Land Cover 2000. https://forobs.jrc.ec.europa.eu/glc2000. Last Accessed: 7 July 2023.

European Commission, 2025. Global Land Cover 2000. https://forobs.jrc.ec.europa.eu/glc2000. Last Accessed: 6 January 2025.

Finlayson-Pitts, B., Pitts Jr, J., 1993. Atmospheric chemistry of tropospheric ozone formation: scientific and regulatory implications. Air and Waste 43(8), 1091–1100.

Fioletov, V.E., McLinden, C.A., Krotkov, N., Yang, K., Loyola, D.G., Valks, P., Theys, N., Van Roozendael, M., Nowlan, C.R., Chance, K., Liu, X., Lee, C., Martin, R.V., 2013. Application of OMI, SCIAMACHY, and GOME-2 satellite SO_2 retrievals for detection of large emission sources. Journal of Geophysical Research: Atmospheres 118, 11399–11418.

Fiore, A., Oberman, J., Lin, M., Zhang, L., Clifton, O., Jacob, D., Naik, V., Horowitz, L., Pinto, J., Milly, G., 2014. Estimating North American background ozone in U.S. surface air with two independent global models: Variability, uncertainties, and recommendations. Atmospheric Environment 96, 284–300.

Fischer, E.V., Jacob, D.J., Yantosca, R.M., Sulprizio, M.P., Millet, D.B., Mao, J., Paulot, F., Singh, H.B., Roiger, A., Ries, L., Talbot, R., Dzepina, K., Pandey Deolal, S., 2014. Atmospheric peroxyacetyl nitrate (PAN): a global budget and source attribution. Atmospheric Chemistry and Physics 14(5), 2679–2698.

Flood, V.A., Strong, K., Buchholz, R.R., Kuiper, G., Magzamen, S., 2025a. Assessing the impact of wildfire emissions on the seasonal cycle of CO and emergency room visits in Alberta and Ontario, Canada. GeoHealth 9(9), e2024GH001317.

Flood, V.A., Strong, K., Whaley, C.H., Chen, J., Wunch, D., Drummond, J.R., Colebatch, O., Gillespie, L., Mostafavi Pak, N., 2025b. The Impact of the 2023 Canadian Forest Fires on Air Quality in Southern Ontario. Journal of Geophysical Research: Atmospheres 130(5), e2024JD042254.

Fowler, D., Amann, M., Anderson, R., Ashmore, M., Cox, P., Depledge, M., Derwent, D., Grennfelt, P., Hewitt, N., Hov, O., Jenkin, M., Kelly, F., Liss, P., Pilling, M., Pyle, J., Slingo, J., Stevenson, D., 2008. Ground-level ozone in the 21st century: future trends, impacts and policy implications. The Royal Society, RS Policy document 15/08.

Franco, B., Clarisse, L., Stavrakou, T., Müller, J., Van Damme, M., Whitburn, S., Hadji-Lazaro, J., Hurtmans, D., Taraborrelli, D., Clerbaux, C., Coheur, P., 2018. A General Framework for Global Retrievals of Trace Gases From IASI: Application to Methanol, Formic Acid, and PAN. Journal of Geophysical Research: Atmospheres 123, 13963–13984.

Franco, B., Clarisse, L., Theys, N., Hadji-Lazaro, J., Clerbaux, C., Coheur, P., 2024. Pyrogenic HONO seen from space: insights from global IASI observations. Atmospheric Chemistry and Physics 24, 4973–5007.

Fredrickson, C., Theys, N., Thornton, J., 2023. Satellite evidence of HONO/NO_2 increase with fire radiative power. Geophysical Research Letters 50(17), e2023GL103836.

Fredrickson, C.D., Theys, N., Thornton, J.A., 2023. Satellite Evidence of HONO/NO_2 Increase With Fire Radiative Power. Geophysical Research Letters 50, e2023GL103836.

Freeborn, P.H., Wooster, M.J., Hao, W.M., Ryan, C.A., Nordgren, B.L., Baker, S.P., Ichoku, C., 2008. Relationships between energy release, fuel mass loss, and trace gas and aerosol emissions during laboratory biomass fires. Journal of Geophysical Research: Atmospheres 113, D01301.

Fu, T.M., Jacob, D.J., Palmer, P.I., Chance, K., Wang, Y.X., Barletta, B., Blake, D.R., Stanton, J.C., Pilling, M.J., 2007. Space-based formaldehyde measurements as constraints on volatile organic compound emissions in east and south Asia and implications for ozone. Journal of Geophysical Research: Atmospheres 112, D06312.

Gao, Y., Huang, W., Yu, P., Xu, R., Yang, Z., Gasevic, D., Ye, T., Guo, Y., Li, S., 2023. Long-term impacts of non-occupational wildfire exposure on human health: A systematic review. Environmental Pollution 320, 121041.

van Geffen, J., Eskes, H., Boersma, K., Maasakkers, J., Veefkind, J., 2019. TROPOMI ATBD of the total and tropospheric NO_2 data products, version 1.4. https://sentinel.esa.int/documents/247904/2476257/Sentinel-5P-TROPOMI-ATBD-NO2-data-products.pdf/7a4fdde7-516e-48e7-bf44-da60c62b1e4d?version=1.4. Last Accessed: 24 November 2024.

Giglio, L., Schroeder, W., Hall, J., Justice, C., 2021. MODIS Collection 6 and Collection 6.1 Active Fire Product User's Guide, version 1.0. https://modis-fire.umd.edu/files/MODIS_C6_C6.1_Fire_User_Guide_1.0.pdf. Last Accessed: 24 November 2024.

Gkatzelis, G.I., Coggon, M.M., Stockwell, C.E., Hornbrook, R.S., Allen, H., Apel, E.C., Bela, M.M., Blake, D.R., Bourgeois, I., Brown, S.S., Campuzano-Jost, P., St. Clair, J.M., Crawford, J.H., Crounse, J.D., Day, D.A., DiGangi, J.P., Diskin, G.S., Fried, A., Gilman, J.B., Guo, H., Hair, J.W., Halliday, H.S., Hanisco, T.F., Hannun, R., Hills, A., Huey, L.G., Jimenez, J.L., Katich, J.M., Lamplugh, A., Lee, Y.R., Liao, J., Lindaas, J., McKeen, S.A., Mikoviny, T., Nault, B.A., Neuman, J.A., Nowak, J.B., Pagonis, D., Peischl, J., Perring, A.E., Piel, F., Rickly, P.S., Robinson, M.A., Rollins, A.W., Ryerson, T.B., Schueneman, M.K., Schwantes, R.H., Schwarz, J.P., Sekimoto, K., Selimovic, V., Shingler, T., Tanner, D.J., Tomsche, L., Vasquez, K.T., Veres, P.R., Washenfelder, R., Weibring, P., Wennberg, P.O., Wisthaler, A., Wolfe, G.M., Womack, C.C., Xu, L., Ball, K., Yokelson, R.J., Warneke, C., 2024. Parameterizations of US wildfire and prescribed fire emission ratios and emission factors based on FIREX-AQ aircraft measurements. Atmospheric Chemistry and Physics 24(2), 929–956.

Goode, J.G., Yokelson, R.J., Ward, D.E., Susott, R.A., Babbitt, R.E., Davies, M.A., Hao, W.M., 2000. Measurements of excess O_3, CO_2, CO, CH_4, C_2H_4, C_2H_2, HCN,

NO, NH_3, HCOOH, CH_3COOH, HCHO, and CH_3OH in 1997 Alaskan biomass burning plumes by airborne Fourier transform infrared spectroscopy (AFTIR). Journal of Geophysical Research: Atmospheres 105, D17, 22147–22166.

de Graaf, M., de Haan, J., Sanders, A., 2022. TROPOMI ATBD of the Aerosol Layer Height, issue 2.4.0. https://sentinels.copernicus.eu/documents/247904/2476257/Sentinel-5P-TROPOMI-ATBD-Aerosol-Height.pdf/3c7910e4-f575-4485-bb1f-a72331eecd8e. Last Accessed: 24 November 2024.

Griffin, D., Chen, J., Anderson, K., Makar, P., McLinden, C.A., Dammers, E., Fogal, A., 2024. Biomass burning CO emissions: exploring insights through TROPOMI-derived emissions and emission coefficients. Atmospheric Chemistry and Physics 24(17), 10159–10186.

Griffin, D., McLinden, C.A., Dammers, E., Adams, C., Stockwell, C.E., Warneke, C., Bourgeois, I., Peischl, J., Ryerson, T.B., Zarzana, K.J., Rowe, J.P., Volkamer, R., Knote, C., Kille, N., Koenig, T.K., Lee, C.F., Rollins, D., Rickly, P.S., Chen, J., Fehr, L., Bourassa, A., Degenstein, D., Hayden, K., Mihele, C., Wren, S.N., Liggio, J., Akingunola, A., Makar, P., 2021. Biomass burning nitrogen dioxide emissions derived from space with TROPOMI: methodology and validation. Atmospheric Measurement Techniques 14(12), 7929–7957.

Griffin, D., Sioris, C., Chen, J., Dickson, N., Kovachik, A., de Graaf, M., Nanda, S., Veefkind, P., Dammers, E., McLinden, C.A., Makar, P., Akingunola, A., 2020. The 2018 fire season in North America as seen by TROPOMI: aerosol layer height intercomparisons and evaluation of model-derived plume heights. Atmospheric Measurement Techniques 13(3), 1427–1445.

Griffin, D., Zhao, X., McLinden, C.A., Boersma, F., Bourassa, A., Dammers, E., Degenstein, D., Eskes, H., Fehr, L., Fioletov, V., Hayden, K., Kharol, S.K., Li, S., Makar, P., Martin, R.V., Mihele, C., Mittermeier, R.L., Krotkov, N., Sneep, M., Lamsal, L.N., Linden, M.t., Geffen, J.v., Veefkind, P., Wolde, M., 2019. High-

resolution mapping of nitrogen dioxide with TROPOMI: First results and validation over the Canadian oil sands. Geophysical Research Letters 46, 1049–1060.

Gualtieri, G., 2022. Analysing the uncertainties of reanalysis data used for wind resource assessment: A critical review. Renewable and Sustainable Energy Reviews 167, 112741.

Hahn, M., Kuiper, G., O'Dell, K., Fischer, E., Magzamen, S., 2021. Wildfire smoke is associated with an increased risk of cardiorespiratory emergency department visits in Alaska. GeoHealth 5(5), e2020GH000349.

Hair, J.W., Hostetler, C.A., Cook, A.L., Harper, D.B., Ferrare, R.A., Mack, T.L., Welch, W., Izquierdo, L.R., Hovis, F.E., 2008. Airborne high spectral resolution lidar for profiling aerosol optical properties. Applied Optics 47(36), 6734–6752.

Hall, J., Schroeder, W., Rishmawi, K., Wooster, M., Schmidt, C., Huang, C., Csiszar, I., Giglio, L., 2023. Geostationary active fire products validation: GOES-17 ABI, GOES-16 ABI, and Himawari AHI. International Journal of Remote Sensing 44(10), 3174–3193.

Harriss, R.C., Wofsy, S.C., Hoell, J.M., Bendura, R.J., Drewry, J.W., McNeal, R.J., Pierce, D., Rabine, V., Snell, R.L., 1994. The Arctic Boundary Layer Expedition (ABLE-3B): July–August 1990. Journal of Geophysical Research: Atmospheres 99, 1635–1643.

Hayden, K.L., Li, S.M., Liggio, J., Wheeler, M.J., Wentzell, J.J.B., Leithead, A., Brickell, P., Mittermeier, R.L., Oldham, Z., Mihele, C.M., Staebler, R.M., Moussa, S.G., Darlington, A., Wolde, M., Thompson, D., Chen, J., Griffin, D., Eckert, E., Ditto, J.C., He, M., Gentner, D.R., 2022. Reconciling the total carbon budget for boreal forest wildfire emissions using airborne observations. Atmospheric Chemistry and Physics 22(18), 12493–12523.

Hearne, T., Griffin, D., Stockwell, C., Hung, J., Fried, A., Peischl, J., Bourgeois, I., Toshiko Moser, S., Strong, K., 2025a. Replication Data for: Summer 2023

Canadian Boreal Forest Wildfires: An Analysis of CO, HCHO, and NO_2 Downwind Enhancement Rates. Borealis, V1. doi:https://doi.org/10.5683/SP3/2RRB4Q.

Hearne, T., Griffin, D., Stockwell, C., Hung, J., Fried, A., Peischl, J., Bourgeois, I., Toshiko Moser, S., Strong, K., 2025b. Summer 2023 Canadian Boreal Forest Wildfires: An Analysis of CO, HCHO, and NO_2 Downwind Enhancement Rates. Submitted to Journal of Geophysical Research: Atmospheres.

Hearne, T., Griffin, D., Strong, K., 2026. Replication Data for: Canadian 2023 and 2025 Boreal Forest Wildfires: Downwind Formaldehyde to Nitrogen Dioxide Ratios and Implications for Surface Ozone Production. Borealis, V1. doi:https://doi.org/10.5683/SP3/CJLVQ6.

Hersbach, H., Bell, B., Berrisford, P., Hirahara, S., Horányi, A., Muñoz-Sabater, J., Nicolas, J., Peubey, C., Radu, R., Schepers, D., Simmons, A., Soci, C., Abdalla, S., Abellan, X., Balsamo, G., Bechtold, P., Biavati, G., Bidlot, J., Bonavita, M., De Chiara, G., Dahlgren, P., Dee, D., Diamantakis, M., Dragani, R., Flemming, J., Forbes, R., Fuentes, M., Geer, A., Haimberger, L., Healy, S., Hogan, R.J., Hólm, E., Janisková, M., Keeley, S., Laloyaux, P., Lopez, P., Lupu, C., Radnoti, G., de Rosnay, P., Rozum, I., Vamborg, F., Villaume, S., Thépaut, J., 2020. The ERA5 global reanalysis. Quarterly Journal of the Royal Meteorological Society 146(730), 1999–2049.

Hu, W., Yang, J., 2024. Effect of ambient ozone pollution on disease burden globally: A systematic analysis for the global burden of disease study 2019. Science of the Total Environment 926, 171739.

Hua, Q., Meng, X., Gong, J., Qiu, X., Shang, J., Xue, T., Zhu, T., 2025. Ozone exposure and cardiovascular disease: A narrative review of epidemiology evidence and underlying mechanisms. Fundamental Research 5(1), 249–263.

Ichoku, C., Kaufman, Y., 2005. A method to derive smoke emission rates from MODIS fire radiative energy measurements. IEEE Transactions on Geoscience and Remote Sensing 43(11), 2636–2649.

IPCC, 2023. Climate Change 2023: Synthesis Report. Contribution of Working Groups I, II and III to the Sixth Assessment Report of the Intergovernmental Panel on Climate Change [Core Writing Team, H. Lee and J. Romero (eds.)]. IPCC, Geneva, Switzerland. 184 pp. doi:10.59327/IPCC/AR6-9789291691647.

Isidorov, V.A., Pirożnikow, E., Spirina, V.L., Vasyanin, A.N., Kulakova, S.A., Abdulmanova, I.F., Zaitsev, A.A., 2022. Emission of volatile organic compounds by plants on the floor of boreal and mid-latitude forests. Journal of Atmospheric Chemistry 79(3), 153–166.

Jacob, D.J., 1999. Introduction to Atmospheric Chemistry. Princeton University Press.

Jain, P., Barber, Q.E., Taylor, S., Whitman, E., Acuna, D.C., Boulanger, Y., Chavardès, R.D., Chen, J., Englefield, P., Flannigan, M., Girardin, M.P., Hanes, C.C., Little, J., Morrison, K., Skakun, R.S., Thompson, D.K., Wang, X., Parisien, M.A., 2024. Drivers and impacts of the record-breaking 2023 wildfire season in Canada. Nature Communications 15, 6764.

Jin, X., Fiore, A., Boersma, K.F., Smedt, I.D., Valin, L., 2020. Inferring changes in summertime surface Ozone–NO_x–VOC chemistry over US urban areas from two decades of satellite and ground-based observations. Environmental Science and Technology 54(11), 6518–6529.

Jin, X., Zhu, Q., Cohen, R.C., 2021. Direct estimates of biomass burning NO_x emissions and lifetimes using daily observations from TROPOMI. Atmospheric Chemistry and Physics 21(20), 15569–15587.

Juncosa Calahorrano, J.F., Payne, V.H., Kulawik, S., Ford, B., Flocke, F., Campos, T., Fischer, E.V., 2021. Evolution of Acyl Peroxynitrates (PANs) in Wildfire Smoke Plumes Detected by the Cross-Track Infrared Sounder (CrIS) Over the Western U.S. During Summer 2018. Geophysical Research Letters 48, e2021GL093405.

Kaiser, J., Jacob, D.J., Zhu, L., Travis, K.R., Fisher, J.A., González Abad, G., Zhang, L., Zhang, X., Fried, A., Crounse, J.D., St. Clair, J.M., Wisthaler, A., 2018. High-resolution inversion of OMI formaldehyde columns to quantify isoprene emission on ecosystem-relevant scales: application to the southeast US. Atmospheric Chemistry and Physics 18(8), 5483–5497.

Kaufman, Y.J., Justice, C.O., Flynn, L.P., Kendall, J.D., Prins, E.M., Giglio, L., Ward, D.E., Menzel, W.P., Setzer, A.W., 1998. Potential global fire monitoring from EOS-MODIS. Journal of Geophysical Research: Atmospheres 103, D24, 32215–32238.

Kirchmeier-Young, M., Gillett, N., Zwiers, F., Cannon, A., Anslow, F., 2019. Attribution of the influence of human-induced climate change on an extreme fire season. Earth's Future 7(1), 2–10.

Koelemeijer, R.B.A., de Haan, J.F., Stammes, P., 2003. A database of spectral surface reflectivity in the range 335–772 nm derived from 5.5 years of GOME observations. Journal of Geophysical Research: Atmospheres 108, 4070.

Konovalov, I.B., Berezin, E.V., Ciais, P., Broquet, G., Zhuravlev, R.V., Janssens-Maenhout, G., 2016. Estimation of fossil-fuel CO_2 emissions using satellite measurements of p̈roxyp̈ecies. Atmospheric Chemistry and Physics 16, 13509–13540.

Koumpagioti, D., Dimitroglou, M., Mpoutopoulou, B., Moriki, D., Douros, K., 2025. The Role of Oxidative Stress in the Pathogenesis of Childhood Asthma: A Comprehensive Review. Children 12(9), 1110.

Lama, S., Houweling, S., Boersma, K.F., Eskes, H., Aben, I., Denier van der Gon, H.A.C., Krol, M.C., Dolman, H., Borsdorff, T., Lorente, A., 2020. Quantifying burning efficiency in megacities using the NO_2/CO ratio from the Tropospheric Monitoring Instrument (TROPOMI). Atmospheric Chemistry and Physics 20, 10295–10310.

Lambert, J.C., Keppens, A., Compernolle, S., Eichmann, K.U., de Graaf, M., Hubert, D., Langerock, B., Ludewig, A., Sha, M., Verhoelst, T., Wagner, T., Ahn, C., Argyrouli, A., Balis, D., Chan, K., Coldewey-Egbers, M., De Smedt, I., Eskes, H., Fjæraa, A., Garane, K., Gleason, J., Goutail, F., Granville, J., Hedelt, P., Heue, K.P., Jaross, G., Kleipool, Q., Koukouli, M., Lutz, R., Martinez Velarte, M., Michailidis, K., Pseftogkas, A., Nanda, S., Niemeijer, S., Pazmiño, A., Pinardi, G., Richter, A., Rozemeijer, N., Sneep, M., Stein Zweers, D., Theys, N., Tilstra, G., Torres, O., Valks, P., van Geffen, J., Vigouroux, C., Wang, P., Weber, M., 2024. Quarterly Validation Report of the Sentinel-5 Precursor Operational Data Products 24: April 2018 - August 2024. https://mpc-vdaf.tropomi.eu/ProjectDir/reports//pdf/S5P-MPC-IASB-ROCVR-24.00.00_FINAL_signed.pdf. Last Accessed: 24 November 2024.

Levelt, P., van den Oord, G., Dobber, M., Malkki, A., Visser, H., de Vries, J., Stammes, P., Lundell, J., Saari, H., 2006. The ozone monitoring instrument. IEEE Transactions on Geoscience and Remote Sensing 44, 1093–1101.

Li, F., Zhang, X., Kondragunta, S., Lu, X., 2020. An evaluation of advanced baseline imager fire radiative power based wildfire emissions using carbon monoxide observed by the Tropospheric Monitoring Instrument across the conterminous United States. Environmental Research Letters 15(9), 094049.

Li, F., Zhang, X., Roy, D.P., Kondragunta, S., 2019. Estimation of biomass-burning emissions by fusing the fire radiative power retrievals from polar-orbiting and geostationary satellites across the conterminous United States. Atmospheric Environment 211, 274–287.

Liao, J., Wolfe, G.M., Hannun, R.A., St. Clair, J.M., Hanisco, T.F., Gilman, J.B., Lamplugh, A., Selimovic, V., Diskin, G.S., Nowak, J.B., Halliday, H.S., DiGangi, J.P., Hall, S.R., Ullmann, K., Holmes, C.D., Fite, C.H., Agastra, A., Ryerson, T.B., Peischl, J., Bourgeois, I., Warneke, C., Coggon, M.M., Gkatzelis, G.I., Sekimoto, K., Fried, A., Richter, D., Weibring, P., Apel, E.C., Hornbrook, R.S., Brown, S.S.,

Womack, C.C., Robinson, M.A., Washenfelder, R.A., Veres, P.R., Neuman, J.A., 2021. Formaldehyde evolution in US wildfire plumes during the Fire Influence on Regional to Global Environments and Air Quality experiment (FIREX-AQ). Atmospheric Chemistry and Physics 21, 18319–18331.

Lin, M., Horowitz, L.W., Hu, L., Permar, W., 2024. Reactive Nitrogen Partitioning Enhances the Contribution of Canadian Wildfire Plumes to US Ozone Air Quality. Geophysical Research Letters 51, e2024GL109369.

Lin, Y.C., Cheng, M.T., 2007. Evaluation of formation rates of NO_2 to gaseous and particulate nitrate in the urban atmosphere. Atmospheric Environment 41, 1903–1910.

Lindaas, J., Pollack, I.B., Garofalo, L.A., Pothier, M.A., Farmer, D.K., Kreidenweis, S.M., Campos, T.L., Flocke, F., Weinheimer, A.J., Montzka, D.D., Tyndall, G.S., Palm, B.B., Peng, Q., Thornton, J.A., Permar, W., Wielgasz, C., Hu, L., Ottmar, R.D., Restaino, J.C., Hudak, A.T., Ku, I., Zhou, Y., Sive, B.C., Sullivan, A., Collett, J.L., Fischer, E.V., 2021. Emissions of reactive nitrogen from western US wildfires during Summer 2018. Journal of Geophysical Research: Atmospheres 126, e2020JD032657.

Liu, Y., Heilman, W.E., Potter, B.E., Clements, C.B., Jackson, W.A., French, N.H.F., Goodrick, S.L., Kochanski, A.K., Larkin, N.K., Lahm, P.W., Brown, T.J., Schwarz, J.P., Strachan, S.M., Zhao, F., 2022. Smoke Plume Dynamics. Springer International Publishing. p. 83–119.

Lutsch, E., Dammers, E., Conway, S., Strong, K., 2016. Long-range transport of NH_3, CO, HCN, and C_2H_6 from the 2014 Canadian wildfires. Geophysical Research Letters 43(15), 8286–8297.

Magaritz-Ronen, L., Raveh-Rubin, S., 2021. Wildfire smoke highlights troposphere-to-stratosphere pathway. Geophysical Research Letters 48(23), e2021GL095848.

Magzamen, S., Gan, R.W., Liu, J., O'Dell, K., Ford, B., Berg, K., Bol, K., Wilson, A., Fischer, E.V., Pierce, J.R., 2021. Differential cardiopulmonary health impacts of local and long-range transport of wildfire smoke. GeoHealth 5(3), e2020GH000330.

Mahsin, M., Cabaj, J., Saini, V., 2022. Respiratory and cardiovascular condition-related physician visits associated with wildfire smoke exposure in Calgary, Canada, in 2015: a population-based study. International Journal of Epidemiology 51(1), 166–178.

Mäki, M., Aaltonen, H., Heinonsalo, J., Hellén, H., Pumpanen, J., Bäck, J., 2019. Boreal forest soil is a significant and diverse source of volatile organic compounds. Plant and Soil 441, 89–110.

Marais, E.A., Jacob, D.J., Guenther, A., Chance, K., Kurosu, T., Murphy, J., Reeves, C., Pye, H., 2014. Improved model of isoprene emissions in Africa using Ozone Monitoring Instrument (OMI) satellite observations of formaldehyde: implications for oxidants and particulate matter. Atmospheric Chemistry and Physics 14(15), 7693–7703.

Martin, I., Velasco, A., Lavin, C., Olalla, E., Bustos, E., 2001. Photoabsorption processes in nitrous oxide and formaldehyde. International Journal of Quantum Chemistry 85(4-5), 345–353.

Martínez-Alonso, S., Deeter, M., Worden, H., Borsdorff, T., Aben, I., Commane, R., Daube, B., Francis, G., George, M., Landgraf, J., Mao, D., McKain, K., Wofsy, S., 2020. 1.5 years of TROPOMI CO measurements: comparisons to MOPITT and ATom. Atmospheric Measurement Techniques 13, 4841–4864.

Matz, C.J., Egyed, M., Xi, G., Racine, J., Pavlovic, R., Rittmaster, R., Henderson, S.B., Stieb, D.M., 2020. Health impact analysis of PM2.5 from wildfire smoke in Canada (2013–2015, 2017–2018). Science of the Total Environment 725, 138506.

McMeeking, G.R., Kreidenweis, S.M., Baker, S., Carrico, C.M., Chow, J.C., Collett, J.L., Hao, W.M., Holden, A.S., Kirchstetter, T.W., Malm, W.C., Moosmüller, H.,

Sullivan, A.P., Wold, C.E., 2009. Emissions of trace gases and aerosols during the open combustion of biomass in the laboratory. Journal of Geophysical Research: Atmospheres 114, D19210.

Mebust, A., Russell, A., Hudman, R., Valin, L., Cohen, R., 2011. Characterization of Wildfire NO_x Emissions Using MODIS Fire Radiative Power and OMI Tropospheric NO_2 Columns. Atmospheric Chemistry and Physics 11(12), 5839–5851.

Menzel, W.P., Purdom, J.F., 1994. Introducing goes-i: The first of a new generation of geostationary operational environmental satellites. Bulletin of the American Meteorological Society 75(5), 757–782.

Mettig, N., Weber, M., Rozanov, A., Arosio, C., Burrows, J.P., Veefkind, P., Thompson, A.M., Querel, R., Leblanc, T., Godin-Beekmann, S., Kivi, R., Tully, M.B., 2021. Ozone profile retrieval from nadir TROPOMI measurements in the UV range. Atmospheric Measurement Techniques 14(9), 6057–6082.

Michail, N.A., Savva, C.S., Koursaros, D., Zachariadis, T., 2019. Anthropogenic greenhouse gas concentrations and global temperature: a smooth transition analysis. SN Applied Sciences 1, 1–15.

Millet, D.B., Jacob, D.J., Boersma, K.F., Fu, T.M., Kurosu, T.P., Chance, K., Heald, C.L., Guenther, A., 2008. Spatial distribution of isoprene emissions from North America derived from formaldehyde column measurements by the OMI satellite sensor. Journal of Geophysical Research: Atmospheres 113, D2, 1–18.

Nanda, S., De Graaf, M., Veefkind, J.P., Ter Linden, M., Sneep, M., De Haan, J., Levelt, P.F., 2019. A neural network radiative transfer model approach applied to the Tropospheric Monitoring Instrument aerosol height algorithm. Atmospheric Measurement Techniques 12(12), 6619–6634.

NASA, 2024a. National Aeronautics and Space Administration. NASA Worldview. https://worldview.earthdata.nasa.gov/. Last Accessed: 24 November 2024.

NASA, 2024b. National Aeronautics and Space Administration. TROPOMI | NASA Earthdata. https://www.earthdata.nasa.gov/data/instruments/tropomi. Last Accessed: 24 November 2024.

NASA, 2025. National Aeronautics and Space Administration. MCD12C1 - MODIS/Terra+Aqua Land Cover Type Yearly L3 Global 0.05Deg CMG. https://ladsweb.modaps.eosdis.nasa.gov/missions-and-measurements/products/MCD12C1/#overview. Last Accessed: 10 November 2025.

NOAA, 2023. National Oceanic and Atmospheric Administration. GOES Schedules and Scan Sectors - Office of Satellite and Product Operations. https://ospo.noaa.gov/Operations/GOES/schedules.html. Last Accessed: 20 November 2023.

NOAA, 2025. National Oceanic and Atmospheric Administration. Geostationary Extended Observations (GeoXO) | NESDIS. https://www.nesdis.noaa.gov/our-satellites/future-programs/geostationary-extended-observations-geoxo/. Last Accessed: 16 October 2025.

NOAA, 2025. National Oceanic and Atmospheric Administration. GOES History. https://www.goes-r.gov/mission/history.html. Last Accessed: 24 June 2025.

Nowroz, F., Hasanuzzaman, M., Siddika, A., Parvin, K., Caparros, P.G., Nahar, K., Prasad, P.V., 2024. Elevated tropospheric ozone and crop production: potential negative effects and plant defense mechanisms. Frontiers in Plant Science 14, 1244515.

NRCan, 2025a. Natural Resources Canada. Canadian Wildland Fire Information System | Canadian National Fire Database (CNFDB). https://cwfis.cfs.nrcan.gc.ca/ha/nfdb. Last Accessed: 21 September 2023.

NRCan, 2025b. Natural Resources Canada. Fire Monitoring, Mapping, and Modeling (Fire M3) data set. https://cwfis.cfs.nrcan.gc.ca/downloads/hotspots/. Last Accessed: 8 November 2025.

Palmer, P.I., Parrington, M., Lee, J.D., Lewis, A.C., Rickard, A.R., Bernath, P.F., Duck, T.J., Waugh, D.L., Tarasick, D.W., Andrews, S., Aruffo, E., Bailey, L.J., Barrett, E., Bauguitte, S.J.B., Curry, K.R., Di Carlo, P., Chisholm, L., Dan, L., Forster, G., Franklin, J.E., Gibson, M.D., Griffin, D., Helmig, D., Hopkins, J.R., Hopper, J.T., Jenkin, M.E., Kindred, D., Kliever, J., Le Breton, M., Matthiesen, S., Maurice, M., Moller, S., Moore, D.P., Oram, D.E., O'Shea, S.J., Owen, R.C., Pagniello, C.M.L.S., Pawson, S., Percival, C.J., Pierce, J.R., Punjabi, S., Purvis, R.M., Remedios, J.J., Rotermund, K.M., Sakamoto, K.M., da Silva, A.M., Strawbridge, K.B., Strong, K., Taylor, J., Trigwell, R., Tereszchuk, K.A., Walker, K.A., Weaver, D., Whaley, C., Young, J.C., 2013. Quantifying the impact of BOReal forest fires on Tropospheric oxidants over the Atlantic using Aircraft and Satellites (BORTAS) experiment: design, execution and science overview. Atmospheric Chemistry and Physics 13, 6239–6261.

Parrington, M., Palmer, P.I., Henze, D.K., Tarasick, D.W., Hyer, E.J., Owen, R.C., Helmig, D., Clerbaux, C., Bowman, K.W., Deeter, M.N., Barratt, E.M., Coheur, P.F., Hurtmans, D., Jiang, Z., George, M., Worden, J.R., 2012. The influence of boreal biomass burning emissions on the distribution of tropospheric ozone over North America and the North Atlantic during 2010. Atmospheric Chemistry and Physics 12, 2077–2098.

Parrington, M., Palmer, P.I., Lewis, A.C., Lee, J.D., Rickard, A.R., Di Carlo, P., Taylor, J.W., Hopkins, J.R., Punjabi, S., Oram, D.E., Forster, G., Aruffo, E., Moller, S.J., Bauguitte, S.J.B., Allan, J.D., Coe, H., Leigh, R.J., 2013. Ozone photochemistry in boreal biomass burning plumes. Atmospheric Chemistry and Physics 13, 7321–7341.

Paugam, R., Wooster, M., Freitas, S., Val Martin, M., 2016. A review of approaches to estimate wildfire plume injection height within large-scale atmospheric chemical transport models. Atmospheric Chemistry and Physics 16(2), 907–925.

Payne, V.H., Kulawik, S.S., Fischer, E.V., Brewer, J.F., Huey, L.G., Miyazaki, K.,

Worden, J.R., Bowman, K.W., Hintsa, E.J., Moore, F., Elkins, J.W., Juncosa Calahorrano, J., 2022. Satellite measurements of peroxyacetyl nitrate from the Cross-Track Infrared Sounder: comparison with ATom aircraft measurements. Atmospheric Measurement Techniques 15, 3497–3511.

Plummer, S., Lecomte, P., Doherty, M., 2017. The ESA Climate Change Initiative (CCI): A European Contribution to the Generation of the Global Climate Observing System. Remote Sensing of Environment 203, 2–8.

Pope, F.D., Smith, C.A., Davis, P.R., Shallcross, D.E., Ashfold, M.N., Orr-Ewing, A.J., 2005. Photochemistry of formaldehyde under tropospheric conditions. Faraday Discussions 130, 59–72.

Province of British Columbia, 2023. Wildfire Averages - Province of British Columbia. https://www2.gov.bc.ca/gov/content/safety/wildfire-status/about-bcws/wildfire-statistics/wildfire-averages. Last Accessed: 7 July 2023.

Raub, J., 1999. Health effects of exposure to ambient carbon monoxide. Chemosphere-Global Change Science 1(1-3), 331–351.

Roberts, G.J., Wooster, M.J., 2008. Fire Detection and Fire Characterization Over Africa Using Meteosat SEVIRI. IEEE Transactions on Geoscience and Remote Sensing 46(4), 1200–1218.

Roberts, J.M., Stockwell, C.E., Yokelson, R.J., de Gouw, J., Liu, Y., Selimovic, V., Koss, A.R., Sekimoto, K., Coggon, M.M., Yuan, B., Zarzana, K.J., Brown, S.S., Santin, C., Doerr, S.H., Warneke, C., 2020. The nitrogen budget of laboratory-simulated western US wildfires during the FIREX 2016 Fire Lab study. Atmospheric Chemistry and Physics 20(14), 8807–8826.

Robinson, M.A., Decker, Z.C.J., Barsanti, K.C., Coggon, M.M., Flocke, F.M., Franchin, A., Fredrickson, C.D., Gilman, J.B., Gkatzelis, G.I., Holmes, C.D., Lamplugh, A., Lavi, A., Middlebrook, A.M., Montzka, D.M., Palm, B.B., Peischl, J., Pierce, B., Schwantes, R.H., Sekimoto, K., Selimovic, V., Tyndall, G.S., Thornton,

J.A., Van Rooy, P., Warneke, C., Weinheimer, A.J., Brown, S.S., 2021. Variability and Time of Day Dependence of Ozone Photochemistry in Western Wildfire Plumes. Environmental Science and Technology 55(15), 10280–10290.

Rogelj, J., Schaeffer, M., Friedlingstein, P., Gillett, N.P., Van Vuuren, D.P., Riahi, K., Allen, M., Knutti, R., 2016. Differences between carbon budget estimates unravelled. Nature Climate Change 6(3), 245–252.

Rowe, J.P., Zarzana, K.J., Kille, N., Borsdorff, T., Goudar, M., Lee, C.F., Koenig, T.K., Romero-Alvarez, J., Campos, T., Knote, C., Theys, N., Landgraf, J., Volkamer, R., 2022. Carbon monoxide in optically thick wildfire smoke: Evaluating TROPOMI using CU Airborne SOF column observations. ACS Earth and Space Chemistry 6, 1799–1812.

R'Honi, Y., Clarisse, L., Clerbaux, C., Hurtmans, D., Duflot, V., Turquety, S., Ngadi, Y., Coheur, P.F., 2013. Exceptional emissions of NH_3 and HCOOH in the 2010 Russian wildfires. Atmospheric Chemistry and Physics 13(8), 4171–4181.

Sachse, G.W., Hill, G.F., Wade, L.O., Perry, M.G., 1987. Fast-response, high-precision carbon monoxide sensor using a tunable diode laser absorption technique. Journal of Geophysical Research: Atmospheres 92, D2, 2071–2081.

Schinke, R., Grebenshchikov, S.Y., Zhu, H., 2008. The photodissociation of NO_2 in the second absorption band: Ab initio and quantum dynamics calculations. Chemical Physics 346(1-3), 99–114.

Schmidt, C., Hoffman, J., Prins, E., Lindstrom, S., 2013. GOES-R Advanced Baseline Imager (ABI) Algorithm Theoretical Basis Document For Fire / Hot Spot Characterization. https://www.star.nesdis.noaa.gov/goesr/documents/ATBDs/Baseline/ATBD_GOES-R_FIRE_v2.6_Oct2013.pdf.

Schneider, S.R., Lee, K., Santos, G., Abbatt, J.P., 2021. Air quality data approach for defining wildfire influence: Impacts on PM2.5, NO_2, CO, and O_3 in Western Canadian cities. Environmental Science and Technology 55(20), 13709–13717.

Schneising, O., Buchwitz, M., Reuter, M., Bovensmann, H., Burrows, J.P., 2020. Severe Californian wildfires in November 2018 observed from space: the carbon monoxide perspective. Atmospheric Chemistry and Physics 20, 3317–3332.

Sha, M.K., Langerock, B., Blavier, J.F.L., Blumenstock, T., Borsdorff, T., Buschmann, M., Dehn, A., De Mazière, M., Deutscher, N.M., Feist, D.G., García, O.E., Griffith, D.W.T., Grutter, M., Hannigan, J.W., Hase, F., Heikkinen, P., Hermans, C., Iraci, L.T., Jeseck, P., Jones, N., Kivi, R., Kumps, N., Landgraf, J., Lorente, A., Mahieu, E., Makarova, M.V., Mellqvist, J., Metzger, J.M., Morino, I., Nagahama, T., Notholt, J., Ohyama, H., Ortega, I., Palm, M., Petri, C., Pollard, D.F., Rettinger, M., Robinson, J., Roche, S., Roehl, C.M., Röhling, A.N., Rousogenous, C., Schneider, M., Shiomi, K., Smale, D., Stremme, W., Strong, K., Sussmann, R., Té, Y., Uchino, O., Velazco, V.A., Vigouroux, C., Vrekoussis, M., Wang, P., Warneke, T., Wizenberg, T., Wunch, D., Yamanouchi, S., Yang, Y., Zhou, M., 2021. Validation of methane and carbon monoxide from Sentinel-5 Precursor using TCCON and NDACC-IRWG stations. Atmospheric Measurement Techniques 14(9), 6249–6304.

Shephard, M.W., Cady-Pereira, K.E., 2015. Cross-track Infrared Sounder (CrIS) satellite observations of tropospheric ammonia. Atmospheric Measurement Techniques 8, 1323–1336.

Shogrin, M.J., Payne, V.H., Kulawik, S.S., Miyazaki, K., Fischer, E.V., 2023. Measurement report: Spatiotemporal variability of peroxy acyl nitrates (PANs) over Mexico City from TES and CrIS satellite measurements. Atmospheric Chemistry and Physics 23, 2667–2682.

Sillman, S., 1995. The use of NO_y, H_2O_2, and HNO_3 as indicators for ozone-NO x-hydrocarbon sensitivity in urban locations. Journal of Geophysical Research: Atmospheres 100, D7, 14175–14188.

Sillman, S., 1999. The relation between ozone, NO_x and hydrocarbons in urban and polluted rural environments. Atmospheric Environment 33(12), 1821–1845.

Simpson, I.J., Akagi, S.K., Barletta, B., Blake, N.J., Choi, Y., Diskin, G.S., Fried, A., Fuelberg, H.E., Meinardi, S., Rowland, F.S., Vay, S.A., Weinheimer, A.J., Wennberg, P.O., Wiebring, P., Wisthaler, A., Yang, M., Yokelson, R.J., Blake, D.R., 2011. Boreal forest fire emissions in fresh Canadian smoke plumes: C 1-C 10 volatile organic compounds (VOCs), CO_2, CO, NO_2, NO, HCN and CH_3CN. Atmospheric Chemistry and Physics 11(13), 6445–6463.

Singh, H., Anderson, B., Brune, W., Cai, C., Cohen, R., Crawford, J., Cubison, M., Czech, E., Emmons, L., Fuelberg, H., 2010. Pollution influences on atmospheric composition and chemistry at high northern latitudes: Boreal and California forest fire emissions. Atmospheric Environment 44, 4553–4564.

Singh, H., Cai, C., Kaduwela, A., Weinheimer, A., Wisthaler, A., 2012. Interactions of fire emissions and urban pollution over California: Ozone formation and air quality simulations. Atmospheric Environment 56, 45–51.

Stavrakou, T., Müller, J.F., De Smedt, I., Van Roozendael, M., Van Der Werf, G., Giglio, L., Guenther, A., 2009. Global emissions of non-methane hydrocarbons deduced from SCIAMACHY formaldehyde columns through 2003–2006. Atmospheric Chemistry and Physics 9(11), 3663–3679.

Stavrakou, T., Müller, J.F., Bauwens, M., De Smedt, I., Van Roozendael, M., De Mazière, M., Vigouroux, C., Hendrick, F., George, M., Clerbaux, C., Coheur, P.F., Guenther, A., 2015. How consistent are top-down hydrocarbon emissions based on formaldehyde observations from GOME-2 and OMI? Atmospheric Chemistry and Physics 15(20), 11861–11884.

Stockie, J.M., 2011. The Mathematics of Atmospheric Dispersion Modeling. SIAM Review 53, 349–372.

Stockwell, C.E., Bela, M.M., Coggon, M.M., Gkatzelis, G.I., Wiggins, E., Gargulinski, E.M., Shingler, T., Fenn, M., Griffin, D., Holmes, C.D., Ye, X., Saide, P.E., Bourgeois, I., Peischl, J., Womack, C.C., Washenfelder, R.A., Veres, P.R., Neuman, J.A.,

Gilman, J.B., Lamplugh, A., Schwantes, R.H., McKeen, S.A., Wisthaler, A., Piel, F., Guo, H., Campuzano-Jost, P., Jimenez, J.L., Fried, A., Hanisco, T.F., Huey, L.G., Perring, A., Katich, J.M., Diskin, G.S., Nowak, J.B., Bui, T.P., Halliday, H.S., DiGangi, J.P., Pereira, G., James, E.P., Ahmadov, R., McLinden, C.A., Soja, A.J., Moore, R.H., Hair, J.W., Warneke, C., 2022. Airborne emission rate measurements validate remote sensing observations and emission inventories of western US wildfires. Environmental Science and Technology 56(12), 7564–7577.

Sullivan, P.C., 2020. GOES-R Series Spacecraft and Instruments, in: The GOES-R Series. Elsevier, pp. 13–21.

Tang, W., Emmons, L.K., Buchholz, R.R., Wiedinmyer, C., Schwantes, R.H., He, C., Kumar, R., Pfister, G.G., Worden, H.M., Hornbrook, R.S., Apel, E.C., Tilmes, S., Gaubert, B., Martinez-Alonso, S., Lacey, F., Holmes, C.D., Diskin, G.S., Bourgeois, I., Peischl, J., Ryerson, T.B., Hair, J.W., Weinheimer, A.J., Montzka, D.D., Tyndall, G.S., Campos, T.L., 2022. Effects of Fire Diurnal Variation and Plume Rise on U.S. Air Quality During FIREX-AQ and WE-CAN Based on the Multi-Scale Infrastructure for Chemistry and Aerosols (MUSICAv0). Journal of Geophysical Research: Atmospheres 127, e2022JD036650.

Team, U., Bontemps, S., Defourny, P., Van Bogaert, E., Team, E., Arino, O., Kalogirou, V., Perez, J.R., 2011. GLOBCOVER 2009 Products Description and Validation Report. https://epic.awi.de/id/eprint/31014/16/GLOBCOVER2009_Validation_Report_2-2.pdf. Last Accessed: 6 January 2025.

Theys, N., Yu, H., Franco, B., Clarisse, L., Volkamer, R., Cha, H., Kim, J., De Smedt, I., Stavrakou, T., van Gent, J., Van Roozendael, M., 2025. Atmospheric HONO Observed Over Global Biomass Burning Regions Using Satellite Observations of TROPOMI and GEMS. Journal of Geophysical Research: Atmospheres 130, e2024JD043163.

Thompson, D.K., Waddington, J.M., 2014. A Markov chain method for simulating bulk density profiles in boreal peatlands. Geoderma 232–234, 123–129.

Uselman, W.M., Lee, E.K., 1976. A study of nitrogen dioxide (2^2B_2) photodecomposition to O(^{1}D) and NO($^2\Pi$) in its second predissociation region 2500-2139 Å. The Journal of Chemical Physics 65(5), 1948–1955.

Valin, L., Fiore, A., Chance, K., González Abad, G., 2016. The role of OH production in interpreting the variability of CH_2O columns in the southeast US. Journal of Geophysical Research: Atmospheres 121(1), 478–493.

Van Geffen, J., Boersma, K.F., Eskes, H., Sneep, M., Ter Linden, M., Zara, M., Veefkind, J.P., 2020. S5P TROPOMI NO2 slant column retrieval: Method, stability, uncertainties and comparisons with OMI. Atmospheric Measurement Techniques 13(3), 1315–1335.

Vasudev, R., 1990. Absorption spectrum and solar photodissociation of gaseous nitrous acid in the actinic-wavelength region. Geophysical Research Letters 17(12), 2153–2155.

Veefkind, J., Aben, I., McMullan, K., Förster, H., de Vries, J., Otter, G., Claas, J., Eskes, H., de Haan, J., Kleipool, Q., van Weele, M., Hasekamp, O., Hoogeveen, R., Landgraf, J., Snel, R., Tol, P., Ingmann, P., Voors, R., Kruizinga, B., Vink, R., Visser, H., Levelt, P., 2012. TROPOMI on the ESA Sentinel-5 Precursor: A GMES mission for global observations of the atmospheric composition for climate, air quality and ozone layer applications. Remote Sensing of the Environment 120, 70–83.

Veraverbeke, S., Rogers, B.M., Goulden, M.L., Jandt, R.R., Miller, C.E., Wiggins, E.B., Randerson, J.T., 2017. Lightning as a major driver of recent large fire years in North American boreal forests. Nature Climate Change 7(7), 529–534.

Viatte, C., Strong, K., Paton-Walsh, C., Mendonca, J., O'Neill, N., Drummond, J., 2013. Measurements of CO, HCN, and C_2H_6 total columns in smoke plumes transported from the 2010 Russian boreal forest fires to the Canadian high Arctic. Atmosphere-Ocean 51(5), 522–531.

Wallace, J.M., Hobbs, P.V., 2006. Atmospheric Science: An Introductory Survey. volume 92. Elsevier.

Wan, N., Xiong, X., Kluitenberg, G.J., Hutchinson, J.S., Aiken, R., Zhao, H., Lin, X., 2023. Estimation of biomass burning emission of NO_2 and CO from 2019–2020 Australia fires based on satellite observations. Atmospheric Chemistry and Physics 23(1), 711–724.

Warneke, C., Schwarz, J.P., Dibb, J., Kalashnikova, O., Frost, G., Al-Saad, J., Brown, S.S., Brewer, W.A., Soja, A., Seidel, F.C., Washenfelder, R.A., Wiggins, E.B., Moore, R.H., Anderson, B.E., Jordan, C., Yacovitch, T.I., Herndon, S.C., Liu, S., Kuwayama, T., Jaffe, D., Johnston, N., Selimovic, V., Yokelson, R., Giles, D.M., Holben, B.N., Goloub, P., Popovici, I., Trainer, M., Kumar, A., Pierce, R.B., Fahey, D., Roberts, J., Gargulinski, E.M., Peterson, D.A., Ye, X., Thapa, L.H., Saide, P.E., Fite, C.H., Holmes, C.D., Wang, S., Coggon, M.M., Decker, Z.C.J., Stockwell, C.E., Xu, L., Gkatzelis, G., Aikin, K., Lefer, B., Kaspari, J., Griffin, D., Zeng, L., Weber, R., Hastings, M., Chai, J., Wolfe, G.M., Hanisco, T.F., Liao, J., Campuzano Jost, P., Guo, H., Jimenez, J.L., Crawford, J., 2023. Fire Influence on Regional to global Environments and Air Quality (FIREX-AQ). Journal of Geophysical Research: Atmospheres 128, e2022JD037758.

Warner, J.X., Wei, Z., Strow, L.L., Barnet, C.D., Sparling, L.C., Diskin, G., Sachse, G., 2010. Improved agreement of AIRS tropospheric carbon monoxide products with other EOS sensors using optimal estimation retrievals. Atmospheric Chemistry and Physics 10, 9521–9533.

van der Werf, G.R., Randerson, J.T., Giglio, L., Collatz, G.J., Mu, M., Kasibhatla, P.S., Morton, D.C., DeFries, R.S., Jin, Y., van Leeuwen, T.T., 2010. Global fire emissions and the contribution of deforestation, savanna, forest, agricultural, and peat fires (1997–2009). Atmospheric Chemistry and Physics 10, 11707–11735.

Whitburn, S., Van Damme, M., Kaiser, J., van der Werf, G., Turquety, S., Hurtmans, D., Clarisse, L., Clerbaux, C., Coheur, P.F., 2015. Ammonia emissions in tropi-

cal biomass burning regions: Comparison between satellite-derived emissions and bottom-up fire inventories. Atmospheric Environment 121, 42–54.

Wizenberg, T., Strong, K., Jones, D.B.A., Lutsch, E., Mahieu, E., Franco, B., Clarisse, L., 2023. Exceptional Wildfire Enhancements of PAN, C2H4, CH3OH, and HCOOH Over the Canadian High Arctic During August 2017. Journal of Geophysical Research: Atmospheres 128, e2022JD038052.

Wizenberg, T., Strong, K., Walker, K., Lutsch, E., Borsdorff, T., Landgraf, J., 2021. Intercomparison of CO measurements from TROPOMI, ACE-FTS, and a high-Arctic ground-based Fourier transform spectrometer. Atmospheric Measurement Techniques 14(12), 7707–7728.

Wolfe, G.M., Nicely, J.M., St. Clair, J.M., Hanisco, T.F., Liao, J., Oman, L.D., Brune, W.B., Miller, D., Thames, A., González Abad, G., Ryerson, T.B., Thompson, C.R., Peischl, J., McKain, K., Sweeney, C., Wennberg, P.O., Kim, M., Crounse, J.D., Hall, S.R., Ullmann, K., Diskin, G., Bui, P., Chang, C., Dean-Day, J., 2019. Mapping hydroxyl variability throughout the global remote troposphere via synthesis of airborne and satellite formaldehyde observations. Proceedings of the National Academy of Sciences 116(23), 11171–11180.

Wooster, M., Zhukov, B., Oertel, D., 2003. Fire radiative energy for quantitative study of biomass burning: Derivation from the BIRD experimental satellite and comparison to MODIS fire products. Remote Sensing of Environment 86(1), 83–107.

Wyatt, N., 2019. Horsefly Fire, outside Lincoln, burns 500 acres. https://nbcmontana.com/news/local/public-meeting-set-for-horsefly-fire. Source: NBC Montana, Last Accessed: 24 November 2024.

Xue, T., Tong, M., Wang, M., Yang, X., Wang, Y., Lin, H., Liu, H., Li, J., Huang, C., Meng, X., Zheng, Y., Tong, D., Gong, J., Zhang, S., Zhu, T., 2023. Health impacts of long-term NO_2 exposure and inequalities among the Chinese population from 2013 to 2020. Environmental Science and Technology 57(13), 5349–5357.

Yamanouchi, S., Strong, K., Lutsch, E., Jones, D.B., 2020. Detection of HCOOH, CH_3OH, CO, HCN, and C_2H_6 in Wildfire Plumes Transported Over Toronto Using Ground-Based FTIR Measurements From 2002–2018. Journal of Geophysical Research: Atmospheres 125(16), e2019JD031924.

Yokelson, R.J., Urbanski, S.P., Atlas, E.L., Toohey, D.W., Alvarado, E.C., Crounse, J.D., Wennberg, P.O., Fisher, M.E., Wold, C.E., Campos, T.L., Adachi, K., Buseck, P.R., Hao, W.M., 2007. Emissions from forest fires near Mexico City. Atmospheric Chemistry and Physics 7, 5569–5584.

York, D., 1968. Least squares fitting of a straight line with correlated errors. Earth and Planetary Science Letters 5, 320–324.

Yurganov, L., Rakitin, V., 2022. Two Decades of Satellite Observations of Carbon Monoxide Confirm the Increase in Northern Hemispheric Wildfires. Atmosphere 13(9), 1479.

Yurganov, L.N., Rakitin, V., Dzhola, A., August, T., Fokeeva, E., George, M., Gorchakov, G., Grechko, E., Hannon, S., Karpov, A., Ott, L., Semutnikova, E., Shumsky, R., Strow, L., 2011. Satellite- and ground-based CO total column observations over 2010 Russian fires: accuracy of top-down estimates based on thermal IR satellite data. Atmospheric Chemistry and Physics 11(15), 7925–7942.

Zhai, S., Jacob, D.J., Franco, B., Clarisse, L., Coheur, P., Shah, V., Bates, K.H., Lin, H., Dang, R., Sulprizio, M.P., Huey, L.G., Moore, F.L., Jaffe, D.A., Liao, H., 2024. Transpacific Transport of Asian Peroxyacetyl Nitrate (PAN) Observed from Satellite: Implications for Ozone. Environmental Science Technology 58, 9760–9769.

Zhang, L., Jacob, D.J., Yue, X., Downey, N.V., Wood, D.A., Blewitt, D., 2014. Sources contributing to background surface ozone in the US Intermountain West. Atmospheric Chemistry and Physics 14, 5295–5309.

Zhang, L., Lin, M., Langford, A.O., Horowitz, L.W., Senff, C.J., Klovenski, E., Wang, Y., Alvarez II, R.J., Petropavlovskikh, I., Cullis, P., Sterling, C.W., Peischl, J., Ryerson, T.B., Brown, S.S., Decker, Z.C.J., Kirgis, G., Conley, S., 2020. Characterizing sources of high surface ozone events in the southwestern US with intensive field measurements and two global models. Atmospheric Chemistry and Physics 20, 10379–10400.

Zhang, G., Pan, X., Hu, Y., Cao, R., Hu, Q., Fu, R., Hamdulla, R., Shang, B., 2024. Both Short-term and Long-term Ozone Pollution Alters the Chemical Composition of rice Grain. Bulletin of Environmental Contamination and Toxicology 113(2), 15.

Zhang, J., Guo, Y., Qu, Y., Chen, Y., Yu, R., Xue, C., Yang, R., Zhang, Q., Liu, X., Mu, Y., Wang, J., Ye, C., Zhao, H., Sun, Q., Wang, Z., An, J., 2020. Effect of potential HONO sources on peroxyacetyl nitrate (PAN) formation in eastern China in winter. Journal of Environmental Sciences 94, 81–87.

Zhang, Q., Wang, Y., Xiao, Q., Geng, G., Davis, S.J., Liu, X., Yang, J., Liu, J., Huang, W., He, C., Luo, B., Martin, R.V., Brauer, M., Randerson, J.T., He, K., 2025. Long-range PM2.5 pollution and health impacts from the 2023 Canadian wildfires. Nature 645(8081), 672–678.

Zhang, S., Solomon, S., Boone, C.D., Taha, G., 2024. Investigating the vertical extent of the 2023 summer Canadian wildfire impacts with satellite observations. Atmospheric Chemistry and Physics 24(20), 11727–11736.

Zhao, Y., Nielsen, C.P., Lei, Y., McElroy, M.B., Hao, J., 2011. Quantifying the uncertainties of a bottom-up emission inventory of anthropogenic atmospheric pollutants in China. Atmospheric Chemistry and Physics 11, 2295–2308.

Zhu, L., Jacob, D.J., Keutsch, F.N., Mickley, L.J., Scheffe, R., Strum, M., González Abad, G., Chance, K., Yang, K., Rappenglück, B., Millet, D.B., Baasandorj, M., Jaeglé, L., Shah, V., 2017. Formaldehyde (HCHO) as a hazardous air pollutant: Mapping surface air concentrations from satellite and inferring cancer

risks in the United States. Environmental Science and Technology 51(10), 5650–5657.